Prom. No. 3103

Potential Flow through Spiral Casings

THESIS

PRESENTED TO

THE SWISS FEDERAL INSTITUTE OF TECHNOLOGY, ZURICH

FOR THE DEGREE OF

DOCTOR OF TECHNICAL SCIENCES

BY

Nicholas Athanassiadis

Dipl. Mechan. and Elec. Engineer

Citizen of Greece

Accepted on the Recommendation of

Prof. Dr. J. Ackeret and Prof. H. Gerber

Zürich 1961

Dissertationsdruckerei Leemann AG

Erscheint als Nr. 30 der Mitteilungen aus dem Institut für Aerodynamik
an der Eidgenössischen Technischen Hochschule in Zürich
Herausgegeben von Prof. Dr. J. Ackeret

Verlag Leemann Zürich

Preface

The present work concerns theoretical and experimental investigations of the potential flow through two-dimensional and three-dimensional spiral casings of turbines and centrifugal pumps and blowers. These investigations were carried out at the Institute of Aerodynamics of the Swiss Federal Institute of Technology in Zurich.

I wish here to express my gratitude and thanks to Professor Dr. J. Ackeret, who suggested this problem and whose continuous interest and helpful directions immeasurably contributed to its success. I also wish to express my appreciation and thanks to Dr. H. Sprenger of the Institute for his help, as well as to Messrs. E. Hürlimann, A. Weiss and A. Berger for the construction of the experimental apparatus used, and to Mr. M. Tardi for the drawings contained in this paper.

Last but not least I wish to express my warm gratitude to the National Technical University of Athens and to the sponsors "Niarchos (London) Limited" — particularly to Mr. S. Niarchos — and "Hellenic Company of Chemical Products & Fertilizers Ltd.", Athens, for the scholarship they generously granted me, as well as to the "Studientkommission für Luftfahrt" of Switzerland for the financial support I received for publishing this paper.

Zurich, August 1960.

Nicholas Athanassiadis

Leer - Vide - Empty

Table of Contents

Principle Symbols 7

PART I

Flow Through Spiral Casings

1.1. Introduction to the Present Investigation 9
1.1.1. General Considerations 9
1.1.2. Design of Spiral Casings 12
1.1.3. Some Experimental Results Useful to the Present Investigation . . . 21
1.1.4. Approach to the Problem through the Potential Flow Theory 29

1.2. Potential Flow through Spiral Casings 32
1.2.1. Summary of the Potential Flow Theory 32
1.2.2. Boundary Conditions on Spiral Casings. Assumptions 35
1.2.3. Method of Solving Potential Flow Problems within Spiral Casings. . . 37

1.3. Electric Analogy Method 39
1.3.1. Potential Flow and Electric Field 39
1.3.2. Boundary Conditions on Electric Analogy Models 42
1.3.3. Electric Analogy on Spiral Casings 48
1.3.4. Some other Applications of the Electric Analogy Method 58

PART II

Experimental Investigation

2.1. Experimental Arrangement 60
2.1.1. Introduction 60
2.1.2. Description of the Spiral Casing Models Used. 61
a) The Logarithmic Shaped Spiral Model 62
b) The Archimedes' Shaped Spiral Model 64
c) The Three-Dimensional Spiral Model 64
d) The Collectors of the Electrodes 66
e) The Polar Circle 67
f) The Water-Level Indicator 68
2.1.3. Electrical Devices. 69
a) The Feeding Circuit 69
b) The Measuring Circuit 73
c) The Potential Pick-Up (Probe). 79

2.1.4. Measurement of the Specific Resistance of the Water 80
2.1.5. Procedure of the Measurements 82

2.2. Measurements on Two-Dimensional Models 87

2.2.1. Preliminary Experiments. Modification of the Collector Form 87
2.2.2. Measurements on the Logarithmic and Archimedes' Models for c_{r_0} Constant. Results 98
a) Measurements on the Logarithmic Model 100
b) Measurements on the Archimedes' Model 105
c) The Quasi-Logarithmic Law for c_{r_0} Constant. 110
d) Moment of Momentum and Dynamical Reaction of the Fluid . . . 111
2.2.3. Measurement on the Logarithmic and Archimedes' Models for c_{r_0} Variable along S_0. Results 117
a) The Quasi-Logarithmic Law for c_{r_0} Variable along S_0 120
b) The Circulation along S_0 123
c) The Generation of the Circulation 124

2.3. Measurements on the Three-Dimensional Model 128

2.3.1. Form of the Collector Used 128
2.3.2. Measurements for c_{r_0} Constant. Results 131
a) The Quasi-Logarithmic Law for c_{r_0} Constant. 136
b) Mean Radial Component of the Velocity 139
c) Moment of Momentum and Dynamical Reaction of the Fluid . . . 140
2.3.3. Measurements for c_{r_0} Variable along S_0. The Quasi-Logarithmic Law (General Expression) 143

PART III

Evaluation of the Experimental Results

3.1. Comparison between the Potential Flow and the Real Viscous Flow Described in § 1.1.3 146

3.2. General Considerations on Spiral-Casing Design 148

3.2.1. Boundary Conditions along S_0 and Spiral Form 148
3.2.2. Significance of Eq. (3.02) in Spiral Casing Design 150
a) Experimental Verification: Potential Flow through a Three-Dimensional Archimedes' Model 151
b) Moment of Momentum and Dynamical Reaction of the Fluid . . . 154
c) Meridian Sections Form 155
d) Some Notes on the Boundary Conditions along S_0. Operating Conditions other than Normal. 157
3.2.3. Spiral Casing Design Deviating from Eq. (3.02) 158
a) Turbine Spiral Casings Deviating from Eq. (3.02) 160
b) Centrifugal Pump and Blower Spirals Deviating from Eq. (3.02) . . 161
c) Comparison between Eq. (1.17) and Eqs. (3.02) and (3.06) 162
3.2.4. Fixed Blade Design 163
a) Fixed Blade Design in Casings which Are According to Eq. (3.02) . 163
b) Fixed Blade Design in Casings Deviating from Eq. (3.02) 166

Summary 173

Zusammenfassung 174

List of References 175

Principle Symbols

x, y, z	=	cartesian coordinates.
r, θ, z	=	cylindrical coordinates.
$\vec{c}\,(c_x, c_y, c_z)$	=	velocity along cartesian coordinates.
$\vec{c}\,(c_r, c_t, c_z)$	=	velocity along cylindrical coordinates.
α	=	$\sphericalangle\,(c, c_t)$ angle between c and c_t.
ϕ	=	velocity potential.
ψ	=	stream function in two-dimensional problems.
ρ	=	fluid density.
p	=	static pressure.
q	=	$\rho/_2\, c^2$ dynamic pressure.
p_{tot}	=	$p+q$ total pressure.
V	=	electric potential.
J	=	electric current.
R	=	electric resistance.
σ	=	specific resistance of isotropic and homogeneous electrolyte.
$\vec{i}\,(i_r, i_t, i_z)$	=	electric current density along cylindrical coordinates.
A	=	discontinuity point of the velocity potential of a spiral casing (tongue-edge).
S	=	control surface on potential flow.
S_0	=	surface surrounding the guide vanes (turbines), or the impeller (pumps, blowers).
r_0	=	radius of S_0.
S_a	=	surface surrounding the fixed blades.
r_a	=	radius of S_a.
S_p or S_e	=	cross-section of the inlet pipe (turbines), or discharge pipe (pumps, blowers).
Q_0	=	volume flow-rate through a spiral casing.
c_∞ or c_e	=	Q_0/S_p or Q_0/S_e velocity through Sp or S_e respectively.
b	=	moment of momentum of the fluid, passing through a surface per unit time, with respect to the z-axis.
μ	=	moment or torque of the static pressure with respect to the z-axis.

but because of larger capacities which require considerable space around every turbine. Thus, in both cases, there occurred the necessity of developing a casing of a suitably compact form, through which the water passes into the guide vanes of the turbine. In such a casing the water must have a somewhat higher velocity. It is well known that the main purpose of the guide vanes is to give a rotation (moment of momentum) to the water, thus producing a better efficiency of the runner; at the same time, the guide vanes are used as regulating equipment (speed control). Consequently, the casing should be designed to give the water either a part or even the total amount of the required moment of momentum.

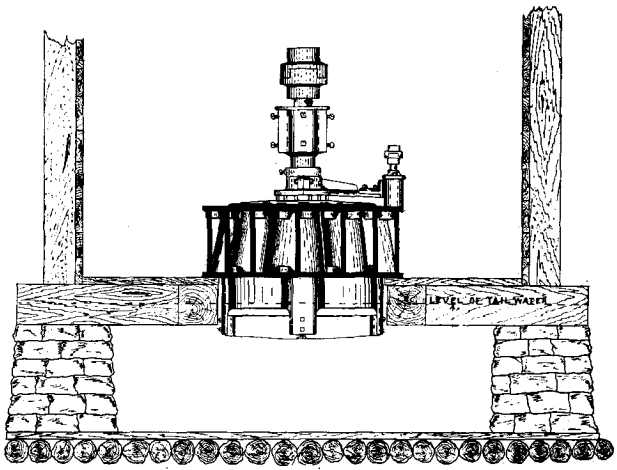

Fig. 1.01. General layout of an old-type hydraulic turbine; adjustable guide vanes were already in use. (Courtesy of the Allis-Chalmers Co.)

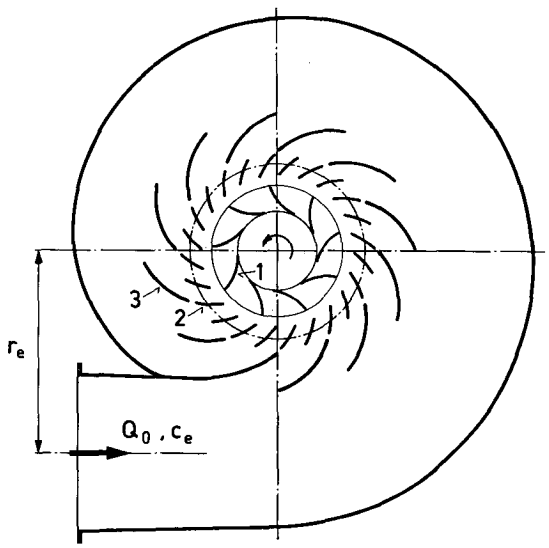

Fig. 1.02. Typical form of a turbine spiral casing (Francis-type). 1. runner; 2. adjustable guide vanes; 3. fixed blades.

The motion of the water through the guide vanes has, in general, two components; a radial component, which is a measure of the quantity of the water that passes through per unit time, and a tangential component, which is a measure of its *moment of momentum* per unit mass. The water passing through the guide vanes is thereby given a centripetal *spiral motion*. Accordingly, the casing should be, above all else, *a spiral-shaped casing*. A typical Francis-turbine spiral casing is shown in Fig. 1.02. One can see the *runner*, the *guide vanes* and, outside them, the *fixed blades*, the main purpose of which is the straingthening of the turbine casing; the fixed blades neverthe-

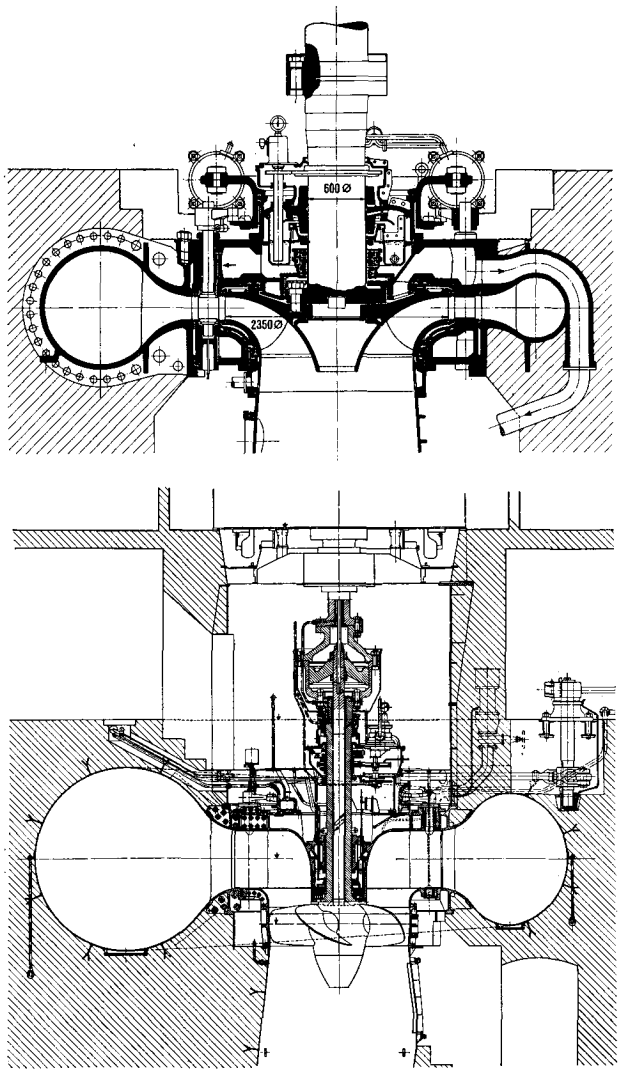

Fig. 1.03. Longitudinal sections of modern reaction type hydraulic turbines: *Upper:* A Francis turbine of large size. *Below:* A Kaplan turbine of moderate size. The casings have the typical spiral form as shown in Fig. 1.02. (Courtesy of the Escher Wyss Co.)

less, often contribute to a better guidance of the water flow. The casing is directly connected to the inlet pipe.

In Kaplan-type or Propeller-type turbines of moderate and small sizes the spiral casing has, in general, the same form as that of the Francis-type (Fig. 1.03). The casing in the modern large-size Kaplan turbines, however, has a different shape (Fig. 1.04).

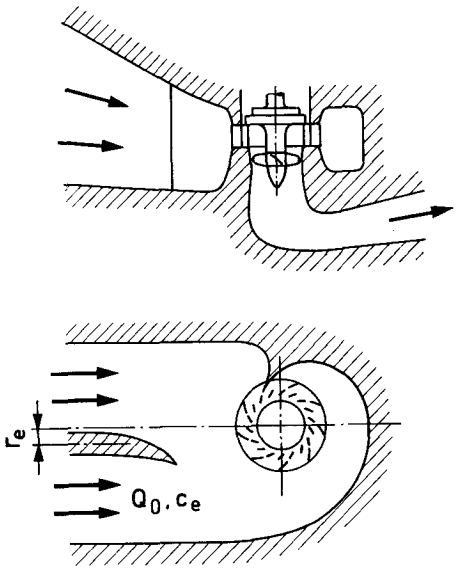

Fig. 1.04. Typical casing form of a modern large-size Kaplan turbine.

The main characteristic of the casings in question is that the shapes of their inlet cross-sections are designed to give a moment of momentum to the water with respect to the turbine shaft from the section where the water enters the casing. The moment of momentum at the inlet can be given by

$$B_e = \rho\, Q_0\, c_e\, r_e .$$

In the case of centrifugal pumps, blowers, or compressors, the fluid leaves the impeller and is collected in a casing. A spiral casing is a suitable arrangement for this purpose. Guide vanes are not needed; in the usual constructions there are not even fixed blades. The function of the spiral casing here is also different from that in the turbines. In general, a considerable part of the kinetic energy of the fluid that leaves the impeller is transformed into pressure in the casing; in other words, the casing is, for the pumps and the blowers, not only a collector of the discharged fluid but also a *diffuser* in a spiral form. Hence it requires a design more detailed than that of the casings of the turbines.

1.1.2. Design of Spiral Casings

As an introduction to the present investigation we would like to give a brief description of the design of spiral casings as carried out in practice. Our purpose is not to pay attention to strength of material calculations or other

constructional details etc. We are interested especially in the design of spiral casing forms of Francis-type turbines derived from the characteristics of the flow about the runner. In particular, we shall examine the designing of those of the above casings which are *symmetrical* on a plane normal to the z-axis (axis of the runner) and have a guide-case bounded between two planes parallel to the plane of symmetry. Such a casing is usually considered bounded between its walls, its inlet cross-section S_e, and the cylindrical surface S_0 of radius r_0 which passes through the trailing edge of the fixed blades. Fig. 1.05a

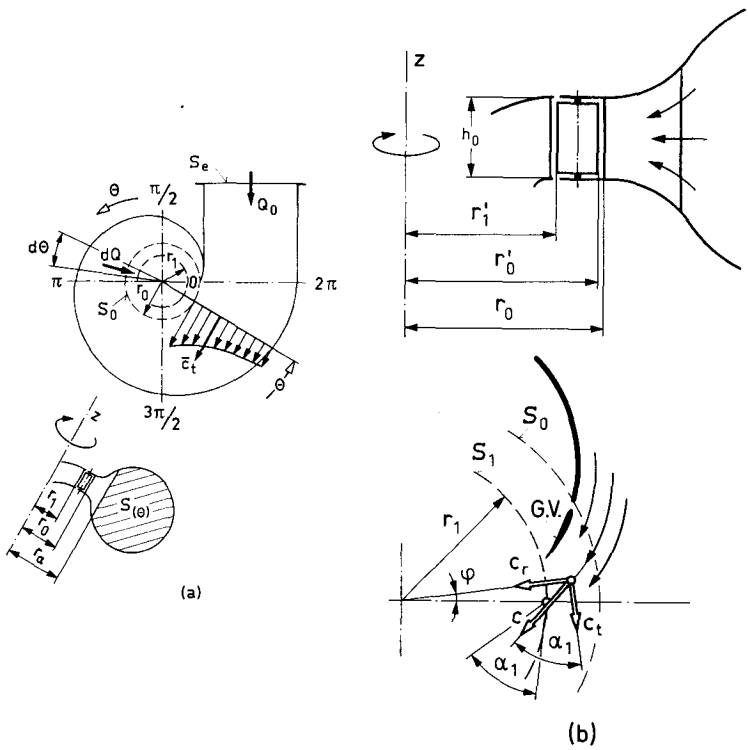

Fig. 1.05. Typical view of a turbine spiral casing; r_1 is the radius of the runner. The guide case is included between radii r_1 and r_a; r_a is the outer radius of the fixed blades.

shows the casing form in question diagrammatically. To simplify the picture both the guide vanes (which are in the space between radii r_0 and r_1) and the fixed blades (which extend from r_0 to r_a) have been omitted. The cylindrical surface S_1 of radius r_1 is the outer surface of the runner.

The above casing form is also used for centrifugal pump and blower spiral casings; the only differences are that the rotational direction of the impeller and the velocity of the fluid are opposite to those shown in Fig. 1.05 and that, often, neither guide vanes nor fixed blades exist.

The problem can be first approached by assuming that the water is an *incompressible* and *frictionless fluid*. Hence, the flow can be assumed to be two-dimensional on the surface S_0 and in the guide case inward up to the surface S_1. On the condition that the flow through the turbine is steady and con-

tinuous (constant runner speed and constant load) the designing of the spiral casings and also of the guide vanes is based on the two following desired conditions:

a) The differential fluid volume dQ passing per unit time through the differential sector $dS_1 = h_0 r_0 d\theta$ of the surface S_1 remains constant along S_1; i. e., since the flow through S_1 is considered two-dimensional,

$$\frac{dQ}{d\theta} = c_{r_1} r_1 h_0 = \text{const.}, \tag{1.01}$$

where $c_{r_1} = \text{const.}$ is the radial component of the velocity. The total volume flow-rate Q_0 through S_1 is

$$Q_0 = 2\pi r_1 h_0 c_{r_1};$$

and the volume flow-rate Q_θ between the origin $\theta = 0$ of the casing and the angle θ[1]) is:

$$Q_\theta = c_{r_1} r_1 h_0 \theta. \tag{1.02}$$

b) The tangential component c_{t_1} of the velocity along S_1 is constant; i. e.

$$c_{t_1} = \text{const.} \tag{1.03}$$

It is plain from the conditions (1.01) and (1.03) that the assumed two-dimensional flow on S_1 is identical to that generated by a *sink strength*

$$q = \frac{Q_0}{h_0} = 2\pi r_1 c_{r_1} = \text{const.},$$

and a circulation

$$\Gamma = 2\pi r_1 c_{t_1} = \text{const.},$$

both at the center of the runner (z-axis). Supposing, therefore, that the guide vanes and the fixed blades are removed, it is logical to assume that, for reasons of *continuity* and *inertia*, the water holds the same conditions at neighbouring places outside S_1, for example up to the surface S_0. Hence, in the region $r_1 \leqq r \leqq r_0$,

$$c_r r = \frac{q}{2\pi} = \text{const.}, \qquad c_t r = \frac{\Gamma}{2\pi} = \text{const.} \tag{1.04}$$

Namely, in the above region the fluid motion could be assumed to be a logarithmic spiral motion, the streamlines of which are of the form

$$r = r_1 e^{\varphi \operatorname{tg} \alpha_1}, \tag{1.05}$$

where: $\sphericalangle \varphi = \sphericalangle (r, r_1)$ (see also Fig. 1.05b),

and where:

$$\operatorname{tg} \alpha_1 = \frac{c_{r_1}}{c_{t_1}} = \frac{c_r}{c_t} = \frac{q}{\Gamma} = \text{const.} \tag{1.06}$$

The design of the guide-vanes assembly is based on the above reasonings (see also refs. [28] and [29]); we can see in Fig. 1.05b the position of the guide

[1]) The positive direction of θ shown in Fig. 1.05 and according to which Eq. (1.02) is derived, is used in the case of pumps rather than turbines. In the present investigation, however, we shall use this direction for both cases because of the simplicity of the formulas so obtained.

vanes under normal running conditions of the turbine. The guide vanes are identical to each other, and equally spaced about the runner; their *mean camber line* is in general a segment of the logarithmic spiral form, given by Eq. (1.05), between $r_0'\,(r_0' < r_0)$ and $r_1'\,(r_1' > r_1)$.

Let us now examine the spiral casing form outside S_0. Let the casing be bounded between the previously mentioned two parallel planes at a distance h_0, which now are extended from S_0 to infinity, and a *logarithmic spiral* cylindrical wall, normal to these planes, of the form

$$r_s = r_1 e^{\theta \operatorname{tg} \alpha_1}$$

of Eq. (1.05), where here $0 \leqq \theta < \infty$ (see Fig. 1.06). It is well known that if the conditions (1.01) and (1.03) are valid on S_1, the flow through this casing, outside S_1, is determined, since the motion of the fluid there is a logarithmic

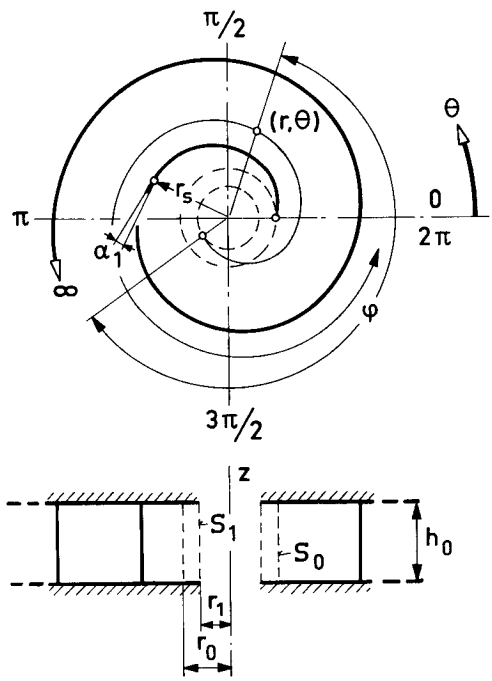

Fig. 1.06. Two-dimensional logarithmic spiral casing extended to infinity.

spiral motion to infinity. Eqs. (1.04) and (1.06) are no longer approximate consequences of Eqs. (1.01) and (1.03) but, on the contrary, exact conditions which are valid on every radius $r_1 \leqq r < \infty$. The flow outside S_1 is a pure logarithmic one, generated from a (q, Γ) pair at the axis of the runner. The streamlines of this flow are of the form given by Eq. (1.05):

$$r = r_1 e^{\varphi \operatorname{tg} \alpha_1},$$

where

$$0 \leqq \varphi < \infty.$$

Consider now an *axially symmetric* casing outside S_0 extended to infinity (as shown in Fig. 1.07). If, in this generalized casing,

$$c_{r_0}(r_0, \theta, z) = \text{const.}$$
$$c_{t_0}(r_0, \theta, z) = \text{const.} \tag{1.07}$$

along S_0, the flow is axially symmetric and free from any vortex ($\text{rot}\,\vec{c} = 0$) outside S_0; that is, it remains the same on every meridian plane of the casing to infinity. The components (c_r, c_t, c_z) of the velocity in cylindrical coordinates are functions of the coordinates r and z only (independent of angle θ). Under this limitation it is proved (see in Lamb § 94 ref. [17] and also in ref. [24]) that the meridian motion (c_r, c_z) of the fluid can be assumed as analogous in some of its properties to the two-dimensional flow. Consequently, as mentioned by *W. Kucharski*, ref. [16] (see also *C. Pfleiderer*, ref. [21]), it is possible to trace the *meridian streamlines* in some symmetrical casing forms; for example, if at a distance from S_0 the casings are bounded by two parallel planes, or two conical surfaces, or two z-axis coaxial cylindrical surfaces etc. as shown in Fig. 1.07 a at (1), (2), and (3), respectively. The intersections between the meridian planes and the stream-surfaces of the flow (surfaces a, b, c, etc.) are curves normal to the meridian velocities c_m, $(c_m = \sqrt{c_r^2 + c_z^2})$; these are the meridian streamlines.

If we now choose one particular stream-surface as a *boundary* and extend it to infinity, e. g. the surface (b) in Fig. 1.07 a at (2) which passes through the generatrix $(r_0, \theta = 0)$ of S_0, we form a *spiral casing* which is extended in the θ direction to infinity; obviously the flow through such a casing is axially symmetric. The volume flow-rate Q_θ through a meridian section at angle θ, $(0 \leqq \theta \leqq 2\pi)$, is

$$Q_\theta = \int_{r_0}^{r_s} c_t h \, dr .$$

Hence the continuity condition of the flow through the differential segment $d\theta$ at the angle θ, can be expressed by the following relation:

$$\frac{dQ}{d\theta} = c_{r_0} r_0 h_0 = \frac{d}{d\theta}\left(\int_{r_0}^{r_s} c_t h \, dr\right). \tag{1.08}$$

To examine the tangential motion (c_t) of the fluid, let us consider an infinitesimally thin flow-sheet lying between the cylindrical surfaces S_e and S_0 (see Fig. 1.07 b) and the similarly axially symmetric stream-surfaces S_a and S_b; then the continuity condition of the flow passing through this sheet is expressed as

$$\int_0^{2\pi} (c_{r_0} \delta z_0) r_0 \, d\theta = \int_0^{2\pi} (c_{r_e} \delta z_e) r_e \, d\theta ,$$

i. e.
$$2\pi r_0 \delta z_0 c_{r_0} = 2\pi r_e \delta z_e c_{r_e}, \tag{1.09}$$

where c_{r_e} is the radial component of the velocity on δz_e.

Let us now apply the *moment of momentum* theorem to the above flow sheet. Since the flow is considered stationary, this theorem is expressed as follows:

$$M_z = \iint_S \rho c_n c_t r \, ds - \iint_S p \cos(n, n_t) r \, ds , \tag{1.10}$$

where: $S = \delta S_e + \delta S_0 + S_a + S_b$, $(\delta S_e = 2\pi r_e \delta z_e,\ \delta S_0 = 2\pi r_0 \delta z_0)$ is the bounding surface of the sheet.

M_z is the torque (Force $\times$ radius) with respect to the z-axis applied on a solid object which may be within the surface S.

c_n is the normal component of the velocity on S;
n is the outward normal direction;
n_t is the tangential direction in relation to z-axis (n_t/c_t).

p is the static pressure distributed on S.

ρ is the fluid mass density ($\rho = \text{const.}$).

Since there is no object inside the flow sheet in question,

$$M_z = 0 .$$

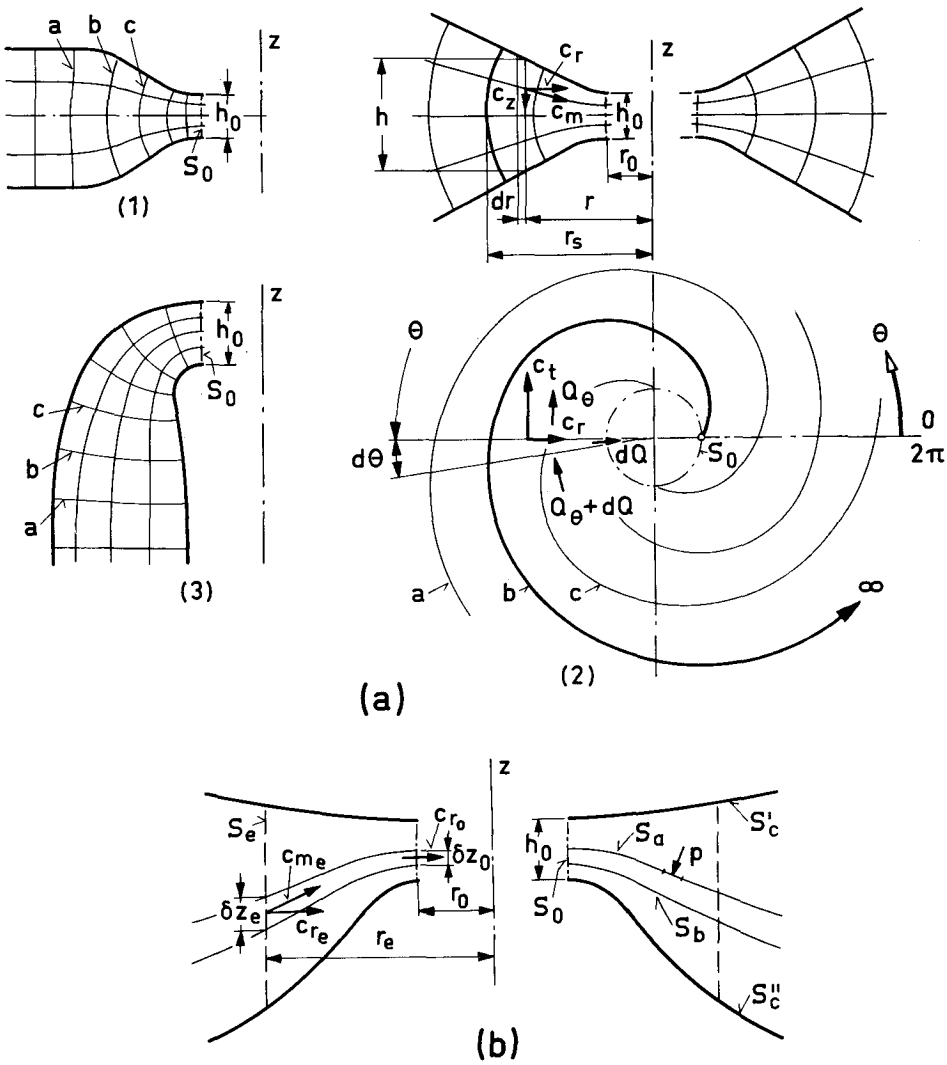

Fig. 1.07. Axially symmetric casings. In a) at (1), (2), (3) are shown three typical forms.

Furthermore, since the constituent surfaces of S are axially symmetric,

$$n \perp n_t$$

throughout S. Therefore, the second integral on the right-hand member of Eq. (1.10) vanishes. Consequently,

$$\iint_S \rho c_n c_t r \, dr = 0. \tag{1.11}$$

Because S_a, S_b are stream-surfaces,

$$(c_n)_{S_a, S_b} = 0.$$

Hence we obtain from the above Eq. (1.11)

$$\int_0^{2\pi} (c_n c_t r_0^2 \delta z_0) \, d\theta + \int_0^{2\pi} (c_n c_t r_e^2 \delta z_e) \, d\theta = 0,$$

where:

$$\text{on } \delta S_0\text{: } c_n = c_{r_0} = \text{const.}; \quad c_t = c_{t_0} = \text{const.},$$
$$\text{on } \delta S_e\text{: } c_n = -c_{r_e} = \text{const.}; \quad c_t = c_{t_e} = \text{const.}$$

(We take as positive the outward direction of the velocity); thus,

$$2\pi r_0 c_{r_0} \delta z_0 c_{t_0} r_0 - 2\pi r_e c_{r_e} \delta z_e c_{t_e} r_e = 0.$$

Taking into account the continuity condition (1.09) we obtain

$$c_{t_0} r_0 = c_{t_e} r_e$$

and, since both the radius r_e and the flow sheet S are arbitrary, and $c_{t_0} = \text{const.}$ along S_0,

$$c_t r = c_{t_0} r_0 = \text{const.} \tag{1.12}$$

Eq. (1.12) expresses the fact that the *moment of momentum* of the fluid per unit mass remains *constant* throughout an axially symmetric casing extended outside a coaxial cylindrical surface S_0 to infinity, if along S_0,

$$c_{r_0}(r_0, \theta, z) = \text{const.},$$
$$c_{t_0}(r_0, \theta, z) = \text{const.},$$

or if, more generally,

$$c_{r_0}(r_0, \theta, z) = f(z),$$
$$c_{t_0}(r_0, \theta, z) = \text{const.}$$

Eq. (1.12) is fundamental in the design of spiral casings. We have seen that it is also used in the design of the guide vanes of the turbines (logarithmic flow between S_0 and S_1 (see Fig. 1.05b). Thus, for a spiral casing derived from an axially symmetric one in the manner previously mentioned (see Fig. 1.07a (2)) we have, according to Eq. (1.12), $c_t = c_{t_0} r_0 / r$. Inserting this value in Eq. (1.08) we obtain

$$\frac{dQ}{d\theta} = c_{r_0} r_0 h_0 = \frac{d}{d\theta}\left(c_{t_0} r_0 \int_{r_0}^{r_s} \frac{h}{r} dr\right).$$

Since $(c_{r_0}, c_{t_0}) = \text{const.}$ along S_0 (see Eq. (1.07)), by integration of the above relation between the origin $\theta = 0$ and θ we get

$$Q_\theta = c_{r_0} r_0 h_0 \theta = c_{t_0} r_0 \int_{r_0}^{r_s} \frac{h}{r} dr;$$

hence:

$$\frac{1}{h_0} \int_{r_0}^{r_s} \frac{h}{r} dr = \frac{c_{r_0}}{c_{t_0}} \theta = \theta \operatorname{tg} \alpha_0, \tag{1.13}$$

where α_0 is the angle between the velocity c_0 on S_0 and its c_{t_0} component.

Eq. (1.13) constitutes a relationship between the shape of a meridian section of the spiral casing and its position with respect to the origin $(r_0, \theta = 0)$ of the casing. The design of spiral casings, particularly of centrifugal pumps and blowers, is based on this relationship.

Thus, if we put

$$H_R(\theta) = \int_{r_0}^{r} \frac{h}{r} dr,$$

we obtain

$$\frac{H_R}{h_0} = \theta \operatorname{tg} \alpha_0, \tag{1.14}$$

throughout the casing to infinity ($\theta \to \infty$).

In the case of a two-dimensional casing, Eq. (1.14) takes the form of a logarithmic spiral

$$r_s = r_0^{\theta \operatorname{tg} \alpha_0},$$

as already mentioned.

In the literature on centrifugal pumps and blowers (see, for example, refs. [5], [9], [10], [21]) graphical and numerical methods for finding several desired meridian sections are described; e. g. circular, trapezoidal, trapezoidal and rectangular, which satisfy the dimensionless Eq. (1.14) between the origin $(r_0, \theta = 0)$ of the casing and $\theta = 2\pi$. Beyond $\theta = 2\pi$ the casing surface is extended in a convenient way to form the discharge pipe (or duct) of the casing. The flow in the pipe (or the duct) is *no longer* axially symmetric. By so changing the configuration in which Eq. (1.12), consequently Eq. (1.14), is valid, a *deviation* from the desired flow must also occur at every point of the casing within the region $\theta < 2\pi$. It is plain, however, that this deviation decreases as we approach the origin $(r_0, \theta = 0)$ of the casing.

A second deviation may arise because Eq. (1.14) can be satisfied by any of an infinite number of forms of meridian sections at the same angle θ; for, this relationship is a necessary but *not* a sufficient condition for a correct formation of the meridian sections of the casing. It is valid only if the spiral casing is derived from *one and the same* stream-surface of an *axially symmetric* flow which is chosen as a boundary and is extended to infinity. Hence, using Eq. (1.14) alone, it is possible to design a casing form which is far from being an appropriate one.

In the design of spiral casings described above the fluid is assumed to be incompressible and frictionless. But since water and air are viscous fluids a correction of the shape obtained should be made, taking into account the

influence of the friction (see, for example, refs. [9] and [21]). In the case of blowers an additional correction is necessary because of the compressibility of the air (see refs. [5] and [10]).

For the design of the spiral casings of turbines the above-mentioned method, i.e. the design by means of Eq. (1.14), is not the only one in use. Several authors, as for example *R. Thomann* (see ref. (29]), favor Eq. (1.14). But others as *A. Tenot* (see ref. [28]), give an entirely different method, even if, for the design of the guide vanes, they use Eqs. (1.04). According to the latter method, by assuming that Eq. (1.01), consequently Eq. (1.02), is valid (and ignoring Eq. (1.03)) we can calculate the area S_θ (see Fig. 1.05a) of a meridian section of the casing at an angle θ from the relationship

$$S_\theta = \frac{Q_\theta}{\bar{c}_t}, \tag{1.15}$$

where

$$\bar{c}_t = \frac{1}{S_\theta} \iint_{S_\theta} c_t \, d\,S,$$

is the mean value of the tangential component of the velocity on S_θ, and where, according to Eqs. (1.01) and (1.04),

$$Q_\theta = \int_0^\theta c_{r_0} r_0 h_0 \, d\,\theta = c_{r_0} r_0 h_0 \theta, \quad (c_{r_0} = \text{const.}).$$

The area $S_{2\pi}$, of the entrance section of the casing at $\theta = 2\pi$, is

$$S_{2\pi} = \frac{Q_0}{c_T}, \tag{1.16}$$

where

$$c_T \equiv \bar{c}_t(2\pi);$$

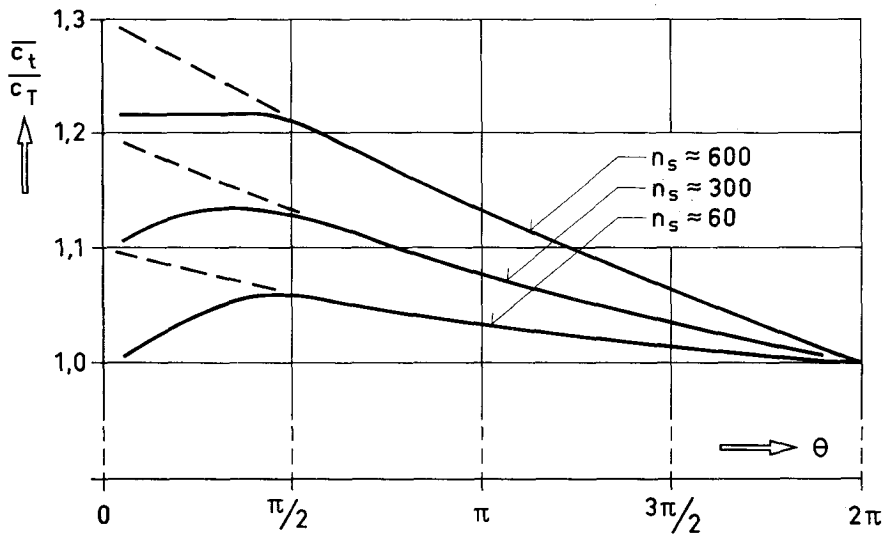

Fig. 1.08. Typical form of $\bar{c}_t/c_T$-curves for circular meridian sections. The corresponding actual values in any particular casing form will not be too far different from those indicated.

thus from Eqs. (1.15) and (1.16) we obtain

$$\frac{S_\theta}{S_{2\pi}} = \frac{Q_\theta}{Q_0}\frac{1}{\bar{c}_t/c_T} = \frac{\theta}{2\pi}\frac{1}{\bar{c}_t/c_T}. \tag{1.17}$$

To calculate S_θ, therefore, we must determine the values of c_T and $\bar{c}_t/c_T$. Both are determined empirically. The value of c_T is assumed, varying with the construction, not to exceed a few meters/sec. The original value of $\bar{c}_t/c_T$, according to this method, was $\bar{c}_t/c_T = 1$ throughout the region $\theta \leqq 2\pi$. But in the casings so designed an excessive hydraulic shock occurred, especially between the vanes of the rotating runner and the *tongue* of the casing ($\theta = 0,2\pi$). The ratio $\bar{c}_t/c_T$, therefore, is generally taken as a function of the angle θ having as parameter the specific speed n_s of the turbine.[2]) These curves are traced experimentally in such a way as to obtain, under the influence of both *inertia* and *friction* forces, the best flow conditions possible (velocities, and static pressure) around S_0. It is plain that a particular family of curves of the above kind corresponds to every casing form (which is mainly characterized by the form of its meridian shapes). Comparing the form of the above $\bar{c}_t/c_T$ curves to the law (1.12) of constant moment of momentum (see also Fig. 1.05a), we see that they agree qualitatively from about $\theta = \pi/2$. For angles less than $\pi/2$, $\bar{c}_t$ is assumed constant or having a slightly decreasing slope. In general, as n_s increases, $\bar{c}_t/c_T$ also increases and will always be greater than one except at $\theta = 2\pi$ where it is unity. There are many spiral-casing constructions, however, in which $\bar{c}_t = c_T$ throughout the region $\theta \leqq 2\pi$ and others in which, for special reasons, $\bar{c}_t < c_T$ for $\theta < 2\pi$. In all the above cases the angle $\alpha_0 = \alpha_1$, ($\operatorname{tg}\alpha_1 = c_{r_1}/c_{t_1}$), at the tongue of the casing (see Fig. 1.05) is calculated by Eq. (1.06) under normal running conditions of the turbine.

It can be concluded from the two methods of designing spiral casings described above that neither the first nor the second can give a clear picture of the flow through an actual casing form, even if the fluid is assumed incompressible and frictionless. Thus, in order to secure an optimum uniform flow along the surface S_0 (since in addition the guide vanes are adjustable because they are used as speed control equipment of the turbine), an assembly of fixed blades is often placed outside S_0 (see Figs. 1.02 and 1.05). Like the guide vanes, the fixed blades are identical and equally spaced. Moreover, the fixed blades play an important part in strengthening the casing and the entire turbine installation.

1.1.3. Some Experimental Results Useful to the Present Investigation

A program of experiments to see the formation of the flow, particularly through the region of the fixed blades and the guide vanes of turbine spiral casings, was carried out in the S.F.I.T. Institute of Aerodynamics. For these experiments some turbine spiral casing models were used, and air instead of water.[3]) It is outside our scope to go through these experiments; the results

[2]) This modification as well as the diagram in Fig. 1.08 and the empirical values of c_{r_0}/c_e, c_T, α_w, etc. with respect to n_s, mentionned in § 3.2.3 at c), where obtained mainly from the lectures of Professor *H. Gerber* on *Hydraulic Machinery* at the *Swiss Federal Institute of Technology*, Zurich.

[3]) In this place we want to express our thanks to the firm *Charmilles Maschinenbau AG, Genf, Schweiz*, which generously left us a spiral casing model for the above experiments.

for one of these models, however, are of interest in our investigation. By means of them we can estimate the probable flow conditions along the surface S_0 (which surrounds the guide vanes) and, in this manner, approach the problem using the *potential flow* theory, which is our purpose. In this section we shall give a short description of these experiments and the most interesting of their results for our purposes. In the next section we shall discuss these results in detail.

The model used was made of plastic material and wood; inside the casing there was a guide case with 24 adjustable guide vanes; outside the vanes,

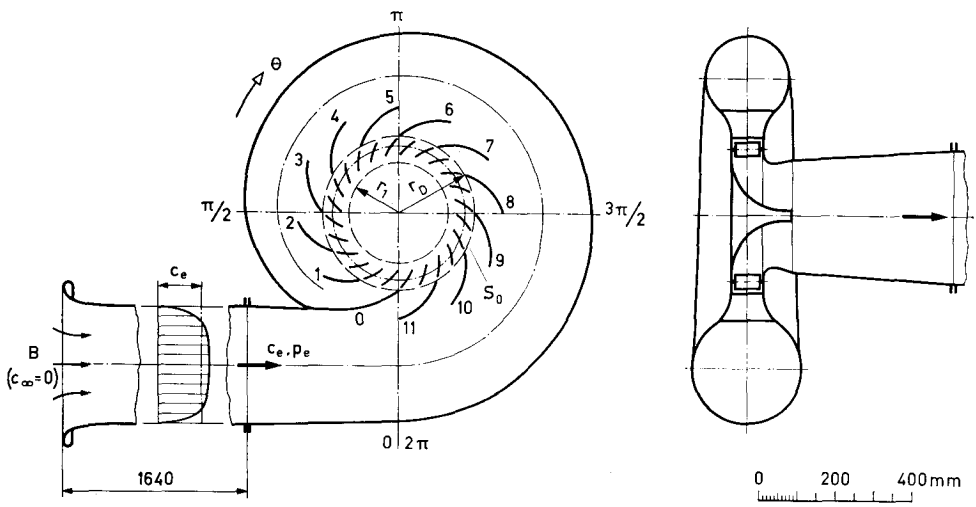

Fig. 1.09. The spiral casing model used for the experiments with air.

a) *Guide-vane shape:* Chord length 51,4 mm; max. thickness 7,3 mm, at $^1/_3$ of its length; normal position at $\approx 45°$.

b) *Fixed-blade shape:* Circular arc of radius 150 mm; chord length 140 mm; thickness 5 mm (constant); inner diameter $2r_0 = 395$ mm; outer diameter $2r_a = 545$ mm.

c) *Inlet pipe:* Diameter 300 mm. (Detailed dimensions of the casing are given in § 2.1.2, *Table I* on a scale 1 : 0,6).

there was an assembly of 12 identical, equally-spaced, fixed blades. In Fig. 1.09 are shown the longitudinal and cross-sections of the model. Plots of the characteristics $H_s(\theta)/h_0$ and $\bar{c}_l/c_T$ vs. θ of this casing (see § 1.1.2) are shown in Fig. 1.10 at (a) and (b), respectively. The dotted line at (a) presents the form of the function H_R/h_0 according to Eq. (1.14) where $\alpha_s(0) = 45°$, ($\operatorname{tg} 45° = 1$); thus according to Eq. (1.14) we should have:

$$\frac{H_R}{h_0} = \theta \operatorname{tg} \alpha_s(0) = \theta, \qquad (0 \leqq \theta \leqq 2\pi).$$

One can see from the plots in Fig. 1.10 that the geometrical form of the model used was not designed according to the first method mentioned in § 1.1.2. It could not possibly have been designed by the second method either, since the form of its $\bar{c}_l/c_T$-curve shows no similarity to the convenient typical forms given in

Fig. 1.08. The model was designed so as to provide a rather small inlet pipe cross-section[4]). Inside the guide case the wood has the form of the runner hub without its vanes. The air passing through the casing model was sucked by a fan (which is not shown in Fig. 1.09). The suction duct was long enough (1640 mm) to avoid any disturbance of the velocity profile at the entrance of the casing. During the measurements, the pressure in the casing did not fall below 100 mm of water under atmospheric pressure; therefore, the air was assumed to be an incompressible fluid. The Reynolds' number at the entrance was about $Re \approx 200\,000$.

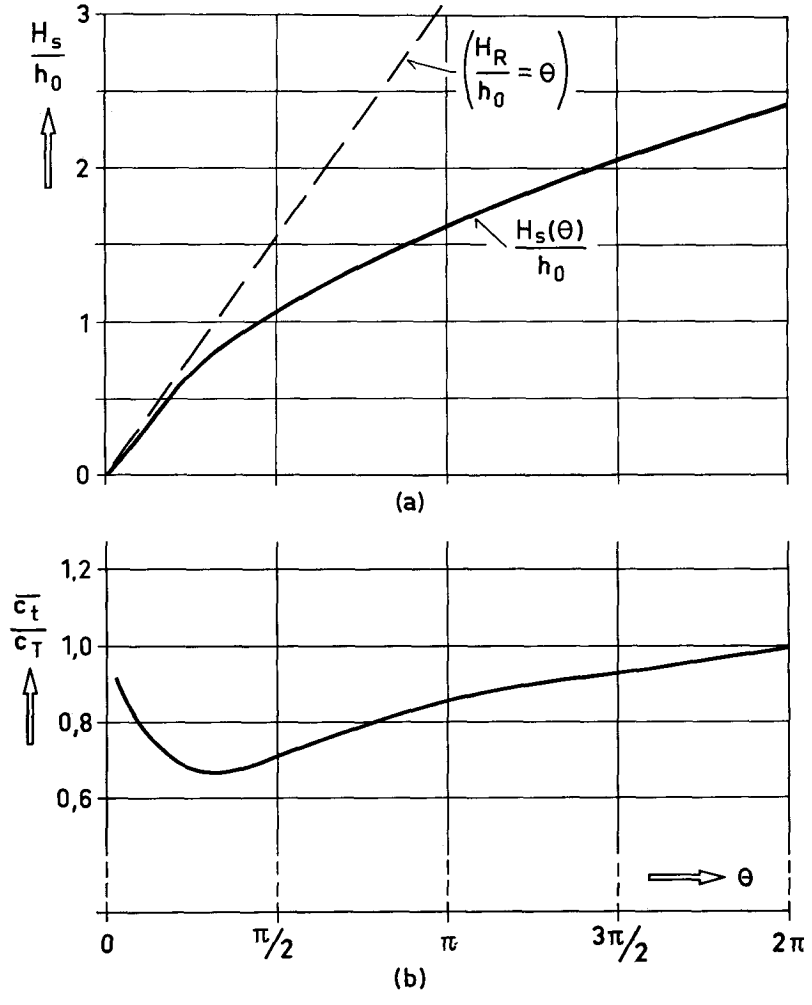

Fig. 1.10. Characteristics of the spiral casing model shown in Fig. 1.09; a) The ratio $H_s(\theta)/h_0$ (see § 1.1.2); b) the ratio $\bar{c}_t/c_T$, according to Eq. (1.17).

[4]) This model was taken from an actual turbine spiral casing drawing where, because of limited space in the power station, the inlet pipe had to be of a rather small diameter.

From the experiments done on this model, we shall examine two series of measurements concerning the distributions of static and total pressures and velocity. The first measurements were made on the cylindrical surface of radius $r_1' = 180$ mm inside the fixed blades when the guide vanes were removed; this surface corresponds to that surrounding the guide vanes when the turbine runs under normal conditions. The second measurements were made on the cylindrical surface of radius $r_1 = 130$ mm inside the guide vanes; this corresponds to the entrance surface of the runner. In these measurements the guide vanes were replaced and adjusted to correspond to the normal running conditions of the turbine.

The static and total pressures were measured as pressure differences between the measuring point and the atmospheric pressure B. Static pressure was measured by the difference

$$\Delta p = p - B,$$

and total pressure by the difference

$$\Delta g = g - B = \Delta p + \frac{\rho}{2} c^2;$$

c is the velocity; Δg represents the loss of energy per unit volume of the fluid between atmospheric conditions (B, $c_\infty = 0$) and the examined point in the casing.

The results were plotted in a normalized dimensionless form, with respect to the mean velocity c_e and the dynamic pressure q_e at the entrance of the casing (see Fig. 1.09) where

$$q_e = \frac{\rho}{2} c_e^2 = B - p_e = \Delta p_e.$$

On the diagrams in Figs. 1.11, 1.12, 1.13 the following normalized ratios are plotted:

a) the velocity distribution: c/c_e,
b) the static pres. distribution: $\Delta p/q_e$,
c) the energy losses distribution: $\Delta g/q_e$.

The above distributions along the circumferences of radii r_0' and r_1' at the plane of symmetry of the casing are plotted in Figs. 1.11 and 1.12, respectively, under steady air-flow conditions through the casing. The diagrams in Figs. 1.13 a and (b) give the static and total pressure axial distribution (parallel to the z-axis).

As already mentioned, the diagrams in Figs. 1.12 and 1.13 correspond to the normal running conditions of the turbine; in this case the camber lines of the guide vanes are logarithmical extrapolations of those of the fixed blades; their inclination is about 45°.

To facilitate the study of the diagrams in Figs. 1.11 and 1.12, the angular distance between successive fixed blades is taken as abscissa unit, instead of the angle θ; the numbers $0, 1, 2, \ldots, 11$, correspond to the fixed blade numbers shown in Fig. 1.09; the angle between them equals 30°.

From the diagrams some observations can be made, which are valid for both series of measurements, i. e. without or with guide vanes:

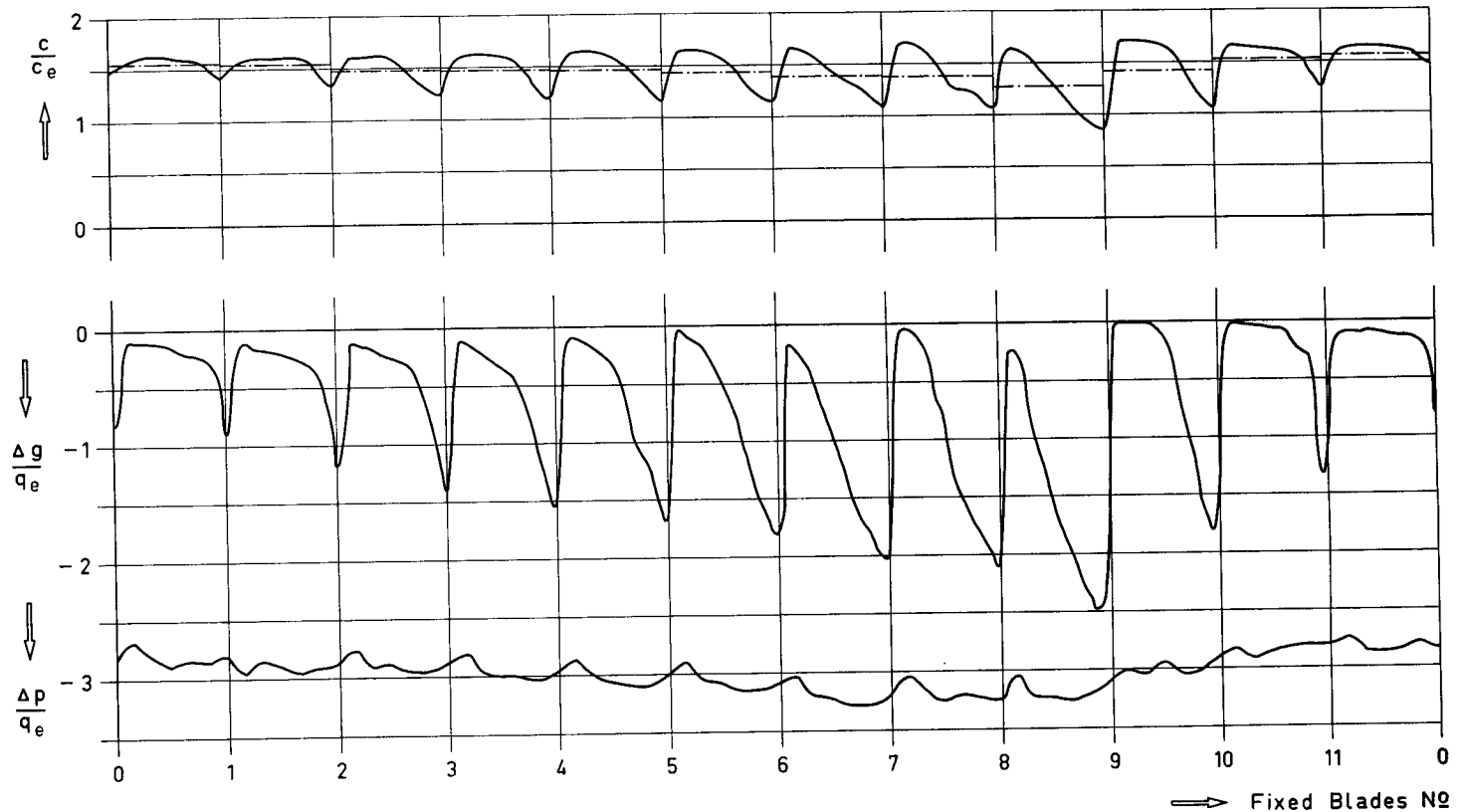

Fig. 1.11. Velocity, Static- and Total-pressure distributions on the plane of symmetry of the casing, at $r_0' = 180$ mm, without guide vanes.

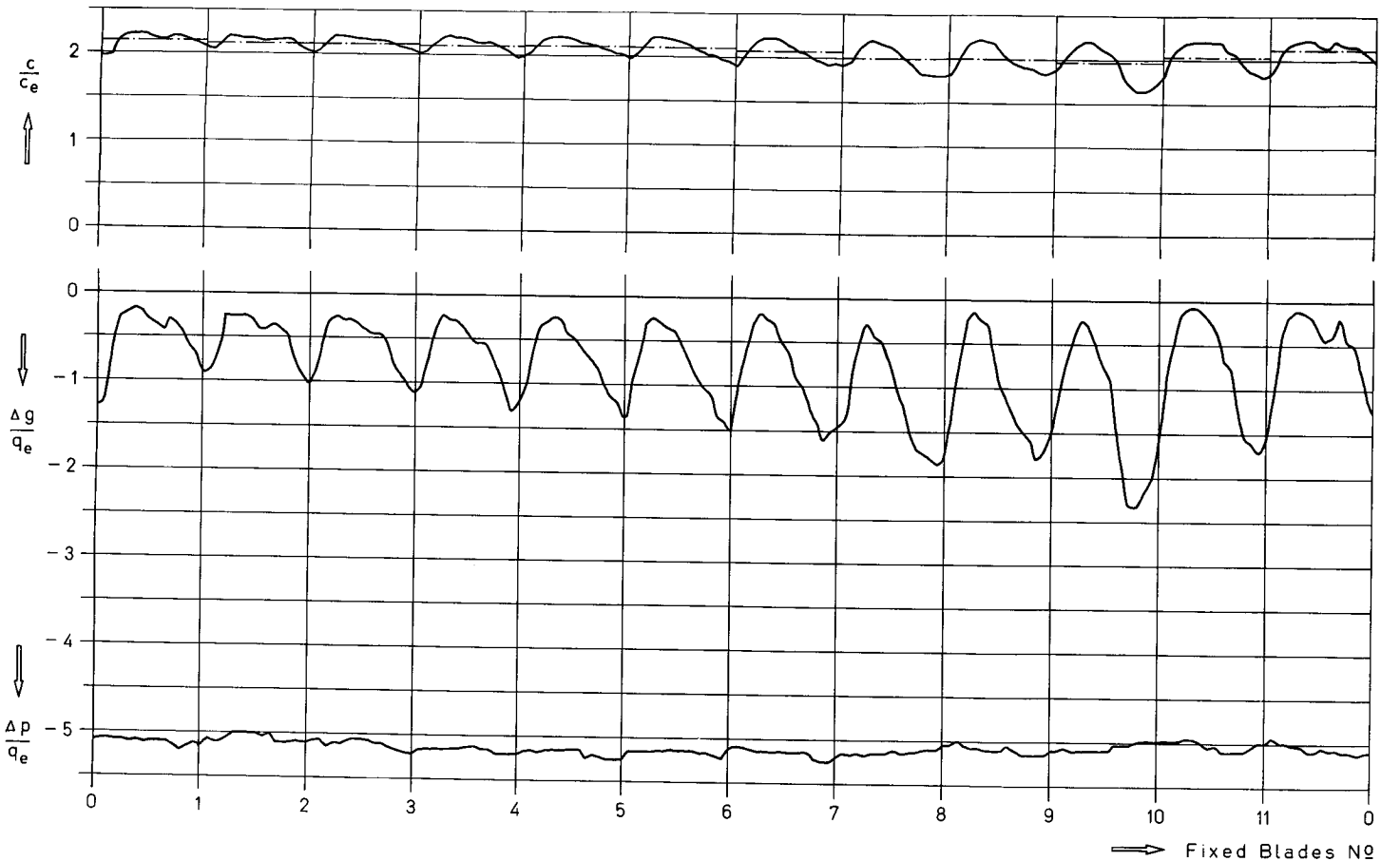

Fig. 1.12. Velocity, Static- and Total-pressure distributions on the plane of symmetry of the casing, at $r_1 = 130$ mm, with guide vanes adjusted to their normal position.

a) There is a periodic change of the velocity c/c_e as well as of the $\Delta g/q_e$ between successive fixed blades; the influence of the guide vanes on the angular amplitude of the period is negligible. Hence the periodic forms of the c/c_e and the $\Delta g/q_e$ distributions seem to be mainly due to the fixed blades (friction influence).

b) Both the $\max(c/c_e)$ and the $\min|\Delta g/q_e|$ on every fixed-blade opening remain relatively constant; this is valid especially for $\max(c/c_e)$. A slight increase of the $\min|\Delta g/q_e|$ near the tongue of the casing (openings between 0, 1, 2, 3 fixed blades) is due to the existing boundary layer at the entrance of the casing (see Fig. 1.09). There is an extremely large variation of $\max|\Delta g/q_e|$, however, between fixed blade openings. The biggest loss of energy occurs through the (9) and (10) openings (see Figs. 1.11 and 1.12 respectively).

c) The periodic change of the velocity through the openings shows that the boundary layer on the concave side of the fixed blades is larger than that on their convex side (see Figs. 1.11 and 1.12). An exception occurs at the

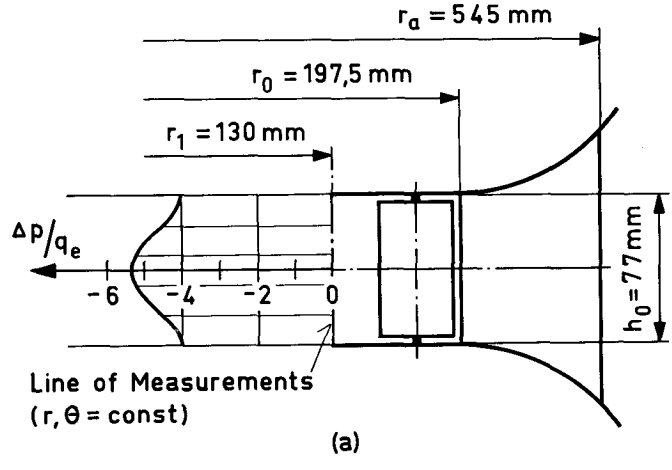

Fig. 1.13a. Static pressure distribution along h_0 ($\theta = \text{const.}$), in a narrow region behind each one of the guide vanes. Except for very small changes, this diagram is typical for points behind the guide vanes which correspond to the (3)-, (4)-, ..., and (9)-fixed blades.

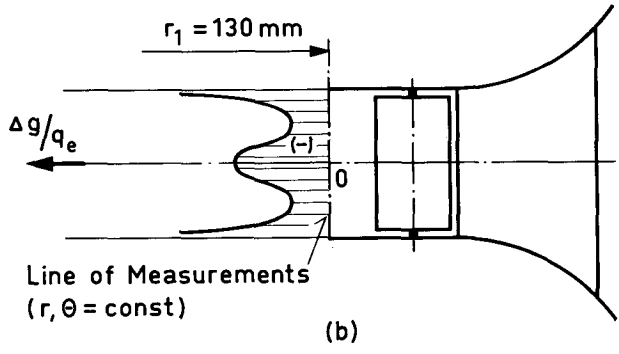

Fig. 1.13b. Distribution of energy losses measured at same planes as the above static pressures. The $\Delta g/q_e$-curves v.s. h are typical; because of the large variations of $\max|\Delta g/q_e|$ from blade to blade (see Fig. 1.12) their numerical values are not given.

openings between the (3) and (0) fixed blades where the distribution of the velocity is somewhat symmetrical.

d) The mean velocity c_n^{n+1} $(n=0, 1, \ldots, 11)$ undergoes rather small changes between successive fixed blades. As shown in Fig. 1.11, its maximum decrease of about 12 % occurs only at the (9) opening. With guide vanes (see Fig. 1.12), the decrease is even smaller; the minimum of the mean velocity exists now at the (10) opening, and it is only 7 % smaller than that in the others.

Comparing the diagrams in Figs. 1.11, 1.12, and 1.13a we can see that the following results are obtained in the case using guide vanes.

I. A perfect uniformity of the static pressure distribution on the plane of symmetry of the casing within the guide vanes (see Fig. 1.12). Moreover, this uniformity holds also at planes parallel to the plane of symmetry, as shown in Fig. 1.13a; in the same figure, however, we see that the static pressure increases from the plane of symmetry to the walls of the guide case.

II. A perceptible decrease of the variations of the velocity through the openings between fixed blades. Thus, while in Fig. 1.11 the velocity through the (9) opening varies by 50 % of its maximum, Fig. 1.12 shows that at the (10) opening the variation is only 25 %. On the other hand, in the region between the (3), (2), (1), and (0) fixed blades the velocity variation does not exceed ± 5 % of its mean value.

III. A rectification of the mean velocity between openings. Thus, as mentioned at observation d), in the most irregular area (the (10) opening) its decrease does not exceed 7 %.

From the above we infer the following: Even the assembly of 24 guide vanes alone (without runner) constitutes a very efficient *rectifier* of the static pressure distribution as well as of that of the mean velocity through every opening on planes normal to the z-axis. Although measurements of the velocity distribution in a direction parallel to the z-axis were not made, it is indisputable that its periodic variation in planes parallel to that of symmetry will be even smaller than in the plane of symmetry itself. Consequently, in an actual turbine where there are guide-vanes and a *runner*, we can accept the first assumption mentioned in § 1.1.2 as true, according to which the flow-rate distribution around the runner remains constant. If, therefore, the casing is symmetrical with respect to a plane normal to the z-axis, and the fluid is assumed to be frictionless, Eq. (1.01) expresses an experimental fact.

Since the guide vanes as well as the fixed blades are equally spaced, using Eq. (1.01) we obtain the following relationship between the n and $n+1$ guide vanes:

$$\begin{aligned} &\text{on radius } r_1\colon\ (c_{r_1})_n^{n+1} \approx \frac{Q_0}{2\pi r_1 h_0}, \\ &\text{on radius } r_0\colon\ (c_{r_0})_n^{n+1} \approx \frac{Q_0}{2\pi r_0 h_0}, \end{aligned} \tag{1.18}$$

where $(c_{r_1})_n^{n+1}$, $(c_{r_0})_n^{n+1}$ are the mean radial components of the velocity, through the above intervals, on the surfaces S_1 (radius r_1) and S_0 (radius r_0), respectively.

Let us now consider the distribution $\Delta g/q_e$ of the energy losses. As can be seen from Figs. 1.11, 1.12, and 1.13b the influence of the guide vanes on this distribution is negligible. Apparently, the loss of energy is mainly due to the presence of the fixed blades; its distribution remains practically the same,

whether the guide vanes are present or not. Large irregularities of the same form in both Figs. 1.11 and 1.12 characterize the distribution of $\Delta g/q_e$ and its maximum from opening to opening between the fixed blades. On the other hand, the distribution of the energy losses on lines parallel to the z-axis within the guide vanes is also very irregular, and it shows a typical form as can be seen in Fig. 1.13b. Now, a logical consequence of the velocity profile form at the entrance of the casing (see Fig. 1.09) is that $\max |\Delta g/q_e|$ should occur at the (12) opening and at the openings between the (3) and the (0) fixed blades; we see in both Figs. 1.11 and 1.12, however, that $\max |\Delta g/q_e|$ occurs somewhere between the (7) and (10) fixed blades; i.e. in a region through which pass streamlines coming from places at the inlet pipe cross-section, where the fluid possesses its highest total energy; likewise, in the same region the variation of the velocity attains its maximum. Therefore, although the distribution of the mean velocity according to Eq. (1.18) is uniform, the flow form through the fixed-blade openings is far from being uniform.

It is suspected that a part of the irregularity of the velocity-distribution and energy losses-distribution may be caused by unsatisfactory relative configurations between the fixed blades and the spiral-casing form.

1.1.4. Approach to the Problem through the Potential Flow Theory

A detailed scrutiny of the causes of the extremely large variations of $\max |\Delta g/q_e|$ along S_0, already mentioned in the preceding section, could give us an interesting picture of the process of the flow through the spiral casing model. In our case, there are, in general, two main causes, each involving an increase of the energy losses of the air. The first is constituted of extremely high velocities through fixed blade openings; thus we observe rather high energy losses due to friction between the air and the walls. The second is constituted of a half- or a total separation of the stream from the fixed-blades walls, and is accordingly a turbulence. It is obvious from observations (II) and (III) of the preceding section that the first cause should be excluded, because the flow-rate through the various fixed-blade openings remains constant throughout S_0. All the observations led us to conclude that the variations of $\max |\Delta g/q_e|$ along S_0 are due to the presence of turbulence of a higher or a lower intensity between the various fixed blade openings.

Let us examine the phenomenon more closely; the turbulence in question could be generated, either before arriving at the fixed blades, or more probably, inside the openings between them. It is well known that a spiral casing, because of its curvature, causes a double vortex meridian secondary flow through itself (see refs. [6] and [15]); also, the velocity profile at the entrance cross-section has the typical form of a turbulent flow through straight circular pipes. Nevertheless, the fact that $\max |\Delta g/q_e|$ varies along S_0 while $\min |\Delta g/q_e| \approx$ $\approx$ const. and the maximum of $\max |\Delta g/q_e|$ occurs at the openings (8), (9), and (10) of Figs. 1.11 and 1.12, is evidence that the above causes have, in our case, a rather negligible influence.

We infer, therefore, that this turbulence is generated inside the fixed-blade region, and is due only to a quick increase of the boundary layer, with a possible ensuing result of a half or a toral separation of the flow from the blade walls.

The fixed blades are cylindrical surfaces having thin airfoil sections; they are also equally spaced along S_0; thus, turbulence in our case will occur chiefly as a result of the following independent conditions:

1. The openings between the fixed blades of the model constitute diffusers.
2. The radius of curvature of the blades is either much bigger or much smaller, etc., than that of the stream surfaces of the flow, in the case in which the fixed blades are not present.
3. An intensive *circulation* is generated around each one of the fixed blades because, as is well known, the fluid tends to satisfy Kutta-Joukowski's condition on the trailing edge of each one of them (see Fig. 1.14).

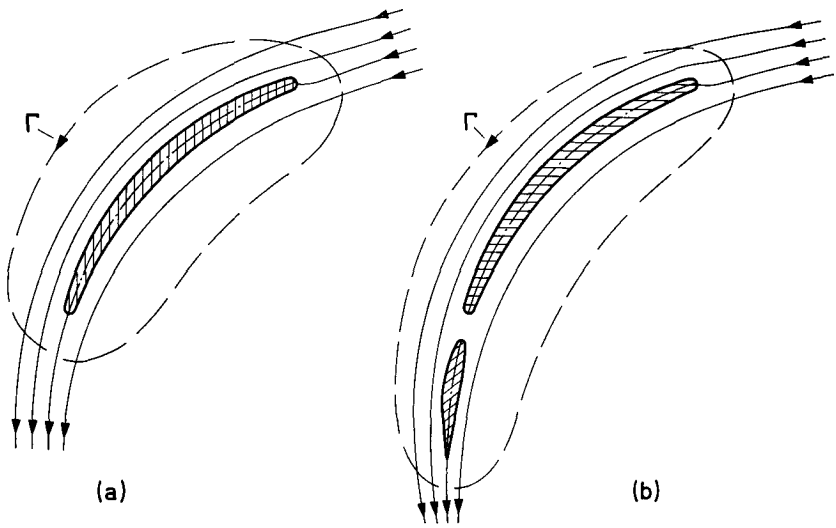

Fig. 1.14. Satisfaction of Kutta-Joukowski's condition: a) without guide vanes; b) with guide vanes adjusted to their normal position (see also refs. [7] and [23]).

The first cause should be excluded because the openings between fixed blades form nozzles and not diffusers. If we examine carefully the velocity distribution diagrams in Figs. 1.11 and 1.12, we see that between the (3), (2), (1), and (0) fixed blades the velocity shows very small variations, not exceeding ± 5 per cent of its mean value; furthermore, this variation is symmetrical (see observation c) § 1.1.3); on the other hand, the loss of energy in this region is the smallest we have along S_0. Consequently, the second reason, i.e. the influence of the curvature of the fixed-blades, should also be excluded.

We, therefore, infer that the main cause of the extremely large variations of $\max |\Delta g/q_e|$ along S_0 is a *distribution* of *circulation*, generated on each fixed blade. The typical form of Δp-distribution (see Fig. 1.13a) corroborates this hypothesis. In other words, because of their equally spaced position along S_0, the fixed-blades impose a uniform spiral motion on the flow through them; this kind of flow is, of course, desirable. However, it appears not to coincide with that which the spiral casing would impose if the fixed-blades were eliminated. In this circumstance, an *angle of attack* is formed between the fixed blades and the streamlines, generating a circulation. As the angle of attack

increases, the circulation becomes more intense. In the fixed blades where the magnitude of the circulation exceeds a limit value, there occurs a quick rise of the thickness of the boundary layer along one of their surfaces. Thus, the possibility of a half- or even a total separation of the flow is effected; it appears that this is the case between the (7) and (10) fixed blades. Keeping in mind observation c) of § 1.1.3 and the distribution of Δp shown in Figs. 1.11

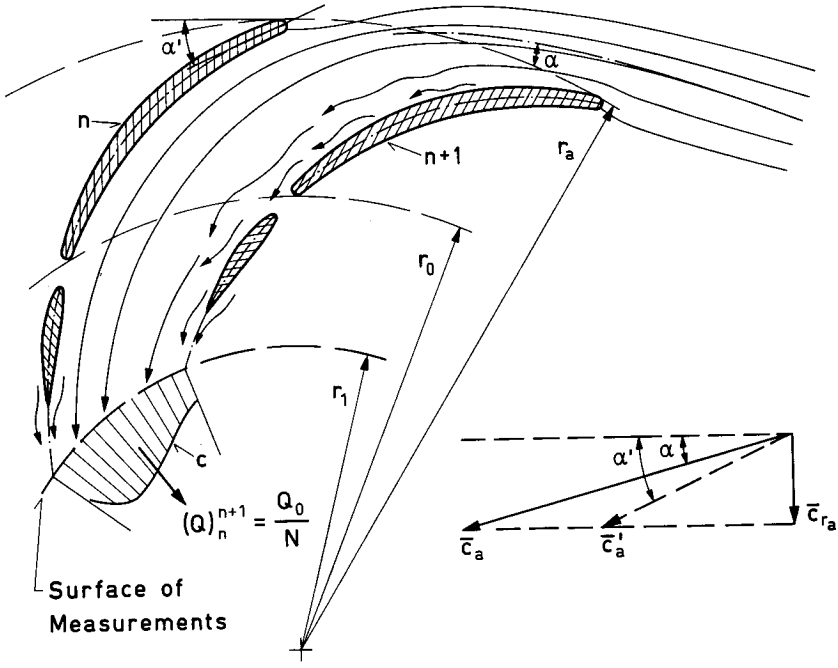

Fig. 1.15. A possible flow form through those fixed blades intervals where a high energy loss occurs (see also ref. [7]).

and 1.13a we can illustrate the flow through these fixed blades as in Fig. 1.15. The turbulence occurs on the suction surface of the blades. The lower side of Fig. 1.15 shows the mean velocity $\bar{c}_a$ which the casing imposes at the entrance of the fixed-blade region; $\bar{c}_a'$ is the mean velocity imposed by the fixed blades; both $\bar{c}_a$ and $\bar{c}_a'$ have the same radial component $\bar{c}_{r_a}$ because, as already mentioned in § 1.1.3 (Eq. (1.18)), $(c_{r_0})_n^{n+1} \approx$ const. throughout S_0.

The result of the above considerations is remarkable. The initial reason for the variation of max $|\Delta g/q_e|$ along S_0 is a circulation of greater or smaller intensity generated around each fixed blade; namely, it is a *potential effect.* The increase of the thickness of the boundary layer, and, possibly, the separation of the flow somewhere, are undoubtedly due to friction; in our case, however, they occur only because an intensive circulation is generated at these places.

Suppose for a moment that the fluid is not only incompressible but also frictionless, and that throughout the inlet pipe there does not exist any vorticity, i.e. $\mathrm{rot}\,\vec{c} = 0$. Then the flow through the region which is surrounded by the spiral casing and the surface S_0, excepting the fixed blades, is a *potential*

flow. Now, although, there are neither boundary layers and turbulances, nor any loss of energy the circulation around the fixed blades remains. It is evident that the most desired flow form is obtained when the fixed blades are placed so that the circulation around each one of them vanishes. Optimization occurs when the surfaces of the blades coincide with those potential flow stream surfaces generated in the case when the blades are removed. Returning to the motion of the actual viscous fluid, it is obvious that its flow through the so placed fixed blades, should be rather uniform; of course the loss of energy Δg, will reappear; however maximum energy loss between successive fixed blades will be uniformilly distributed and reduced to a *minimum*.

To summarize, we can say that from the experimental results given in the preceding section, we are led to the following conclusions:

a) The guide vane assembly constitutes an efficient rectifier of the flow through it (see Eq. (1.18)).

b) The potential effect constitutes the main factor in the formation of the flow through spiral casings, although an additional secondary meridian flow due to friction is also present. We wish to note here that we can be led to the same conclusion by studying the results obtained by *H. Kranz*, ref. [15], by means of his "Versuch No. 17" in a logarithmic spiral casing. The fluid he used was water. From "Abb. 32" of ref. [15] it is obvious that the influence of the friction is, in general, rather small, and it is observable in the region around the spiral tongue only.

1.2. Potential Flow through Spiral Casings

1.2.1. Summary of the Potential Flow Theory

It is known that a continuous and stationary flow of an incompressible and frictionless fluid is called *potential flow* in a considered region, if its velocity $\vec{c}$, as a vector, can be expressed as the *gradient* of a scalar function of (x, y, z) in it; i. e., if

$$\vec{c} = \operatorname{grad} \phi, \qquad c_x = \frac{\partial \phi}{\partial x}; \qquad c_y = \frac{\partial \phi}{\partial y}; \qquad c_z = \frac{\partial \phi}{\partial z}, \tag{1.19}$$

where $\phi = \phi(x, y, z)$ is the *velocity potential;* it is also known, that the necessary and sufficient condition for the validity of Eq. (1.19), is

$$\operatorname{rot} \vec{c} = 0.$$

Furthermore, if in the considered region there are no sources or sinks of the flow, the condition of continuity is expressed by

$$\operatorname{div} \vec{c} = \frac{\partial c_x}{\partial x} + \frac{\partial c_y}{\partial y} + \frac{\partial c_z}{\partial z} = 0,$$

or

$$\operatorname{div} \operatorname{grad} \phi = 0.$$

This relation constitutes *Laplace's* differential equation of potential flow, and in rectangular coordinates is written as:

$$\Delta\phi = \frac{\partial^2\phi}{\partial x^2} + \frac{\partial^2\phi}{\partial y^2} + \frac{\partial^2\phi}{\partial z^2} = 0. \tag{1.20}$$

In cylindrical coordinates (r, θ, z) it is given by:

$$\Delta\phi = \frac{\partial^2\phi}{\partial r^2} + \frac{1}{r}\frac{\partial\phi}{\partial r} + \frac{1}{r^2}\frac{\partial^2\phi}{\partial\theta^2} + \frac{\partial^2\phi}{\partial z^2} = 0. \tag{1.21}$$

The velocity potential ϕ, therefore, is a finite and continuous function, satisfying Laplace's equation; that means, it is a *harmonic function* in the region considered.

Consider a region τ and its bounding surface S, and let us assume that both τ and S constitute the field of a harmonic function, e.g. the velocity potential ϕ. Then, according to Gauss' *divergence theorem* we get

$$\iint_S c_n \, dS = \iiint_\tau \operatorname{div}\vec{c}\, d\tau = 0, \tag{1.22}$$

where $c_n = \partial\phi/\partial n$ is the component of the velocity $\vec{c}$, normal to S; n is the outward normal to S.

Let us now consider two scalar functions $\phi(x, y, z)$ and $F(x, y, z)$ which are both continuous and uniform with first derivatives also continuous and uniform in τ and on S. Applying Gauss' divergence theorem to a *compound lamellar* vector

$$\vec{A} = F \operatorname{grad}\phi,$$

we obtain

$$\iint_S A_n \, dS = \iiint_\tau \operatorname{div}\vec{A}\, d\tau, \tag{1.23}$$

where A_n is the component of $\vec{A}$ normal to the surface S. Thus,

$$A_n = F(\operatorname{grad}\phi)_n = F\frac{\partial\phi}{\partial n}.$$

On the other hand, forming the divergence, we get

$$\operatorname{div}\vec{A} = F\Delta\phi + \operatorname{grad}F \operatorname{grad}\phi.$$

Inserting these expressions in Eq. (1.23), we obtain *Green's Theorem (A):*

$$\iint_S F\frac{\partial\phi}{\partial n} dS = \iiint_\tau F\Delta\phi\, d\tau + \iiint_\tau \operatorname{grad}F \operatorname{grad}\phi\, d\tau. \tag{1.24}$$

Putting $F = \phi$ we get the relation

$$\iiint_\tau (\operatorname{grad}\phi)^2 d\tau = \iiint_\tau \left[\left(\frac{\partial\phi}{\partial x}\right)^2 + \left(\frac{\partial\phi}{\partial y}\right)^2 + \left(\frac{\partial\phi}{\partial z}\right)^2\right] d\tau = \iint_S \phi\frac{\partial\phi}{\partial n} dS - \iiint_\tau \phi\Delta\phi\, d\tau. \tag{1.25}$$

Furthermore, if ϕ is a harmonic function, for example a velocity potential, the second integral in the right-hand member of Eq. (1.25) vanishes, since $\Delta\phi = 0$; thus we obtain the important relationship

$$\iiint_{\tau} (\operatorname{grad}\phi)^2 d\tau = \iint_{S} \phi \frac{\partial \phi}{\partial n} dS, \tag{1.26}$$

which constitutes a direct connection between the distribution of the $(\operatorname{grad}\phi)^2$ (that is, the distribution of twice the kinetic energy of the field per unit mass of the fluid) within the region τ and the boundary conditions on its bounding surface S. It cannot be assumed, however, that both ϕ and $\partial\phi/\partial n$ can be arbitrarily given. On the contrary, we can show by means of Eq. (1.26), that if ϕ alone is given on S, the potential function in the region τ is uniquely determined; this is called, the *first boundary* — or *Dirichlet's problem.* Also, that if $\partial\phi/\partial n$ alone is prescribed on S, again the potential function in τ is determined; this is known as the *second boundary* — or *Neumann's problem.*

To prove the first, suppose there exist two different solutions ϕ_1 and ϕ_2 of Laplace's equation $\Delta\phi = 0$, in the region τ which throughout S give equal values,

$$(\phi_1)_S = (\phi_2)_S.$$

Their difference $u = \phi_1 - \phi_2$ is also a harmonic function in τ ($\Delta u = 0$), which vanishes ($u_s = 0$) on S. Thus, applying Eq. (1.26) to u, we obtain

$$\iiint_{\tau} \left[\left(\frac{\partial u}{\partial x}\right)^2 + \left(\frac{\partial u}{\partial y}\right)^2 + \left(\frac{\partial u}{\partial z}\right)^2\right] d\tau = \iint_{S} u \frac{\partial u}{\partial n} dS. \tag{1.27}$$

Since $u_s = 0$, the integral on the right vanishes; hence,

$$\iiint_{\tau} \left[\left(\frac{\partial u}{\partial x}\right)^2 + \left(\frac{\partial u}{\partial y}\right)^2 + \left(\frac{\partial u}{\partial z}\right)^2\right] d\tau = 0.$$

Here, the integrand is a sum of real squares; consequently we must have at every point of τ

$$\frac{\partial u}{\partial x} = \frac{\partial u}{\partial y} = \frac{\partial u}{\partial z} = 0.$$

In other words, u = const., and, since it is zero on S ($u_s = 0$), it must be zero throughout τ. Thus,

$$\phi_1 = \phi_2$$

in τ and on S; consequently $\partial\phi/\partial n$ on S is determined if ϕ on it is given.

We can prove Neumann's problem in the same way. Suppose two harmonic functions ϕ_1, ϕ_2 in τ, whose normal derivatives on S are

$$\left(\frac{\partial \phi_1}{\partial n}\right)_S = \left(\frac{\partial \phi_2}{\partial n}\right)_S.$$

Their difference $u = \phi_1 - \phi_2$ is also a harmonic function in τ, that is $\Delta u = 0$, and by definition $(\partial u/\partial n)_S = 0$. Therefore, from Eq. (1.27) we get again

$$\iiint_{\tau} \left[\left(\frac{\partial u}{\partial x}\right)^2 + \left(\frac{\partial u}{\partial y}\right)^2 + \left(\frac{\partial u}{\partial z}\right)^2\right] d\tau = 0.$$

Hence u = const., i.e. either $\phi_1 = \phi_2$, or $\phi_1 - \phi_2$ = const. ($\neq 0$). Thus, in the

case of the Neumann Problem, the potential function is uniquely determined in τ except perhaps for an additive constant.

As we shall see in the next section, the second boundary problem is of fundamental importance in our investigation, where ϕ is the velocity potential, because it allows us to use the experimental fact (see § 1.1.3) that the guide vanes and the runner of a turbine act as rectifiers of the flow through them. As noted ϕ is uniquely determined inside a region τ when $c_n = (\partial\phi/\partial n)_S$, the normal component of the velocity, is prescribed on every point of the boundary surface S.

1.2.2. Boundary Conditions on Spiral Casings. Assumptions

Let us consider a turbine spiral casing (see Fig. 1.16) whose inlet pipe is straight, of a constant cross-section, and extended to infinity.

To investigate the flow through this casing by means of the *potential theory*, we assume that:

1. The flow is continuous and stationary.
2. The fluid is incompressible and frictionless.
3. The fluid passing a section S_p of the pipe, far enough from A (see Fig. 1.16) is free from any *vortex* motion; that is $\mathrm{rot}\,\vec{c} = 0$, and
4. the fixed blades, or any other obstacles outside S_0, are removed; as mentioned in § 1.1.2, S_0 is the cylindrical surface of radius r_0 which passes through the location of the trailing edges of the fixed blades (see Fig. 1.05).

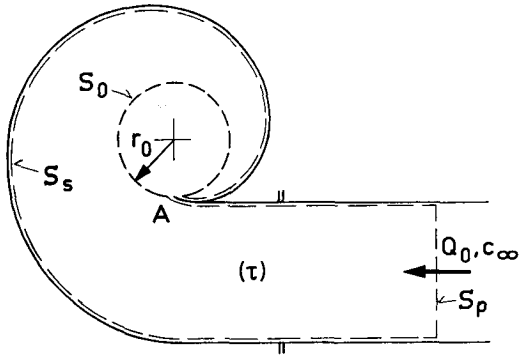

Fig. 1.16. Control surface of a spiral casing.

Furthermore, we take as a *control surface*, the surface S made up of S_0, the walls S_s of the casing, and a cross-section S_p of the inlet pipe far enough from A.

Thus,
$$S = S_p + S_s + S_0.$$

According to the above assumptions, the flow through the region τ bounded by S, and on S, is a *potential flow*. At A we have a *discontinuity;* in two-dimensional casings, A is a point; in the general case of three-dimensional casings, A represents a line on S_0. If $\phi(x, y, z)$ represents the velocity potential

function of the flow, the solution of the problem is referred to the solution of Laplace's differential equation $\Delta \phi = 0$.

We should, first of all, prescribe the boundary conditions on S; let us examine its components indiviudally:

a) The total volume flow-rate Q_0, through the section S_p passes into τ. Since the inlet pipe is straight, of a constant cross-section, and S_p is far enough from A, the flow through S_p may be assumed to be a *parallel* flow. Thus the velocity c_∞ there is constant,

$$c_\infty = \frac{Q_0}{S_p} = \left(\frac{\partial \phi}{\partial n}\right)_{S_p} = \text{const.}, \tag{1.28}$$

and the velocity potential on S_p is also constant,

$$\phi_p = \text{const.}$$

b) The surface S_s, of the casing and the inlet pipe walls up to S_p, is a *stream-surface;* thus,

$$\left(\frac{\partial \phi}{\partial n}\right)_{S_s} = 0. \tag{1.29}$$

c) The fluid leaves the casing through the surface S_0; thus,

$$Q_0 = S_p c_\infty = \iint_{S_0} \frac{\partial \phi}{\partial n} d S = \iint_{S_0} c_{r_0} d S, \tag{1.30}$$

where $c_{r_0} \equiv c_n = \partial \phi / \partial n$, is the radial component of the velocity through the cylindrical surface S_0. We can also write Eq. (1.30) in cylindrical coordinates (r, θ, z) [radius, angle, direction parallel to z-axis (see also Fig. 1.05)], as:

$$Q_0 = \iint_{S_0} r_0 c_{r_0}(\theta, z) d\theta dz.$$

One can see that the boundary conditions (normal velocity) are constant, respectively zero, on the surfaces S_p and S_s; however, this is not the case on S_0 since there only Q_0 is determined. Therefore, as mentioned in § 1.2.1, if we prescribe an arbitrary c_{r_0}-distribution on S_0 satisfying Eq. (1.30), we obtain, by means of Eq. (1.21), one solution of the potential flow through the casing.

From a purely mathematical point of view, this suffices, since, by means of Eqs. (1.29) and (1.30), we could obtain a general solution of the problem where the c_{r_0}-distribution on S_0 constitutes a given function. In the present investigation we shall be especially interested in trying to develop ways of finding this kind of general solution in two- as well as in three-dimensional casings.

However, we cannot ignore the fact that, from a technical point of view, this is rather too general, since there exist an infinity of solutions, satisfying Eq. (1.30). We should, therefore, look for those c_{r_0}-distributions fulfilling Eq. (1.30), which seem to be the most plausible in relation to the running conditions of the turbine. For this purpose the first experimental result in § 1.1.3, according to which the guide vanes and even more the runner act as flow rectifiers, could be useful. Thus Eq. (1.18) leads us to conclude that those c_{r_0}-distributions which satisfy both Eq. (1.18) and Eq. (1.30), seem to be the most probable; that is, when

$$(\bar{c}_{r_0})_n^{n+1} = \frac{Q_0}{2\pi r_0 h_0} = c_\infty \frac{S_p}{2\pi r_0 h_0} = \text{const.}, \tag{1.31}$$

for any $n = 1, 2, \ldots, N_v$; N_v is here the number of the guide vanes. Although this boundary condition is much more restrictive than that expressed by Eq. (1.30), the problem continues to present an infinity of solutions, since one can choose arbitrarily any c_{r_0}-distribution satisfying Eq. (1.31). Let us consider the usual case, where the spiral casing is symmetrical with respect to a plane perpendicular to the z-axis (axis of the runner), and where the surface S_0 and the guide case inside it are bounded between two planes parallel to the plane of symmetry (see § 1.1.2 and Figs. 1.05 and 1.09). Here, the potential flow on S_0 and inside it is two-dimensional. The *equipotential* surfaces cut S_0 on its generatrix lines; thus, the velocity $\vec{c}_0$ passing through it does not have a component in the z-direction ($c_{z_0} = 0$), and its components c_{r_0} and c_{l_0} are independent of z. Now, among the infinite number of c_{r_0}-distributions satisfying Eq. (1.31) the distribution

$$c_{r_0} = \text{const.} \tag{1.32}$$

on S_0 is of major importance. For, as mentioned in § 1.1.4 the initial reason for a large variation of the energy losses which could occur along S_0 is the appearance of an angle of attack on the fixed blades, viz. of a circulation of variable intensity from blade to blade. Supposing the fluid to be frictionless and removing the fixed blades, which is the case under consideration, we obtain a potential flow outside S_0. We do not have any more energy losses; a new distribution of the circulation, however, will appear from guide vane to guide vane; on the other hand, Eq. (1.31) continues to be valid. Suppose the camber lines of the guide vanes are logarithmic spirals and the turbine is under its normal running conditions (see § 1.1.2 and Fig. 1.05). Further, let us disregard for a moment the thickness of the guide vanes. Then, in the case where variations of the magnitude of c_{r_0} inside any of the N_v intervals of S_0 occur, we infer that these variations must be due to circulations generated about the guide vanes on both sides of these intervals. In other words, as long as the experimental condition (1.31) is valid, we conclude that the potential flow through the casing demands further that $c_{r_0} = \text{const.}$, since the number N_v of the guide vanes could be arbitrarily chosen. In addition, any periodic variation of c_{r_0} along S_0 is caused by processes occurring inside the volume bounded by S_0. These reasons explain why we shall pay particular attention to the distribution $c_{r_0} = \text{const.}$

It is not necessary to examine here the boundary conditions imposed on S_0 in more technical detail, since Eqs. (1.29) and (1.30) are sufficient for a general mathematical solution of the problem. We shall later attempt a detailed discussion of this subject in the special case of spiral casings of turbines.

1.2.3. Method of Solving Potential Flow Problems within Spiral Casings

We have stated in § 1.1.2 that the potential flow problem has been solved for those spiral casings which are derived from one and the same stream-surface of an axially symmetric flow which is chosen as a boundary and is extended to infinity. The logarithmic spiral casing constitutes a particular case, when the flow is two-dimensional.

In the actual casings, where it is impossible to follow the above law of formation exactly, the potential flow problem is extremely complicated, even if c_{r_0} is constant along S_0 (see § 1.2.2, and the related Fig. 1.16). In other words, it would appear to be extremely difficult to obtain an analytic solution to Laplace's equation $\Delta\phi=0$, in this case. We therefore tried to solve the problem experimentally through the *Electric Analogy* method.

We form the potential flow picture through a two-dimensional or a three-dimensional casing in the following way:

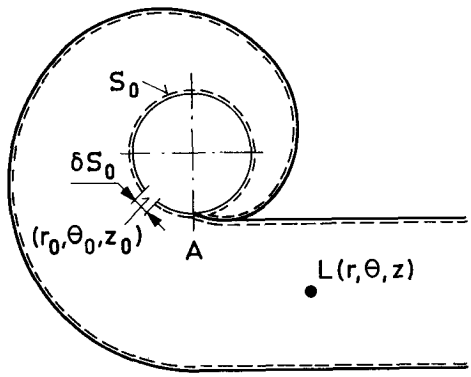

Fig. 1.17.

Consider the casing shown in Fig. 1.17, and let us imagine for a moment that the surface S_0 forms a wall, on whose small element δS_0 at the point (r_0, θ_0, z_0) there exists a sink of intensity δq_1. Thus the radial component $c_{r_0}(r_0, \theta_0, z_0)$ of the velocity through δS_0 is

$$(c_{r_0})_1 = \frac{\delta q_1}{(\delta S_0)_1}.$$

It is obvious that, if δq_1 is independent of time, a continuous and stationary potential flow occurs through the casing. The velocity potential $\delta\phi_1$, therefore, at any arbitrary point $L(r, \theta, z)$ of the casing (except the discontinuity point A) due to the sink $\delta q_1(r_0, \theta_0, z_0)$ can be expressed as

$$\delta\phi_1 = \delta q_1 G_1,$$

where $G = G(r, \theta, z, r_0, \theta_0, z_0)$ is a function of the geometrical locations $L(r, \theta, z)$ and (r_0, θ_0, z_0) with respect to the shape of the casing. Consider now another sink δq_2 on another point of the surface S_0; the potential $\delta\phi_2$ imposed by δq_2 alone on the same point L is

$$\delta\phi_2 = \delta q_2 G_2.$$

Thus, combining the effects of δq_1 and δq_2 we obtain on L

$$\delta\phi_{1,2} = \delta\phi_1 + \delta\phi_2 = \delta q_1 G_1 + \delta q_2 G_2.$$

Hence, from n sinks on S_0

$$\delta\phi_{1,2,\ldots,n} = \sum_1^n \delta\phi = \sum_1^n \delta q_k G_k.$$

If we consider a continuous distribution

$$c_{r_0} = \frac{dq}{dS_0}$$

of elementary sinks δq throughout S_0, we obtain the potential ϕ of a point (r, θ, z):

$$\phi(r, \theta, z) = \iint_{S_0} G\,\delta q = \iint_{S_0} c_{r_0} G\,dS_0.$$

(It is obvious that the function $G(r, \theta, z, r_0, \theta_0, z_0)$ is also continuous in every one of its six variables.)

Since $\phi(r, \theta, z)$ is the velocity potential function within the casing (except on the discontinuity point A),

$$c_{r_0} = \left(\frac{\partial \phi}{\partial n}\right)_{r_0, \theta_0, z_0};$$

thus,

$$\phi(r, \theta, z) = \iint_{S_0} \left(\frac{\partial \phi}{\partial n}\right)_{r_0, \theta_0, z_0} G(r, \theta, z, r_0, \theta_0, z_0)\,dS_0. \tag{1.33}$$

The integral shown in Eq. (1.33) is the solution of Laplace's equation $\Delta \phi = 0$ for this potential flow; this expression yields an important advantage, since it connects the potential ϕ at a point of the field directly with the boundary condition $c_{r_0} = \partial \phi / \partial n$ on S_0. We can, therefore, make use of the characteristic mentioned in the preceding sections about the boundary conditions etc. It is difficult, however, to evaluate the integral of Eq. (1.33) by analysis, especially in the three-dimensional casings, because of the very complicated form of the function G. It led us, nevertheless, to try to solve the problem experimentally, through the electric analogy method, since the electric field in an electrically isotropic and homogeneous conductor is a potential field. Thus in an electric analogy model of an actual casing, we can impose electric boundary conditions corresponding to those expressed by $c_{r_0} = \partial \phi / \partial n$ on S_0 of the actual casing, and obtain the value of ϕ at an arbitrary point in the form of an *electric potential.*

1.3. The Electric Analogy Method

1.3.1. Potential Flow and Electric Field

As is known from the theory of electricity, the steady electric field in an electrically *isotropic* and *homogeneous* conductor of specific resistance σ, is expressed as the field of a scalar function,

$$V = V(x, y, z),$$

where V is the *electric potential,* and where the vector of the field *intensity,*

$$\vec{E} = -\operatorname{grad} V$$

is, according to *Ohm's law,* the product of σ times the *current density* $\vec{i}$; viz.

$$\vec{E} = \sigma \vec{i} = -\operatorname{grad} V. \tag{1.34}$$

That is, the electric field is an *irrotational field*; viz.,

$$\operatorname{rot} \vec{E} = 0.$$

Since in the considered region there are no electric sources (+) or (−), the continuity condition of the field is expressed by means of the relation

$$\operatorname{div} \vec{E} = \operatorname{div} (-\operatorname{grad} V) = 0,$$

which is no other than Laplace's differential equation

$$\Delta V = \frac{\partial^2 V}{\partial x^2} + \frac{\partial^2 V}{\partial y^2} + \frac{\partial^2 V}{\partial z^2} = 0.$$

Hence, the field V and the potential flow belong to the same family; both are *potential fields*, since, as already mentioned in § 1.2.1, a potential flow is expressed by the fundamental relations

$$\vec{c} = \operatorname{grad} \phi,$$

viz. $$\operatorname{rot} \vec{c} = 0,$$

and $$\Delta \phi = 0.$$

Therefore, the two vectors $\vec{c}$ and $\vec{E}$ correspond to each other if we assume that the two fields ϕ and V are related by means of:

$$\phi = -\lambda V,$$

where λ is an arbitrary real constant. Consequently,

$$\vec{c} = \lambda \sigma \vec{i}.$$

Because there is not any physical connection between ϕ and V, we shall write the above relations in the form ($\rightarrow$) instead of (=) as follows:

$$\begin{aligned} &\phi \rightarrow -\lambda V, \\ &\vec{c} \rightarrow \lambda \sigma \vec{i} = -\lambda \operatorname{grad} V. \end{aligned} \tag{1.35}$$

These relations express the *Electric Analogy* of a potential function.

Let us now consider two regions τ and τ' which are bounded by two geometrically similar surfaces S and S' respectively. We choose unit lengths in τ and τ' respectively (see Fig. 1.18) so that the numerical measurements of corresponding lengths, areas and volumes are identical; that is, the components (x, y, z) and (x', y', z') of any pair of corresponding points are expressed by the *same number*. Suppose two harmonic functions, $\phi(x, y, z)$ and $V(x', y', z')$ are determined in τ and on S and in τ' and on S', respectively. Then, Eqs. (1.35) are valid when the boundary conditions of ϕ on S and of V on S' are identical; namely, if on geometrically corresponding points of the surfaces S and S' we have (see § 1.2.1)

either $$\phi_S \rightarrow -\lambda V'_S, \tag{1.36}$$

(first boundary problem)

or $$(c_n)_S = \left(\frac{\partial \phi}{\partial n}\right)_S \rightarrow \lambda \sigma (i_{n'})_S = -\lambda \left(\frac{\partial V}{\partial n'}\right)_{S'}, \tag{1.37}$$

(second boundary problem)

where $i_{n'}$ is the normal component of $\vec{i}$ on S'.

To solve potential flow problems by means of the *Electric Analogy* method, it is necessary and sufficient to satisfy the boundary relations as are expressed by either Eq. (1.36) or Eq. (1.37). Let us consider Eq. (1.37), for, as we shall see, it is more convenient in our investigation. Since λ can be arbitrarily chosen, we put

$$\lambda = 1$$

to simplify the presentation of the problem. Therefore, Eq. (1.37) can be written:

$$(c_n)_S \to \sigma\,(i_{n'})_{S'}. \tag{1.38}$$

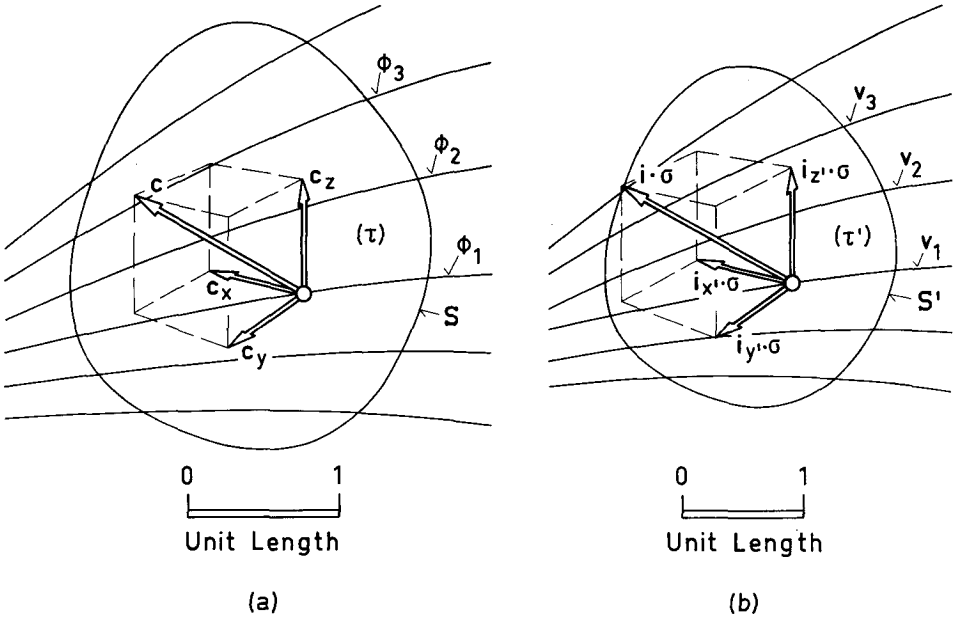

Fig. 1.18. Potential flow and electric field joined by the relationship: $\phi \to -\lambda V$.

If the correspondence (1.38) is valid, we can write

$$\phi \to -V$$

and

$$\vec{c} \to \sigma \vec{i} = -\operatorname{grad} V \tag{1.39}$$

throughout τ and τ', respectively. Consequently, at geometrically corresponding points (x, y, z), (x', y', z') of τ and τ', the following relations between velocity $\vec{c}\,(c_x, c_y, c_z)$ and current density $\vec{i}\,(i_{x'}, i_{y'}, i_{z'})$ components could be written:

$$\begin{aligned} c_x &= \frac{\partial \phi}{\partial x} \to \sigma i_{x'} = -\frac{\partial V}{\partial x'}, \\ c_y &= \frac{\partial \phi}{\partial y} \to \sigma i_{y'} = -\frac{\partial V}{\partial y'}, \\ c_z &= \frac{\partial \phi}{\partial z} \to \sigma i_{z'} = -\frac{\partial V}{\partial z'} \qquad (\lambda = 1). \end{aligned} \tag{1.40}$$

In cylindrical coordinates (r, θ, z), (r', θ, z') the corresponding $\vec{c}\,(c_r, c_l, c_z)$ and $\vec{i}\,(i_{r'}, i_{l'}, i_{z'})$ are as follows:

$$\begin{aligned} c_r &= \frac{\partial \phi}{\partial r} \quad \rightarrow \sigma\, i_{r'} = -\frac{\partial V}{\partial r'}, \\ c_l &= \frac{1}{r}\frac{\partial \phi}{\partial \theta} \rightarrow \sigma\, i_{l'} = -\frac{1}{r'}\frac{\partial V}{\partial \theta'}, \\ c_z &= \frac{\partial \phi}{\partial z} \quad \rightarrow \sigma\, i_{z'} = -\frac{\partial V}{\partial z'} \qquad (\lambda = 1). \end{aligned} \tag{1.41}$$

Investigations, either analytical or experimental, can be made of one of the fields ϕ or V; then, by means of Eq. (1.37) or of Eq. (1.38), where $\lambda = 1$, the results will also be valid for the other.

The fundamental advantage of an electric field in relation to a potential flow is that it is susceptible to a perfect experimental representation, since it is a *real field*, whereas the potential flow is a flow of an *ideal fluid*. Using the electric analogy method we could, therefore, solve potential flow problems which are not easily treated by analysis; e. g. in our case, to solve an equation such as Eq. (1.33). To this end, by means of a suitable electric analogy model, we can measure the values of the electric potential V, point by point; that is, solving numerically Laplace's equation $\Delta V = 0$. By means of Eqs. (1.40) or Eqs. (1.41) we can refer the results to the ϕ-field. Consequently, we can express the pressure distribution along any direction l inside the region τ by using *Bernoulli's* differential relation

$$\frac{1}{\rho}\frac{dp}{dl} = -\frac{d}{dl}\left(\frac{c^2}{2}\right) = -\frac{d}{dl}\left[\frac{(\operatorname{grad}\phi)^2}{2}\right],$$

where ρ is the fluid density. Thus according to Eqs. (1.39),

$$-\frac{1}{\rho}\frac{dp}{dl} \rightarrow \sigma^2 \frac{d}{dl'}\left(\frac{i^2}{2}\right) = \sigma^2 \frac{d}{dl'}\left[\frac{(\operatorname{grad} V)^2}{2}\right]. \tag{1.42}$$

1.3.2. Boundary Conditions on Electric Analogy Models

The mathematical identification of the boundary conditions between the ϕ-field and its electric analogy, V-field, on their control surfaces S and S' (see Fig. 1.18) are prescribed by means of either Eq. (1.36) or Eq. (1.37); instead of Eq. (1.37), we can use the simplified Eq. (1.38), where $\lambda = 1$.

Let us consider Eq. (1.38), which says that the distribution of c_n on S is given. For the boundary conditions on S and S' to be identical, the following must be satisfied:

a) S' should be geometrically similar to S.

b) The space inside S' should be occupied by an electrically homogeneous conductor, viz. a conductor of a specific resistance $\sigma = \text{const.}\ (\neq 0)$, at every point of τ' and in every direction.

c) The parts of S, which are walls or stream surfaces of the ϕ-field, should correspond on S' to the insulating surfaces of V-field.

$$\left(\frac{\partial \phi}{\partial n}\right)_{wall} \to -\left(\frac{\partial V}{\partial n}\right)_{insul.} = 0.$$

d) The parts of S which are equipotential surfaces of the ϕ-field should correspond on S' to *electrodes*, viz. conductors having an effectively zero specific resistence ($\sigma_{el} \approx 0$).

e) The parts of S which are neither stream-surfaces or walls, nor equipotential surfaces, should correspond to parts of S' in such a way that Eq. (1.38) be satisfied; viz.

$$c_n \to \sigma i_{n'}.$$

It is obvious that where S consists of stream and equipotential surfaces only, the formation of the boundary surface S' of the model is a simple matter. However, the formation of the parts of S' which should correspond to parts of S where the velocity c does not pass normally through it, viz. where

$$\sphericalangle (c, n) \neq \frac{\pi}{2} \text{ or } 0,$$

is rather complicated. We shall therefore, discuss these cases in detail. As is shown in Fig. 1.19a, the volume of fluid passing per unit time through the element $dS = db\,dh$ of S, is

$$dQ = c_n\, dS,$$

where, the directions b and h are chosen so as to be parallel and normal to the intersections between the equipotential surfaces and S, respectively.

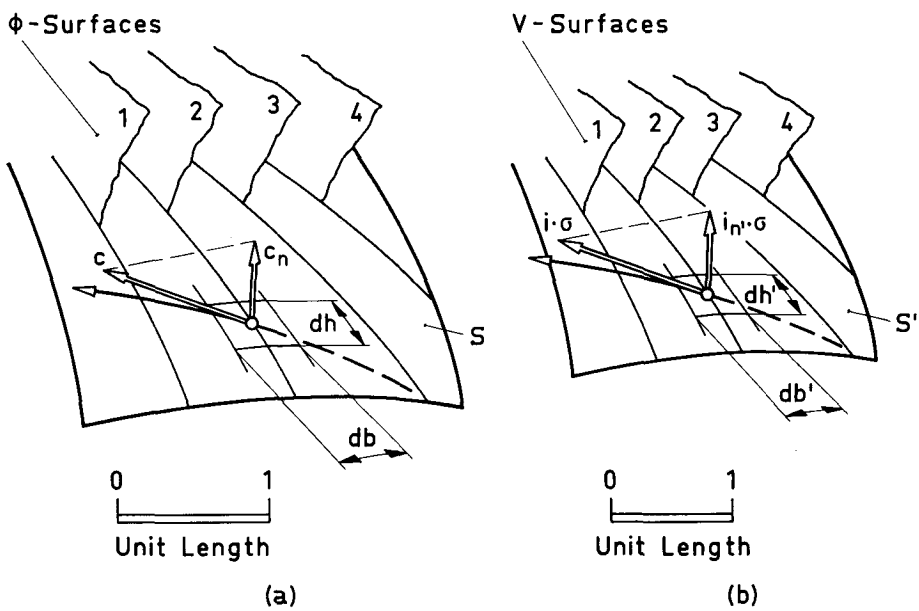

Fig. 1.19. Potential flow and its electric analogy through a slant-wise surface.

Consequently, on S', there should correspond an element $dS' = db'\,dh'$, similar to dS (see Fig. 1.19b), through which an electric current dJ, passes;

$$dJ = i_{n'}\,dS'.$$

To satisfy the boundary condition (1.38) we should have:

$$c_n = \frac{dQ}{dS} \to \sigma i_{n'} = \sigma \frac{dJ}{dS'}. \tag{1.43}$$

A common way to attain this is to replace this part of S' by a net of insulating material and electrodes. Theoretically, the area of each elementary electrode and the thickness of the insulating material surrounding it should be infinitesimally small. This is, in fact, impossible. Therefore, that part of S' in question could be made up of electrodes of finite area (see Fig. 1.20a), insulated by an insulation net of finite thickness. The area of a single electrode is now:

$$\delta S' = \delta b'\,\delta h'$$

and, instead of Eq. (1.43) we obtain

$$\bar{c}_n = \frac{\delta Q}{\delta S} \to \sigma \bar{i}_{n'} = \sigma \frac{\delta J}{\delta S'}, \tag{1.44}$$

where $\bar{c}_n$ and $\bar{i}_{n'}$ are the mean values of the normal component of the velocity and the current density through the corresponding areas δS and $\delta S'$ of S and S', respectively.

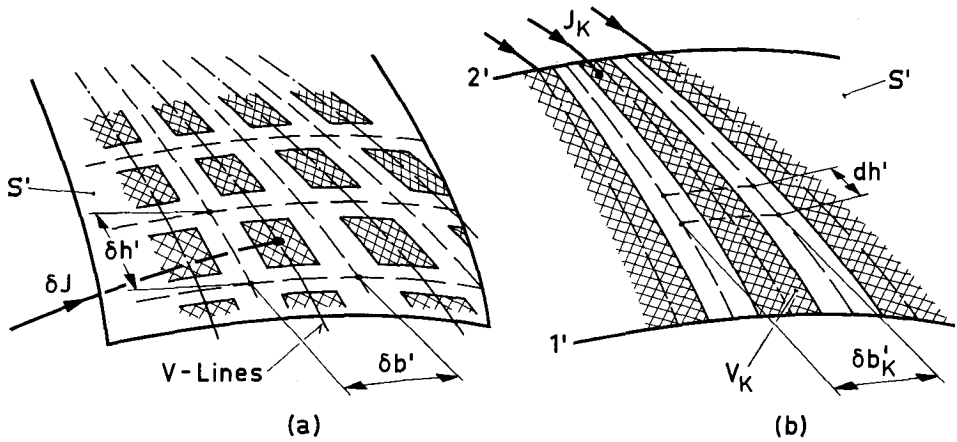

Fig. 1.20. Electric analogy of a slant-wise bounding surface. a) Grid of electrodes. b) Band of equipotential electrodes of a grid.

Since the electrodes lying on the intersection between an equipotential surface and S' should have the same electric potential V, we can replace all of them by one elongated and narrow electrode, as shown in Fig. 1.20b. Thus, if the part of S under consideration is bounded by the lines 1 and 2, S' will be limited on 1′ and 2′, and the current, e. g. through the K-electrode, should be

$$\sigma J_K = \sigma \int_{1'}^{2'} (\bar{i}_{n'}\,\delta b'_K)\,dh' \to Q_K = \int_1^2 (\bar{c}_n\,\delta b_K)\,dh. \tag{1.45}$$

It is obvious that, to apply this arrangement of the electrodes, we should know the orientations of the intersections of the equipotentials of the ϕ-field with S. If such orientations are known, it is evident from Eq. (1.45) that it is not necessary to know the c_n-distribution along S, but only the Q-distribution.

Suppose, for example, that the ϕ-field is two-dimensional and S is a cylindrical surface normal to it and bounded by two parallel planes of the field separated by a distance h. Therefore, the intersections of the equipotential surfaces with S are the generatrix lines of S; c_n is now constant along h. The arrangement of the electrodes on the corresponding surface S' of the model is shown in Fig. 1.21. Here the current through K-electrode is

$$\sigma J_K = \sigma \bar{i}_{n'} \delta b'_K h' \rightarrow Q_K = \bar{c}_n \delta b_K h. \tag{1.46}$$

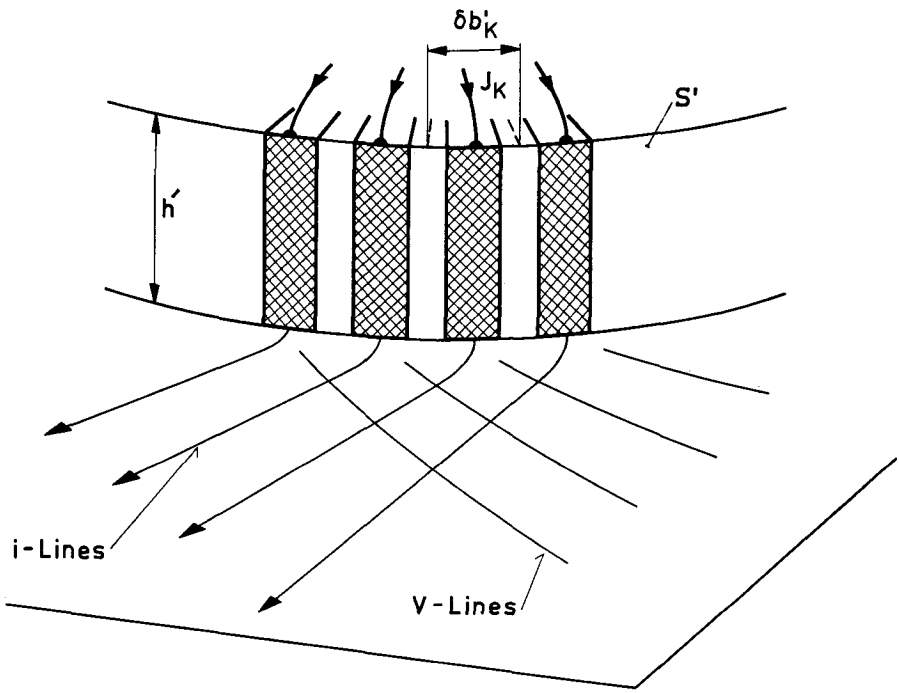

Fig. 1.21. Band-electrodes' assembly in a two-dimensional field.

However, the replacement of the theoretically infinitesimally small individual electrode or infinitesimally narrow band of electrodes and insulators, needed on S' by those of a finite size imposes on the V-field an additional boundary condition that, in general, does not exist for the ϕ-field. In fact, the surface of every electrode is an equipotential surface of the V-field; i.e. the electrode potential $V_{el} = \text{const}$. On the other hand, the surfaces of the insulating material between electrodes are stream surfaces, viz. $i_{in} = 0$. Hence, it is an undisputable fact that at least near S', the V-field will be distorted in relation to the ϕ-field.

To elucidate the above, let us consider a *parallel* potential flow (see Fig. 1.22a) and let us try to form the electric analogy arrangement of a surface S

of the flow. Suppose, at first, that S is an equipotential line (S_1). Then when we put a single electrode on the model at the place of the corresponding surface S', the correspondence between the ϕ- and V-fields is perfect. Suppose that, instead of a single electrode, we apply the arrangement shown in Fig. 1.22b, where the electrodes of the same electric potential are equally spaced on S_1' and separated by insulators of finite thickness. Then, near S_1', the V-field is no longer parallel; we observe a stagnation point on the middle of each insulator. However, the two fields ϕ and V become similar with increasing distance from S_1'.

Consider now the case where the boundary is the straight line S_2 which cuts the equipotentials at an angle. The corresponding boundary line S_2', in this case, must be made up of electrodes and insulators; the simplest arrangement for both electrodes and insulators is to be spaced alternately at equal intervals. If S_2 has a small inclination to the ϕ-lines, and the width of the electrodes and the insulators are of the same order, then Fig. 1.22c shows a typical form of the V-field. The same amount of current ($\ldots = J_{K-1} = J_K = J_{K+1} = \ldots$) passes through each one of the electrodes. We now see, that the V-field is heavily distorted near S_2'; nevertheless, as in Fig. 1.22b the two fields ϕ and V again become similar with increasing distance from S_2'.

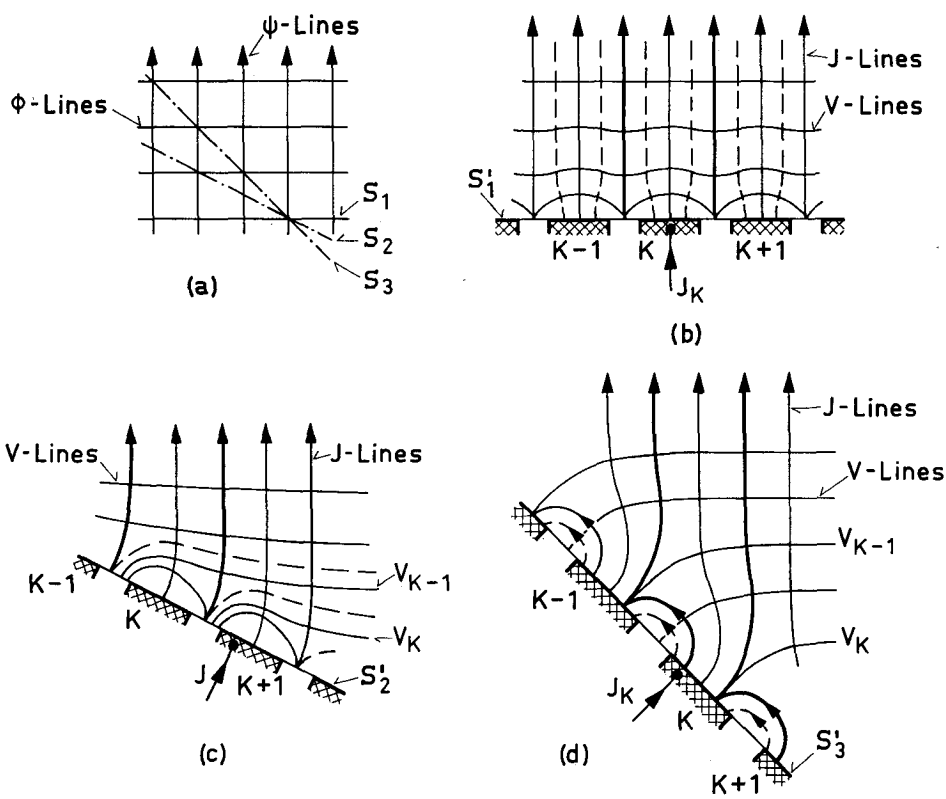

Fig. 1.22. Three characteristic types of distortion of the V-field due to the orientation of the bounding surface S'.

The cases of Fig. 1.22b and (c) present a common characteristic: the current from each electrode passes directly into the field; i.e., the *electric flow-tubes* from every electrode can be considered strictly separated along their paths. It is seen that, as the angle between the ϕ-lines and S increases, the distortion of the V-field near S' also increases, if the arrangement of electrodes remains unchanged.

Nevertheless, the form of the V-field undergoes a remarkable change when the inclination of S to the ϕ-lines, consequently of S', exceeds a limit. This occurs because the potential difference between successive electrodes, which keep the same distance on S', must always increase with increasing angle. In this manner a *secondary ohmic current* could form between them. This case is shown in Fig. 1.22d; the V-field has an extremely large distrotion on S' which, in general, extends further into it than the distortion in cases (b) and (c). Moreover, the current through an electrode *does not pass directly* into the field; the K-electrode, for example, receives a part of the current from the $(K+1)$-electrode and gives a part of its current to the $(K-1)$-electrode.

It cannot be stated definitely, therefore, that the current J_K passes into the field from the corresponding K-electrode only. Namely, the boundary conditions given by Eqs. (1.44) or (1.45) are not, in general, satisfied; thus, if this case occurs, the fields ϕ and V are not identical even rather far from S.

It is evident, from the above example, that an arrangement of electrodes placed on the surface S' cannot bring about the identification of the boundary conditions between the ϕ and V fields on S and S' respectively, as prescribed by Eq. (1.43). By means of such an arrangement, we can obtain an approximate representation, far enough from S', if the case illustrated in Fig. 1.22d does not occur; but if we are interested in investigating the form of the potential flow near S, this arrangement is *unsuitable* since it is impossible for both the electrodes and insulators to be infinitesimally narrow.

We can, nevertheless, overcome the above difficulties if we *remove* the electrodes from the surface S' *outwards*, outside of the region τ'. In other words, as the potential flow passes through S, the electric field similarly passes through S', and does not terminate on it. Such an arrangement, for our example of Fig. 1.22a, is shown in Fig. 1.23. The electrodes are separated from each other by means of thin insulating plates parallel to the stream surfaces, the plates extending from outside τ' to S'. Every electrode is normal to the plates on both its sides.

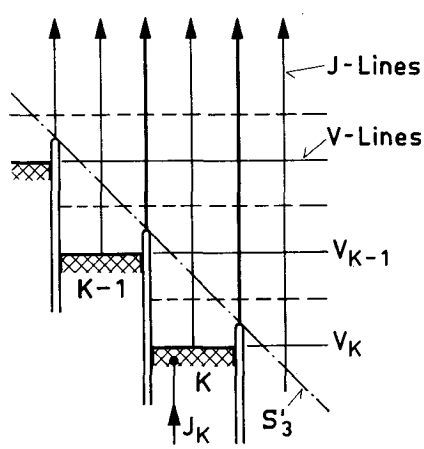

Fig. 1.23. A new arrangement of the electrodes by means of which possible distortions of the V-field can be avoided.

By means of this arrangement we can directly satisfy the condition of Eq. (1.43) on S' (without using the mean values given by Eqs. (1.44) or (1.45)). We can, therefore, obtain an electric field mathematically identical to a potential flow. In the next section, we shall discuss this problem in detail in the case of electric analogy models of spiral casings.

1.3.3. Electric Analogy on Spiral Casings

Let us first consider a *two-dimensional* spiral casing, bounded by two parallel planes at a distance h_0. The inlet pipe is assumed to be straight to infinity and of constant width L. On the other hand, the casing is bounded on the inside (see Fig. 1.24a) by the surface S_0, which surrounds the guide vanes in the case of a turbine, or the impeller in the case of a usual pump.

As a control surface S, of the potential flow through this casing, we shall assume the surface

$$S = S_0 + S_s + S_p$$

in the circumstances stated in § 1.2.2. In polar coordinates (r, θ), the components c_r, c_t of the velocity $\vec{c}$ inside S are

$$c_r = \frac{\partial \phi}{\partial r}, \qquad c_t = \frac{1}{r}\frac{\partial \phi}{\partial \theta};$$

consequently we obtain on S_0

$$c_{r_0} = \left.\frac{\partial \phi}{\partial r}\right|_{r=r_0}, \qquad c_{t_0} = \left.\frac{1}{r}\frac{\partial \phi}{\partial \theta}\right|_{r=r_0}; \qquad \operatorname{tg} \alpha_0 = \frac{c_{r_0}}{c_{t_0}}.$$

The velocity c_∞ through S_p is, according to Eq. (1.30),

$$c_\infty = \frac{Q_0}{h_0 L} = \frac{r_0}{h_0}\int_0^{2\pi} c_{r_0}\, d\theta. \tag{1.47}$$

Let us now form the electric analogy model of the above casing. To simplify the description, we assume a geometrical scale 1 : 1 between them. The model, therefore, should be made up of a casing made of an *insulating material* in such a way that

$$S_s = S'_s,$$

as shown in Fig. 1.24b. In place of the equipotential surface S_p we shall put a plane electrode, the *P-Electrode*. Corresponding to the surface S_0, through which the flow passes, we shall put, in the model, *a Collector of electrodes*. We thus form the control surface S' of the model, corresponding to S of the casing. Filling up the space inside S' with an homogeneous conductor of a specific resistance σ, e. g., an electrolyte, or just *tap water*, we obtain our electric analogy model. To represent the ϕ-field within the actual casing by means of an electric V-field within the model, it is enough to introduce through the P-electrode a current

$$J_0 = i_\infty h_0 L \rightarrow \frac{1}{\sigma} Q_0 = \frac{1}{\sigma} c_\infty h_0 L \tag{1.48}$$

and, to get part of J_0 through each one of the electrodes of the collector, so that Eq. (1.46) is satisfied. Assuming the electrodes and the insulators between them to be equally spaced on S_0, the length of the sector δb_0 corresponding to each electrode (see Fig. 1.24c) is then

$$\delta b_0 = \frac{1}{2} b_{i_n} + b_e + \frac{1}{2} b_{i_n} = b_e + b_{i_n} = r_0 \delta\theta = \frac{2\pi r_0}{N_e},$$

where N_e is the number of the electrodes. Thus, through the K-electrode, we should have

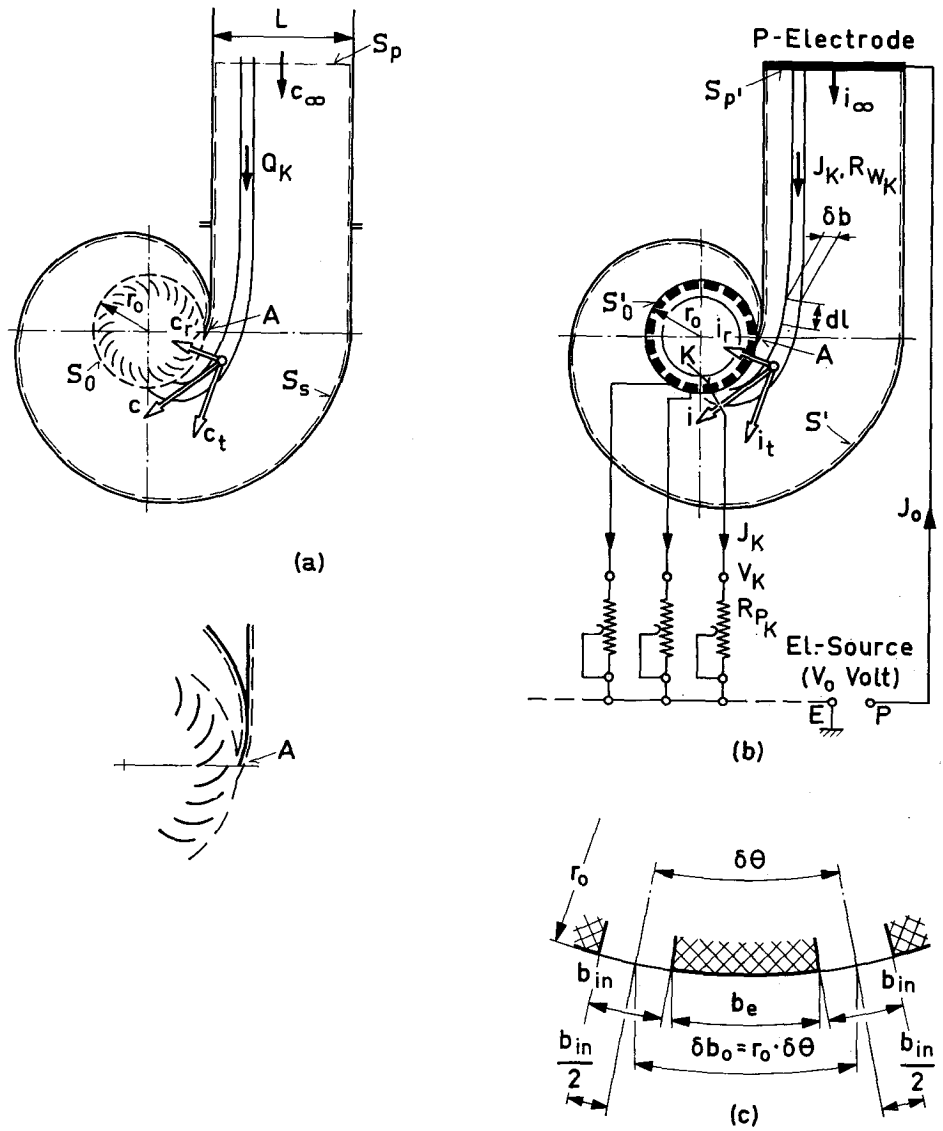

Fig. 1.24. a) Spiral casing. b) Typical arrangement of the electric analogy of the casing at a).

$$J_K = (i_{r_0})_K h_0 \delta b_0 \to \frac{1}{\sigma} Q_K = \frac{1}{\sigma} (c_{r_0})_K h_0 \delta b_0, \tag{1.49}$$

where $(i_{r_0})_K$, $(c_{r_0})_K$ are the mean radial components of the current density and the velocity respectively, passing through the element $\delta S_0 = \delta b_0 h_0$ of S_0, since $S_0' = S_0$. Accordingly,

$$\sum_1^{N_e} J_K = J_0 \to \frac{1}{\sigma} \sum_1^{N_e} Q_K = \frac{1}{\sigma} Q_0. \tag{1.50}$$

Since the distribution of c_{r_0} on S_0 is known, it is very easy to calculate, by means of Eq. (1.49), the distribution of J_K along S_0, as shown in Fig. 1.25.

The principle of a possible electric circuit arrangement is shown in Fig. 1.24 b. The electrodes are connected one by one, with *potentiometers* which are in parallel on the end E of the source. The other end of the electric source is connected with the P-electrode. Thus, an electric current circulates through the conductor. The main question is how to attain the desired distribution of

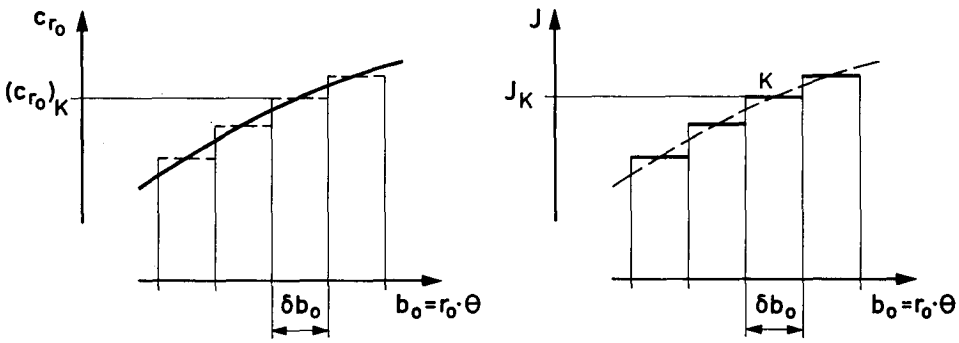

Fig. 1.25.

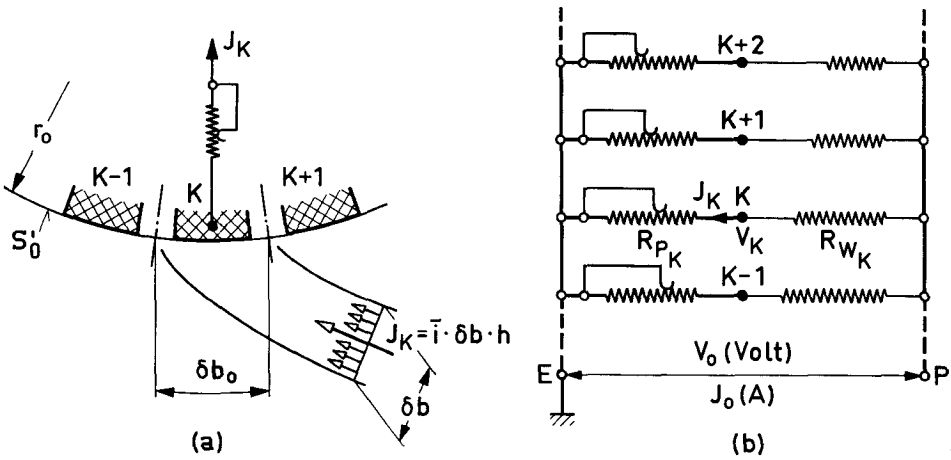

Fig. 1.26. The desired electrically equivalent circuit of the set-up shown in Fig. 1.24 b.

$J_K\,(K=1,2,\ldots,N_e)$. Let us assume that N_e *current-tubes* start from the P-electrode and one by one end on the N_e electrodes of the collector (see Figs. 1.24b and 1.26a). Thus, we can form the equivalent circuit between E and the P-electrode (Fig. 1.26b), which consists of N_e branches in parallel. The endpoints of each branch are under a voltage difference $V_0=\text{const.}$, and each branch is made up of two *ohmic resistances* in series: a) the resistance of one potentiometer and b) the resistance of the corresponding current-tube. Hence, for the K-branch (branch through the K-electrode) we obtain

$$J_K = \frac{V_0}{R_{P_K}+R_{w_K}}, \tag{1.51}$$

where R_{P_K} is the resistance of the potentiometer,

and

$$R_{w_K} = \frac{\sigma}{h_0}\int_K^P \frac{dl}{\delta b} \tag{1.52}$$

is the resistance of the K-current-tube (the conducting resistance between electrolyte and the electrodes is not considered in Eq. (1.51)). The voltage difference V_K, between the K-electrode and E, is

$$V_K = R_{P_K} J_K; \tag{1.53}$$

also,

$$V_0 - V_K = R_{w_K} J_K.$$

The total current J_0, on the other hand, is

$$J_0 = \sum_1^{N_e} J_K = \frac{V_0}{\sum_1^{N_e} \frac{1}{R_{P_K}+R_{w_K}}}.$$

It is evident from Eqs. (1.51) and (1.53) that changing the resistance R_{P_K} of the potentiometer means changing, at the same time, both J_K and V_K. If we had, therefore, the equivalent circuit of Fig. 1.26b, we could regulate, one by one, the N_e potentiometers so as to obtain the desired distribution of the current $J_K\,(K=1,2,\ldots,N_e)$ through its N_e branches. This cannot be done easily, however, with an electric analogy model, for the shapes of the imaginary current-tubes (as determined by the current flow) through the electrolyte are not independent. Hence, the change of the resistance of any one of the N_e potentiometers, e.g., of the K-potentiometer, involving a direct change of J_K and V_K of the K-current-tube, involves also a change of the V-field as a whole. If the total current J_0 remains constant, any change of any J_K involves a change of the currents $\ldots, J_{K-1}, J_{K+1}, \ldots$, as well as a change of the form of the field, especially in places surrounding the K-electrode. It is obvious, nevertheless, that on the electrodes of the collector and on the places of the field which are far enough from the K-electrode, the influence should be negligible.

From a mathematical point of view our electric analogy circuit shown in Fig. 1.24b, constitutes an experimental device for solving an *integral equation.* Indeed, since there exists a mutual influence between the current J_K and, let us say, the current J_Ξ which passes through the Ξ-electrode, we can write

$$J_K = \frac{J_0 R_0'}{R_{P_K}} - \sum_{\substack{\Xi=1 \\ \Xi \neq K}}^{\Xi=N_e} \frac{J_0 R_0'}{R_{P\Xi}} \lambda(K, \Xi) \tag{1.54}$$

under the condition that J_0 remains constant. In this relation R_0' is an arbitrary constant having the dimension of a resistance and $R_{P\Xi}$ is the resistance of the Ξ-potentiometer. $\lambda(K, \Xi)$, denotes a function concerning the influence of the presence of the Ξ-branch on the current J_K of the K-branch; given the spiral form, the position of the P-electrode and the specific resistance σ, the λ is a function of the locations of the electrodes K and Ξ. We can introduce the current density i_{r_0}, instead of J_K, by dividing both members of Eq. (1.54) by $\delta b_0 h_0$ and assuming $N_e \to \infty$ while every $\delta b_0 \to 0$. Let us further consider that under the above assumption, the assembly of the R_{P_K} resistances $(K = 1, 2, \ldots, N_e)$ constitutes a homogeneous and isotropic conductor, with cross-section $2\pi r_0 h_0$ which is divided by infinitesimally thin insulators in N_e parallel bands $(N_e \delta b_0 = 2\pi r_0)$. Then the length of each band, for example the length l_K of the band which corresponds to the K-electrode, fulfills the relation

$$\sigma_P l_K = R_{P_K} \delta b_0 h_0 \quad (K = 1, 2, \ldots, N_e);$$

σ_P is the specific resistance of the conductor. If θ is the angle between the tongue A of the spiral and the K-electrode, then

$$\sigma_P l_K \underset{N_e \to \infty,\, \delta b_0 \to 0}{\to} \sigma_P l(\theta);$$

similarly, we obtain for the Ξ-electrode which is at an angle ξ

$$\sigma_P l_\Xi \underset{N_e \to \infty,\, \delta b_0 \to 0}{\to} \sigma_P l(\xi).$$

We thus can form from Eq. (1.54) the expression

$$i_{r_0}(\theta) = \frac{J_0 R_0'}{\sigma_P l(\theta)} - \int_0^{2\pi} \frac{J_0 R_0'}{\sigma_P l(\xi)} \lambda(\theta, \xi)\, d\xi.$$

Introducing

$$I = \frac{J_0 R_0'}{\sigma_P l}$$

we obtain

$$I(\theta) = i_{r_0}(\theta) + \int_0^{2\pi} I(\xi) \lambda(\theta, \xi)\, d\xi \tag{1.54.1}$$

which is an *integral equation* on $I(\theta)$, where $i_{r_0}(\theta)$ is known and $\lambda(\theta, \xi)$ is the *kernel*. Hence, for establishing the desired J_K-distribution along S_0, that is finding the R_{P_K}-distribution (in the limit the $l(\theta)$), we have to apply the method of *iterations* experimentally. The process is as follows: As a first step, we must regulate, one by one, every potentiometer in such a way as to obtain the desired current through each one of them, ignoring the changes of the current introduced into the other branches of the circuit from any single potentiometer change. The second step is to return the total current J_0 to its prescribed value by regulating the voltage V_0, and to repeat the previous regulation of the potentiometers. The distribution of J_K obtained at the

second step is, *in any case*, nearer to the one looked for, than that of the first step. Repeating, therefore, this regulating procedure a number of times, we can obtain the prescribed distribution of J_K to any experimentally measurable degree of accuracy. In Part II, we shall describe, in detail, the above step-by-step procedure to obtain a series of J_K-distributions which converge rapidly to the desired one within four to six iterations. That is, we obtain a single valued V-field throughout the model, which has the prescribed boundary conditions on its bounding surface $S'(=S'_p+S'_s+S'_0)$. Using a suitable voltage pick-up (Probe) we can measure the voltage V of any point (r,θ,z) of the electric field; this enables us to investigate this field, point by point, in other words, to solve Eq. (1.33) experimentally.

We must be very careful, nevertheless, in arranging the electrodes of the collector. Indeed, the relation between J_K and Q_K (see Eq. (1.49)) is a relation between the mean values $(i_{r_0})_K$ and $(c_{r_0})_K$ of i_{r_0} and c_{r_0}, while the desired one, according to Eq. (1.43) is

$$i_{r_0} \to \frac{1}{\sigma} c_{r_0}. \tag{1.55}$$

As mentioned in the preceding section (see Fig. 1.22), the replacement of the exact condition (1.55) by Eq. (1.49) introduces not only a disturbance of the V-field near S_0 but also something of greater consequence, viz. the possibility of obtaining a completely different V-field, such as that shown in Fig. 1.22d, even if the J_K-distribution satisfies Eq. (1.49). Consider now Fig. 1.22d. This figure shows secondary ohmic currents between successive electrodes which cannot be tolerated and must therefore be eliminated. It is also desirable to avoid big distortions of the electric field near S_0, whether secondary currents are present or not.

Let us consider the phenomenon more closely. Electrodes and insulators constitute the cylindrical surface S_0. The components of the current density on it are

$$\sigma i_{r_0} = -\frac{\partial V}{\partial r}_{r=r_0}, \qquad \sigma i_{t_0} = -\frac{1}{r_0}\frac{\partial V}{\partial \theta}_{r=r_0},$$

and

$$\operatorname{tg}\alpha_0 = \frac{i_{r_0}}{i_{t_0}}.$$

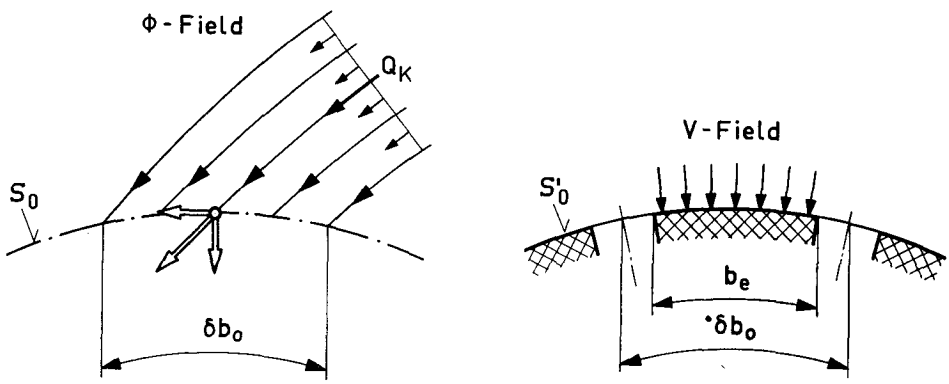

Fig. 1.27.

Therefore, along the length δb_0, which corresponds to an electrode (see Fig. 1.27), we get:

on each b_e:

$$V_{e_l} = \text{const.}$$

$$(i_{r_0})_{e_l} = -\frac{1}{\sigma}(\text{grad } V)_{e_l}$$

$$(i_{t_0})_{e_l} = 0$$

$$(\alpha_0)_{e_l} = \frac{\pi}{2},$$

on each insulator:

$$(i_{r_0})_{i_n} = 0$$

$$(i_{t_0})_{i_n} = -\frac{1}{\sigma}(\text{grad } V)_{i_n}$$

$$(\alpha_0)_{i_n} = 0.$$

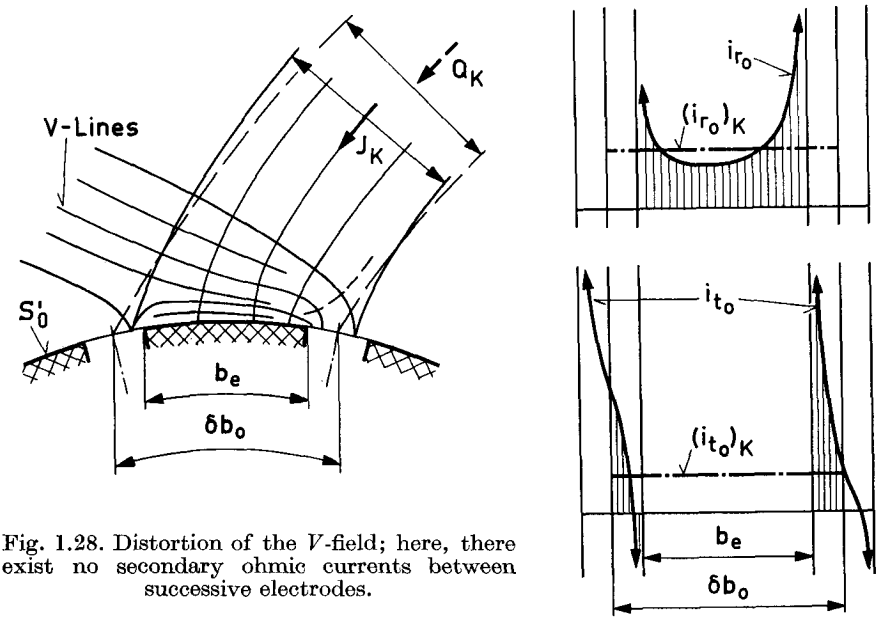

Fig. 1.28. Distortion of the V-field; here, there exist no secondary ohmic currents between successive electrodes.

As shown in the same figure these equations impose additional constraints which, in general, are not valid for the ϕ-field. Fig. 1.28 illustrates a typical form of the electric field near S_0 and of the i_{r_0}-, i_{t_0}-distributions on it, in the case in which the K-current-tube from the P-electrode arrives directly on K-electrode (no secondary current exists); thus, if J_{w_K} is the current through the K-tube, then,

$$J_K = J_{w_K} \to \frac{1}{\sigma} Q_K.$$

We thus obtain an approximate boundary for the model, which corresponds to the exact boundary condition as expressed by Eq. (1.55). The approximation,

of course, is improved by taking smaller δb_0, consequently b_e. Since the V-field depends on the orientation of the ϕ-field on S_0 and the dimensions b_e of the electrodes and b_{i_n} of the insulators, a completely different V-field would be obtained by altering any of these independent variables. The form of the V-field is, therefore, generally not similar to the ϕ-field, because of possible secondary ohmic currents between successive electrodes. See, for example, Fig. 1.29, which shows the secondary currents δJ_e and δJ_a to and

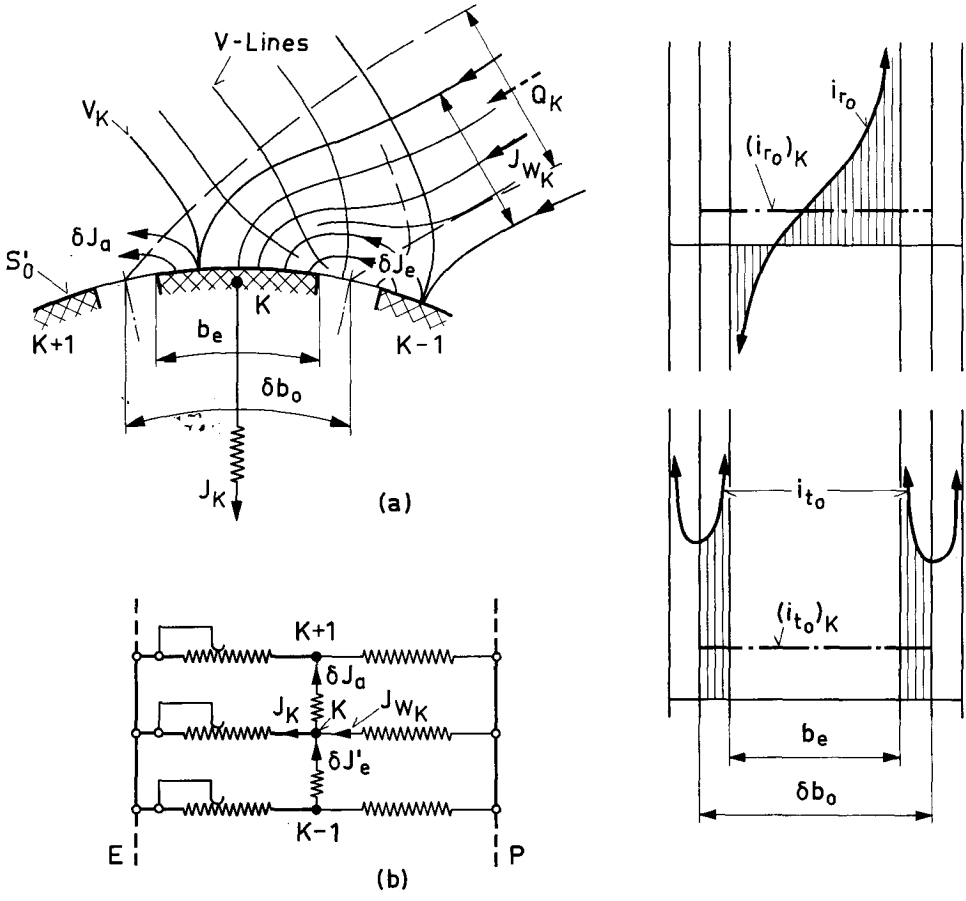

Fig. 1.29. Heavily distorted V-field, due to the presence of secondary ohmic currents between successive electrodes.

from the K-electrode. In fact, the application of *Kirchoff's* law to the K-electrode yields

$$J_K + J_{w_K} + \delta J_e + \delta J_a = 0.$$

The equivalent electric circuit in this case is shown in the same figure, and it is completely different from that shown in Fig. 1.26b, which is the only means of satisfying the boundary condition needed. The case of Fig. 1.29, however, gives us

$$J_{w_K} \neq J_K \to \frac{1}{\sigma} Q_K ;$$

that is, Eq. (1.49) no longer provides a sensible approximation to the exact condition expressed by Eq. (1.55), as it does in the case of Fig. 1.28.[5]) We, therefore, infer that Eq. (1.49) alone cannot secure, in general, an acceptable approximate correspondence between the ϕ-field and the V-field. The sufficient condition for this correspondence is

$$J_{w_K} \to \frac{1}{\sigma} Q_K .$$

Hence, in order to obtain the above correspondence by means of the electric analogy arrangement shown in Fig. 1.24b, in which we can regulate the currents J_K only, we must, in addition to the Eq. (1.49), secure that

$$J_{w_K} = J_K ;$$

viz., instead of Eq. (1.49) we must satisfy the relations:

$$J_{w_K} = J_K \to \frac{1}{\sigma} Q_K . \tag{1.56}$$

It might be possible to avoid the case of Fig. 1.29, for a given δb_0, by assuming $b_e < b_{i_n}$; such an arrangement, however, introduces rather large unacceptable distortions of the V-field near S_0.

It is clear from the above that we should abandon the solution involving a

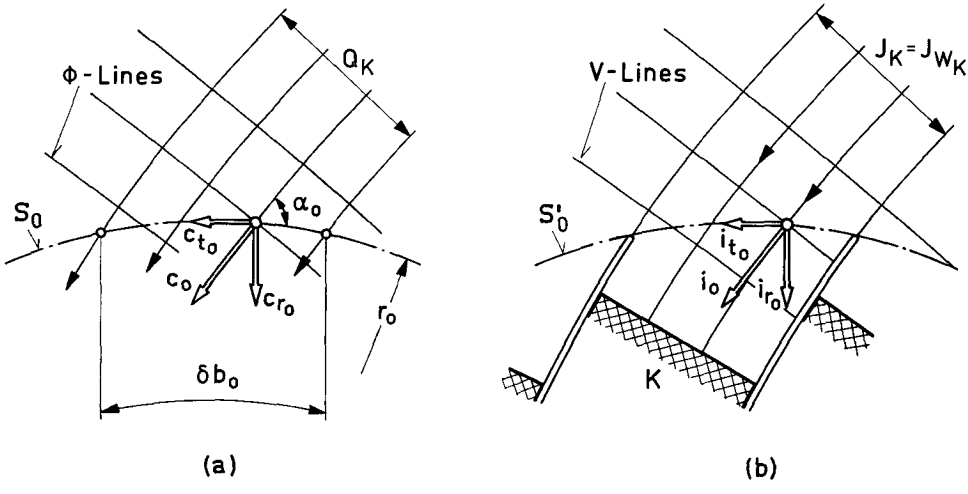

Fig. 1.30. New arrangement of the electrodes, permiting the electric current lines to pass through the bounding surface S'_0.

---

[5]) We note here that the picture of the V-field is invariant near each electrode if δb_0, b_e and b_{i_n} increase proportionally. Therefore, if the number of the collector electrodes (see Fig. 1.24b) increases, the deviation beetwen V and ϕ decreases. For $\delta b_0 \to 0$, $-V \equiv \phi$ even if the case of Fig. 1.29 occurs; in fact, the secondary ohmic currents δJ_e and δJ_a in the ends of a finite arc-length of the collector tend to zero when $\delta b_0 \to 0$.

collector whose electrodes and insulators have to be placed on S_0. To obtain an acceptable approximation to the exact condition of Eq. (1.55) on S_0 by means of Eqs. (1.56), viz. a condition of mean values on the intervals δb_0, we should place the electrodes *inside* the cylinder bounded by S_0.

A first introduction to the problem using this approach has been given in the preceding section (see Fig. 1.23). Suppose, for a moment, that we know both the c_{r_0}- and the $\sphericalangle \alpha_0$-distributions along S_0 as shown in Fig. 1.30a. Choosing a suitable interval length δb_0, we can form, in the model, the arrangement shown in the same figure at (b). The electrodes here are separated from each other by means of thin insulating plates which extend to S_0'; the faces of these plates lie along the flow lines, while each electrode inside S_0' lies, in general, on the normal plane whose point of contact with the plate is nearest the surface S_0' (see Fig. 1.30b). It is evident that in such an arrangement the disturbance of the V-field is negligible. Thus, since Eq. (1.56) is satisfied by this arrangement, we can write along *every interval* δb_0 of S_0, because the disturbance is ≈ 0,

$$i_{r_0} \to \approx \frac{1}{\sigma} c_{r_0}, \qquad i_{t_0} \to \approx \frac{1}{\sigma} c_{t_0}.$$

An exception could occur only in the region near the ends of δb_0 because of the thickness of the insulator-plates. The representation of the ϕ-field by the V-field becomes more accurate with decreasing intervals δb_0; we can then place the electrodes nearer S_0'.

In reality, however, neither the α_0-distribution nor the curvature of the streamlines passing through S_0 are known, since the potential flow inside the casing is determined by means of the c_{r_0}-distribution only. From a purely mathematical point-of-view, on the other hand, we are not interested in investigating the field inside S_0 but only the field inside the casing to S_0; furthermore, we are not interested if, for instance, the potential function passing through S_0 shows any discontinuity or if it has no meaning any more inside S_0. The insulating plates could, therefore, be equally spaced on the inside surface of S_0 and be of a plane form, having, as a first approximation, an arbitrarily chosen inclination on S_0.

In Fig. 1.31a and 1.31b, two typical forms of V-field on the edge of a plate are shown, the figures illustrating angles of inclination of the plates which

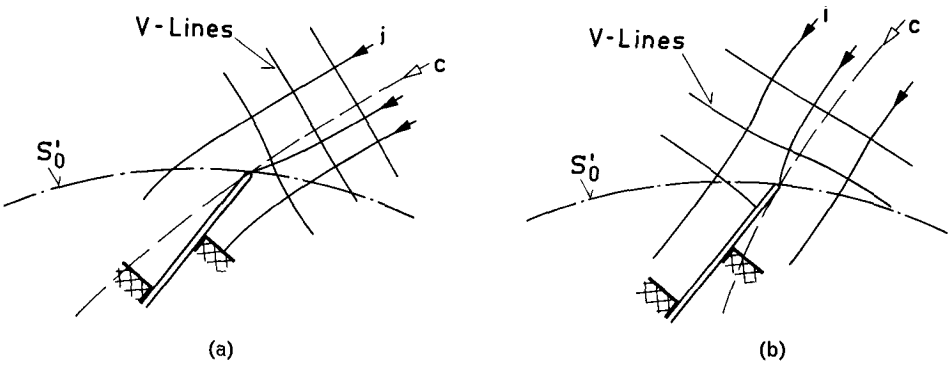

Fig. 1.31. New arrangement of the electrodes; small distortions of the V-field about the edges of the insulating plates.

are larger and smaller than α_0 respectively. As the difference between α_0 and the angle of inclination decreases, the distortion of the V-field likewise decreases. It is obvious, therefore, that this arrangement allows us to approximate the ϕ-field very closely; that is, we obtain small deviations of i_{r_0} from the given c_{r_0}-distribution. Indeed, by one or two preliminary experiments, we could modify the inclination of all the plates, one by one, in such a way as to minimize the periodic change in the direction of streamlines on S_0 from edge to edge as much as possible. We shall discuss the procedure for these modifications later. For the moment we wish to emphasize that the removing of the electrodes from the bounding surface could be used in *every case* where a fine representation of the boundary conditions of the potential function is needed.

In the case of a general three-dimensional casing, the principle of the electric analogy model shown in Fig. 1.24 remains valid, since the given meaning of the electric tubes through the electrolyte remains. But, an additional difficulty now occurs for, in general, the generatrices of S_0 are not equipotential lines. In our investigation, however, we have to examine Francis-type and centrifugal pump casings only, which usually are symmetrical with respect to a plane normal to the z-axis. (See Figs. 1.05 and 1.09.) In these casings, as we have already seen, the potential flow passing through S_0 could be characterized on it as a two-dimensional one. Therefore, everything said so far concerning the electrode arrangement, etc., is also valid for these types of casings.

1.3.4. Some other Applications of the Electric Analogy Method

The electric analogy of a potential flow through spiral casings according to the fundamental correspondence

$$\phi \rightarrow -\lambda V$$

between the potentials ϕ and V, has been developed in the preceding sections.

Because of its convenience and accuracy, the electric analogy method is used to solve problems of potential flow, strength of materials, etc. (see, e. g., ref. [26]). Let us consider the application of the electric analogy method to fluid mechanics:

The *meridian flow* of an axially symmetric casing, especially through the runners of hydraulic turbines, was investigated by *J. Ackeret* and *H. Gerber*, ref. [2].

A method similar to the one we described in § 1.3.3 to solve the integral Eq. (1.54.1) in our spiral casings was invented by *L. Malavard* (ref. [18]) to solve the well-known Prandtl's equation concerning circulation around airfoil wings of finite length (see also refs. [3] and [23]).

T. Ginsburg (ref. [11]) used the electric analogy method in his investigation of three-dimensional potential flow through an axial cascade (e. g. Kaplan turbines) to represent the flow which is generated from two circulation-distributions on two normal axes.

Several fundamental investigations in aerodynamics were carried out for two-dimensional problems using the electric analogy *type B* as it is called. This method is based on the fact that the two-dimensional flow described by

the *complex potential*

$$\chi_1 = \phi + i\psi, \qquad (i = \sqrt{-1}),$$

where ϕ and ψ are the velocity potential and the stream function respectively, and the one described by the complex potential

$$\chi_2 = -\psi + i\phi,$$

are normal to each other; i.e. the potential lines of the one are streamlines of the other and inversely. Thus we can form the electric analogy *type B*, by the correspondences

$$\phi \rightarrow W$$
$$\psi \rightarrow -\lambda V,$$

where $\lambda = \sigma/h$; h is the depth of the electrolyte, and W is the electric-current function.

In other words, the bounding equipotential lines correspond to the insulating walls, and the bounding streamlines correspond to the electrodes. The important advantage of this type of analogy is that the *circulation* around any obstacle (which is represented by an electrode surrounded by the electrolyte) can be represented, and is equal to the electric current through the surface of the electrode ($|\Gamma| \rightarrow J$). By this type of analogy we can investigate the potential flow around airfoil sections of infinite length (see ref. [18]), the potential flow through cascades of small height, etc. (see refs. [12] and [20]).

We close these few remarks by stating that in the two-dimensional problems, *G. Renard* (ref. [25]), using a suitable transformation, was able to trace the curves of equal velocity of the flow directly, for example, around an airfoil section. *Taylor and Sharman* also (ref. [27]), using a suitable type of correspondence between the fields ϕ and V (when ϕ is two-dimensional), were able to investigate some problems of flow of compressible fluids.

PART II

Experimental Investigation

In Part II a detailed description of the electric analogy set-up used is given. The investigation has been based on the theoretical considerations stated in Part I. Everything mentioned above about the iterations method to solve integral equations, as well as about secondary ohmic currents and the necessity of a convenient formation of the electrodes of the collector to avoid these currents was proved experimentally. A weak point of the electric analogy method is that we are obliged to use alternating current (to avoid polarization of the electrodes), which introduces capacitive currents. Particular precautions were therefore necessitated to avoid errors which would be caused by the presence of these currents during the adjustment of the boundary conditions around the collector and during the measurements of the electric potential V.

The result of the experimental investigations on the two-dimensional and three-dimensional casings can be summarized as follows. The moment of momentum $c_t r$ per unit mass of the fluid remains constant on a meridian section of the casing; its value is a function of the shape of the casing, the azimuth θ of the section and the distribution of the boundary condition c_{r_0} along the surface S_0.

By using the above experimental fact we formulated some relationships concerning the radial component of the velocity, the moment of momentum of the fluid etc., with respect to the shape of the spiral casing.

2.1. Experimental Arrangement

2.1.1. Introduction

The experimental arrangement used was based on the electric analogy principle as mentioned in the preceding section 1.3.

As electrolyte, we used *tap water* which, in our experiments, showed very good properties; the value of its specific resistance σ varied roughly between 3000 and 3300 Ω cm from season to season; the value of σ, however, for the same water in any single experiment, remained practically constant for variations of temperature not exceeding $\pm 2°$ C. We would like to say, however, that σ is not a function of the temperature only. For, as we observed, the tap water had to stay in the model for about 24 hours to allow for the escape

of its various volatile contents. During this time σ changes gradually until it acquires a stable value. We can cut this time almost by half by removing as much as possible of the air from the tap water and simultaneously much of its other volatile contents by means of a jet-vacuum pump. In this way, we can also eliminate any air-bubble formation on the surfaces of the electrodes. It is recommended that the same water should not be kept in the model longer than six or seven days, because of the organic matter in it.

The material used for the electrodes was *porous graphite* which, as is well known, shows very good endurance against polarization and also a negligible conducting resistance with water.

We used alternating current (A.C.) to avoid any polarization of the electrodes during the measurements. Thus the symbols V, J, i which we shall use from this point will refer to the *effective values* of the electric potential, current, and current density respectively. From a series of preliminary experiments we found that the frequency $f = 300$ Hz gave the best compromise between polarization of the electrodes and parasitic capacities generated between the various elements of the electric circuit and between these elements and the earth. As we shall see later, these capacities, due to the use of A.C., cause some difficulties in making an accurate representation of the potential flow by means of an electric field. It is desirable, therefore, to minimize these capacities as much as possible; viz. with polarization in mind, we must use the lowest permissible frequency. Moreover, at $f = 300$ Hz both the oscillator, viz. the electric source, and the transformers used in the circuit, introduce harmonic oscillations at rather small amplitude in relation to the basic sine curve.

Applying all of the above stated conditions, we succeeded in obtaining angular displacements of the equipotential surfaces of the electric field of less than 0,1° for time intervals longer than four hours; we wish to note, however, that the main part of this displacement was due to temperature variations and also to a lowering of the water-level in the model, due to its evaporation. Consequently, all series of measurements were taken within this four-hour period.

2.1.2. Description of Spiral Casing Models Used. Accessories

The present experimental investigation was carried out on three spiral casing electric analogy models.

The first two models were *two-dimensional;* one of logarithmic spiral form, and the other of Archimedes' spiral form (arithmetic spiral). The cylindrical surface S_0 was of the same radius $r_0 = 75$ mm for both of them; they also had the same depth, $h_s = 70$ mm. Further they had the same width $L = 186{,}6$ mm in the places of the inlet pipes of the actual casings.

The third model was *three-dimensional*, and geometrically similar to that used for the measurements with air, mentioned in § 1.1.3 (see Fig. 1.09). The reason this model was so chosen was to make a comparison possible between the experimental results with a viscous fluid and those of a potential flow through the casing.

In this section we shall give a description of the above models and of some other auxiliary equipment used in our experimental investigations.

a) The Logarithmic-Shaped Spiral Model

The form and the constructional details of this model are shown in Fig. 2.01; its shape is expressed in polar coordinates (r_s, θ) by the relation

$$r_s = r_0 e^{\theta \operatorname{tg} \alpha_s} \tag{2.01}$$

for $$0 \leqq \theta \leqq 2\pi + \frac{\pi}{6} (= 390°)$$

and $$r_0 = 75 \text{ mm},$$

and where $$\operatorname{tg} \alpha_s = \frac{1{,}2}{2\pi} = 0{,}191;$$

i.e. $$\alpha_s = 10° 50'.$$

The sides of the inlet of the spiral are parallel planes, tangential on the points $\theta = \pi/6$ and $\theta = 2\pi + \pi/6$ $(= 390°)$, respectively, and inclined to the $\theta = 0$ axis with an angle

$$\theta_p = \pi/2 + (\pi/6 - \alpha_s) = 90° + 19° 10' = 109° 10'.$$

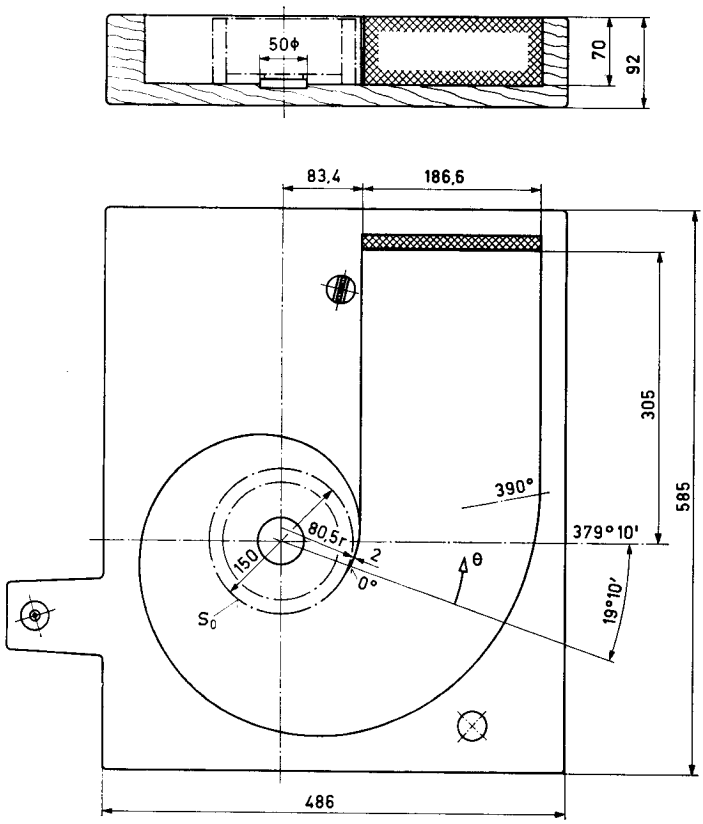

Fig. 2.01. The logarithmic spiral-casing model.

The distance between these parallel sides is

$$L = r_s(2\pi) - r_s(\pi/6) = 186{,}6 \text{ mm}.$$

The P-electrode is placed at a distance of $l = 305$ mm from the $\theta = 19° 10'$ axis, as shown in the drawing. The ration $l/L = 1{,}65$ is assumed to be big enough to allow the potential flow through a casing similar to this model to obtain a parallel form at the place of the P-electrode. The exact depth of the model was $h_s = 70{,}3$ mm. During the measurements the water-level was 3 to 10 mm lower than the upper surface of the model. The actual water-level is inconsequential as long as there is enough water in which good measurements can be made.

The model was made of wood. The 2 mm-thin spiral tongue at $\theta = 0$ to about 45°, as shown in the drawing, was of "Epoxide Resin" cast in place. The surface of the model was painted with many coats of a water-proof lacquer and after that with a special insulating lacquer mixed with "Epoxide Resin". For the centering of the collector of the electrodes a guide 50 mm diam. × 8 mm height was fixed on the plane bottom in the center of the spiral.

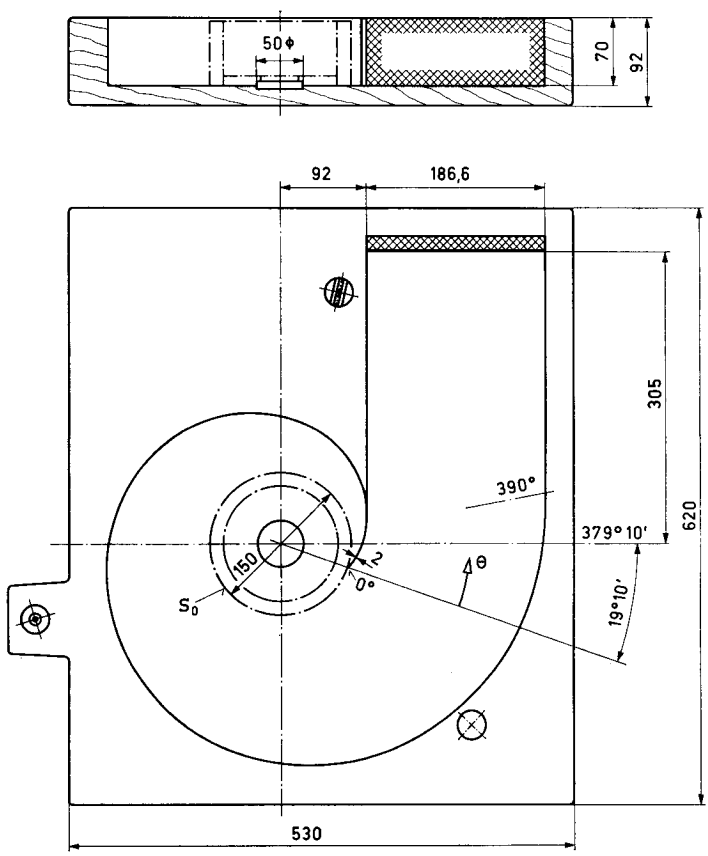

Fig. 2.02. The Archimedes' shaped spiral model.

b) The Archimedes' Shaped Spiral Model

The form and the constructional details of this model are shown in Fig. 2.02. Its shape is expressed in polar coordinates (r_s, θ) by the relation

$$r_s = r_0 + \tau\theta, \tag{2.02}$$

where $r_0 = 75$ mm and where the constant τ is chosen so that the orientation of the two parallel sides which represent the inlet pipe be the same as that of the logarithmic model; viz. $\theta_p = 119° 10'$, and at the same time the distance $L = 186{,}6$ mm between the sides remain fixed. Thus,

$$\tau = \frac{191}{2\pi}\,\text{mm/rad}.$$

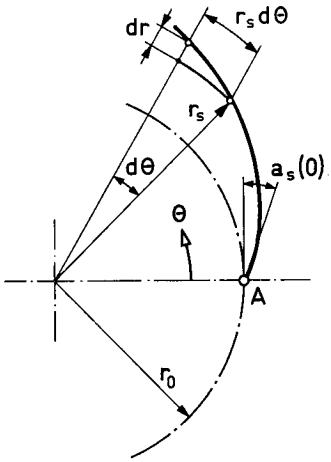

Fig. 2.03.

The angle α_s at the point (r_s, θ) formed between the spiral and the tangent of the circle of radius r_s, is expressed as:

$$\operatorname{tg}\alpha_s = \frac{1}{r_s}\frac{dr_s}{d\theta} = \frac{\tau}{r_s}.$$

Thus, at the beginning of the spiral, where $\theta = 0$ (see Fig. 2.03), we obtain

$$\operatorname{tg}\alpha_s(0) = \frac{\tau}{r_0} = \frac{191/2\pi}{75} = 0{,}4053, \tag{2.02.1}$$

$$\alpha_s(0) = 22° 3'.$$

The P-electrode is placed at a distance of $l = 305$ mm from the $\theta = 19° 10'$ axis as shown in the drawing. The exact depth of the model was $h_s = 70{,}2$ mm. The material, as well as the constructional details of this model, were the same as with the above-mentioned model.

We can see that both these models have the same collector radius $r_0 = 75$ mm, the same inlet pipe width $L = 186{,}6$ mm, and the same orientation of the inlet pipe in relation to the $\theta = 0$ axis. Comparing, therefore, after the measurements, the potential flow form through the arithmetic casing with that through the logarithmic one, we can study the influence of the spiral shape on the form of the flow.

c) The Three-Dimensional Spiral Model

The three-dimensional model we used was, as previously mentioned, similar to that of Fig. 1.09. The scale between this model and that shown in Fig. 1.09 was 0,6 : 1. Since the casing under consideration is symmetrical to a plane perpendicular to the z-axis, we used the one half only. Hence, the water level had to be kept carefully on this plane of symmetry. The form and the constructional details of the model are shown in Fig. 2.04. The plane of symmetry coincides with a depth 15 mm below the surface of the model. The dimensions of the various meridian sections at every 15° are given in *Table I*. The collector radius r_0 of the surface S_0 is (see also Fig. 1.09)

$$r_0 = 0{,}6\frac{395}{2} = 118{,}5\,\text{mm}$$

and its actual height $h_0/2$ is

$$\frac{h_0}{2} = 0{,}6\frac{77}{2} = 23{,}1\,\text{mm}.$$

The inlet pipe diameter is here

$$d_p = 0{,}6 \cdot 300 = 180\ \text{mm}.$$

The P-electrode is placed at a distance of 335 mm from the entrance ($\theta = 0$ axis) of the casing. As already mentioned in § 1.3.2 the fixed blades shown in Fig. 1.09 have been removed from this model.

The model is made of a plastic material, "Polyester Resin", and is supported by a wooden frame. For the centering of the collector of the electrodes, a suitable cylindrical surface of 175 mm dia. and 10 mm height, is provided.

Table I. The Three-Dimensional Model (see Fig. 2.04)
(Dimensions of the meridian sections)

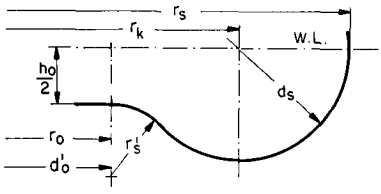

$\frac{h_0}{2} = 23{,}1$ mm
$r_s' = 63{,}0$ mm
$d_0' = 235{,}2$ mm

θ (Degrees)	r_K (mm)	d_s (mm)	$r_s = r_K + d_s/2$ (mm)
45	166,7	72,2	202,8
60	176,1	82,2	217,2
75	182,3	89,4	227,0
$\pi/2$ 90	187,7	96,0	235,7
105	192,5	102,2	243,6
120	196,8	108,0	250,8
135	200,8	113,4	257,5
150	204,3	118,4	263,5
165	207,5	123,0	269,0
π 180	210,6	127,4	274,3
195	213,4	131,6	279,2
210	216,1	135,6	283,9
225	218,6	139,4	288,3
240	221,0	143,2	292,6
255	223,4	146,8	296,8
$(3\pi)/2$ 270	225,7	150,4	300,9
285	227,9	153,8	304,8
300	229,9	157,0	308,4
315	231,8	160,0	311,8
330	233,5	162,8	314,9
345	235,2	165,4	317,9
2π 360	236,8	168,0	320,8

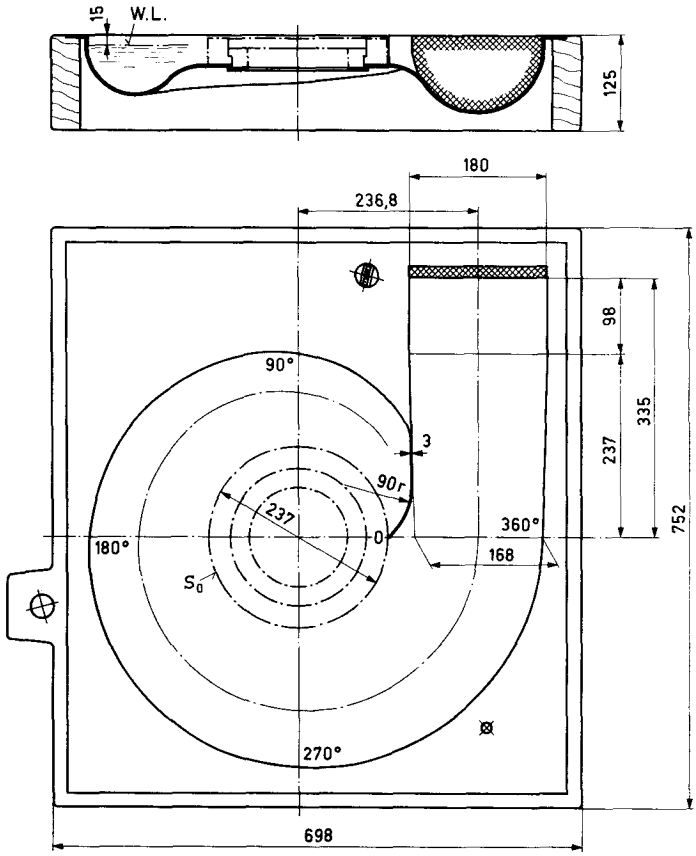

Fig. 2.04. The three-dimensional model.

d) The Collectors of the Electrodes

The basic constructional details of the collectors used in the two-dimensional models are shown in Fig. 2.05. It can be seen that the collector shown in this drawing is a simple cylindrical surface of 150 mm diameter and 70 mm height, on which there are $N_e = 36$ equally spaced electrodes. The circumferential length corresponding to (the width of) an electrode (see also Fig. 1.24) is:

$$\delta b_0 = \frac{2\pi \cdot 75}{36} = 13{,}1 \text{ mm}.$$

The actual width of an electrode surface is $b_e = 9{,}1$ mm and of the insulator $b_{i_n} = 4$ mm.

The electrodes are made of *porous graphite* pieces set in a mass of a plastic insulating material (Epoxide Resin). The undersurface of the collector is painted with a plastic insulating lacquer with a thickness of 0,2 mm, to avoid any current leakage between successive electrodes at the bottom of the collector.

The collector is fastened to the bottom of the spiral model by means of four screws. To protect the wood, a water-proof rubber seal ring is also provided, as shown in the drawing. To avoid current leakage between the 1st and the 36th electrodes an insulating grease was added between the spiral and the

collector surfaces at the tongue A (discontinuity edge of the field) during the assembly of the collector.

The collector form shown in Fig. 2.05 *(Collector I)* was used in the preliminary experiments carried out in order to verify the facts mentioned in § 1.3.3 regarding secondary electric current between successive electrodes etc. Thus the final arrangement of the electrodes used in the experimental investigation on the two-dimensional models (all the other constructional details of the collectors remain the same) is described later in § 2.2.1. The form of the collector used in the three-dimensional model will be described in section 2.3.

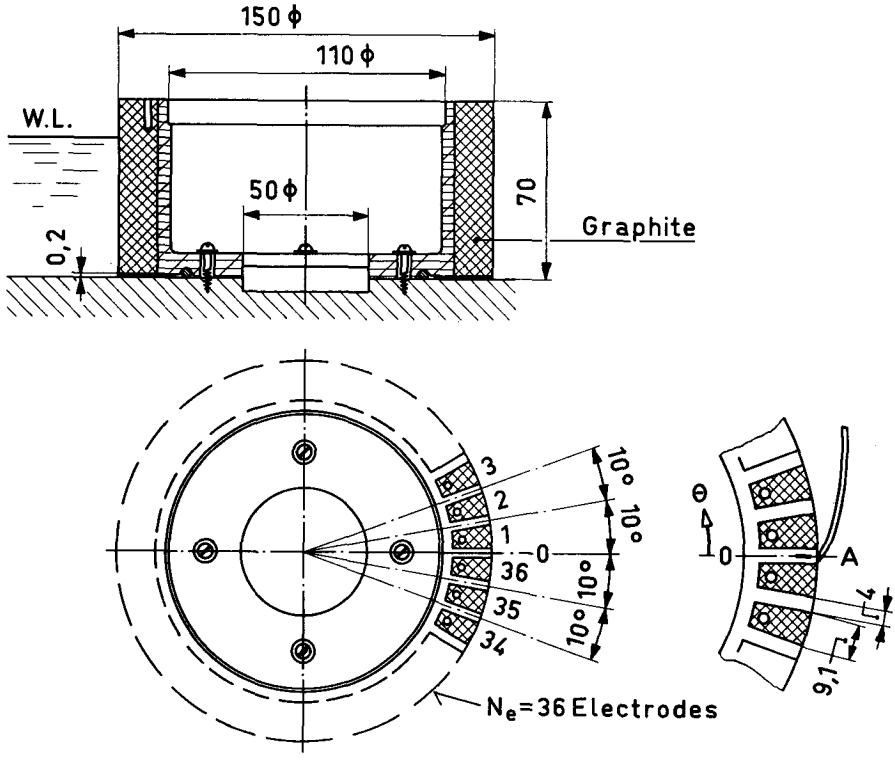

Fig. 2.05. Collector I.

e) The Polar Circle

To investigate the electric field in any one of the models, we used cylindrical coordinates (r, θ, z). The *Probe*, by means of which we measured the electric potential of every point of the water, was supported on a *Polar Circle* (Fig. 2.06), which affords motion in both r and θ directions. By means of this circle we can fix the probe on the coordinates (r, θ) [radius, angle] at any point (r, θ, z) of the field, while the third coordinate z of the point can be fixed by means of a scale which constitutes a part of the probe assembly (see § 2.1.3 and accompanying Fig. 2.17). In Fig. 2.06 the polar circle is shown on the three-dimensional casing. The probe is assembled in a carrier, which can be moved from zero radius to $r = 200$ mm. The radius r can be read in mm and

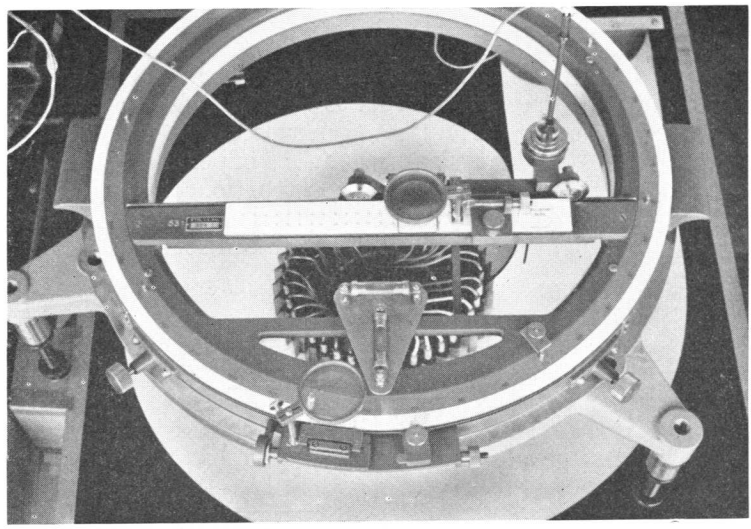

Fig. 2.06. Polar Circle.

tenths of a mm by means of a *vernier*. We can read the angle θ in degrees (°) and 20ths of a degree by means of an angular vernier. The polar circle rests on a base which is supported by means of three levelling-screws on the model; levelling is effected through two *water levels* in normal direction to each other. By two side-regulating screws one can fix the center of the polar circle to coincide with the center of the spiral.

f) The Water-Level Indicator

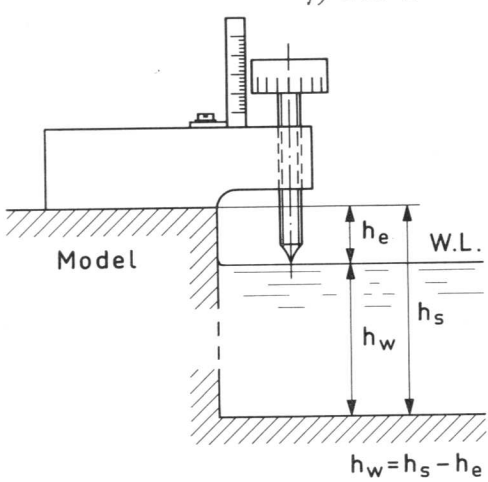

Fig. 2.07. Water-level Indicator.

We shall see later that although the depth h of the water in the two-dimensional models is taken at random, it is of additional importance in our investigation to know its exact value, since we calculate the specific resistance σ of the water by means of the depth. In the case of the three-dimensional model, on the other hand, we must fix the level of the water at the plane of symmetry. Fig. 2.07 shows the depth indicator used. The accuracy of the depth h_e measurements was $\pm 0{,}02$ mm, namely sufficient for our purpose. The depth h_w of the water is:

$$h_w = h_s - h_e .$$

The measurements of h_e of the water were carried out at a fixed point of each of the models.

2.1.3. Electrical Devices

In Fig. 1.24 of § 1.3.3 we gave a simplified form of the electric circuit necessary for obtaining an electric field in a spiral casing model representing the potential flow through the actual casing. We shall here describe this in detail and discuss its ramifications.

The electric circuit in question is shown in full detail in the diagram of Fig. 2.08. As mentioned in § 2.1.1 we used alternating current of frequency $f \approx 300$ Hz. From the operational point-of-view the electric circuit can be divided into two parts. *The first,* which is shown by thick lines, is the part which feeds the current by means of which we obtain the electric field in the model. *The second,* which is shown by thin lines, is the part by means of which we can measure the electric potential at any point (r, θ, z) of the field. Let us examine the two sub-circuits individually.

a) The Feeding-Circuit (see Fig. 2.08)

The source (1) of the electric current is a Low Frequency Philips GM 3156 Oscillator which is indirectly connected with the remaining circuit via a 1 : 1 transformer (2). This transformer is inserted only to protect the oscillator from any eventual short circuit. One end of the transformer (2) is directly connected to the P-electrode of the model (3); the other end is connected to the forty parallel branches of the circuit (part (4)) through the point E. Every one of these branches consists of four constant, pure ohmic resistances (R_0, R_a, R_b, R_c) and of one variable resistance (R_p-potentiometer) in series. Each of the above branches is to be connected with one of the electrodes of the collector. Fig. 2.09 shows the detailed form of one of these branches, e. g. that one connected to the K-electrode. As mentioned in § 1.3.3, to represent the potential flow in our model we should introduce a current of prescribed value through every electrode of the collector. The current J_K through, e. g. the K-electrode, can be measured by means of the resistance R_0 and the electronic Voltmeter (5) (Philips GM 6015) which can be connected with every one of the branches through a selector switch. Since the one end of the electronic voltmeter should be grounded, we ground the point E of the whole circuit; by grounding we can check the current through any one of the electrodes during the measurements.

If V_K^* is the voltage difference between the two ends of R_0, then

$$J_K = \frac{V_K^*}{R_0}. \tag{2.03}$$

The resistance R_0 is chosen so that the desired values of V_K^*, in accordance with J_K, can be read on the most accurate part of the dial of the voltmeter, viz. between 0,1 and 0,8, 1,0 and 8,0, or 10 and 80, etc. Thus, supposing the mean value $\bar{J}_K$ of $J_K (K = 1, 2, \ldots)$ to be 0,1 mA, and the corresponding $V_K^* = 0{,}4$ Volt, we obtain

$$R_0 \approx \frac{0{,}4}{0{,}1} \cdot 10^3 = 4000 \Omega.$$

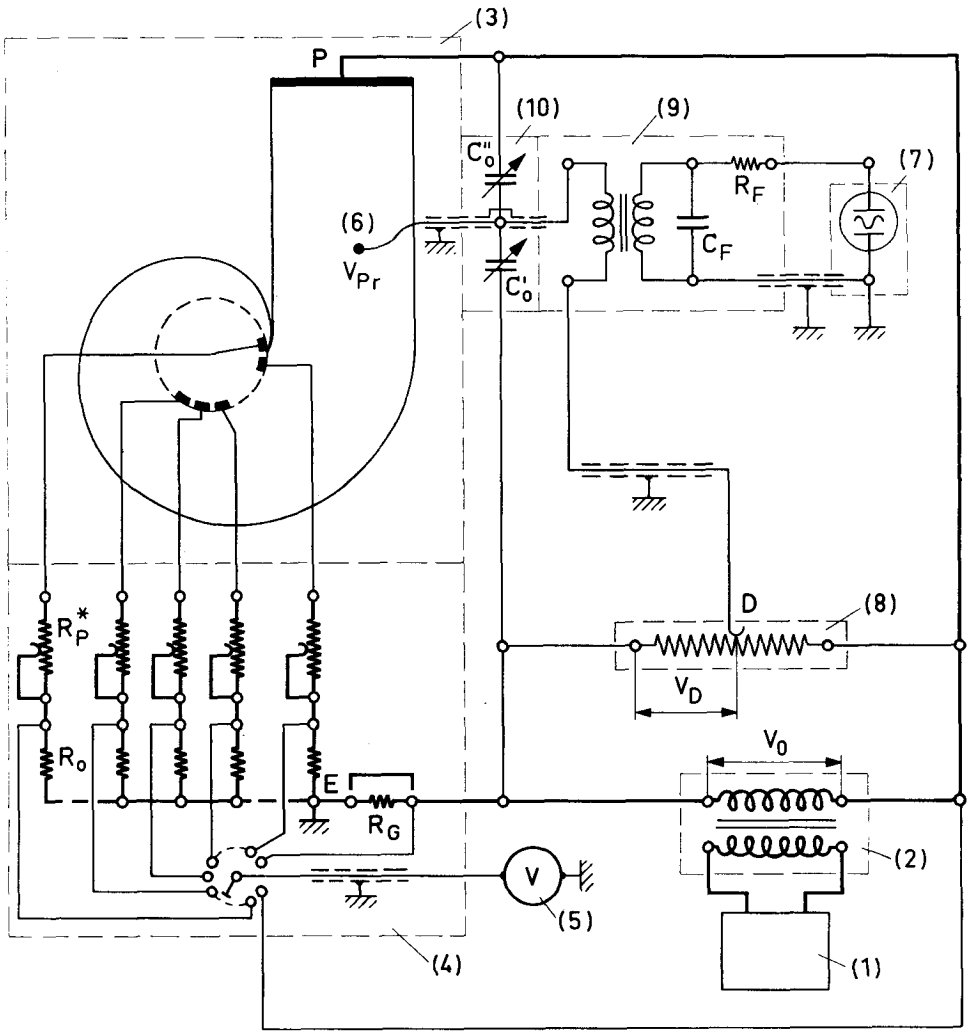

Fig. 2.08. Diagramatic view of the electric analogy circuit used (a picture of the set-up is shown in Fig. 2.16).

1. Low frequency oscillator (Philips type GM 3156).
2. Transformer 1 : 1.
3. Spiral casing model.
4. Potentiometer regulating boards (see also Figs. 2.09 and 2.11).
5. Electronic Voltmeter (Philips type GM 6015).
6. Potential pick-up (Probe) — see also Fig. 2.17.
7. Zero-indicator unit (Cathode-ray oscilloscope; Philips type GM 2308).
8. Decade potentiometer 10 KΩ (Tena type ME 218/2019).
9. Pick-up transformer and filter (see also Fig. 2.15a).
10. Variable capasitors.

(A necessary modification of the above circuit at the position (4) is shown in Fig. 2.28c.)

To simplify the calculations between the V^* of the various branches in accordance with the distribution of J_K ($K = 1, 2, \ldots$), we chose the resistance R_0 to have the same value for all of them; therefore, our set-up contains forty identical graphite resistances:

$$R_0 = 3930 \pm 0{,}6\ \%\ \Omega .$$

The rough regulation of the J_K, i.e. by Eq. (2.03) of the V_K^*, can be done by short circuiting the resistances R_a, R_b, R_c, or a combination of them; fine adjustment can be obtained by using the R_p-potentiometer (see Fig. 2.09). To fix a suitable scaling of the values of the resistances R_a, R_b, R_c and R_p (see Fig. 2.09), we took into account the field in the logarithmic model because, for the same J_K-distribution along S_0, the difference between the resistance R_{w1} of the (1)-current-tube and the resistance R_{w36} of the (36)-current-tube ($N_e = 36$) is greater in this model than the corresponding (1)—(36) differences in the other models. Furthermore, for this purpose, we use the simplest existing boundary condition along S_0, that is $J_K = \text{const}$. As shown in Fig. 2.10 for

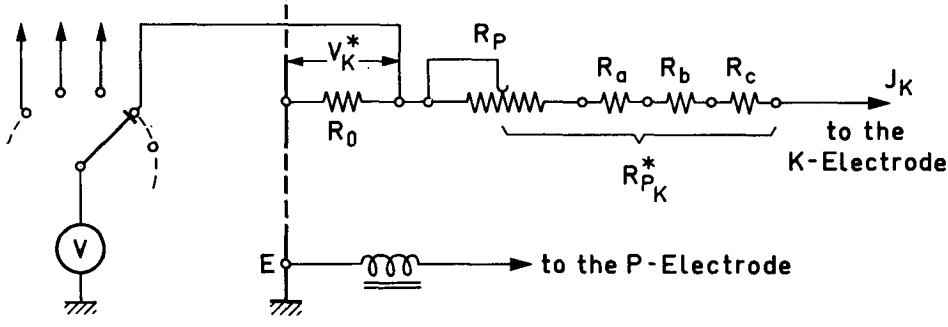

Fig. 2.09.

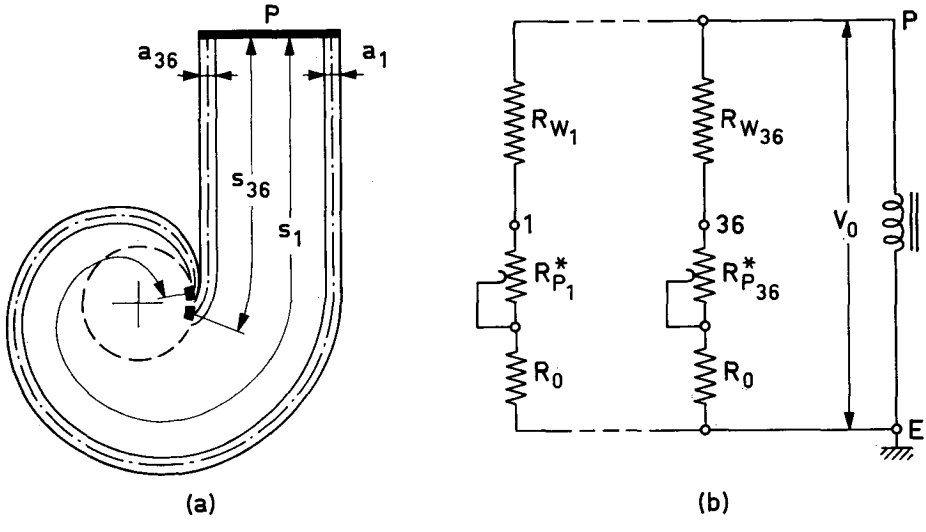

Fig. 2.10.

$J_K = \text{const.}$, we may write

$$R_{w_1} \approx \frac{\sigma s_1}{\bar{a}_1 h} \quad \text{(resistance of the (1)-current-tube)}$$

and

$$R_{w_{36}} \approx \frac{\sigma s_{36}}{\bar{a}_{36} h} \quad \text{(resistance of the (36)-current-tube),}$$

where $s_1 \approx 131$ cm, $s_{36} \approx 36$ cm, h is the depth of the water, and where the mean widths of both tubes may be taken as equal, i. e.

$$\bar{a}_1 \approx \bar{a}_{36} \approx 0{,}4 \text{ cm}.$$

Inserting the above expressions in Eq. (1.42) we can write (see Fig. 2.09),

$$R_0 + R^*_{p_1} + \frac{\sigma s_1}{\bar{a}_1 h} = R_0 + R^*_{p_{36}} + \frac{\sigma s_{36}}{\bar{a}_{36} h} = \frac{V_0}{J_K}.$$

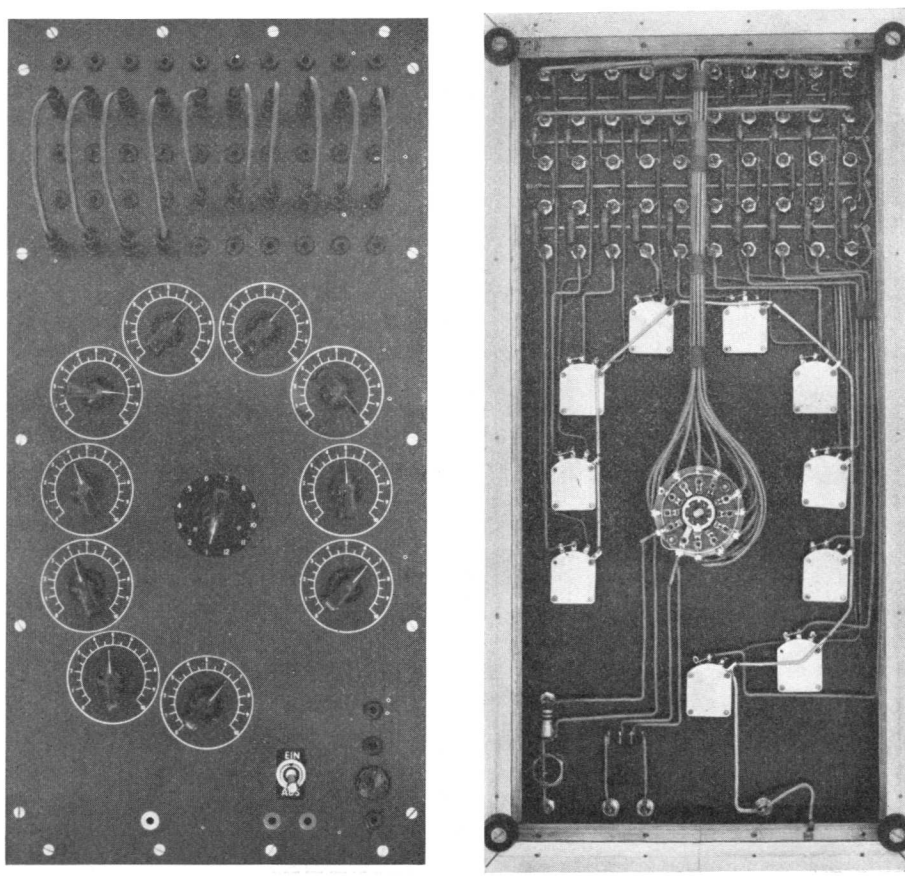

Fig. 2.11. Potentiometer regulating board containing a group of ten branches in parallel and a selector switch in the center.
Left: Front view. *Right:* Uncovered rear view; in the upper side are seen the 10 groups of resistances R_0, R_a, R_b, R_c.

Taking the specific resistance of the water, $\sigma \approx 3000\,\Omega$ cm, the depth $h = 5$ cm, the current $J_K = 0{,}1$ mA ($J_0 = 36 \cdot 0{,}1$ mA $= 3{,}6$ mA), and the voltage $V_0 = 21$ volt, we immediately obtain

$$\max R_p^* = R_{p_1}^* \approx 152\ \mathrm{k}\Omega,$$
$$\min R_p^* = R_{p_{36}}^* \approx 9\ \mathrm{k}\Omega.$$

To obtain a fine adjustment of V_K^* we used an R_p-potentiometer of range 0—25 KΩ. Using the above limiting values of R_p^*, we chose

$$R_a = 20 \pm 5\ \%\ \mathrm{k}\Omega,$$
$$R_b = 40 \pm 5\ \%\ \mathrm{k}\Omega,$$
$$R_c = 80 \pm 5\ \%\ \mathrm{k}\Omega.$$

Combining these resistances with the R_p provides us with a continuous change of the resistance R_p^* of any one of the branches from 0 to 165 KΩ.

The forty branches in question were assembled in groups of ten on four independant metallic boards. Fig. 2.11 shows the front view and the rear uncovered view of these boards. The selector switch which connects the branches to the electronic voltmeter has eleven positions and is set in the center of the board. Ten of its positions are connected, in a one-to-one manner, with the ten branches of the board. The eleventh position can be connected to a resistance $R_G = 50 \pm 0{,}5\ \%\ \Omega$ (see Fig. 2.08). This latter combination enables us to measure the total current through the ten branches during the rough regulation of the J_K. During the final regulation of J_K and during the measurements, however, R_G *must* be short-circuited. Every board was constructed to constitute a *Faraday cage* for its branches, when grounded.

The cables connecting the branches with the electrodes of the collector were identical in length (3000 mm), cross-section (1,5 mm^2), and insulation. They were grouped in tens and placed as far as possible from grounded objects.

The parasitic capacities in the boards were negligible. The capacities between the cables were unavoidable but their effects could be eliminated by suitable balancing condensers, as we shall show later.

b) The Measuring Circuit (Fig. 2.08)

The measurement of the electric potential $V(r, \theta, z)$ or more correctly of the potential difference $V - V_E$ between any point (r, θ, z) of the field and the grounded point E ($V_E = 0$), was made by means of a *Wheatstone bridge* arrangement. One end of the bridge, *a probe* (6) to be described later, was dipped in the water; the other end of the bridge is an arbitrary point D on a *decade potentiometer* (*8*). This potentiometer has a maximum resistance $R_D = 10\,000\,\Omega$ (Tena ME 218/2019) with five decade scales. Thus we can fix the resistance at the point D to 0,1 Ω. Consequently, the ratio of resistance R'_D to R_D, where R'_D is the resistance between the points E and D, can be obtained to 1.10^{-5}. The capacitance and the inductance of the decade potentiometer are negligible.

We used as *zero-indicator* unit (7), a cathode-ray oscilloscope (C.R.O.) (Philips GM 2308) supplied with an amplifier, whose maximum amplification corresponds to 1 cm $\widehat{=}$ 10^{-5} Volt$_{eff}$ in the vertical-direction on the screen. Because one end of the amplifier had to be grounded, the oscilloscope was

indirectly connected with the bridge by means of the small transformer (9). This transformer was carefully *isolated* from the earth.

The potential difference

$$\delta \vec{V} = \vec{V} - \vec{V}_D$$

between the voltage of the probe ($V_{P_r} = V$) placed at a point (r, θ, z) of the field and the voltage at the point D of the potentiometer (8) (see Fig. 2.08) is indicated by the vertical-direction on the screen of the C.R.O. For the traversing motion of the electron beam in the horizontal-direction we used the time-base system of the instrument synchronized in such a way as to obtain on the screen either one sine wave curve or two sine waves 180 degrees out of phase; these are shown in Fig. 2.12 a and (b), respectively. Fig. 2.13 shows diagrammatically the arrangement of the bridge when the probe is placed, for example, at a point of the K-current-tube which corresponds to the K-electrode of the collector.

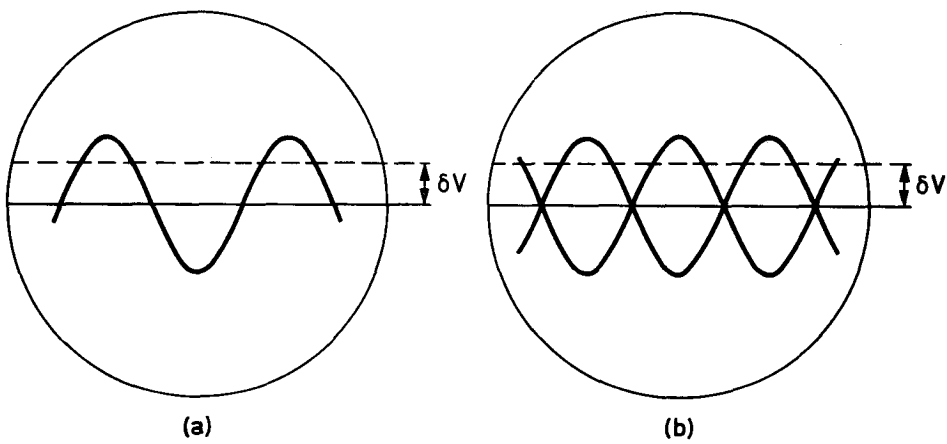

Fig. 2.12.

Suppose for a moment that our circuit is free from any capacitive or inductive influence on its elements, i.e., it is composed of pure ohmic resistances only. Then, the two (A.C. potential) vectors $\vec{V}$ and $\vec{V}_D$ will be coaxial; hence, for a given point D of the potentiometer (8) we can, by moving the probe, balance the bridge; that is, we can gradually obtain a perfect horizontal line through the center of the screen. This would imply that there exists a point D corresponding to each point of the field which satisfies $\delta \vec{V} = 0$ at that point. Thus,

$$V_{P_r} = V = \frac{R_0 + R^*_{P_K} + R'_{w_K}}{R_0 + R^*_{P_K} + R_{w_K}} V_0 = \frac{R'_D}{R_D} V_0,$$

where $R_{w_K} = R'_{w_K} + R''_{w_K}$ (see Fig. 2.13 a and b).

Introducing the dimensionless ratio

$$U = \frac{V}{V_0},$$

we obtain

$$U = \frac{V}{V_0} = \frac{R_0 + R^*_{P_K} + R'_{w_K}}{R_0 + R^*_{P_K} + R_{w_K}} = \frac{R'_D}{R_D}. \tag{2.04}$$

We could, therefore, by means of this relation, trace the equipotential surfaces of the field, i. e., we can solve the problem numerically.

Our circuit is, in fact, far from being free of parasitic capacitance because of its cables, the water, and the nearby metallic masses which may or may not be grounded; on the other hand, we could *characterize* it as free from parasitic inductance. The real bridge arrangement, therefore, is the one shown in Fig. 2.13b where the c'_p and c''_p represent the *unknown* parasitic

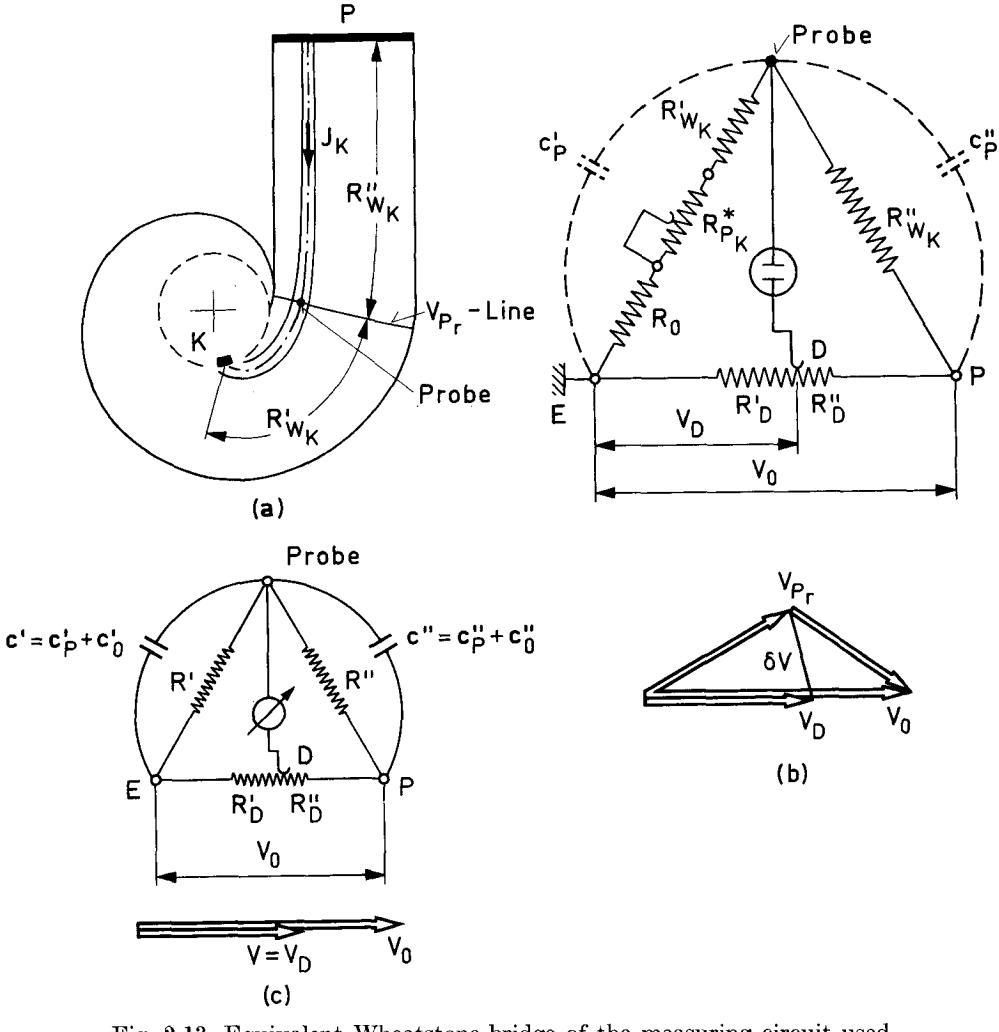

Fig. 2.13. Equivalent Wheatstone-bridge of the measuring circuit used.

capacities between the point E and the Probe, and the P-electrode and the Probe respectively; we can see also in the lower part of Fig. 2.13b a typical form of the electric potential between the probe and the point D. The potentials $\vec{V}(=\vec{V}_{P_r})$ and $\vec{V}_D$ cannot, in general, be coaxial; this means it is impossible to satisfy $\delta\vec{V}=0$ at each point in the field and so to balance the bridge. The bridge may be balanced, however, at particular points in the field. As is well known, the necessary and sufficient conditions to balance a Wheatstone bridge having capacitors in parallel with two of its branches, as shown in Fig. 2.13c, are

$$\frac{R'}{R''}=\frac{R'_D}{R''_D}=\frac{Z'}{Z''}, \tag{2.05}$$

where $$Z'=\frac{1}{c'\omega} \quad \text{and} \quad Z''=\frac{1}{c''\omega}$$

are the impedances of the capacitors c' and c'', respectively; $\omega=2\pi f$ is the circular frequency of the alternating potential (see also references [11] and [13]).

We can satisfy the conditions (2.05) in our measuring circuit if we introduce two variable condensers c'_0 and c''_0, as shown in Fig. 2.08 at (10), between the point E and the probe, and the probe and the P-electrode, respectively. Thus, inserting in the Eqs. (2.05) the values

$$\begin{aligned} R' &= R_0+R^*_{P_K}+R'_{w_K}, & c' &= c'_p+c'_0 \\ R'' &= R''_{w_K}, & c'' &= c''_p+c''_0, \end{aligned}$$

we have the following

$$\begin{aligned} \frac{R_0+R^*_{P_K}+R'_{wK}}{R''_{w_K}} &= \frac{R'}{R''}=\frac{R'_D}{R''_D}, \\ R'_D(c'_p+c'_0) &= R''_D(c''_p+c''_0). \end{aligned} \tag{2.06}$$

Now we can satisfy the balancing conditions (2.06) for a given point D of the potentiometer (8) by the following procedure: we first move the probe to attain a minimum available amplitude δV of the sine curve on the C.R.O. screen and then we regulate one of the condensers (10) to decrease it even more. If the alternating potential V_0 of the source is a pure sine curve, by repeating the above two or three times, we could obtain a horizontal line through the origin on the screen, i.e. we could balance the bridge. Thus, Eqs. (2.06) are fulfilled; consequently, for the dimensionless potential U of the point where the probe is, we obtain

$$U=\frac{V}{V_0}=\frac{R'_D}{R_D}.$$

This is not yet our case, however, since the cables and the transformer (9) introduce a small parasitic inductance into the circuit which cannot be balanced by using the condensers (10). Hence, if the transformer (9) is connected to the C.R.O. as shown in Fig. 2.14a, we do not obtain our required horizontal line on the screen, but a line of the form shown in part (b) of the same figure. The amplitude of its ridge is, in fact, very small, not exceeding 3 or 4 mm, which means that an extremely small amount of current circulates between the

Probe and the point D. This current is of course negligible and will not affect the accuracy of our measurements; the form of the curve on the screen, however, shows up the difficulties in pinpointing a position of the probe to obtain exactly $\delta V = 0$. Keeping the probe, for example, in $r, z = \text{const.}$, we cannot fix the third coordinate θ of the point in which $\delta V = 0$, i.e. $V = V_D$, with an accuracy greater than $\pm 0{,}4°$, which is insufficient. We overcame this difficulty by introducing, between the transformer (9) and the C.R.O., a filter (c_F, R_F), as shown in Figs. 2.08 and 2.15a. Preliminary experiments revealed

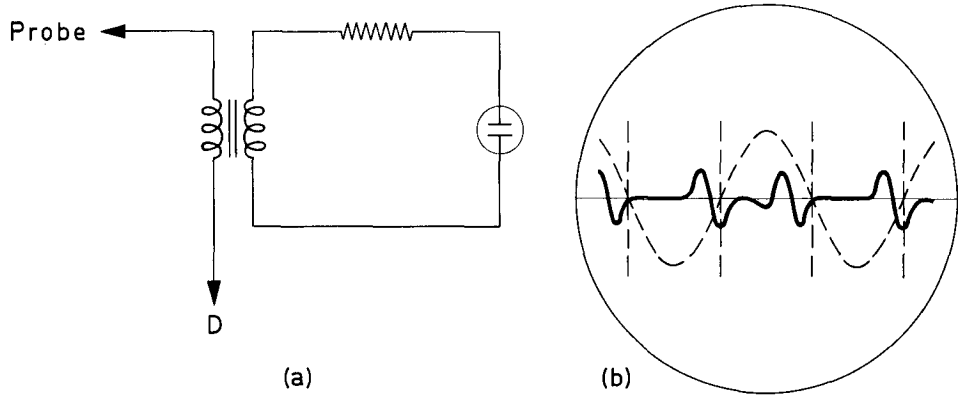

Fig. 2.14. Indication on the C.R.O.-screen, when a simple pick-up circuit a) was used.

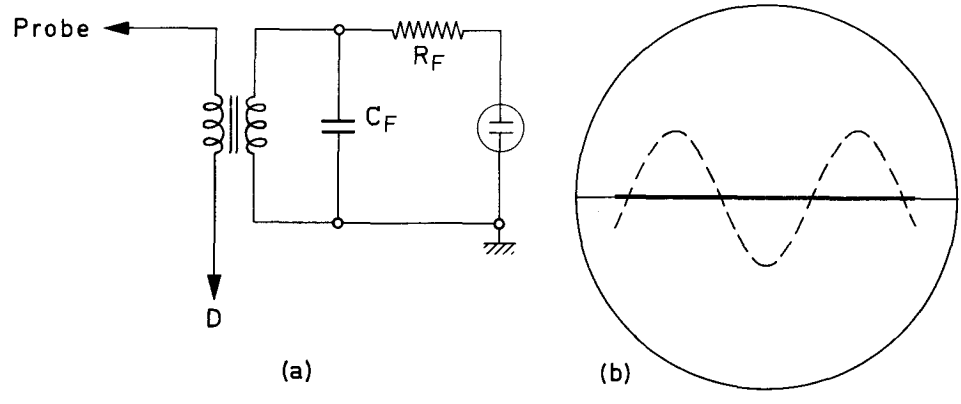

Fig. 2.15. Indication on the C.R.O.-screen, when a suitable filter (c_F, R_F) on the pick-up circuit a) was used.

the best compromise between c_F and R_F to be:

$$c_F = 0{,}1\ \mu\text{F},$$
$$R_F = 500\ \text{k}\Omega.$$

Following the previously mentioned procedure, we can now balance the bridge and obtain our perfect horizontal line through the origin on the screen, as shown in Fig. 2.15b. Keeping the probe in $r, z = \text{const.}$, we can determine the angle θ with an accuracy of $\pm 0{,}05°$ to $\pm 0{,}1°$, depending on θ and r.

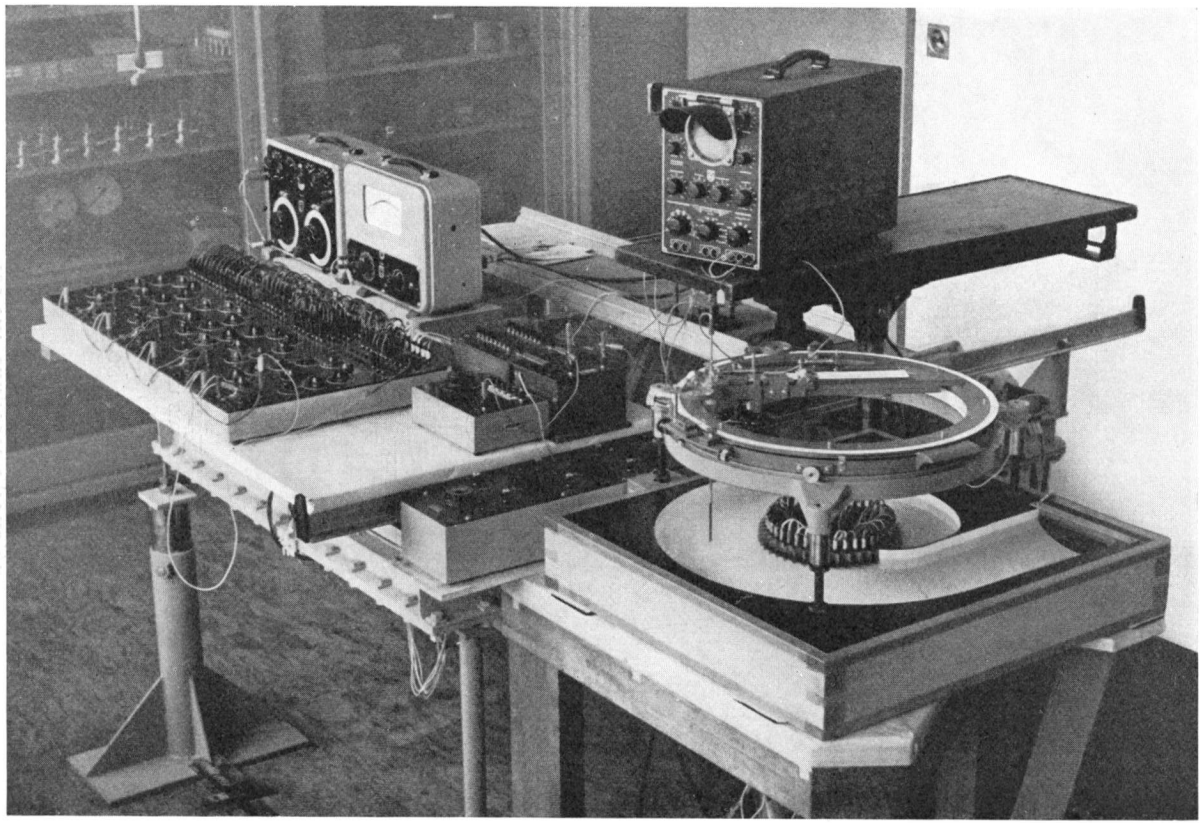

Fig. 2.16. A general view of the electric analogy set-up used.

To avoid any influence of the electric fields which surround the model etc. we shielded the cables between the probe, the transformer (9), the point D, and the C.R.O. as shown in Fig. 2.08. We also shielded the cable between the boards (4) and the electronic voltmeter (5). Furthermore, we grounded the polar circle assembly and other metallic objects near the model. A photograph showing the experimental set-up used in our investigations (spiral model and electrical device) is shown in Fig. 2.16.

c) The Potential Pick-Up (Probe)

In Fig. 2.17 are shown the two types of probe we used. We propose to describe first that shown in (a). This probe is constituted of a 360 mm long 5 mm diameter brass bar (1) which can move in the z-direction through a *plexiglass* insulating sleeve (2); the sleeve is assembled on the carrier (3) of the polar circle (see § 2.1.2e)). The lowest part of the bar (1) has, for a

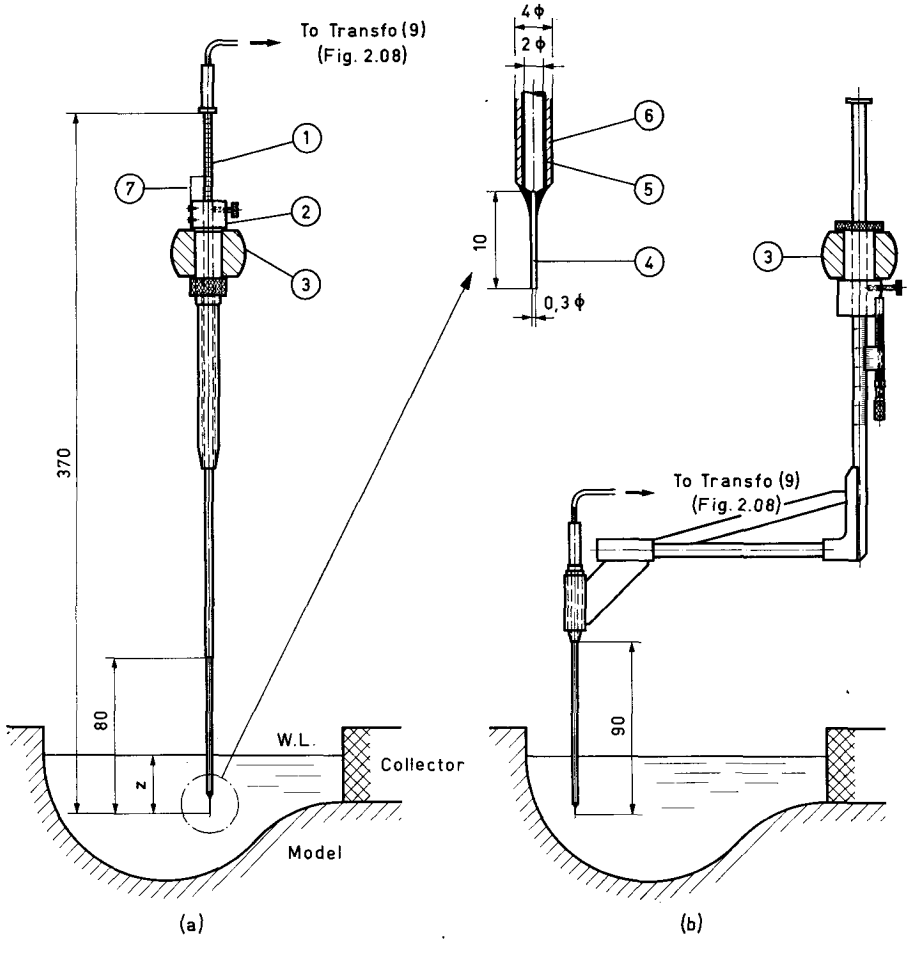

Fig. 2.17. The potential pick-ups (Probes) used.

length of about 80 mm, a diameter reduced to 2 mm and at the end there is a thin Platinum wire (4) 10 mm long, 0,3 mm in diameter. Both the cylindrical surfaces of the wire and of the lower part of the bar (1) are protected by an insulating lacquer (5). The conducting surface of the probe is the lowest cross-section of the P_t-wire. The measurement of the potential $V(r, \theta, z)$ is obtained by means of this surface. The plexiglass insulating sleeve (6) of thickness 1,0 mm was added, to prevent excessively great parasitic capacities and, therefore, parasitic current between the dipped part of the bar and the water. The upper part of the bar (1) was scaled in mm; by means of the indicator (7), we can measure the depth (z) of the conducting surface of the probe in the water.

The second type of probe we used is shown in the same Fig. 2.17 in (b). The principle of its construction is exactly the same as that of the first probe. As shown in the figure, the second type of probe was used as an extension to measure the potential at points with radii $r > 20$ cm, since the radius available by the first type extended to $r = 20$ cm only. The photograph in Fig. 2.18 shows the probe of the second type assembled on the polar circle.

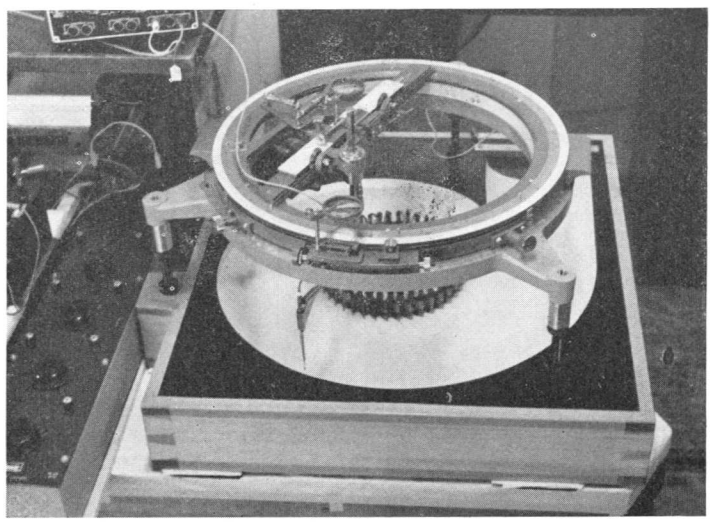

Fig. 2.18. The second probe (at b) of Fig. 2.17) assembled on the polar circle.

2.1.4. Measurement of the Specific Resistance of the Water

The knowledge of the specific resistance σ of the water for every series of measurements is of great importance in our investigation, as we shall see in § 2.1.5. To measure σ we used the equipment shown in Fig. 2.19a, which was first mentioned in ref. [12]. This equipment consists of two coaxial cylindrical electrodes of porous graphite, whose radii are $r_a \gg r_i$. The equipment is sunk vertically in the water of the model to a depth h_w. Enclosing its lower part by an insulating plane with several small holes and introducing a potential difference V_w between the two electrodes, we obtain a pure radial electric field in the water between them. Thus we can write

$$V_w = J \frac{\sigma}{2\pi h_w} \ln \frac{r_a}{r_i},$$

where J is the current. The ohmic resistance R_w of the system is therefore

$$R_w = \frac{V_w}{J} = \frac{\sigma}{h_w} \frac{1}{2\pi} \ln \frac{r_a}{r_i}.$$

Consequently,

$$\frac{\sigma}{h_w} = R_w \frac{2\pi}{\ln \frac{r_a}{r_i}}.$$

The electrode diameters were

$$d_a = 2r_a = 120{,}20 \text{ mm}$$
$$d_i = 2r_i = 12{,}33 \text{ mm};$$

thus,

$$\frac{\sigma}{h_w} = 2{,}76\, R_w.$$

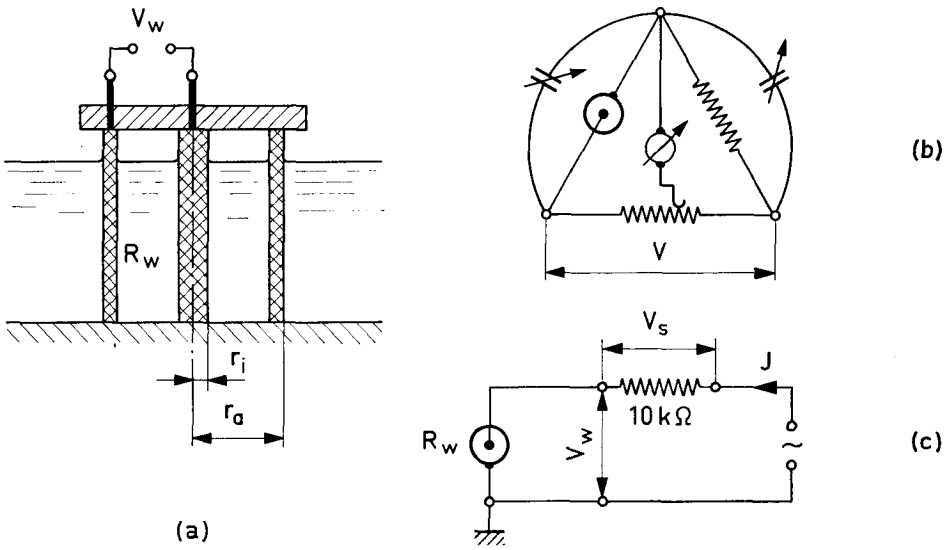

Fig. 2.19. The arrangement used for the measurements of the specific resistance σ of the water.

For an accurate measurement of R_w and thus of σ/h_w we could form a Wheatstone bridge as shown in Fig. 2.19 b. Applying $f = 300$ Hz and $h_w > 30$ mm, however, the resistance R_w is so small that the influence of the parasitic capacity of the arrangement was negligible. Thus we used the simple arrangement shown in the same figure in (c). We used the decade potentiometer (8) (see Fig. 2.08) of 10 KΩ as auxiliary resistance. The current J through this circuit is, therefore,

$$J = \frac{V_s}{10000} \frac{V_w}{R_w}.$$

Hence $$R_w = 10000 \frac{V_w}{V_s} (\Omega),$$

or $$\frac{\sigma}{h_w} = 27600 \frac{V_w}{V_s} (\Omega).$$

Preliminary experiments to check the above method yielded a deviation not exceeding $\pm 0{,}8$ per cent of the real value of σ.

We measured the σ of the water before and after every series of measurements in the models.

2.1.5. Procedure of the Measurements

A careful preparation of the experimental set-up mentioned in the preceding sections 2.1.2 and 2.1.3 was of fundamental importance for the accuracies of the measurements.

We had to level the spiral model. The levelling of the two-dimensional models was done by means of their plane bottoms. For this task we used a water-level with an accuracy $\pm 0{,}2$ mm/m. For the levelling of the three-dimensional model we used the same water-level placed on the upper surface of the collector of the electrodes. An initial checking of the levelling so-obtained was carried out by the water-level indicator described in § 2.1.2. A second checking of the levelling of the model was done by means cf the water-levels of the polar circle, which were of an accuracy of $\pm 0{,}1$ mm/m. Thus, after the levelling of the polar circle by its levelling-screws, we checked the distance between the polar-circle carrier and the level of the water in various places of the model. This checking was carried out by means of one of the probes used as water-level indicator.

The constancy of the specific resistance σ of the water during the experiments was a very important factor for the accuracy of the measurements, and, consequently, of the validity of the results. As mentioned in § 2.1.1, to secure the constancy of σ, we had to keep the ambient temperature within $\pm 2^\circ$C of a mean value and to start the measurements no sooner than 12 hours after filling the model with fresh tap-water. To check the constancy of σ the following method was used. We put our experimental arrangement into operation and balanced the bridge at an arbitrary point (r, θ, z) of the field in the model by the process described in § 2.1.3. We obtained a horizontal line through the origin on the screen of the C.R.O. We carefully observed this oscillogramm on the screen during the first 20 or 30 minutes; if the oscillogramm remained a straight line, it meant that σ was constant. If σ was not constant the oscillogramm gradually took the form of a sine wave. When this happened, keeping $(r, z) = \text{const.}$, we moved the probe, adjusting the angle θ, to rebalance the bridge; if this movement corresponded to a value of less than 0,10 degrees per hour, the value of σ was assumed to be steady enough for 3 or 4 hours of measurements. We could therefore measure the value of σ using the equipment described in § 2.1.4.

The first step for the measurements was to fix the desired current distribution (J_K-distribution) on the electrodes of the collector. During this stage the probe must be out of the water. The principle of this procedure has been described in § 1.3.3. Thus, according to the relation (1.49), we formed the

J_K-distribution (see also Fig. 1.25) and from this, according to Eq. (2.03), we formed the V_K^*-distribution, viz. the distribution of the voltage difference at the ends of the resistances R_0 of the various branches, which we had to read from the voltmeter (5) (see Fig. 2.08). If $\bar{J}_K$ is the mean value of the current through the electrodes, taking into account Eq. (1.50), we can write

$$\bar{J}_K = \frac{J_0}{N_e} = \frac{1}{N_e}\sum_1^{N_e} J_K \to \frac{1}{N_e}\sum_1^{N_e} \frac{(c_{r_0})_K}{\sigma} h_0 \delta b_0 = \frac{Q_0}{\sigma N_e},$$

where N_e is the number of the electrodes. Consequently, if $\bar{V}_K^*$ is the mean value of the V_K^* we get

$$\bar{V}_K^* = \frac{1}{N_e}\sum_1^{N_e} V_K^*.$$

It is obvious that the form of the V-field in the model stays fixed if the distribution of the ratio $V_K^*/\bar{V}_K^*$ along the N_e branches of the circuit remains the same. Thus, because the total voltage difference V_0 between E and P cannot exceed 25 Volt (maximum output of the oscillator), we determined, by some preliminary experiments, a suitable mean voltage difference $(\bar{V}_K^*)_s$ for every one of the three models; by means of this $(\bar{V}_K^*)_s$ we can tabulate the desired $(V_K^*)_s$-distribution so that it satisfies the relation:

$$\frac{(V_K^*)_s}{(\bar{V}_K^*)_s} = \frac{V_K^*}{\bar{V}_K^*} = \frac{J_K}{\bar{J}_K} = \frac{(c_{r_0})_K}{Q_0/N_e} h_0 \delta b_0. \tag{2.07}$$

We thus found $(\bar{V}_K^*)_s = 0{,}40$ Volt for our two-dimensional models, and $(\bar{V}_K^*)_s = 0{,}74$ Volt for the three-dimensional; the corresponding voltage V_0 lay between 12 and 20 Volt in both instances. (We shall explain later why we chose these particular mean values.) The total current J_0 through the circuit is

$$J_0 = \frac{(\bar{V}_K^*)_s}{R_0} N_e. \tag{2.08}$$

Thus, the voltage difference V_G at the ends of the resistance R_G (see Fig. 2.08) is

$$V_G = J_0 R_G = \frac{N_e R_G}{R_0} (\bar{V}_K^*)_s. \tag{2.09}$$

The procedure for fixing the $(V_K^*)_s$-distribution along the collector is as follows. We first regulate the voltage of the oscillator (1) until we obtain the voltage V_G between the ends of the resistance R_G, as given by the Eq. (2.09). Then we make a rough regulation of the $(V_K^*)_s$-distribution by short-circuiting some of the resistances R_a, R_b, R_c, and then by regulating one by one, the potentiometers R_{P_K} $(K = 1, 2, \ldots, N_e)$, for each of the N_e branches. It is simpler to start this process at the last branch, e.g., for the collector in Fig. 2.05 at the branch of the (36)-electrode. After one complete cycle (last $\to$ (1)), we again regulate the V_G voltage and repeat the regulation of the $(V_K^*)_s$ in the same way as before. Then, for the fine regulation we short-circuit the resistance R_G, and we iterate on the $(V_K^*)_s$ using this same cycle, changing the oscillator voltage slightly when necessary, until we obtain the desired $(\bar{V}_K^*)_s$-distribution.

In the case of two-dimensional models, we attained any desired distribution by five or six iterations; in the case of the three-dimensional model, five iterations were, in general, sufficient, as for example is shown in *Table II*. As soon as this stage was completed, we measured the voltage V_0 between E and P. We would like to note here that the most difficult voltages to regulate were those of the electrodes lying in angles between $\theta = 0$ and $\theta \approx 90°$, especially in the two-

Table II. Iteration Procedure to Adjust $(V_K^*)_s = 400$ *mV on the Three-Dimensional Model* ($N_e = 40$)

Serial Branch Number (K)	$(V_K^*)_s$-distribution obtained by the rough adjustment	Fine Adjustment of $(V_K^*)_s$ (values in mV)				
		Iteration I	Iteration II	Iteration III	Iteration IV	Iteration V (values within less then ± 1 mV)
1	160	200	280	390	400	400
2	210	250	360	400	400	↑
3	250	310	400	410	400	
4	300	370	405	420	400	
5	360	400	415	420	401	
6	430	400	420	425	401	
7	500	420	420	430	401	
8	580	430	420	430	400	
9	700	440	420	425	400	
10	840	450	420	420	400	
1	230	460	420	420	401	
2	270	430	420	420	401	
3	310	420	420	420	402	
4	340	410	420	420	403	
5	370	410	415	420	403	
6	410	405	415	420	403	
7	450	405	415	420	402	
8	470	410	415	415	402	
9	510	410	415	415	402	
20	570	410	410	415	402	
1	380	415	410	415	400	
2	400	410	410	415	400	
3	440	410	410	415	400	
4	460	410	410	410	400	
5	490	410	410	415	400	
6	520	410	410	415	400	
7	550	410	410	415	400	
8	300	410	410	410	400	
9	320	410	410	410	400	
30	340	405	410	410	400	
1	290	405	410	410	400	
2	300	400	410	405	400	
3	320	400	405	405	400	
4	330	400	405	405	400	
5	340	400	405	405	400	
6	350	395	405	405	400	
7	360	395	405	405	400	
8	480	395	405	405	400	
9	470	395	405	405	400	
40	490	400	405	405	400	400

dimensional models, because in this region the wall of the spiral model lies rather near to the electrodes; a consequence of this proximity was that even small changes of the current through an electrode during the regulation involved a significant change of the currents of the electrodes nearby. In contrast, in the region $\theta > 90°$, the above influence between electrodes became smaller and smaller; for $\theta > 200°$ the influence was practically negligible.

As mentioned in § 2.1.3 the tolerances of the resistances R_0 were $\pm 0{,}6$ per cent. On the other hand, the error of the electronic voltmeter we used did not exceed $\pm 0{,}5$ per cent. We had, therefore, an error in our $(V_A^*)_s$-distribution:

$$e = \pm \sqrt{0{,}6^2 + 0{,}5^2} \approx 0{,}8 \text{ per cent}.$$

After the above mentioned regulation was completed we started the point-by-point measurements of the potential V in the model. To do this we had to dip the probe into the water; then we balanced the bridge by the method mentioned in § 2.1.3, keeping either the point D on the potentiometer (8) constant (see Fig. 2.08) or keeping the probe at a constant point (r, θ, z) of the field, and trying to find the corresponding point D on the potentiometer. Fixing the point D is the easier; we can thus trace the equipotential lines $U_1, U_2, U_3, \ldots$ point-by-point (where, as defined in Eq. (2.04), $U = V/V_0$), by keeping one of the coordinates r, θ, or z constant. The best way to do this is to choose the above potentials equidistant, e.g., $U_1 = 0{,}1$; $U_2 = 0{,}2$; $U_3 = 0{,}3$, ... etc.; then, if z is held fixed, and since $U = \text{const.}$ constitutes a relationship between r and θ, we are left with only one independent variable, which we choose to be θ. By choosing constant intervals δr along r and possible varying θ, we can balance the bridge at various points on U. Moreover, it is convenient to balance the bridge on U_1, U_2, etc. at these same values of r with, of course, different θ's. The method of fixing the probe at a point (r, θ, z) and trying to find the potential $U = R'_D/R_D$ on the potentiometer (8) is very difficult. However we followed this method for some measurements in the three-dimenional model, taking $z = \text{const.}$; thus, keeping the difference of the angles $\theta_1, \theta_2, \ldots$ constant, viz. $\theta_1 - \theta_2 = \theta_2 - \theta_3 = \ldots$ we measured the potential U on radii $r_1, r_2, r_3, \ldots$ also constant.

To evaluate the measurements we introduced for the velocity $c\,(c_r, c_t, c_z)$ and the static pressure p the dimensionless expressions:

$$C = \frac{c}{c_\infty}; \qquad C_r = \frac{c_r}{c_\infty}; \qquad C_t = \frac{c_t}{c_\infty}; \qquad C_z = \frac{c_z}{c_\infty}; \qquad P = \frac{p - p_\infty}{q_\infty}, \tag{2.10}$$

where c_∞ is the velocity and $p_\infty, q_\infty = \rho/2\, c_\infty^2$ are the static and dynamic pressures at the cross-section S_p (see Fig. 1.24) which corresponds to the position of the P-electrode of the model. Hence, from the fundamental Eq. (1.39) of the electric analogy, and Eq. (2.04),

$$U = \frac{V}{V_0}, \tag{2.04}$$

we obtain

$$c \to -V_0 \operatorname{grad} U = -V_0 \nabla U,$$

and

$$c_\infty \to -V_0 (\operatorname{grad} U)_\infty = -V_0 (\nabla U)_\infty, \tag{2.11}$$

where

$$(\nabla U)_\infty = \frac{1}{V_0} (\operatorname{grad} V)_\infty = -\frac{\sigma}{V_0} i_\infty = -\frac{\sigma J_0}{V_0 S_p},$$

or, by Eq. (2.08),

$$(\nabla U)_\infty = -\frac{(\bar{V}_K^*)_s N_e}{V_0} \frac{\sigma}{R_0 S_0}. \tag{2.12}$$

Now using the Eqs. (1.41) and inserting the expressions (2.11) into Eqs. (2.10) we obtain

$$\begin{aligned} C &= \frac{\nabla U}{(\nabla U)_\infty} = \frac{\nabla \phi}{(\nabla \phi)_\infty}, \\ C_r &= \frac{\frac{\partial U}{\partial r}}{(\nabla U)_\infty} = \frac{\frac{\partial \phi}{\partial r}}{(\nabla \phi)_\infty}, \\ C_t &= \frac{\frac{1}{r}\frac{\partial U}{\partial \theta}}{(\nabla U)_\infty} = \frac{\frac{1}{r}\frac{\partial \phi}{\partial \theta}}{(\nabla \phi)_\infty}, \\ C_z &= \frac{\frac{\partial U}{\partial z}}{(\nabla U)_\infty} = \frac{\frac{\partial \phi}{\partial z}}{(\nabla \phi)_\infty}. \end{aligned} \tag{2.13}$$

Further, according to Bernoulli's equation, $p + \rho/2\, c^2 = p_\infty + \rho/2\, c_\infty^2 = \text{const.}$, we obtain,

$$P = 1 - C^2 = 1 - (C_r^2 + C_t^2 + C_z^2). \tag{2.13.1}$$

Using the values of the $U(r)$, $U(\theta)$, $U(z)$ obtained by the measurements, we can trace, by means of the Eqs. (2.13), the distributions of the C_r, C_t, C_z along the directions r ($\theta, z = \text{const.}$) or θ ($r, z = \text{const.}$) or z ($r, \theta = \text{const.}$), respectively. Let us consider the C_t-distribution with $(r, z) = \text{const}$. To trace it we can use either a graphical or a numerical method; the graphical method is shown in Fig. 2.20 where, through the measuring points $\nu - 1$, ν, $\nu + 1, \ldots$, plotted against θr, we get, e.g., at the point B of the field,

$$(C_t)_B = \frac{\operatorname{tg} \varphi}{(\nabla U)_\infty}.$$

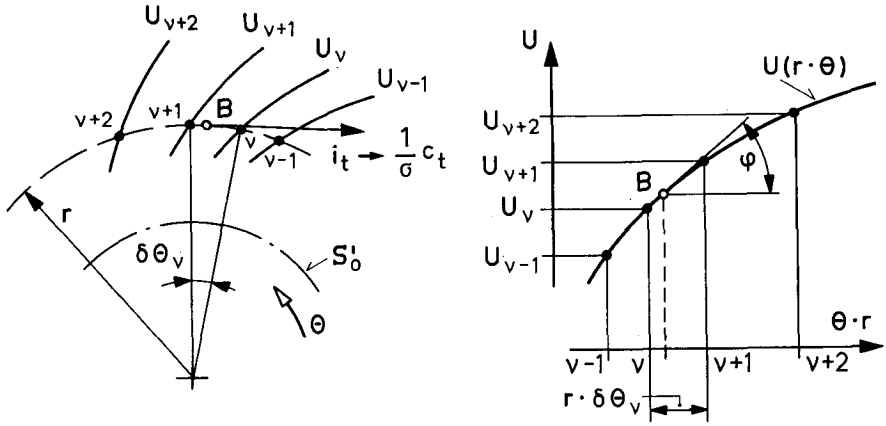

Fig. 2.20.

By the numerical method, in the middle m of the interval between any successive measuring points ν and $\nu+1$ on the circle r, we obtain

$$(C_t)_m = \frac{1}{r}\frac{\frac{\delta\phi}{\delta\theta}}{(\nabla\phi)_\infty} = \frac{1}{r}\frac{\frac{\delta U}{\delta\theta}}{(\nabla U)_\infty}.$$

Likewise

$$(C_r)_m = \frac{\frac{\delta\phi}{\delta r}}{(\nabla\phi)_\infty} = \frac{\frac{\delta U}{\delta r}}{(\nabla U)_\infty}, \qquad (2.14)$$

$$(C_z)_m = \frac{\frac{\delta\phi}{\delta z}}{(\nabla\phi)_\infty} = \frac{\frac{\delta U}{\delta z}}{(\nabla U)_\infty},$$

where $\delta U = U_{\nu+1} - U_\nu$ in the three directions θ, r, and z, respectively; correspondingly $\delta\phi = \phi_{\nu+1} - \phi_\nu$ is the velocity potential interval.

To evaluate the measurements, we followed the second method since it was able to yield greater degrees of accuracy for our purposes.

If $\bar{c}_{r_0}$ is the mean radial component of the velocity along S_0 we can write, according to Eqs. (1.30) and (1.47):

$$Q_0 = c_\infty S_p = \int_0^{2\pi} h_0 r_0 c_{r_0} d\theta = 2\pi r_0 h_0 \bar{c}_{r_0} = S_0 \bar{c}_{r_0}.$$

Consequently by Eqs. (2.10):

$$\bar{C}_{r_0} = \frac{\bar{c}_{r_0}}{c_\infty} = \frac{S_p}{2\pi r_0 h_0} = \frac{S_p}{S_0}. \qquad (2.14.1)$$

In our two-dimensional models, $r_0 = 7{,}5$ cm and $S_p = L h_0$, $L = 18{,}66$ cm, while in the three-dimensional model $r_0 = 11{,}85$ cm, $h_0/2 = 2{,}31$ cm and $\frac{1}{2} S_p = \frac{1}{2}\frac{\pi}{4} 18^2 = 128{,}2$ cm^2. We therefore obtain

a) for the two-dimensional models: $\bar{C}_{r_0} = 0{,}40$,

b) for the three-dimensional model: $\bar{C}_{r_0} = 0{,}74$.

It is now clear, since $\bar{C}_{r_0} \sim (\bar{V}_K^*)_s$, why we chose the values of $(\bar{V}_K^*)_s$ to be 0,40 volt for the two-dimensional models and 0,74 volt for the three-dimensional model. In this way the $(V_K^*)_s$- and C_{r_0}-distribution along S_0 are expressed by the same numbers (or by the same curve).

2.2. Measurements on Two-Dimensional Models

2.2.1. Preliminary Experiments. Modifications of the Collector Form

The preliminary experiments which are described in this section are of fundamental importance in our investigation. Indeed, before starting the measurements in the spiral casing models it was necessary to verify the validity of the principle of our previously described iterative method. For, as we have seen in § 1.3.3, it is not the satisfaction of the relationship (1.49) but that of the relationship (1.56),

$$J_K = J_{w_K} \to \frac{1}{\sigma}(c_{r_0})_K h_0 \delta b_0, \quad (K = 1, 2, \ldots, N_e) \tag{1.56}$$

which is sufficient to secure a sensible approximation to the boundary condition (1.55),

$$i_{r_0} \to \frac{1}{\sigma} c_{r_0}, \tag{1.55}$$

along S_0, which is the *necessary* and *sufficient* condition for a perfect correspondence between the two fields ϕ and V. On the other hand the use of alternating current, which introduces parasitic capacities and consequently a separation of the measured current J_K into an *ohmic current* and a *capacitive current* immediately after leaving the boards (4) (see Fig. 2.08), may present some additional difficulties for the satisfaction of the boundary condition needed.

To check the method, we used the well-known two-dimensional *logarithmic field* generated from a *source* q and a *circulation* Γ both at a point 0. The main advantage of this field is that it is the nearest known field to the potential flow through spiral casings; on the other hand, we can use, for the preliminary

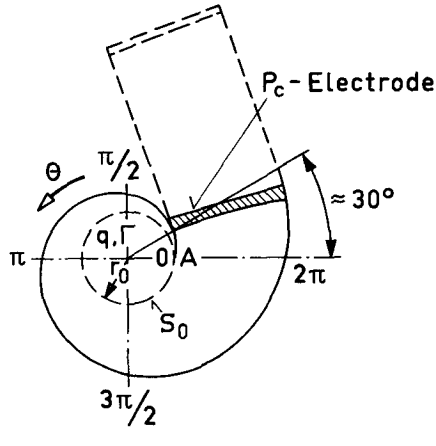

Fig. 2.21. Diagramatic view of the logarithmic spiral model with the P_c-Electrode.

experiments in question, the same logarithmic model described in § 2.1.2 (see Fig. 2.01). Let us thus remove the P-electrode from this model and fix the *P_c-Electrode*, which is a segment of a logarithmic spiral normal to the logarithmic spiral of the model walls at about 30° away from point A. This arrangement is shown in Fig. 2.21. Suppose that throughout the surface S_0 we introduce a current density i_{r_0} = const. into the water. The electric field in the region between S_0, the walls of the spiral and the P_c-electrode must, therefore, be a pure logarithmic field; in other words, we must obtain throughout this region

$$\begin{aligned} i_r r &= i_{r_0} r_0 = \text{const.} \\ i_t r &= i_{t_0} r_0 = \text{const.} \\ \sphericalangle\, \alpha &= \sphericalangle\, \alpha_0 = \text{const.}, \end{aligned} \tag{2.15}$$

where $$\operatorname{tg}\alpha = \frac{i_r}{i_t}; \qquad \operatorname{tg}\alpha_0 = \frac{i_{r_0}}{i_{t_0}}.$$

As mentioned in § 2.1.2, $\operatorname{tg}\alpha_0$ of the logarithmic shape of the model under consideration is $\operatorname{tg}a_0 = 1{,}2/2\pi$, viz. if $i_{r_0} = \text{const.}$ along S_0 we must obtain throughout the field

$$\frac{i_r}{i_t} = \frac{i_{r_0}}{i_{t_0}} = \frac{1{,}2}{2\pi}. \tag{2.16}$$

Thus the current-lines will be logarithmic spirals of the form

$$r_{sl} = r_0 e^{\varphi_{sl}\operatorname{tg}\alpha_0}, \tag{2.17}$$

where $\sphericalangle \varphi_{sl} = \sphericalangle (r_0, r_{sl})$, and the equipotential curves will therefore be logarithmic segments

$$r_c = r_0 e^{\varphi_c \operatorname{tg}\left(\frac{\pi}{2}+\alpha_0\right)}, \tag{2.18}$$

where $\sphericalangle \varphi_c = -\sphericalangle (r_0, r_c)$; the shape of the P_c-electrode is such a segment.

The similarity of this electric field to a potential flow generated from a pair (q, Γ) in the center of the cylindrical surface S_0 is expressed by the relations

$$\begin{aligned} i_r r &\to \frac{1}{\sigma} c_r r = \frac{1}{\sigma}\frac{q}{2\pi} = \frac{1}{\sigma} r \frac{\partial \phi}{\partial r} \\ i_t r &\to \frac{1}{\sigma} c_t r = \frac{1}{\sigma}\frac{\Gamma}{2\pi} = \frac{1}{\sigma}\frac{\partial \phi}{\partial \theta}, \end{aligned} \tag{2.19}$$

where, as is well known, the *velocity potential* ϕ is expressed as

$$\phi = \frac{q}{2\pi}\ln r + \frac{\Gamma}{2\pi}\theta + \text{const.}$$

(q is the source strength per unit length normal to the field). Therefore

$$\frac{q}{2\pi r_0} = c_{r_0} \to \sigma i_{r_0}, \qquad \frac{\Gamma}{2\pi r_0} = c_{t_0} \to \sigma i_{t_0}, \qquad \frac{q}{\Gamma} = \operatorname{tg}\alpha_0. \tag{2.20}$$

Further, since $$\sigma i_{t_0} = -\frac{1}{r_0}\left(\frac{\partial V}{\partial \theta}\right)_{r=r_0},$$

and $$c_{t_0} = \frac{1}{r_0}\left(\frac{\partial \phi}{\partial \theta}\right)_{r=r_0},$$

we must obtain

$$\Gamma = \oint_{S_0} c_{t_0} r_0 \, d\theta = \oint_{S_0} d\phi \to -\sigma \oint_{S_0} i_{t_0} r_0 \, d\theta = -\oint_{S_0} dV;$$

viz. $$\Gamma = [\phi(2\pi) - \phi(0)]_{r=r_0} \to [V(0) - V(2\pi)]_{r=r_0}. \tag{2.21}$$

As a first stage of the preliminary experiments intended to investigate the above electric field we used the *Collector I*, whose form is shown in Fig. 2.05. Thus, following the iterative procedure mentioned in § 2.1.3, we fixed, in about six iterations, a voltage $V_K^* = \text{const.}$ $(K = 1, 2, \ldots, 36)$ for each of the 36 electrodes of the collector. Then we investigated the electric field point by

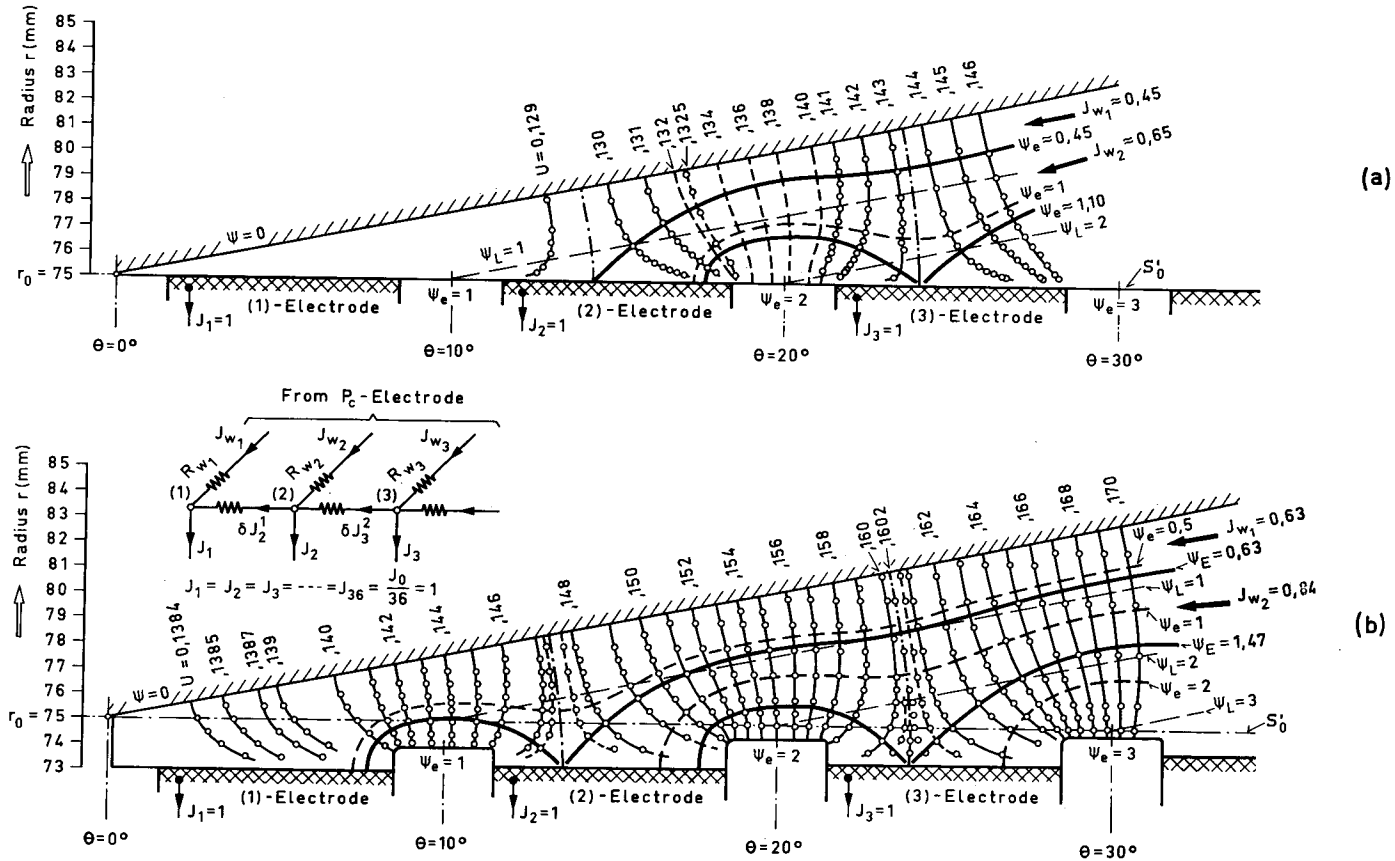

Fig. 2.22. Form of the V-field near the first three electrodes of Collector I, for $J_k = \text{const}$.

point in the region near the first three electrodes, i.e. the electrodes (1), (2) and (3). The unrolled form of the V-field in this region is shown in Fig. 2.22a. It can be seen immediately that this field is far from being a logarithmic one; its current-lines ψ_e, which are traced as normals to the equipotentials U ($U = V/V_0$), indicate that strong secondary ohmic currents occurred between successive electrodes, while the dotted lines ψ_L show the current-lines of the desired pure logarithmic field according to Eq. (2.17). Because the region between the (1)-electrode and the spiral wall was extremely narrow (not exceeding 2 mm), as shown in this figure, the measurements of the potential there could not be effected. To facilitate the measurements, we therefore made, as shown in Fig. 2.22b, a 2 mm undercut on the (1)-electrode and proportionately smaller undercuts on the insulators and the electrodes up to the fourth electrode. This figure shows the point-by-point measured, and the traced, equipotential lines; some characteristic current-lines ψ_e of the field are also traced. The form of the field remains practically unchanged in both Figs. 2.22a and 2.22b, before and after the undercuts, respectively. In 2.22b, we can more easily observe the form of the secondary ohmic currents between successive electrodes. Thus, if at each of the 36 branches of the circuit we write the current distribution which was regulated by the potentiometers to be constant, as

$$J_1 = J_2 = \cdots = J_{36} = \frac{J_0}{36} = 1{,}0,$$

we see that the actual current in the tube through the (1)-electrode, is $J_{w_1} = 0{,}63$ only, and that in the tube through the (2)-electrode, is $J_{w_2} = 0{,}84$ only. In other words, the real current distribution in the field is far from being the one regulated. Thus, in the region between $\theta = 0$ and the (3)-electrode the equivalent circuit of the current-tubes is the one shown in the upper left side

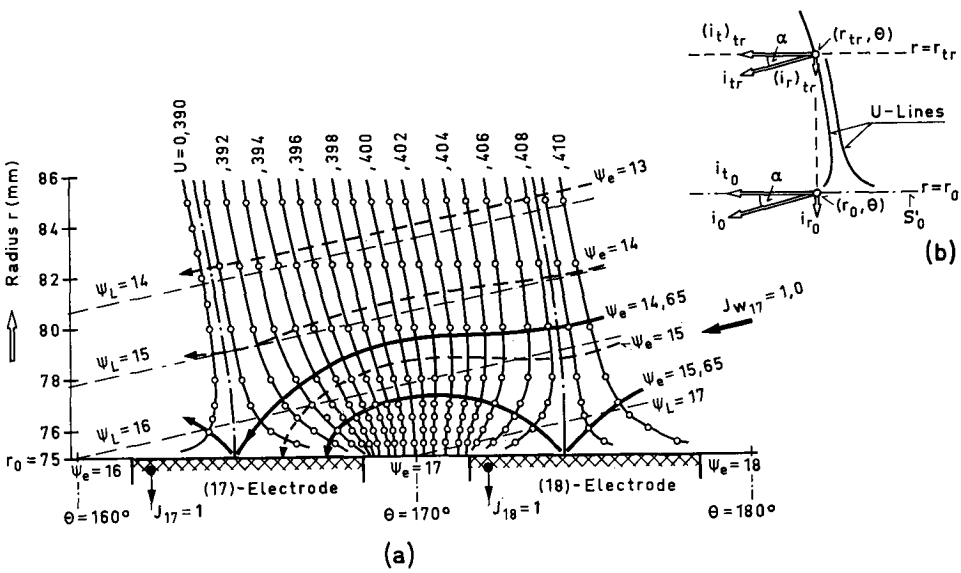

Fig. 2.23. Form of the V-field near the electrodes at $\theta \approx 160° - 180°$; Collector I, $J_K = \text{const.}$

of Fig. 2.22b. The secondary ohmic currents according to *Kirchoff's* law are:

from the (2)- to the (1)-electrode, $\delta J_2^1 = J_1 - J_{w_1} = 0{,}37$,

from the (3)- to the (2)-electrode, $\delta J_3^2 = (J_1 + J_2) - (J_{w_1} + J_{w_2}) = 0{,}53$.

The shape of the equipotential lines, for example in the region between the (17)- and the (18)-electrode, i.e. far from the tongue of the spiral, is shown in Fig. 2.23a. Evidently, the field here is of the same kind as that in the region of the first few electrodes since secondary currents between successive electrodes, still exist. Tracing the current-lines ψ_e of the field, we see that the current of the (17)-tube is $J_{w_{17}} \approx 1{,}0$, while the secondary ohmic current between the (17)- and the (18)-electrode is

$$\delta J_{18}^{17} = 1{,}35.$$

We therefore infer from the above that the electric field obtained by means of the collector form under consideration has no other boundary relationship with the desired logarithmic field along S_0, in spite of the fact that its total current J_0 remains the same; viz.

$$J_0 = \sum_1^{36} J_K = \sum_1^{36} J_{w_K}.$$

In other words, we adjusted:

$$J_1 = J_2 = \cdots = J_{36} = \frac{J_0}{36}$$

and we obtained:

$$J_{w_1} \neq J_{w_2} \neq \cdots \neq J_{w_K} \neq \cdots \neq J_{w_{36}}.$$

Hence, the electric field obtained cannot be characterized as an electric analogy to a logarithmic potential flow, since neither the approximating condition (1.56) nor, what is more, the conditions (2.20) are valid. It is nevertheless remarkable that the equipotential lines, and therefore the ψ_e-lines, take a rather uniform shape at a short distance from the surface S_0', as shown in Figs. 2.22 and 2.23a. Furthermore, we see in Fig. 2.23a, that for $r > 82{,}5$ mm, i.e. for $r > 1{,}1\, r_0$, the orientation of the field obtained is very near to that of the desired logarithmic field. It is obvious, therefore, that, if we could avoid the secondary currents δJ_{K+1}^K or if we could obtain $\delta J_{K+1}^K = \text{const.}$ throughout the collector, the influence of the width of the electrodes and the insulators between them practically vanishes not far from S_0'. Furthermore, as the length δb_0 (see Fig. 1.24c) is decreased, the transition zone outside S_0' becomes narrower. We could therefore investigate the field in the region $r \geqq r_{tr}$ (= transition-radius) and, if $r_{tr} - r_0 \ll r_0$, extrapolate the results by $\theta = \text{const.}$ up to the surface S_0', applying the logarithmic law

$$i_r(\theta)\, r = i_{r_0}(\theta)\, r_0$$
$$i_t(\theta)\, r = i_{t_0}(\theta)\, r_0, \quad (\theta = \text{const.}),$$

for $r_{tr} \geqq r \geqq r_0$, as shown in Fig. 2.23b.

We can employ this method in our case of variable δJ_{K+1}^K to see the influence of these secondary currents on the i_{r_0}- and i_{t_0}-distributions, since the transition zone does not exceed roughly 10 per cent of r_0. In the diagram of Fig. 2.24,

the curves (1) give the values of the i_{r_0} and i_{t_0} obtained by the above method of extrapolation, from measurements at $r = 80$; 85 and 90 mm. The line $j_n = 1{,}0$ presents the desired average normal component of the current density on every sector δb_0 of the S_0'. This would be obtained if $J_K = J_{w_K}$ throughout S_0'. The line $(i_{t_0})_{th} = 5{,}23$ presents the tangential component of the current density along S_0' in this case, since, for a pure logarithmic field in the model under consideration, we must have, according to Eq. (2.16),

$$(i_{t_0})_{th} = \frac{j_n}{\frac{1{,}2}{2\pi}} = 5{,}23\, j_n .$$

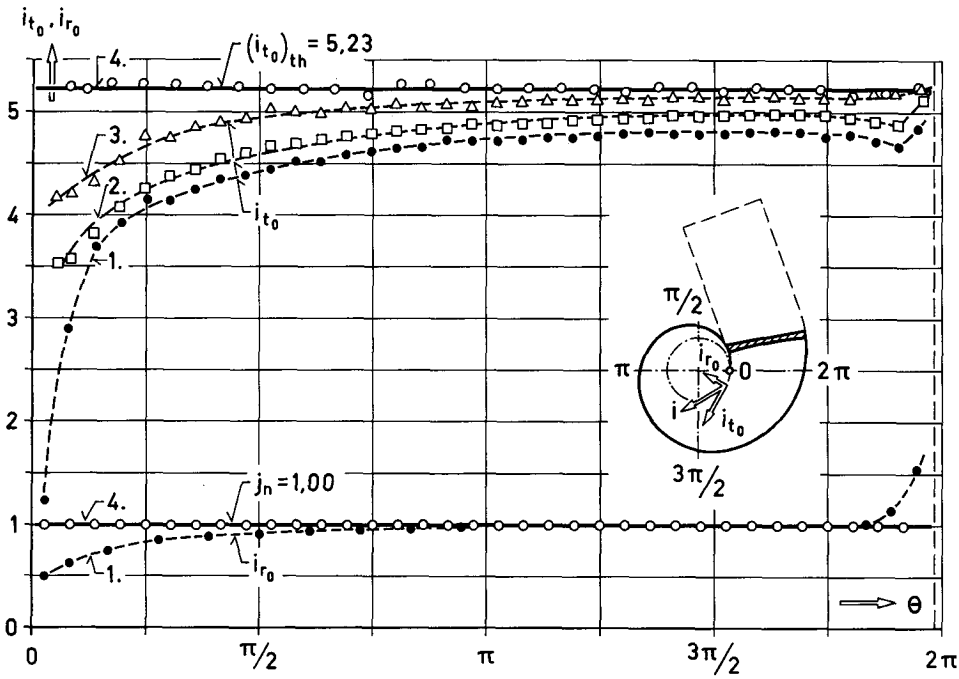

Fig. 2.24. Current-density distributions i_{t_0} and i_{r_0} along S_0 for $J_K = \text{const}$.

1. For the Collector I.
2. For the Collector II.
3. For the Collector III.
4. For the Collector III by using the modification of the circuit shown in Fig. 2.28c.

Comparing the j_n and $(i_{t_0})_{th}$-distribution with those obtained from $(i_{r_0}, i_{t_0})_1$, we see that the error imposed by the secondary ohmic currents and, possibly, also by unknown causes is unacceptable.

The best way to overcome this difficulty is to modify the form of the collector, following the method mentioned in § 1.3.3. The first step of this modification *(Collector II)* is shown in Fig. 2.25; the electrodes were placed inside S_0' and were under an inclination of 60° to it. The results obtained for i_{t_0}, again taking $j_n = \text{const.}$, are given by the curve (2) of Fig. 2.24. It can be seen immediately that there is an improvement which, however, is still insufficient.

The second step of the collector modification *(Collector III)* is shown in Fig. 2.26; this collector is of the form proposed at the end of § 1.3.3 (see Fig. 1.30b). The insulating plates between the electrodes are made of *plexiglass* with a thickness of 0,5 mm; they are planes inclined to S_0' in about 25°. The results of the measurements to investigate whether secondary ohmic currents occur between successive electrodes of this configuration are shown in Fig. 2.27; these measurements were made in the most sensitive region, which lies between the (1)- and the (2)-electrode. It can be seen from this figure that secondary currents no longer exist; that is $\delta J_{K+1}^{K} = 0$ throughout the surface S_0'. Moreover, the field is not deformed except in a region about 1,5 mm around the edge of an insulating plate. Thus, since $j_n = \text{const.}$, we can say that $i_{r_0} \approx \text{const.}$ throughout S_0'. It is obvious, therefore, that, if no *unknown* significant perturbative causes exist, the boundary condition $i_{r_0} \to 1/\sigma c_{r_0}$ along S_0' will be satisfied by means of the arrangement of the electrodes in the collector III; consequently, the field obtained should be a logarithmic field, i.e. we must find, according to Eq. (2.16), $i_{t_0} = 5{,}23$ along S_0. From carefully made measurements, however, we obtained as i_{t_0}-distribution the curve (3) shown in Fig. 2.24. This curve is much nearer to the $(i_{t_0})_{th}$ in relation to the curves (1) and (2), but it is not quite acceptable, since it gives, near the beginning of the spiral, values of the i_{t_0} 25 per cent lower than its theoretical value $(i_{t_0})_{th} = 5{,}23$. This error seems to be caused by the use of alternating current, because the masses of the water on both sides of the 2 mm thick diaphragm between the edge A and the P_c-electrode (see Fig. 2.28a) forms a condenser; a *secondary capacitive*

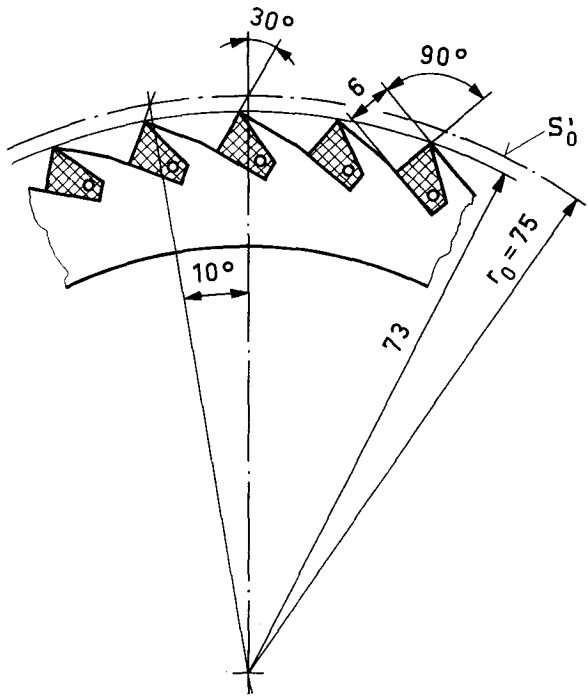

Fig. 2.25. Collector II.

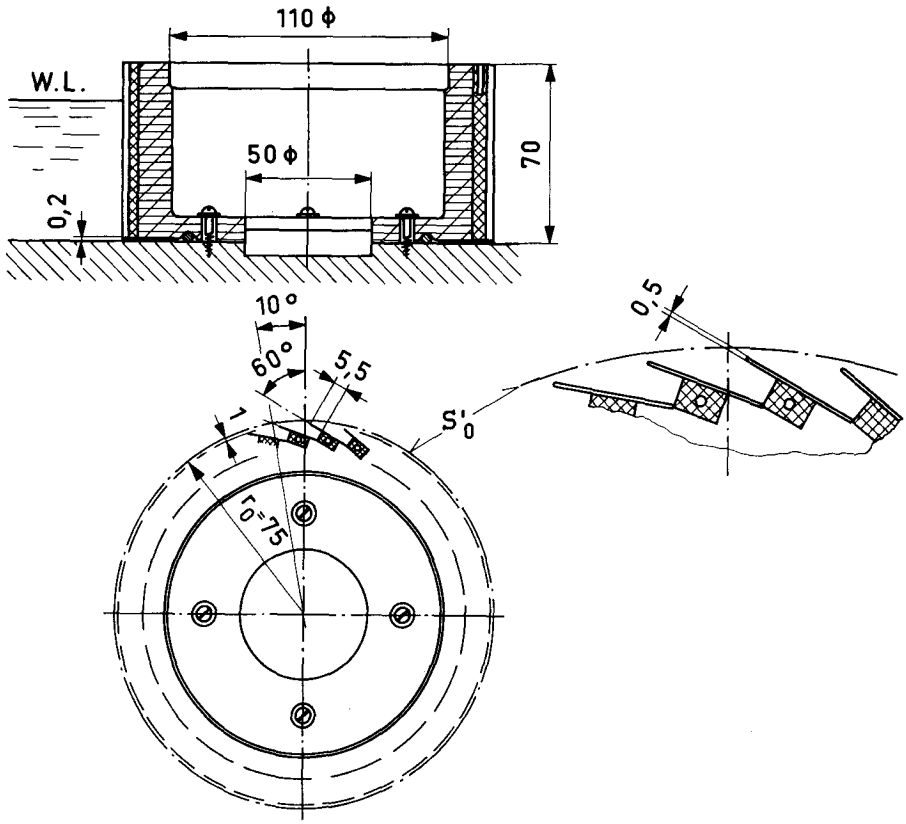

Fig. 2.26. Collector III.

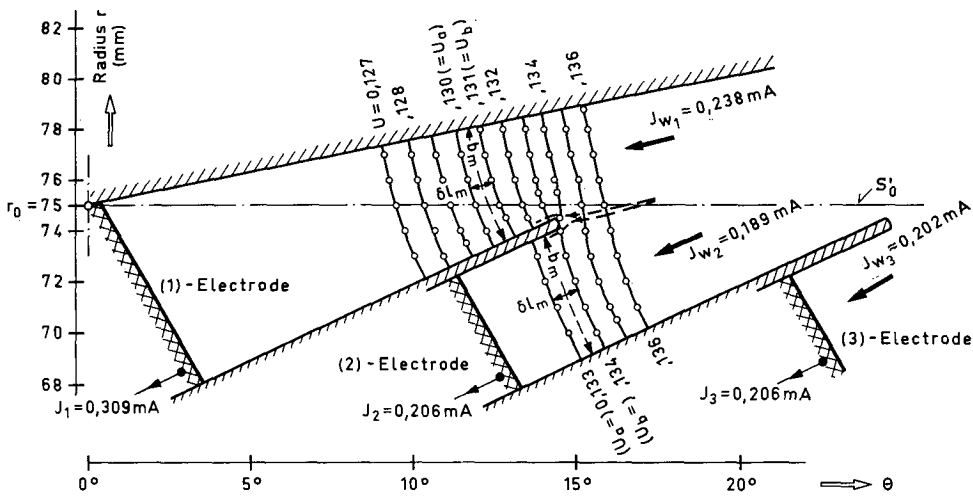

Fig. 2.27. Form of the V-field near the first two electrodes of Collector III, for J_K = const.; secondary ohmic currents do not exist anymore.

current, therefore, must be passing through this diaphragm since there is a voltage difference between its sides. The equivalent circuit in this region is shown in Fig. 2.28b. We adjust, for example, a current J_1 through the (1)-branch of the circuit. This current, passing the (1)-electrode, is divided into an ohmic current J_{w_1} and a capacitive current J_{c_1}, which are normal to each other. It is obvious from the current diagram shown in the same figure that $J_{w_1} < J_1$.

To verify the above hypothesis, let us calculate the ohmic currents J_{w_1} and J_{w_2} through the first two current-tubes from the equipotential lines of Fig. 2.27. The characteristics of the circuit and the results of this calculation are given in *Table III*. We see from this table that $J_{w_1} = 0{,}770\,J_1$ and $J_{w_2} = 0{,}917\,J_2$, i.e. we did not yet fulfill the boundary condition (1.47). On the other hand, if the condenser in question really existed, the capacitive currents through the (1)- and (2)-tubes, according to the current-diagram in Fig. 2.28b, would be $J_{c_1} = 0{,}638\,J_1$ and $J_{c_2} = 0{,}399\,J_2$. From measurements in the region of the (3)-electrode we found, by the same method,

$$\frac{J_{w_3}}{J_3} \approx 0{,}98, \quad \text{consequently} \quad \frac{J_{c_3}}{J_3} \approx 0{,}196.$$

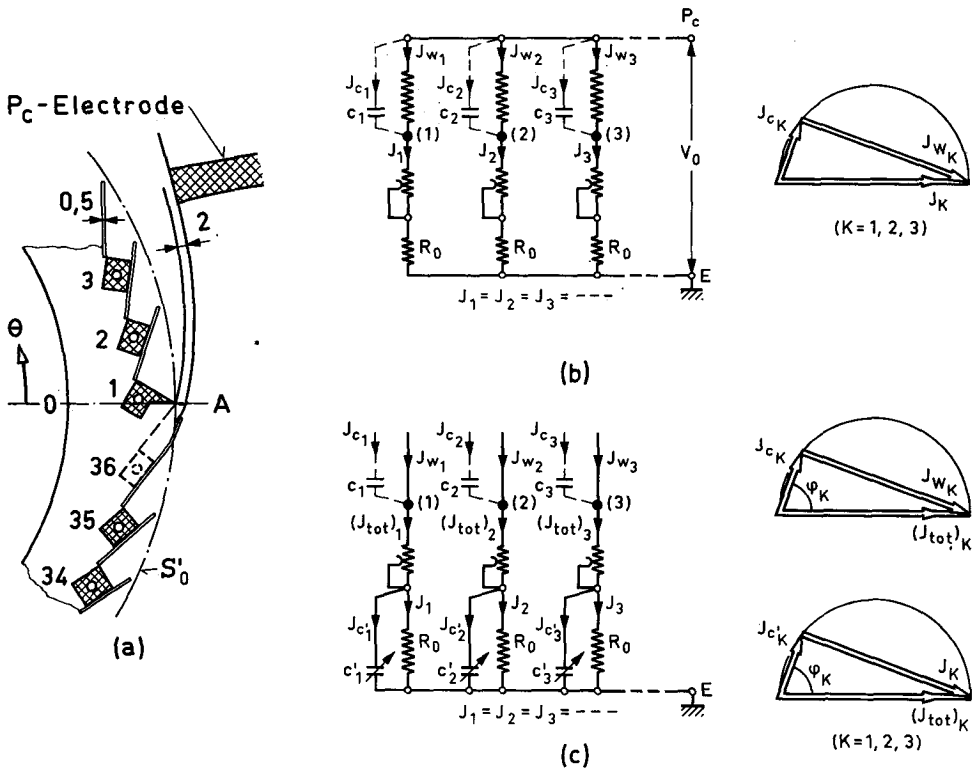

Fig. 2.28. Feeding-circuit modification in order to avoid the influence of the secondary capacitive currents during the regulation of the J_K-distribution; b) unmodified circuit, c) modified circuit.

Table III. Ohmic and Capacitive Currents through the (1)- and the (2)-Current-Tube (see also Figs. 2.24 and 2.28b)

Voltage:	$V_0 = 21{,}20$ Volt	
Adjusted Current[1]):	$J_K = 0{,}206$ mA; $(K = 2, 3, \ldots, 34)$	
Specific Resistance of the Water:	$\sigma = 3045\ \Omega$ cm	
Depth of the Water:	$h_0 = 6{,}32$ cm	
Nominal Current Density along S_0':	$j_n = \frac{J_K}{\delta b_0 h_0} = 0{,}025$ mA/cm²	
	(1)-Current-Tube ($K=1$)	(2)-Current-Tube ($K=2$)
J_K (mA)	0,309	0,206
U_a	0,130	0,133
U_b	0,131	0,134
$\delta U = U_b - U_a$	0,001	0,001
$\delta V = V_0 \delta U$ (mV)	21,20	21,20
b_m (cm)	0,475	0,460
δl_m (cm)	0,088	0,107
$\delta R_{wK} = \sigma \frac{b_m}{\delta l_m}$ (Ω)	89,0	112,0
$J_{wK} = \frac{\delta V}{\delta R_{wK}}$ (mA)	0,238	0,189
$\frac{J_{wK}}{J_K}$	0,770	0,917
$\frac{J_{cK}}{J_K} = \frac{\sqrt{J_K^2 - J_{wK}^2}}{J_K}$ (see Fig. 2.28b)	0,638	0,399

[1]) For constructional reasons the interval δb_0 corresponding to the (1)-electrode was made 50 per cent larger than the normal 13,1 mm. The (36)-electrode was 85 per cent covered by the 2 mm insulating plate at the tongue of the spiral and put out of the circuit by placing an insulating plate over the remaining 15 per cent (see Fig. 2.28a); the interval corresponding to the (35)-electrode was thus made 15 per cent larger. We therefore have the adjusted avlues: $J_1 = 0{,}206 \times 1{,}5 = 0{,}309$ and $J_{35} = 0{,}206 \times 1{,}15 = 0{,}237$ mA.

In the region beyond the (3)-electrode $J_K = J_{wK}$, $(K = 4, 5, \ldots)$. It is worth noting that the magnitudes of the currents J_{wK} approach one as soon as we pass the region of the (1)- and (2)-current-tubes, since for the (3)-tube we can say that $J_{w3} \approx J_3$.

If the above hypothesis is true, we can avoid any difference between the adjusted current J_K $(K = 1, 2, 3)$ and the current J_{wK} obtained by introducing three variable capacitors in parallel with the first three branches, as shown in Fig. 2.28c, and regulating them simultaneously with the adjustment of the J_K-distribution to obtain

$$\frac{J'_{c1}}{J_1} = R_0 c_1' \omega = 0{,}638, \qquad \frac{J'_{c2}}{J_2} = R_0 c_2' \omega = 0{,}399, \qquad \frac{J'_{c3}}{J_3} = R_0 c_3' \omega \approx 0{,}196,$$

where $\omega = 2\pi f$; $f = 300$ Hz. Thus the current diagrams between the point E

and the electrodes (1), (2), (3) are identical to those between the electrodes (1), (2), (3) and the P_c-electrode, respectively (see Fig. 2.28c). Hence,

$$J_{w_1} = J_1, \qquad J_{w_2} = J_2, \qquad J_{w_3} = J_3.$$

Following the above procedure, we obtained the desired logarithmic field as shown by the curves 4, in Fig. 2.24, where

$$i_{r_0} = j_n \quad = \text{const.} \quad (=1{,}00)$$
$$i_{t_0} = (i_{t_0})_{th} = \text{const.} \quad (=5{,}23)$$

throughout S_0'.

Summarizing the most important points of this section we conclude:

a) An arrangement of electrodes which are placed on the boundary surface S_0' is unsuitable for representing potential flow, except perhaps for some particular form or orientation of S_0; furthermore, even in this particular arrangement, a quite complicated procedure is needed to check whether the boundary condition (1.56) is fulfilled.

b) In contrast, electrodes arranged outside of the region of interest at a suitable distance from S_0' and insulated from each other by thin insulating plates extending to S_0' comprise the best available set-up. Thus, not only the approximative condition (1.56) but also the exact condition (1.55) can be fulfilled; furthermore, to check whether the latter condition is satisfied a relatively small number of preliminary measurements around the edge of some particular insulating plates are needed. Moreover, using a suitable pair of equipotential lines, we can easily calculate the ohmic current through any one of the current-tubes, as shown in Table III.

c) The use of alternating current introduces, in particular regions of the electric-analogy field, secondary capacitive currents which could considerably change the distribution of ohmic current density believed to be obtained by adjusting the arrangement (4) shown in Fig. 2.08. The set-up of the electrodes shown in Collector III permits an easy calculation of the above secondary capacitive currents as indicated in Table III. To overcome the deviations caused by secondary capacitive currents, we introduce additional capacitors into the arrangement (4) of Fig. 2.08, as shown in Fig. 2.28c.

The above conclusions are valid not only for the particular case of electric analogy models of spiral casings but also for any case in which the potential flow passes slant-wise through a part of or the whole of the considered bounding surface.

2.2.2. Measurements on the Logarithmic and Archimedes' Spiral Models for $C_{r_0} = \text{const.}$ Results

The respective models used are shown in Figs. 2.01 and 2.02. Collector III was used in both models. Fig. 2.29 illustrates the Collector III assembled on the logarithmic model. The procedures followed for the measurements (i.e. the adjusting of the desired J_K-distribution along S_0 and the point-by-point investigation of the V-field) and their evaluation have been mentioned in § 2.1.5.

In both models we first considered the case of $c_{r_0} = \text{const.}$ ($J_K = \text{const.}$ along S_0') since, as we have seen in § 1.2.2, this condition around S_0 is of particular practical importance.

The first stage of the measurements after the adjusting of the J_K-distribution was to check whether secondary ohmic and capacitive currents occur (see § 2.21). In both models there was no secondray ohmic current along S_0. In the logarithmic model, the secondary capacitive currents were of exactly the same values as those mentioned in the preceding section, where the P_c-electrode was used. Namely:

$$\frac{J_{c_1}}{J_1} = 0{,}638\,; \qquad \frac{J_{c_2}}{J_2} = 0{,}399\,; \qquad \frac{J_{c_3}}{J_3} \approx 0{,}196\,.$$

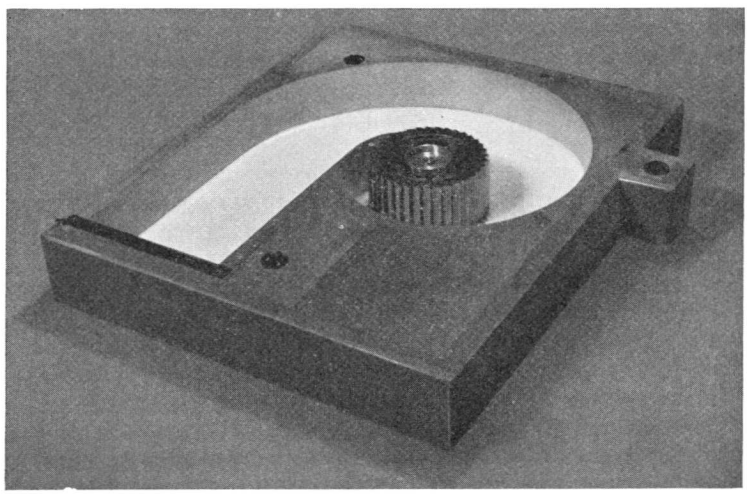

Fig. 2.29. Collector III assembled on the logarithmic spiral model.

Therefore, to secure the identification of the currents J_K and J_{w_K} in this region we applied the arrangement of the capacitors c_1', c_2', c_3' as shown in Fig. 2.28c.

In the Archimedes' model the secondary capacitive currents were much smaller and they were perceptible in the first two current-tubes only; thus we found

$$\frac{J_{w_1}}{J_1} = 0{,}895\,; \qquad \frac{J_{w_2}}{J_2} = 0{,}950\,;$$

consequently,

$$\frac{J_{c_1}}{J_1} = 0{,}440\,; \qquad \frac{J_{c_2}}{J_2} = 0{,}300\,,$$

and by $K = 3, 4, 5, \ldots, J_K = J_{w_K}$.

During the measurements we therefore applied the same arrangement of capacitors shown in Fig. 2.28c but on the two first branches only.

In the remainder of this section we shall describe, individually, the measurements made and the results obtained using $J_K = \text{const.}$, for each one of the two models in question.

a) Measurements on the Logarithmic Model

The form of the equipotential lines obtained by $c_{r_0} = \text{const.}$ in this model is shown in Fig. 2.30 where, instead of the dimensionless electric potential U, the velocity potential ϕ is written directly

$$\phi \to -V = -V_0 U,$$

or

$$\phi \to -V_0 U + \text{const.} \tag{2.22}$$

As shown in this figure, the measuring points were obtained on various radii

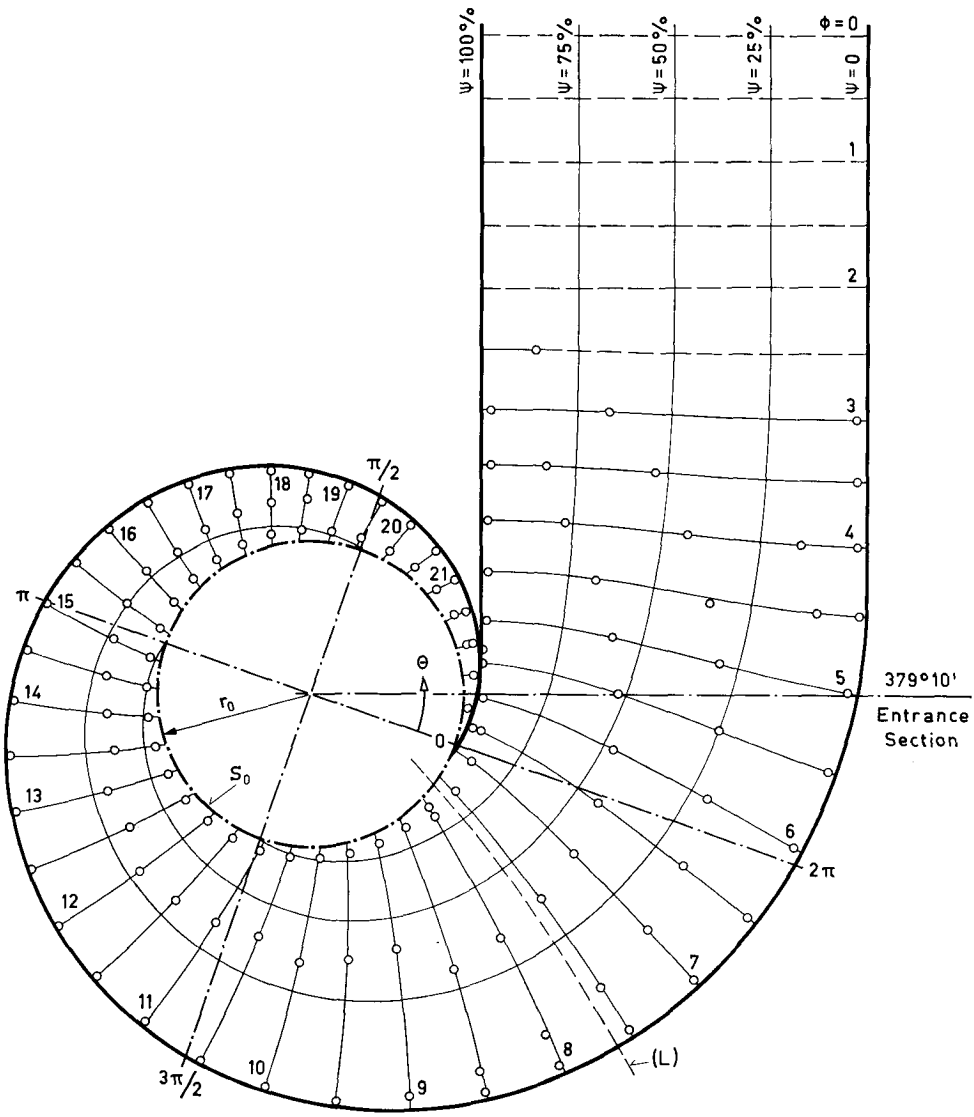

Fig. 2.30. Potential flow through the logarithmic spiral model for $C_{r_0} = \text{const.}$

and at a constant potential difference $\delta\phi = 0{,}5$. The potential difference from $\theta = 0$ to $\theta = 2\pi$ around S_0, measured on Fig. 2.30 is

$$\phi(0) - \phi(2)\pi = 15{,}95.$$

If the potential flow were purely logarithmic, the angle difference $(\delta\theta)^*$ between the equally-spaced equipotential lines by $\delta\phi = 0{,}5$ should be

$$(\delta\theta)^* = \frac{360^\circ}{\phi(0) - \phi(2\pi)} 0{,}5 = 10{,}62^\circ,$$

throughout S_0; furthermore, this angle difference should remain constant between successive equipotential lines of $\delta\phi = 0{,}5$ at $(\delta\theta)^* = 10{,}62^\circ$ throughout the entire field. This is not so in our case, however, since the model consists of a logarithmic spiral up to $\theta = 390^\circ$ only, and from there on the walls of its inlet pipe are parallel. Thus we see in Fig. 2.30 that the equipotential lines in this latter region are straight lines normal to the parallel walls and that they gradually change until they coincide with the logarithmic curve given by Eq. (2.18) at about $\phi = 7{,}5$. This is shown in Fig. 2.30 by the curve (L); further, the equipotential lines obtained for $\phi > 7{,}5$ are logarithmic curves identical to this form. To study the flow more closely, let us plot the angle differences $\delta\theta$ obtained between successive equipotential lines ϕ_{n+1} and ϕ_n where $\phi_{n+1} - \phi_n = \delta\phi = 0{,}5$ at various radii r against the angle θ of the *mean point* of every interval. The results are given in Fig. 2.31 a. From the plotted points, we see immediately that, throughout the region $0 \leqq \theta \leqq 300^\circ$, $\delta\theta$ is

$$\delta\theta = (\delta\theta)^* = 10{,}62^\circ.$$

At the radius $r = r_0$, however, the above value of $\delta\theta$ remains up to $\theta = 2\pi$. At radii greater than r_0, and for θ greater than 300°, the angle difference $\delta\theta$ decreases gradually, but its reduction is rather small, not exceeding 9 per cent at the point $(r_s = 3{,}32\, r_0, \theta = 2\pi)$ of the spiral and 17 per cent at the outer point $r_s = 3{,}546\, r_0$ of the entrance section at $\theta = 379^\circ 10'$. The mean tangential component $(c_t)_m$ of the velocity in any one of the above angle intervals $\delta\theta$ on $r = \text{const.}$ (see also § 2.1.5) is

$$(c_t)_m = \frac{1}{r}\left(\frac{\delta\phi}{\delta\theta}\right)_r.$$

From Fig. 2.31 a, therefore, we concluded that $(c_t)_m r = \text{const.}$ Consequently,

$$c_t r = \text{const.} \tag{2.23}$$

throughout the region $0 \leqq \theta \leqq 300^\circ$,

since there $\delta\theta = \text{const.}$ when $\delta\phi = \text{const.}$ on any radius r. Further, as shown in this figure, Eq. (2.23) is valid up to $\theta = 2\pi$ for $r = r_0$ and up to $\theta = 2\pi^+$ for radii $r < 2r_0$. Along S_0, therefore, we have, experimentally, in our valid region

$$c_{t_0} r_0 = \text{const.} \tag{2.24}$$

In the region $300 < \theta < 379^\circ$ and $r > 2r_0$, Eq. (2.23) is approximately true; the approximation is very good up to $\theta = 2\pi$, since the error does not exceed -9 per cent.

Let us examine the region $0 \leqq \theta \leqq 300^\circ$ where the relation (2.23) is exactly

valid. Let us consider in this region a cylindrical surface S_ν of radius $r_\nu \geqq r_0$ (Fig. 2.32). Then the element dQ_ν of the fluid volume which passes per unit time through the element $dS_\nu = r_\nu h_0 d\theta$ is:

$$dQ_\nu = c_{r_\nu} r_\nu h_0 d\theta = \frac{d}{d\theta}\left(\int_{r_\nu}^{r_s} h_0 c_t dr\right) d\theta,$$

where c_{r_ν} and c_{t_ν} are respectively, the radial and tangential components of the

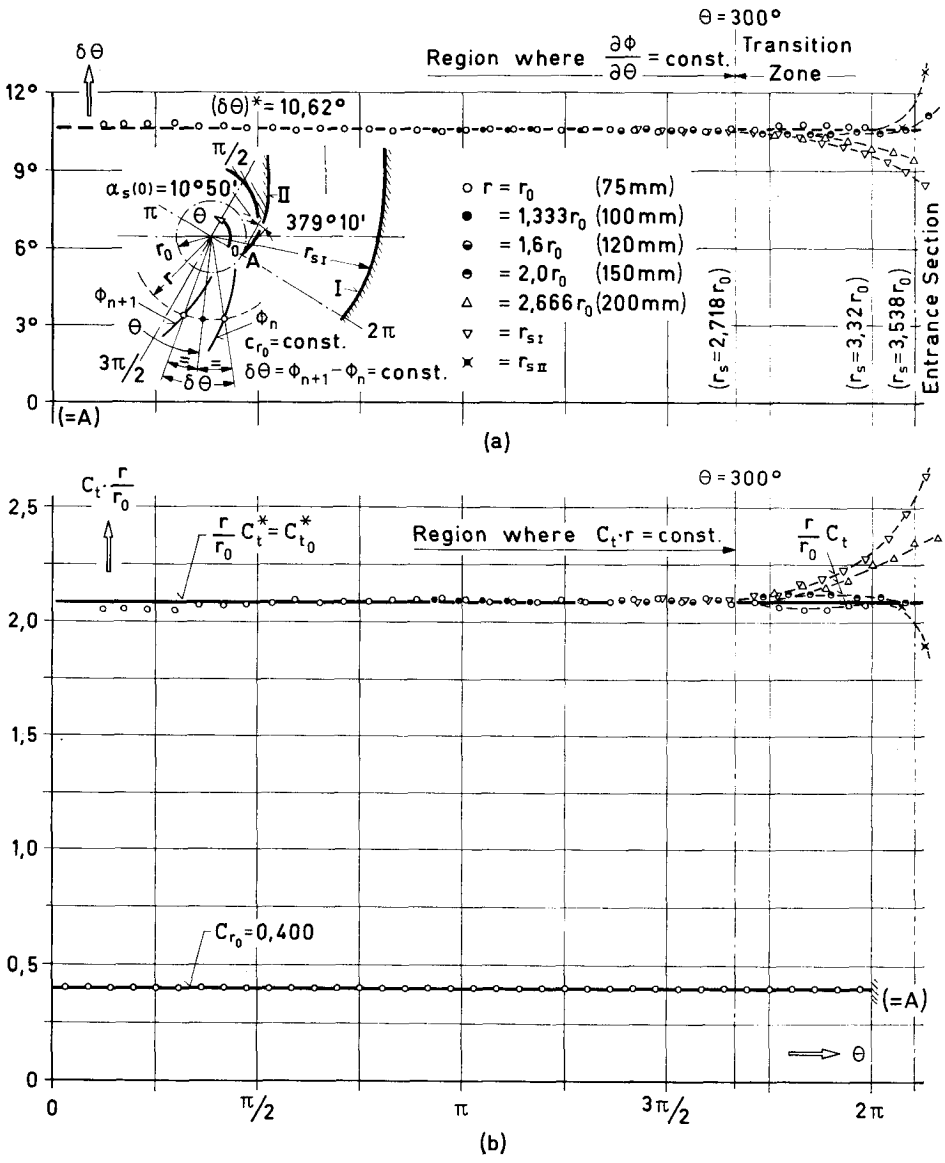

Fig. 2.31. Logarithmic model; C_t-distribution for $C_{r_0} = \text{const.}$

velocity at the point (r_ν, θ). Using Eq. (2.23) the above relation can be written

$$c_{r_\nu} r_\nu = c_{t_\nu} r_\nu \frac{d}{d\theta}\left(\int_{r_\nu}^{r_s} \frac{dr}{r}\right); \tag{2.25}$$

but

$$\frac{d}{d\theta}\left(\int_{r_\nu}^{r_s} \frac{dr}{r}\right) = \frac{d}{d\theta} \ln \frac{r_s}{r_\nu} = \frac{d}{d\theta}\left(\ln \frac{r_s}{r_0} + \ln \frac{r_0}{r_\nu}\right),$$

where

$$\ln \frac{r_0}{r_\nu} = \text{const.}, \quad \text{since} \quad r_\nu = \text{const.}$$

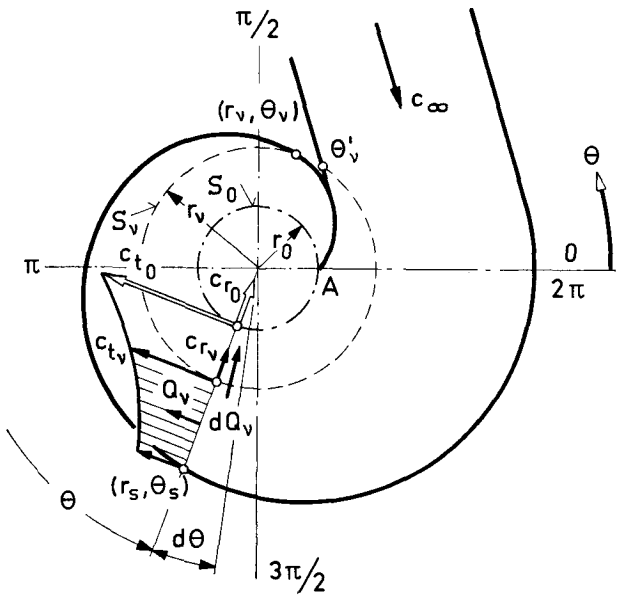

Fig. 2.32.

Thus, according to eq. (2.01), where $r_s = r_0 e^{\theta \operatorname{tg} \alpha_s}$ and $\operatorname{tg} \alpha_s = \frac{1{,}2}{2\pi}$, we obtain

$$\ln \frac{r_s}{r_0} = \theta \operatorname{tg} \alpha_s = \frac{1{,}2}{2\pi} \theta;$$

hence,

$$\frac{d}{d\theta}\left(\int_{r_\nu}^{r_s} \frac{dr}{r}\right) = \frac{d}{d\theta} \ln \frac{r_s}{r_0} = \operatorname{tg} \alpha_s = \frac{1{,}2}{2\pi}.$$

Consequently, from eq. (2.24),

$$c_{r_\nu} r_\nu = c_{t_\nu} r_\nu \operatorname{tg} \alpha_s = \text{const.} \tag{2.25.1}$$

throughout the region examined. Since the radius r_ν was chosen arbitrarily, we conclude from Eqs. (2.23) and (2.25) that for $0 \leqq \theta \leqq 300°$

$$c_{r_0} r_0 = c_r r = \text{const.}, \qquad c_{t_0} r_0 = c_t r = \text{const.},$$
$$\frac{c_{r_0}}{c_{t_0}} = \frac{c_r}{c_t} = \operatorname{tg} \alpha_s = \frac{1{,}2}{2\pi}. \tag{2.26}$$

Hence, if $c_{r_0} = \text{const.}$ along S_0, the potential flow throughout the casing in question attains a pure logarithmic form in the region $0 \leqq \theta \leqq 300°$. Its form is approximately logarithmic in the region $300 < \theta \leqq 2\pi$, where the maximum deviation does not exceed -9 per cent. The approximation improves gradually with smaller radii to $r = r_0$ where, according to Eq. (2.24), the flow is purely logarithmic along S_0. In other words the potential flow through the regions mentioned is identical to that which is generated from a sink-circulation pair (q, Γ) in the center of the casing, where (see also Eq. (2.20))

$$\frac{q}{\Gamma} = \operatorname{tg} \alpha_s = \frac{1{,}2}{2\pi}.$$

In order to show more clearly the validity of the experimentally found Eq. (2.23) in the region $\theta \leqq 300°$ and its deviation from the obtained values of c_t in the *transition zone* $\theta > 300°$ (see Fig. 2.31 a), we plotted the values of the dimensionless quantity $C_t r/r_0$ (dotted lines) against θ as shown in Fig. 2.31 b. The dimensionless component $C_t = c_t/c_\infty$ was calculated by means of Eq. (2.14), while the dimensionless value of C_r (for both two-dimensional casings) was calculated using Eq. (2.14.1), where

$$C_{r_0} = \frac{c_{r_0}}{c_\infty} = 0{,}400.$$

The quantity $C_t^* r/r_0$ (solid line) was calculated by means of Eqs. (2.26). It is obvious, therefore, that

$$C_t^* \frac{r}{r_0} = C_{t_0}^* = \frac{C_{r_0}}{\frac{1{,}2}{2\pi}} = 2{,}09.$$

The index * over C_t is introduced to distinguish its values obtained by Eqs. (2.26) from those which are derived directly from the measuring points. An observation similar to that drawn from inspecting Fig. 2.31 a can be made with equal validity in the case of Fig. 2.31 b viz. Eqs. (2.26) are exact in the region $\theta \leqq 300°$, where

$$C_{t_0}^* = C_t \frac{r}{r_0} \pm 0{,}0,$$

and are valid by a very close approximation in the region $(300° < \theta < 2\pi, r < 2r_0)$, where

$$C_{t_0}^* = C_t \frac{r}{r_0} \pm 1{,}5 \text{ per cent.}$$

In the same angular region $300° < \theta < 2\pi$ but with $r > 2r_0$, the deviation of $C_t^* r/r_0$ in relation to the real $C_t r/r_0$ increases regularly. The magnitude of the deviation, however, is generally small since, at the extreme point $(r_s, 2\pi)$ of the spiral, it amounts to

$$\left(\frac{C_{ts}\frac{r_s}{r_0} - C_{ts}^*\frac{r_s}{r_0}}{C_{ts}\frac{r_s}{r_0}}\right)_{2\pi} = \frac{2{,}31 - 2{,}09}{2{,}31} = 0{,}0955$$

or

$$(C_{ts}^*)_{2\pi} = 0{,}905\,(C_{ts})_{2\pi}.$$

b) Measurements on the Archimedes' Model

The form of the equipotential lines obtained using the boundary condition $c_{r_0} = \text{const.}$ in this model are shown in Fig. 2.33 where, as in Fig. 2.30, they are referred to the velocity potential ϕ. The measuring-points were obtained, as in the preceding model, on various radii and at a constant potential difference $\delta\phi = 0{,}5$.

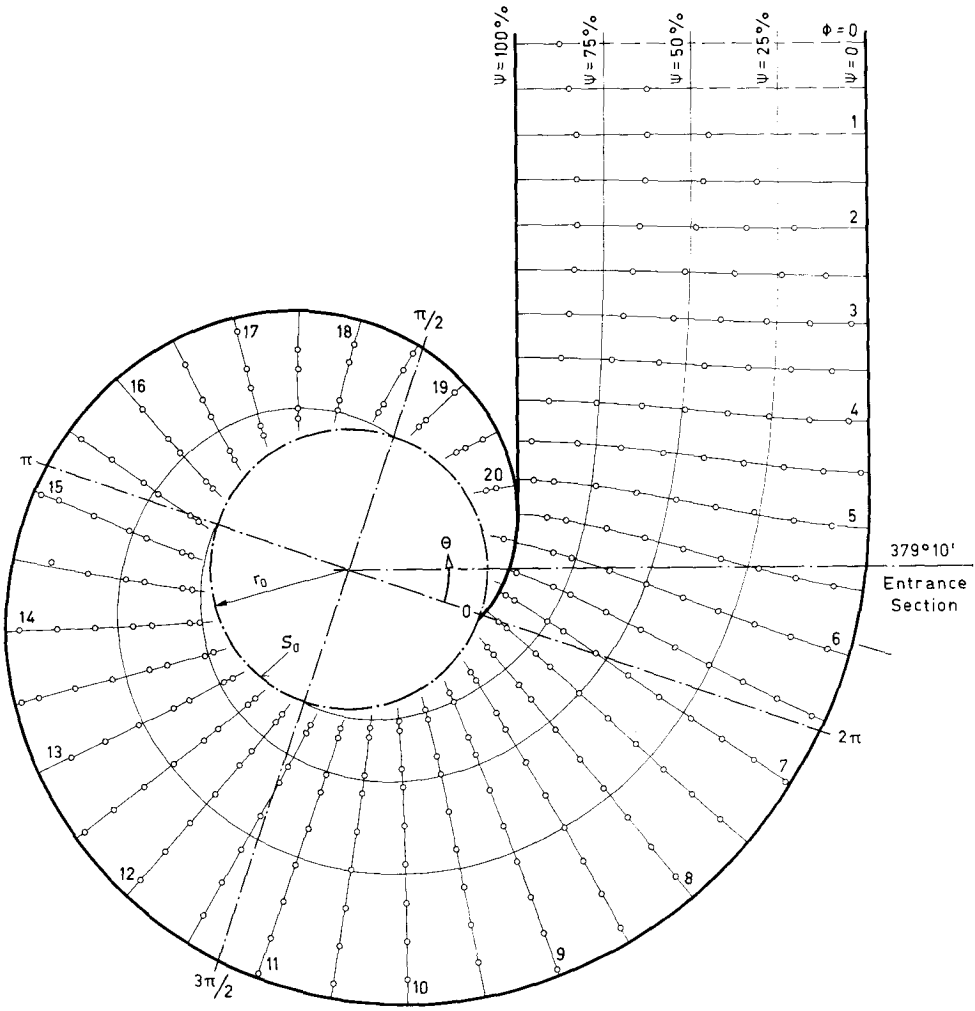

Fig. 2.33. Potential flow through the Archimedes' spiral model for $C_{r_0} = \text{const.}$

As in the logarithmic-shaped model, we observe in Fig. 2.33 that the equipotential lines from about $\phi = 7{,}5$ and upward are curves with slowly changing shapes of not large inclination to the related meridian sections; furthermore, the figure suggests that an equipotential line could be approximately generated from the preceding line by a turn of some degrees around the center of the

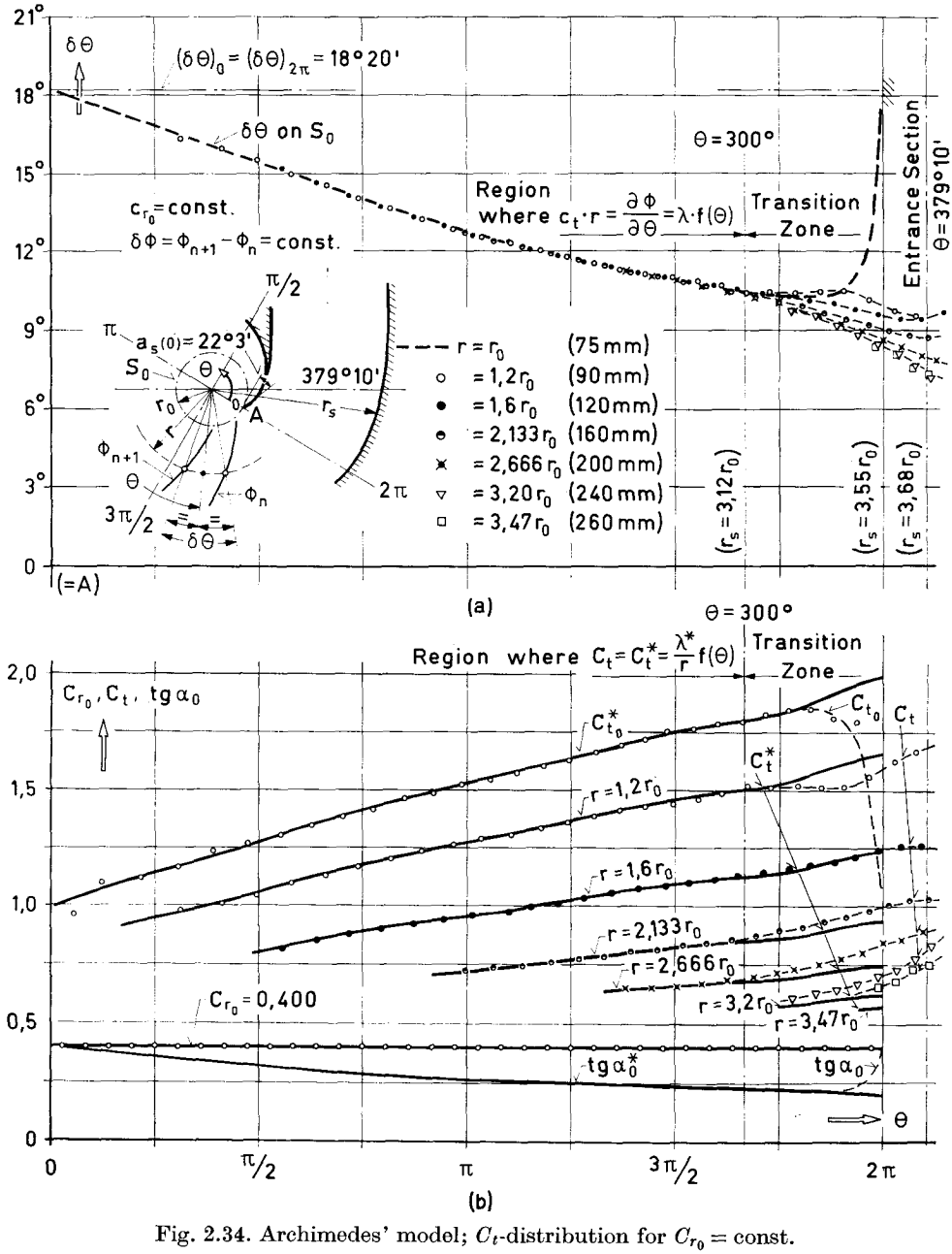

Fig. 2.34. Archimedes' model; C_t-distribution for $C_{r_0} = \text{const.}$

model. To study the flow more closely, therefore, we plotted the angle differences $\delta\theta$ obtained between successive equipotential lines ϕ_{n+1} and ϕ_n, where $\phi_{n+1}-\phi_n=\delta\phi=0{,}5$ at various radii r against the angle θ of the mean point of every interval. The results are given in Fig. 2.34a. We see immediately from the plotted points that, throughout the region $0\leqq\theta\leqq 300°$, the angle difference $\delta\theta$ is a function of the angle θ *only;* namely, it is *independent* of the radius r. Following, therefore, the same procedure as with the preceding model, we conclude from the expression

$$(c_t)_m=\frac{1}{r}\left(\frac{\delta\phi}{\delta\theta}\right)_r,$$

which gives the mean value of the tangential component of the velocity in any one of the above angle intervals $\delta\theta$ on $r=$const., that in this model,

$$c_t r=\frac{\partial\phi}{\partial\theta}=\lambda f(\theta) \tag{2.27}$$

throughout the region $0\leqq\theta\leqq 300°$, since with $\delta\phi=$const. $\delta\theta$ is in this region a function of θ alone; λ is a constant, the value of which depends on the velocity c_∞ and the form of the spiral. Hence, on a meridian section of the model in question,

$$c_t r=c_{t_0}r_0=\lambda f(\theta),\qquad(\theta\leqq 300°). \tag{2.28}$$

In the region between $300°<\theta<2\pi$, the relation (2.27) is approximately valid; excluding the region near the surface $S_0(r<1{,}2\,r_0)$, we observe that the approximation is very good, since the band-spread of the measuring points on various radii does not exceed ± 7 per cent about a mean value corresponding to the point $(r=2{,}133\,r_0,\theta=2\pi)$. In the region $r<1{,}2\,r_0$, on the other hand, the deviation of the values of $\delta\theta$ between $300°<\theta<340°$ in relation to those of the region $r>1{,}2\,r_0$ remains tolerably small; but as the angle increases over 340°, $\delta\theta$ increases rapidly. Thus, the $\delta\theta$-curve of the radius r_0 shows an extremely steep ascent to $\theta=2\pi$. At $\theta=0$ and $\theta=2\pi$, that is the discontinuity point A, $(\delta\theta)_0=(\delta\theta)_{2\pi}$, since by $c_{r_0}=$const. along S_0 the velocity $\vec{c}_0$ on both sides of A is the same; i. e.

$$c_{r_0}(0)=c_{r_0}(2\pi)=c_{r_0}=\text{const.},\qquad c_{t_0}(0)=c_{t_0}(2\pi),$$

and, by Eq. (2.02.1), $\left(\frac{c_{r_0}}{c_{t_0}}\right)_0=\left(\frac{c_{r_0}}{c_{t_0}}\right)_{2\pi}=\operatorname{tg}\alpha_s(0)=0{,}4053.$

We can say, therefore, that Eq. (2.27) is valid throughout the region $\theta<2\pi$, except in a very small part between the limits of $r<1{,}2\,r_0$ and $340°<\theta<2\pi$.

It is obvious from the experimentally derived condition (2.28) that we can determine the components c_r, c_t of the velocity throughout the region $\theta<2\pi$ of the casing in question. Thus the fluid volume Q_θ passing per unit time through a segment of the surface S_0 extended between 0 and $\theta<2\pi$ (see Fig. 2.35) can be expressed by the equation:

$$Q_\theta=\int_0^\theta dQ=\int_0^\theta c_{r_0}h_0 r_0\,d\theta=\int_{r_0}^{r_s}c_t h_0\,dr\quad(\text{at }\theta) \tag{2.29}$$

or, using the dimensionless representation given by Eqs. (2.10),

$$\int_0^{\theta} C_{r_0} h_0 r_0 \, d\theta = \int_{r_e}^{r_s} C_t h_0 \, dr .$$

Hence, since $C_{r_0} = \text{const.}$ we obtain

$$C_{r_0} r_0 \theta = \int_{r_e}^{r_s} C_t \, dr \quad (\text{at } \theta). \tag{2.30}$$

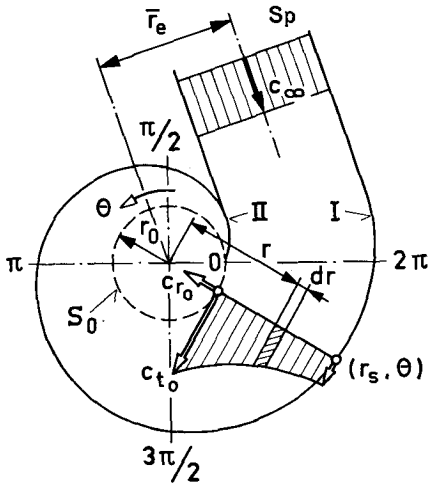

Fig. 2.35.

Suppose for a moment that Eq. (2.28) is exact in the region $\theta \leqq 2\pi$. Thus, as mentioned in the preceding model, introducing the index * over C_t and C_{t_0} to distinguish the values obtained by Eq. (2.28) from those derived from the measuring points, we write

$$C_t^* = C_{t_0}^* \frac{r_0}{r} = \frac{\lambda}{r c_\infty} f(\theta) = \frac{\lambda^*}{r} f(\theta),$$

where

$$\lambda^* = \frac{\lambda}{c_\infty}; \qquad C_{t_0}^* r_0 = \lambda^* f(\theta).$$

Now, introducing C_t^* into Eq. (2.30) we get

$$C_{r_0} r_0 \theta = C_{t_0}^* r_0 \int_{r_0}^{r_s} \frac{dr}{r} = C_{t_0}^* r_0 \ln \frac{r_s}{r_0}.$$

Thus

$$C_{t_0}^*(\theta) = \frac{\theta}{\ln \frac{r_s}{r_0}} C_{r_0}. \tag{2.31}$$

Consequently

$$\lambda^* f(\theta) = C_{t_0}^* r_0 = \frac{r_0 \theta}{\ln \frac{r_s}{r_0}} C_{r_0}, \tag{2.32}$$

and $$C_t^*(r,\theta)=\frac{\lambda^*}{r}f(\theta)=\frac{r_0}{r}\frac{\theta}{\ln\frac{r_s}{r_0}}C_{r_0}; \tag{2.33}$$

also $$\operatorname{tg}\alpha_0^*=\frac{C_{r_0}}{C_{t_0}^*}=\frac{1}{\theta}\ln\frac{r_s}{r_0}. \tag{2.34}$$

In the casing under consideration $r_s=r_0+\tau\theta$; $\tau=\frac{191}{2\pi}$ mm/rad (see Eq. 2.02) and since $C_{r_0}=$ const. along S_0, $C_{r_0}=\bar{C}_{r_0}=0{,}40$ (see Eq. (2.14.1)).

Following the same procedure as in the preceding model (see Fig. 2.32), we can find the distribution of the radial component $C_r^*(r,\theta)$ of the velocity in the region $\theta\leqq 2\pi$. Thus, the volume element dQ_ν which passes per unit time through a cylindrical surface of radius r_ν at a point (r_ν,θ), is

$$dQ_\nu=c_{r_\nu}r_\nu h_0\,d\theta=\frac{d}{d\theta}\left(\int_{r_\nu}^{r_s}c_l h_0\,dr\right)d\theta. \tag{2.35}$$

Supposing that Eq. (2.28) is valid in $\theta\leqq 2\pi$, we obtain from Eqs. (2.35) and (2.33)

$$C_{r_\nu}^* r_\nu=\frac{d}{d\theta}\left(\int_{r_\nu}^{r_s}C_t^*\,dr\right)=\frac{d}{d\theta}\left(\frac{r_0\theta}{\ln\frac{r_s}{r_0}}C_{r_0}\int_{r_\nu}^{r_s}\frac{dr}{r}\right),$$

i.e. $$C_{r_\nu}^* r_\nu=C_{r_0}r_0\frac{d}{d\theta}\left(\frac{\ln r_s-\ln r_\nu}{\ln r_s-\ln r_0}\theta\right)$$

or, since r_ν is an arbitrary radius,

$$C_r^*(r,\theta)=\frac{r_0}{r}\frac{dT_1}{d\theta}\qquad(\theta\leqq 2\pi), \tag{2.36}$$

where $$T_1(r,\theta)=\frac{\ln r_s-\ln r}{\ln r_s-\ln r_0}C_{r_0}\theta\qquad(C_{r_0}=\text{const.}). \tag{2.37}$$

In the differentiation shown on the right-hand of Eq. (2.37), $r=$ const., while $r_s=r_0+\tau\theta$ (see Eq. (2.02));

consequently $$\operatorname{tg}\alpha^*=\frac{C_r^*}{C_t^*}=\frac{\ln\frac{r_s}{r_0}}{C_{r_0}}\frac{dT_1}{d\theta}\frac{1}{\theta}. \tag{2.38}$$

Further the volume Q_r of the fluid which passes per unit time through a part of a meridian section at an angle θ included between radii r and r_s is

$$Q_r^*=c_\infty\int_r^{r_s}C_t^* h_0\,dr=c_\infty C_{r_0}\frac{r_0h_0\theta}{\ln\frac{r_s}{r_0}}\ln\frac{r_s}{r}=c_\infty r_0h_0T_1.$$

Dividing by $Q_0=c_\infty h_0 L$, where L is the width of the inlet pipe, we obtain the dimensionless expression

$$K_r^*(r,\theta)\equiv\frac{Q_r^*}{Q_0}=\frac{r_0}{L}T_1. \tag{2.39}$$

Since in Fig. 2.34a we found that Eq. (2.27) is exact in the region $\theta \leqq 300°$, we conclude that only in this region

$$C_r^* = C_r, \qquad C_t^* = C_t, \qquad \alpha^* = \alpha$$

at every $r_0 \leqq r \leqq r_s$. In the region $300° < \theta \leqq 340°$, Eq. (2.27) is approximately true, viz.

$$C_r^* \approx C_r, \qquad C_t^* \approx C_t, \qquad \alpha^* \approx \alpha.$$

In the region $340° < \theta \leqq 2\pi$, the approximation of Eq. (2.27) in relation to the real experimental results becomes gradually worse, particularly at $r < 1{,}2\, r_0$.

Fig. 2.34b shows more closely the C_t-distributions (dotted lines) and the C_t^*-distributions (solid lines) at various radii. The experimental points shown in this figure correspond to those of Fig. 2.33 and they are found by means of the dimensionless Eqs. (2.14). As previously mentioned on either side of A,

$$c_{t_0}(0) = c_{t_0}(2\pi) = \frac{c_{r_0}}{\operatorname{tg} \alpha_s(0)};$$

therefore

$$C_{t_0}(0) = C_{t_0}(2\pi) = \frac{C_{r_0}}{\operatorname{tg} \alpha_s(0)} = \frac{0{,}400}{0{,}4053} = 0{,}985.$$

The C_t^*-curves are traced by means of Eq. (2.33) at these same radii. In Fig. 2.34b we can easily see the region of validity of Eq. (2.33) and also the magnitude of the deviation of C_t^* from C_t at various radii in the *transition zone*. At $r = 1{,}6\, r_0$, Eq. (2.33) is exact up to $\theta = 2\pi$. At $r > 1{,}6\, r_0$, C_t^* decreases from C_t; for example, at the point $(r = 3{,}2\, r_0, \theta = 2\pi)$ the deviation of C_t^* is about -12 per cent. In the region $r < 1{,}6\, r_0$, we observe that C_t^* increases from C_t; the deviation remains small up to and including the point $(r = 1{,}2\, r_0,\ \theta = 2\pi)$ where it does not exceed $+3{,}8$ per cent. In the region $(r < 1{,}2, \theta > 340°)$, however, C_t decreases sharply since at the point $A\,(r_0, 2\pi)$ the component $C_{t_0}(2\pi)$ must have the value 0,985.

c) The Quasi-Logarithmic Law for c_{r_0} Constant

The study of the C_t-distribution obtained in the logarithmic model has shown that if $C_{r_0} = \text{const.}$ the potential flow follows the *logarithmic law*

$$C_t \frac{r}{r_0} = \frac{C_{r_0}}{\operatorname{tg} \alpha_s} = \text{const.},$$

in a considerably large part of the casing. Thus we can observe in Figs. 2.30 and 2.31 that the flow, which is parallel through the inlet pipe, undergoes a quick transformation within a rather narrow region on both sides of the entrance section of the casing, and from then on the fluid obtains a *logarithmic spiral motion.*

A similarly quick transformation of the flow also occurs in the Archimedes' model, as we see in Figs. 2.33 and 2.34, but in this model the experimental investigation led us to conclude, in the region $\theta \leqq 300°$, the *Quasi-Logarithmic Law*

$$C_t \frac{r}{r_0} = \frac{C_{r_0}}{\ln \frac{r_s}{r_0}} \theta, \qquad C_{r_0} = \text{const.} \tag{2.40}$$

(see Eqs. (2.27) and (2.33)). Contrary to the pure logarithmic law $c_t r = \text{const.}$, the relationship (2.40) indicates that the moment of momentum per unit mass of the fluid remains constant along a meridian section of the casing, and that for a given casing form the value of $C_t r/r_0$ may change from one meridian section to another. This is the reason for choosing the term "quasi-logarithmic law". It therefore seems that, if $C_{r_0} = \text{const.}$, Eq. (2.40) expresses a general property of the *potential flow* through two-dimensional spiral casings of usual form. The well-known relationship $C_t r/r_0 = \text{const.}$ which was found to be valid in our logarithmic model is in fact a particular case of the quasi-logarithmic law in question, because in a logarithmic spiral casing we have

$$\ln \frac{r_s}{r_0} = \theta \operatorname{tg} \alpha_s, \qquad \alpha_s = \text{const.},$$

and, therefore, Eq. (2.40) gives

$$C_t \frac{r}{r_0} = \frac{C_{r_0}}{\theta \operatorname{tg} \alpha_s} \theta = \frac{C_{r_0}}{\operatorname{tg} \alpha_s} = \text{const.},$$

throughout the region of its validity. In any spiral casing form other than a logarithmic one, the $C_t r$ changes from meridian section to meridian section.

d) Moment of Momentum and Dynamical Reaction of the Fluid

To investigate the flow formation within the transition zone $\theta > 300°$ in both models, we plotted the distribution of the $c_t r$ against the ratio r/r_0 along four characteristic sections of this region; i.e. the surface S_p of the inlet pipe ($c_\infty = \text{const.}$) and the three meridian sections at $\theta = 379° 10'$, 2π, $300°$. The diagrams we obtained are shown in the upper part of Fig. 2.36. In the lower part of the same figure we plotted the distribution of the *moment of momentum* b of the fluid which, *per unit time*, passes through the above sections. Both $c_t r$ and b are plotted in dimensionless form. For $c_t r$ we introduced the expression

$$C_t \frac{r}{\bar{r}_e} = \frac{c_t}{c_\infty} \frac{r}{\bar{r}_e},$$

where $\bar{r}_e$ is the distance of the axis of the inlet pipe from the center of the spiral (see Fig. 2.35). For b we introduced the expression

$$B = \frac{b}{b_\infty} = \frac{\rho h_0 \int_{r_i}^{r_s} c_t^2 r \, dr}{\rho h_0 c_\infty^2 \bar{r}_e L} = \frac{r_0}{L} \frac{r_0}{\bar{r}_e} \int_{r_i/r_0}^{r_s/r_0} C_t^2 \frac{r}{r_0} d\left(\frac{r}{r_0}\right), \quad (\text{at } \theta), \tag{2.41}$$

where L is the width of the inlet pipe. The lower limit r_i of the integration is $r_i = r_0$ for the sections at $\theta = 2\pi$ and $300°$, and $r_i = r_{s\,\mathrm{II}}$ for the section at $\theta = 379° 10'$ (see Fig. 2.35). Along the section S_p, the distances r_e from points on S_p to an axis passing through the center of the model and parallel to the inlet pipe axis were taken instead of their radii r. Thus, the limits of integration for S_p are

$$\min r_e = \bar{r}_e - \frac{L}{2}, \qquad \max r_e = \bar{r}_e + \frac{L}{2}.$$

The distribution of B along the above meridian sections, is

$$\frac{dB}{d\left(\frac{r}{r_0}\right)} = C_t^2 \frac{r_0}{L} \frac{r_0}{\bar{r}_e} \frac{r}{r_0} = \frac{r_0}{L} \frac{r}{\bar{r}_e} C_t^2. \tag{2.42}$$

For both models L equals 186,6 mm while $\bar{r}_e$ is slightly longer in the Archimedes' model (see Figs. 2.01 and 2.02). The distribution of B along S_p is

$$\frac{dB_\infty}{d\left(\frac{r_e}{r_0}\right)} = C_\infty^2 \frac{r_e}{\bar{r}_e} \frac{r_0}{L} = \frac{r_0}{L} \frac{r_e}{\bar{r}_e}, \quad (C_\infty = 1{,}0), \tag{2.43}$$

i. e. a straight line.

We can easily see from the plots of $C_t \frac{r}{\bar{r}_e}$ and $\frac{dB}{d}\left(\frac{r}{r_0}\right)$ in Fig. 2.36 that the

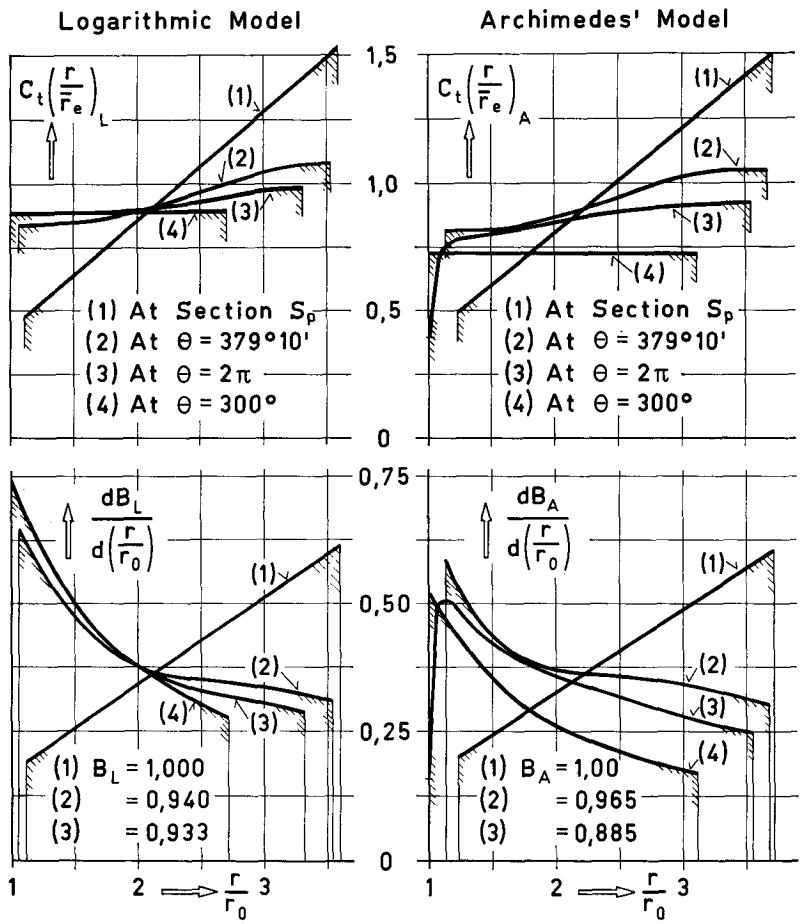

Fig. 2.36. Logarithmic and Archimedes' models; distributions of the velocity-moment ($C_t r$) and the moment of momentum (B) of the fluid passing through the transition zones, for $C_{r_0} = \text{const.}$

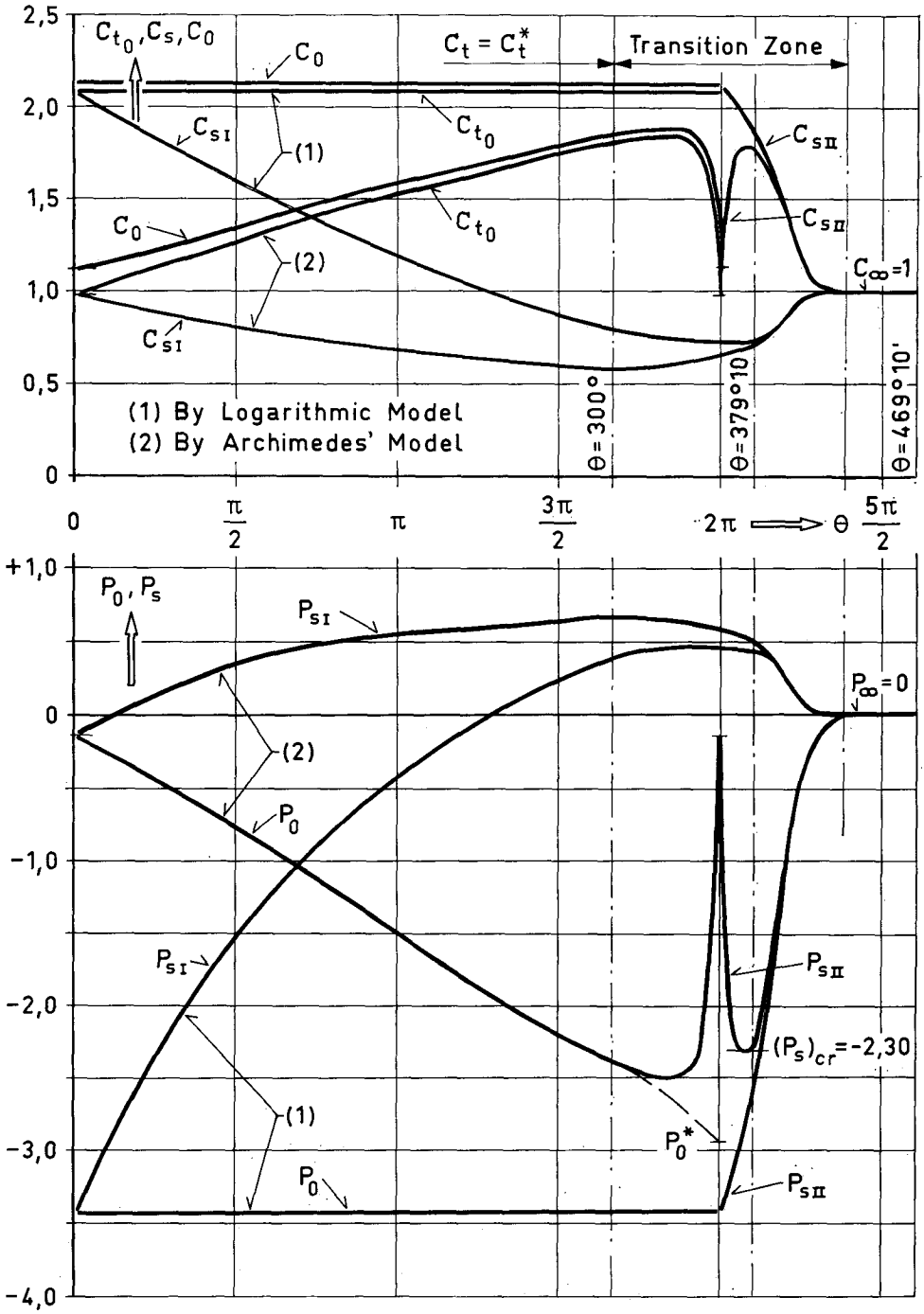

Fig. 2.37. Velocity- and static-pressure-distribution along S_0, and along the walls of the logarithmic and the Archimedes' spiral model for $C_{r_0} = \text{const.}$ (see also Fig. 2.35).

main part of the transformation of the flow form from parallel to spiral occurs, in both casings, before their entrance sections at $\theta = 379° 10'$ (section normal to the inlet pipe axis). The remaining transformation needed until the flow obtains the form given by the law (2.40) is completed at $\theta = 300°$. We also observe that in the Archimedes' casing the flow tends, in the entrance region, to attain a logarithmic form as shown by the curves (2).

The diagrams in Fig. 2.37 which show the distributions of the velocity C_s and C_0 and of the static pressures P_s and P_0 along the walls and along the surfaces S_0 of the two models give a useful picture for our investigation. (The pressures are calculated according to Eq. (2.13.1).) Thus, along the wall (II) of the inlet pipe, within the transition zone, a considerable increase of the velocity takes place, while the velocity decreases along the wall (I) in the same region. In the Archimedes' casing, however, a steep decrease of the velocity occurs in the neighbouring region before the point A, and a sharp increase immediately after it. As shown in both Figs. 2.36 and 2.37 this local irregularity does not have any particular influence on the formation of the flow as a whole.

In order to find the resultant of the fluid reaction against the walls of each casing, let us apply the *moment of momentum theorem* (see Eq. (1.10) in § 1.1.2) in the region included by the casing control surface S ($S = S_0 + S_s + S_p$, see § 1.2.2 and the related Fig. 1.16). Since there are no objects within this region, the above theorem is expressed here, as

$$-b_\infty + b_0 - \mu_\infty + \mu_s = 0, \tag{2.44}$$

where $$b_\infty = \iint_{S_p} \rho c_\infty^2 r_e \, dS = \rho h_0 c_\infty^2 \bar{r}_e L = 2 h_0 q_\infty \bar{r}_e L,$$

(see also eq. (2.41)),

and $$b_0 = \iint_{S_0} \rho c_{r_0} c_{t_0} r_0 \, dS = \rho h_0 \left(\frac{r_0}{c_\infty}\right)^2 \int_0^{2\pi} C_{r_0} C_{t_0} \, d\theta,$$

represent the moments of momentum of the fluid which passes per unit time through the surfaces S_p and S_0 respectively,

and $$\mu_\infty = \iint_{S_p} p_\infty r_e \, dS = h_0 p_\infty \bar{r}_e L,$$

and $$\mu_s = \iint_{S_s} p_s r_s \sin \alpha_s \, dS,$$

represent the *torque*, in relation to the center of the casing, caused by the static pressures (Force $\times$ radius), imposed from the outside upon the plane S_p and the wall surfaces S_s respectively. In the last integral, p_s is the static pressure on the walls (I) and (II) (see Fig. 2.35); the angle α_s is taken as positive ($\alpha_s > 0$) along the wall (I) and as negative ($\alpha_s < 0$) along the wall (II).

We obtain a dimensionless form of Eq. (2.44) by introducing the dimensionless expressions

$$B_0 = \frac{b_0}{b_\infty} = \frac{r_0}{L} \frac{r_0}{\bar{r}_e} \int_0^{2\pi} C_{r_0} C_{t_0} \, d\theta,$$

$$M_s = \frac{\mu_s}{b_\infty},$$

$$M_\infty = \frac{\mu_\infty}{b_\infty} = \frac{p_\infty}{2q_\infty} = \frac{1}{2}(P_{tot}-1), \tag{2.45}$$

where $$P_{tot} = \frac{p_\infty + q_\infty}{q_\infty},$$

is the dimensionless form of the *total pressure*

$$p_{tot} = p + \frac{\rho}{2}c^2 = p_\infty + \frac{\rho}{2}c_\infty^2.$$

Dividing Eq. (2.44) by b_∞, we get

$$-1 + B_0 - M_\infty + M_s = 0;$$

thus $$M_s = 1 - B_0 + M_\infty = \tfrac{1}{2}(P_{tot}+1) - B_0, \tag{2.46}$$

and $$\delta M_s = M_s - M_\infty = 1 - B_0. \tag{2.47}$$

The difference δM_s represents the dimensionless expression for the necessary *additional torque*, which has to be applied on the spiral walls (I) and (II) in order to balance the reaction of the fluid against the transformation of its parallel motion to a spiral one.

To visualize the distribution of the above dynamical reaction of the fluid along the casing, let us consider the region between the origin ($\theta = 0$) of the spiral and a meridian section at azimuth θ. Applying the moment of momentum theorem in this region, we obtain

$$\delta M_\theta = (M_s)_\theta - M_\theta = B_\theta - (B_0)_\theta,$$

where $$(M_s)_\theta = \frac{1}{b_\infty}\iint\limits_{S_s\ (0\to\theta)} p_s r_s \sin\alpha_s \, dS, \tag{2.48}$$

and $$M_\theta = \frac{1}{2}\frac{r_0}{L}\frac{r_0}{\bar{r}_e}\int\limits_{r_i/r_0}^{r_s/r_0} P_\theta \frac{r}{r_0} d\left(\frac{r}{r_0}\right),$$

($P_\theta = p_\theta/q_\infty$ is a dimensionless expression of the static pressure distribution p_θ along the meridian section at θ),

and $$B_\theta = \frac{r_0}{L}\frac{r_0}{\bar{r}_e}\int\limits_{r_i/r_0}^{r_s/r_0} C_t^2 \frac{r}{r_0} d\left(\frac{r}{r_0}\right),$$

(see also Eq. (2.41)), (2.49)

and $$(B_0)_\theta = \frac{r_0}{L}\frac{r_0}{\bar{r}_e}\int\limits_0^\theta C_{r_0} C_{t_0} \, d\theta, \quad ((B_0)_{2\pi} \equiv B_0),$$

(see also Eqs. (2.45)).

Considering now the region $\theta \leqq 300°$, where the law (2.40) is valid, we get

$$B_\theta = \frac{r_0}{L}\frac{r_0}{\bar{r}_e} C_{l_0}^2 \int_1^{r_s/r_0} \frac{r_0}{r} d\left(\frac{r}{r_0}\right) = \frac{1}{2\pi}\frac{r_0}{\bar{r}_e}\frac{C_{l_0}^2}{\ln \frac{r_s}{r_0}}\theta, \tag{2.50}$$

and

$$(B_0)_\theta = \frac{r_0}{\bar{r}_e} C_{r_0} \int_0^\theta \frac{\theta}{\ln \frac{r_s}{r_0}} d\theta.$$

Since, in both casings, the law (2.40) is approximately true up to $\theta = 2\pi$ (with the exception of a very small region surrounding the point A at $\theta = 2\pi$ of the Archimedes' casing) Eqs. (2.50) can be assumed to be valid in the entire region $0 \leqq \theta \leqq 2\pi$.

From the expressions (2.50), it is easy to show for the *logarithmic casing*, where $\ln r_r/r_0 = \theta \operatorname{tg} \alpha_s$, ($\alpha_s = \text{const.}$)

that

$$B_\theta = (B_0)_\theta = \frac{1}{2\pi}\frac{r_0}{\bar{r}_e}\frac{C_{r_0}}{\operatorname{tg} \alpha_s}\theta. \tag{2.51}$$

For this casing, therefore, we have

$$\delta M_\theta = 0$$

i. e.

$$(M_s)_\theta = M_\theta, \quad (\theta \leqq 300°).$$

Hence, in the region $\theta \leqq 300°$ of the logarithmic casing, there is *no* additional reaction of the fluid on its walls; the torque $(M_s)_\theta$ is exactly opposite to, and balanced by, the moment M_θ of the static pressure along the meridian section at θ.

Since along the characteristic meridian section at $\theta = 2\pi$ the law (2.40) is approximately valid, introducing the index * over B_θ (see § 2.2.2a) we obtain from Eq. (2.51)

$$B_{2\pi}^* = B_0^* = \frac{r_0}{\bar{r}_e}\frac{C_{r_0}}{\operatorname{tg} \alpha_s}.$$

For the logarithmic model: $r_0/\bar{r}_e = 75/176{,}7$, $C_{r_0} = 0{,}40$ and $\operatorname{tg} \alpha_s = 1{,}2/2\pi$; hence

$$B_{2\pi}^* = B_0^* = 0{,}895.$$

The real experimental value of $B_{2\pi}$ obtained from the diagrams in Fig. 2.36 (see curve (3) of $dB_L/d(r/r_0)$) is 0,933. As is shown, the deviation of $B_{2\pi}^*$ from $B_{2\pi}$ does not exceed $-3{,}9$ per cent.

The values of B_θ, $(B_0)_{2\pi}$ and δM_θ in some characteristic sections of both casings are given in *Table IV*. It can be easily seen in this table, that, through the Archimedes' casing, an adequate amount (39,1 per cent) of the moment of momentum of the fluid at the section S_p is transformed to a dynamical reaction on the spiral walls; consequently, the moment of momentum B_0 passing through the surface S_0 is reduced to 60,9 per cent, while in the logarithmic casing $B_0 = 89{,}5$ per cent of B_∞. We also observe that, in the Archimedes' casing, $\delta M_\theta > 0$ along the spiral walls from S_p up to $\theta = 0$, whereas in the logarighmic, $\delta M_\theta = 0$ practically from $\theta = 2\pi$.

Table IV. Moment of Momentum of the Fluid and Additional Torque δM_θ along the Walls of the Spiral

Meridian Sections	Validity of Eq. (2.40)	Logarithmic Model			Archimedes' Model		
		B_θ $[B_\theta^*]$	$(B_0)_\theta$ $[(B_0^*)_\theta]$	δM_θ $[\delta M_\theta^*]$	B_θ $[B_\theta^*]$	$(B_0)_\theta$ $[(B_0^*)_\theta]$	δM_θ $[\delta M_\theta^*]$
$\theta =$ 0°		0	0	0	0	0	0
$(\pi/2)$ 90°		0,224	0,224	0	0,130	0,114	0,016
(π) 180°	$C_t^* = C_t$	0,448	0,448	0	0,313	0,258	0,055
$(3\pi/2)$ 270°		0,671	0,671	0	0,541	0,426	0,115
300°		0,746	0,746	0	0,625	0,490	0,135
(2π) 360°	$C_t^* \approx C_t$	0,933 [0,895]	0,895 [0,895]	0,038 [0]	0,885 [0,813]	0,609 [0,617]	0,276 [0,196]
379° 10′	—	0,940	0,895	0,045	0,965	0,609	0,356
S_p	—	$B_\infty = 1{,}0$	$\delta M_s = 0{,}105$		$B_\infty = 1{,}0$	$\delta M_s = 0{,}391$	

Note: The values of B_θ and $(B_0)_\theta$ in the region $\theta \leqq 300°$, and the values with the index *, are calculated by means of Eq. (2.51) for the logarithmic and by means of Eqs. (2.50) for the Archimedes' model. The values in the region $\theta > 300°$ were obtained by planimeter measurement of the respective areas shown in Fig. 2.36.

Natural Spiral, Spiroid Diffuser, Spiroid Nozzle: As we have seen, a logarithmic casing creates a pure logarithmic spiral motion of the fluid in the region of validity of the law (2.40), namely up to about $\theta = 2\pi$, which, in turn, gives $\delta M_\theta = 0$ in this region. In accordance with the values which the additional torque δM_θ reaches, and in the sense that the *natural* two-dimensional *spiral motion* is the logarithmic motion $C_t r = \text{const.}$, we propose the following classification of spiral casings.

(I) *Natural Spiral.* Spiral in which $\delta M_\theta = 0$ in the region $0 \leqq \theta \leqq 2\pi$; e.g. a two-dimensional logarithmic spiral.

(II) *Spiroid Diffuser.* Spiral in which $\delta M_\theta > 0$ in the case of turbines, or $\delta M_\theta < 0$ in the case of pumps and blowers $(0 \leqq \theta \leqq 2\pi)$.

(III) *Spiroid Nozzle.* Spiral in which $\delta M_\theta < 0$ in the case of turbines or $\delta M_\theta > 0$ in the case of pumps and blowers $(0 \leqq \theta \leqq 2\pi)$.

For example an Archimedes' spiral forms a spiroid diffuser in the case of turbines or a spiroid nozzle in the case of pumps.

We shall see later that the same classification can be applied to the three-dimensional casings.

2.2.3. Measurements on the Logarithmic and Archimedes' Models for C_{r_0} Variable along S_0. Results

As has been mentioned in § 1.2.2 for engineering application the most important boundary condition of the flow through the surface S_0 is the condition (1.32), $c_{r_0} = \text{const}$. It is however within our province to investigate the

potential flow through a spiral casing when c_{r_0} varies along S_0, i.e. when in dimensionless expression

$$C_{r_0} = g(\theta) \neq \text{const.}$$

Since the *mean value* $\bar{C}_{r_0}$ of C_{r_0} is

$$\bar{C}_{r_0} = \frac{1}{2\pi} \int_0^{2\pi} C_{r_0} d\theta = \frac{S_p}{S_0}, \quad (C_\infty = 1{,}0),$$

(see Eq. (2.14.1)), the deviation of C_{r_0} from $\bar{C}_{r_0}$ can be expressed as

$$\delta C_{r_0} = \frac{C_{r_0}}{\bar{C}_{r_0}} - 1.$$

In this section we shall examine cases where δC_{r_0} does not exceed ± 25 per cent. Assuming the function $g(\theta)$ as *periodic* with period 2π we can analyse the C_{r_0}-distribution in Fourier sine and cosine series and write

$$C_{r_0} = \bar{C}_{r_0} + \sum a_m \sin m\theta + \sum b_m \cos m\theta, \qquad (2.52)$$
$$(m = 1, 2, 3, \ldots)$$

where a_m, b_m are the Fourier coefficients. It is obvious that, since in the region $0 \leqq \theta \leqq 2\pi$ $g(\theta)$ takes finite values only, the relationship (2.52) always con-

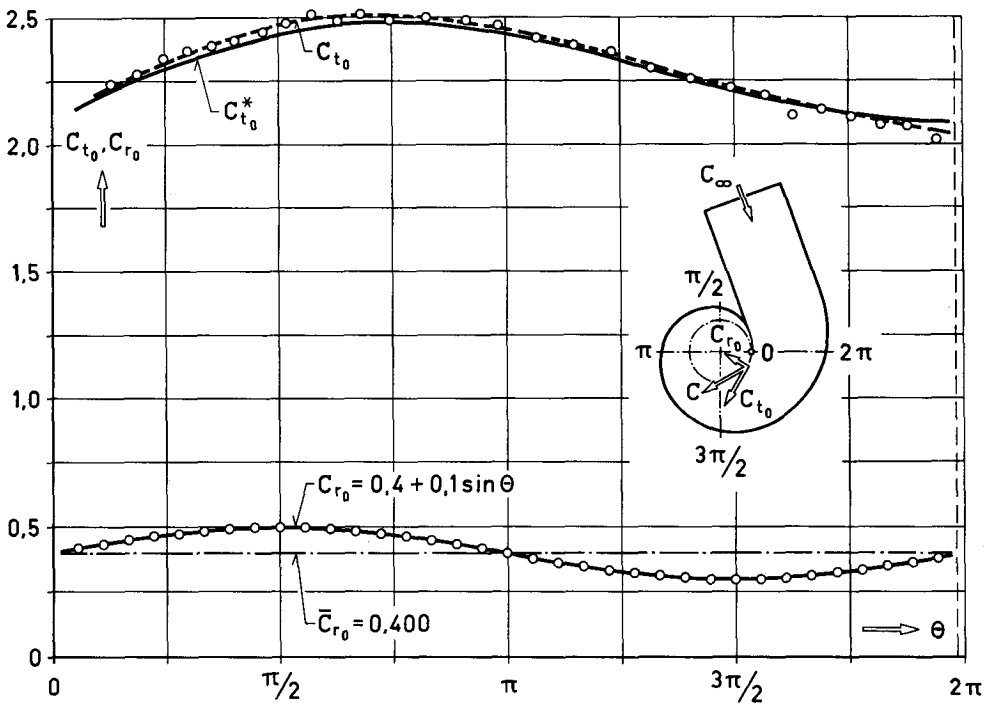

Fig. 2.38a. Logarithmic model: C_{t_0}-distribution for boundary condition $C_{r_0} = 0{,}40 + 0{,}1 \sin\theta$.

verges. In order to investigate the influence of every term of the series on the formation of the potential flow by our electric analogy method we can, one after another, retain one of the coefficients a_m, b_m while eleminating all the others at the same time. We, therefore, used the logarithmic and Archimedes' models as before, and we made a series of measurements adjusting along the electrodes of the collector III the $(V_K^*)_s$-distributions,

$$(V_K^*)_s = (\bar{V}_K^*)_s(1+\beta\sin\ \theta),$$
$$(V_K^*)_s = (\bar{V}_K^*)_s(1+\beta\sin 2\theta),$$
$$(V_K^*)_s = (\bar{V}_K^*)_s(1+\beta\sin 3\theta),$$

(see § 2.1.5) which correspond to the boundary conditions

$$\begin{aligned} C_{r_0} &= \bar{C}_{r_0}(1+\beta\sin\ \theta) \\ C_{r_0} &= \bar{C}_{r_0}(1+\beta\sin 2\theta) \\ C_{r_0} &= \bar{C}_{r_0}(1+\beta\sin 3\theta) \end{aligned} \qquad (2.53)$$

respectively; β was chosen to be 0,25, i.e. the assumed maximum value of δC_{r_0}; in both models it is known $\bar{C}_{r_0}=0{,}400$ (see eq. (2.14.1)). We also made a series of measurements for the distributions with the cosine terms $\beta\cos\theta$, $\beta\cos 2\theta$, $\beta\cos 3\theta$, $[C_{r_0}=\bar{C}_{r_0}(1+\beta\cos\theta),\ldots]$. For all the above measurements we followed the procedure stated in § 2.1.5 and we checked the secondary ohmic and capacitive currents as mentioned in § 2.2.1.

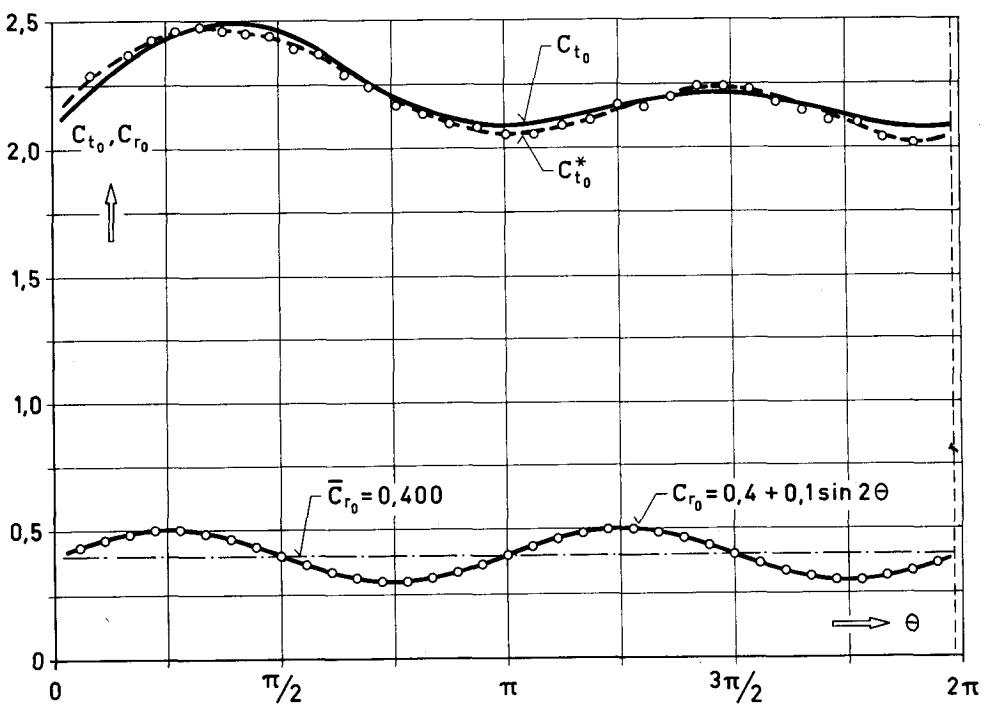

Fig. 2.38b. Logarithmic model: C_{t_0}-distribution for boundary condition $C_{r_0}=0{,}40+0{,}1\sin 2\theta$.

Fig. 2.38 at (a), (b) and (c), gives the C_{t_0}-distributions (points (o) and dotted lines through them) obtained from measurements around the collector on the logarithmic model for the sine group of the C_{r_0}-distribution. In these diagrams we observe immediately that the C_{t_0}-distributions tend to follow the C_{r_0}-distribution with a phase delay of about $\pi/2 \cdot 1/m$ $(m = 1, 2, 3)$, while their wave-amplitude decreases as θ changes from zero to 2π. This qualitative picture of C_{t_0} along S_0 led us to conclude that the quasi-logarithmic law could also be valid here and so enable us to avoid a more detailed experimental investigation on the entire region of the models.

a) The Quasi-Logarithmic Law for c_{r_0} Variable along S_0

Let us suppose that the law (2.27),

$$c_t r = \frac{\partial \phi}{\partial \theta} = \lambda f(\theta), \tag{2.27}$$

is valid in some region of the examined logarithmic model for any one of the boundary conditions (2.53). Thus, as mentioned in the preceding section § 2.2.2 at b) introducing the index * over the dimensionless expressions C_t, C_{t_0} etc. to distinguish the values obtained by Eq. (2.27) from those derived from the measuring points in the above region, we can write

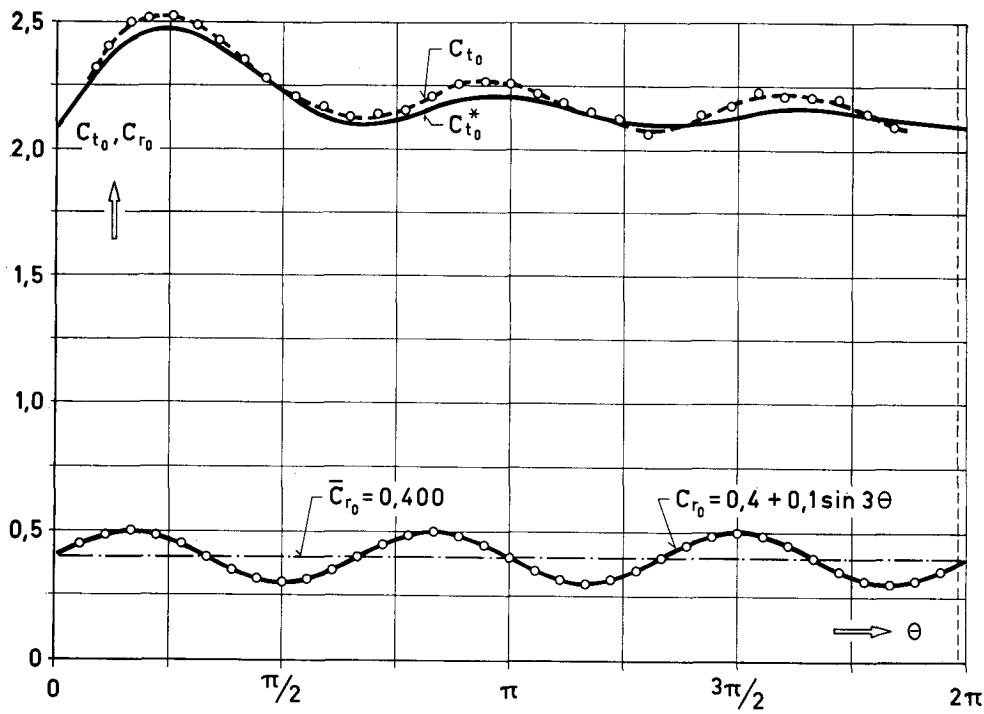

Fig. 2.38c. Logarithmic model: C_{t_0}-distribution for boundary condition $C_{r_0} = 0{,}40 + 0{,}1 \sin 3\theta$.

$$C_t^* = \frac{r_0}{r} C_{t_0}^* = \frac{\lambda}{r c_\infty} f(\theta) = \frac{\lambda^*}{r} f(\theta),$$

where $$\lambda^* = \frac{\lambda}{c_\infty} \quad \text{and} \quad C_{t_0}^* r_0 = C_t^* r = \lambda^* f(\theta).$$

The fluid volume Q_θ^* passing per unit time through a segment of the surface S_0 extended between 0 and $\theta < 2\pi$ (see Fig. 2.35) can be expressed as follows,

$$Q_\theta^* = \int_{r_0}^{r_s} c_t^* h_0 \, dr = \int_0^\theta c_{r_0} h_0 r_0 \, d\theta,$$

or, in dimensionless form

$$\int_{r_0}^{r_s} C_t^* h_0 \, dr = \int_0^\theta C_{r_0} h_0 r_0 \, d\theta.$$

Hence, since $C_t^* r = C_{t_0}^* r_0$, we obtain from this relation

$$C_{t_0}^*(\theta) = \frac{\int_0^\theta C_{r_0} d\theta}{\ln \frac{r_s}{r_0}}. \tag{2.54}$$

Accordingly, $$C_r^*(r, \theta) = \frac{r_0}{r} \frac{\int_0^\theta C_{r_0} d\theta}{\ln \frac{r_s}{r_0}}, \tag{2.55}$$

and $$\operatorname{tg} \alpha_0^* = \frac{C_{r_0}}{C_{t_0}^*} = \frac{C_{r_0}}{\int_0^\theta C_{r_0} d\theta} \ln \frac{r_s}{r_0}. \tag{2.56}$$

In our logarithmic model, $\ln r_s/r_0 = \theta \operatorname{tg} \alpha_s$; $\operatorname{tg} \alpha_s = 1{,}2/2\pi$. The $C_{t_0}^*$-distributions calculated for the three boundary conditions (2.53), using Eq. (2.54), are shown by the solid curves in Fig. 2.38 at (a), (b) and (c) respectively. We can observe immediately in these three diagrams that the deviation of $C_{t_0}^*$ from C_{t_0} does not exceed 1,5 per cent along S_0. It may then be justifiably concluded that, in the region $0 \leqq \theta \leqq 2\pi$, $C_{t_0} = C_{t_0}^*$. We obtained the same agreement between $C_{t_0}^*$ and C_{t_0} for the group of three cosine C_{r_0}-distributions; also from the measurements on the Archimedes' model. Fig. 2.39 shows the results for $C_{r_0} = \bar{C}_{r_0}(1 + 0{,}25 \cos\theta)$ on both models.

In the Archimedes' model, an observable deviation between $C_{t_0}^*$ and C_{t_0} appears at about $\theta = 300°$. This deviation increases gradually up to $\theta = 340°$ where it is less than 5 per cent. From this point, however, C_{t_0} decreases rapidly until it obtains the value 1,230; for, since

$$C_{r_0}(0) = C_{r_0}(2\pi) = 0{,}40 + 0{,}10 = 0{,}50,$$

we get $$C_{t_0}(0) = C_{t_0}(2\pi) = \frac{C_{r_0}}{\operatorname{tg} \alpha_s(0)} = \frac{0{,}50}{0{,}4053} = 1{,}230.$$

Comparing the above results for $C_{r_0} \neq \text{const.}$ with those obtained for $C_{r_0} = \text{const.}$, we are led to conclude that Eq. (2.27) is also valid here in both casings within the region $\theta \leqq 300°$ and is a tolerable approximation in the

remaining region up to $\theta = 2\pi$; further, in the logarithmic casing its validity is extended to $\theta = 2\pi$ in the region neighbouring S_0. As stated in the preceding section, Eq. (2.27) is no other than the *quasi-logarithmic law*, which, according to Eq. (2.55) can be expressed here as follows:

$$C_t \frac{r}{r_0} = \frac{\int_0^\theta C_{r_0} d\theta}{\ln \frac{r_s}{r_0}}. \tag{2.57}$$

We, therefore, infer that if the relative variation δC_{r_0} of C_{r_0} along S_0 does not exceed a value, e.g. ± 25 per cent of $\bar{C}_{r_0}$, the moment of momentum per unit mass of the fluid remains constant along a meridian section of the casing. For a given spiral casing form the value of $C_t r/r_0$ is a function of the azimuth θ of the section and the C_{r_0}-distribution *only*. The relationship (2.57) is the general expression of the quasi-logarithmic law of potential flow through two-dimensional spiral casings of usual form, since Eq. (2.40) can be derived from it in the particular case $C_{r_0} = \text{const}$.

Following the same procedure, according to which we obtained the relationships (2.36), ..., (2.39) in the preceding section, we get the more general expressions

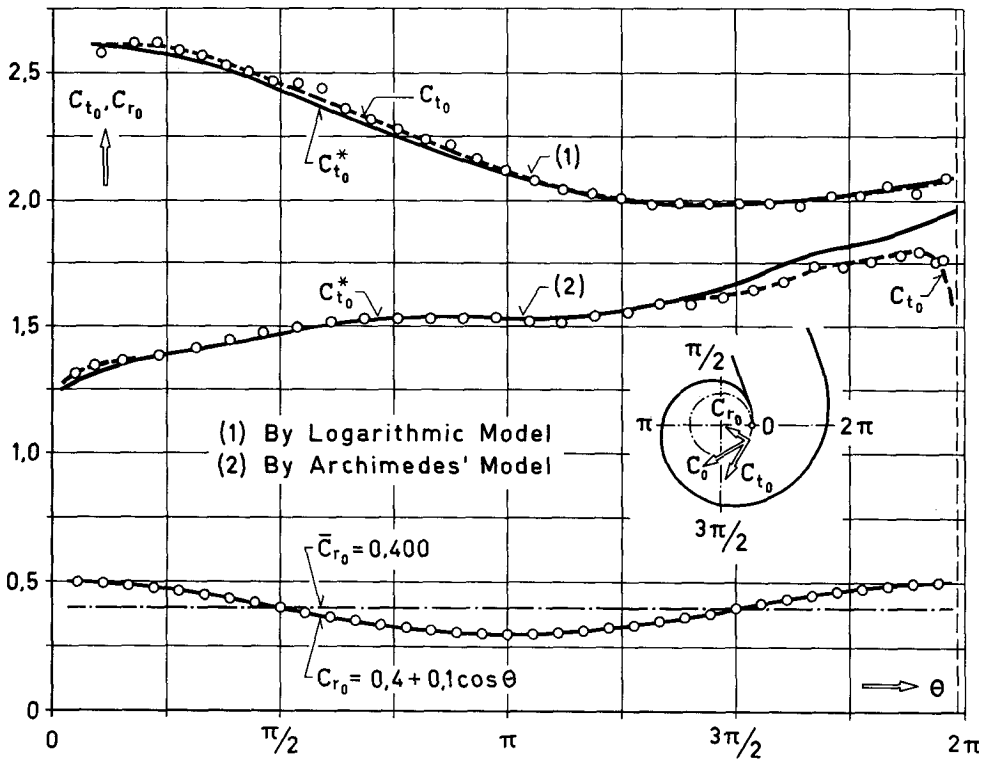

Fig. 2.39. Logarithmic and Archimedes' spiral models: C_{t_0}-distributions for boundary condition $C_{r_0} = 0{,}40 + 0{,}1\cos\theta$.

$$C_t^*(r,\theta) = \frac{r_0}{r}\frac{dT_2}{d\theta}, \tag{2.58}$$

$$\operatorname{tg}\alpha^* = \frac{C_r^*}{C_t^*} = \frac{\ln\frac{r_s}{r_0}}{\int_0^\theta C_{r_0}\,d\theta}\frac{dT_2}{d\theta}, \tag{2.59}$$

and

$$K_r^* \equiv \frac{Q_r^*}{Q_0} = \frac{r_0}{L}T_2, \tag{2.60}$$

where

$$T_2(r,\theta) = \frac{\ln r_s - \ln r}{\ln r_s - \ln r_0}\int_0^\theta C_{r_0}\,d\theta. \tag{2.61}$$

In the same way, we can calculate the moment of momentum and the dynamical reaction of the fluid on the walls of the spiral (see § 2.2.2 d)). Thus, according to Eqs. (2.45), (2,47) and (2.54), B_0 and δM_s are expressed as follows:

$$B_0 \approx B_0^* = 2\pi\bar{C}_{r_0}\frac{r_0}{\bar{r}_e}\int_0^{2\pi}\frac{C_{r_0}}{\ln\frac{r_s}{r_0}}\,d\theta, \tag{2.62}$$

and

$$\delta M_s \approx 1 - B_0^*.$$

b) The Circulation along S_0

As we have already stated, the point A (tongue of the spiral) is a discontinuity of the potential through the examined region of the casing, since it is the beginning and the end of the bounding surface S_0. The line integral

$$\oint_{S_0}\frac{\partial\phi}{\partial s_0}\,ds_0 = \int_0^{2\pi} c_{t_0} r_0\,d\theta, \quad (s_0 = r_0\theta)$$

therefore, expresses the intensity of any existing circulation, along S_0. We obtain the dimensionless form Γ' of the circulation, by dividing both members of the above relationship by the volume flow-rate q per unit height of the casing; i.e. by

$$q = \frac{Q_0}{h_0} = c_\infty L.$$

Hence

$$\Gamma' = \frac{1}{q}\oint\frac{\partial\phi}{\partial s_0}\,ds_0 = \frac{r_0}{L}\int_0^{2\pi} C_{t_0}\,d\theta, \tag{2.63}$$

or, according to the law (2.57)

$$\Gamma' \approx \Gamma'^* = \frac{r_0}{L}\int_0^{2\pi}\frac{\int_0^\theta C_{r_0}\,d\theta}{\ln\frac{r_s}{r_0}}\,d\theta, \tag{2.64}$$

We see from Eq. (2.64) that for usual spiral casing forms and for moderate values of $\max|\delta C_{r_0}|$, e.g. not larger than 25 per cent, circulation is *always*

present along S_0; its intensity is a function of the form of the spiral and the $C_{r_0}(\theta)$. The values of Γ' and Γ'^* for the examined C_{r_0}-distributions are given in *Table V*. As has been stated, the validity of Eq. (2.54) in the logarithmic casing is extended to $\theta = 2\pi$; therefore, $\Gamma' = \Gamma'^*$ there. In the Archimedes' casing the deviation of Γ'^* from Γ' is very small; for $C_{r_0} = \text{const.}$, $\Gamma' = 0{,}987\,\Gamma'^*$, and for $C_{r_0} = 0{,}4 + 0{,}1\cos\theta$, $\Gamma' = 0{,}978\,\Gamma'^*$.

Table V. The Circulation along S_0

C_{r_0}-Distribution	Logarithmic Casing		Archimedes' Casing	
	Γ'	Γ'^*	Γ'	Γ'^*
$C_{r_0} = \bar{C}_{r_0} = 0{,}400$	5,23		3,72	3,77
$C_{r_0} = 0{,}4 + 0{,}1 \sin\theta$	5,80			
$C_{r_0} = 0{,}4 + 0{,}1 \sin 2\theta$	5,59	5,61		
$C_{r_0} = 0{,}4 + 0{,}1 \sin 3\theta$	5,59	5,53		
$C_{r_0} = 0{,}4 + 0{,}1 \cos\theta$	5,67		3,90	3,98

c) The Generation of the Circulation

An experimental picture of the *generation* of the circulation along S_0 is given by the photographs of Fig. 2.40 where three characteristic successive stages of its formation, until the flow becomes stationary, are shown[2]). The two-dimensional spiral model used was free of guide vanes or a wheel inside S_0; the water entered through the inlet pipe (case of turbines) and left the model through discharge slots at its bottom; these slots form a circle around the center of the spiral. We see in the photographs that the *starting-vortex* generation on the tongue edge, and, consequently the circulation along S_0 is of the same nature here as in the well-known cases of the airfoil sections, cascades etc. Within a short time-interval, immediately after the starting of the motion, the fluid obtains a *potential flow* and the velocity on the tongue edge tends to become infinite. Thus, because of the viscosity of the fluid, the starting-vortex is generated and the velocity on this edge obtains a finite value. The starting-vortex, after its generation, grows and is carried to the center of the spiral with the water, while a circulation of the same absolute value of intensity but in opposite direction is generated along the spiral-casing walls. The dynamical reaction M_s, previously mentioned, constitutes the effect of this circulation. In other words, the photographs in Fig. 2.40 lead us to conclude that, as on the trailing edge of an air foil section here, too, *Kutta-Joukowski's condition* must be fulfilled on the *tongue edge* of the spiral. The dynamical reaction of the fluid in the case of an airfoil is expressed by a *lift*, i. e. a force, while in a spiral casing it is expressed by a *moment* of a force. The difference between the two examples is due to the fact that, in the first

[2]) These photographs were selected from a film which had to do with the generation of the circulation within elbows, nozzles, pipe-branches, spirals etc. The film was made by the "Kaiser-Wilhelm-Institut für Strömungsforschung, Göttingen".

a) The starting-point of the water from rest.

b) A short time later; the water obtains a potential motion. A singularity point is observable near the edge of the tongue.

c) Somewhat later than b); formation of the starting-vortex on the edge of the tongue is already completed.

d) The starting vortex grows and is carried to the center of the spiral with the water.

e) Some time later; the motion became stationary with a vortex at the center of the spiral model.

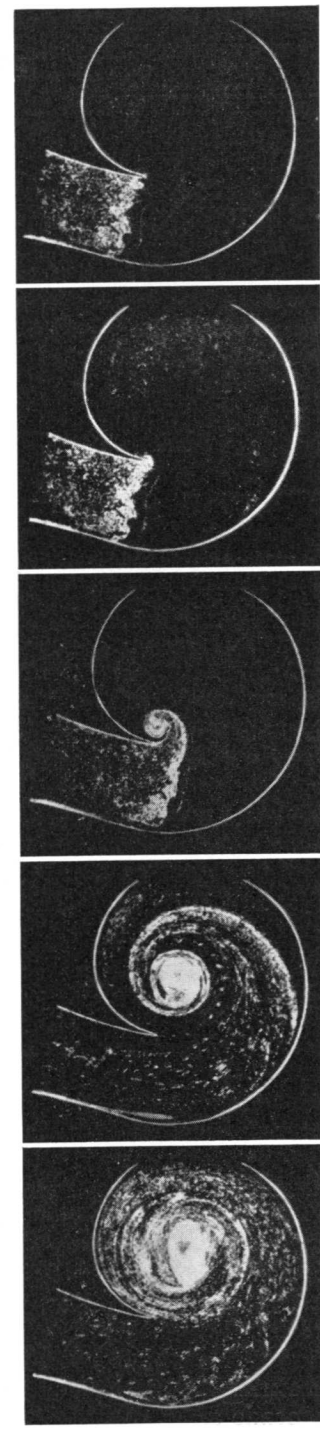

Fig. 2.40. Generation of the circulation in a spiral casing. The camera is at rest in respect of the model.

example, the starting vortex is washed away to infinity, while in the second, it remains on the center of the spiral, i.e. within the surface S_0.

We can conveniently represent the phenomenon using a *conformal transformation* of the flow through the spiral, since, by this kind of transformation, the circulation remains invariant. Thus the logarithmic spiral, shown in the *ζ-Plane* of Fig. 2.41, can be transformed into a *cascade* of *straight lines*, shown in the *w-Plane* of the same figure, by the transformation formula

$$w = \ln \zeta = \ln \frac{r}{r_0} + i\,\theta, \qquad \left(\zeta = \frac{r}{r_0} e^{i\theta}; \quad i = \sqrt{-1}\right).$$

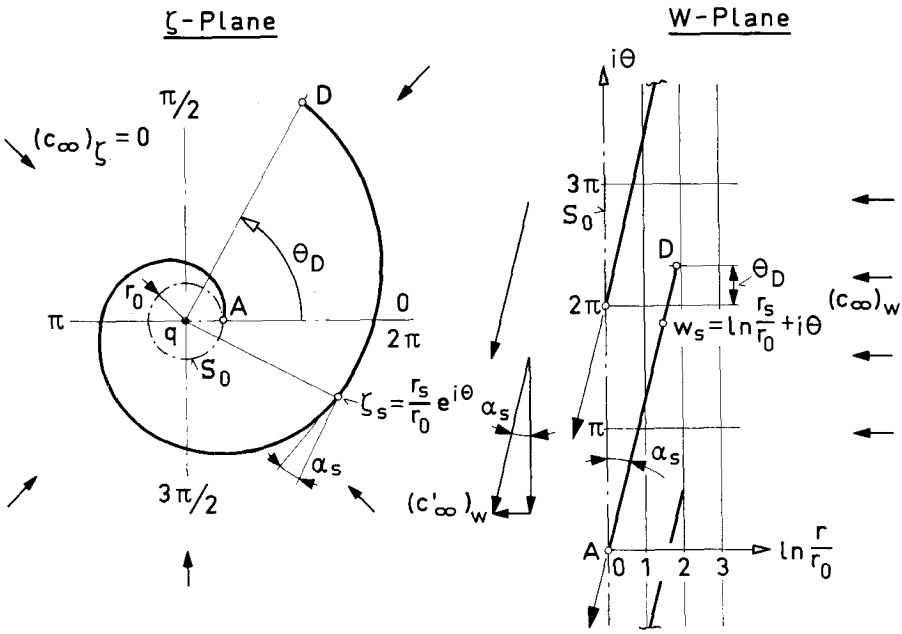

Fig. 2.41.

Let us consider a sink $q = 2\pi r_0 \bar{c}_{r_0}$ (turbine case) at the center of the spiral. Far enough from the casing the flow is a radial one, while, after entering the spiral through the meridian section at D, it becomes gradually logarithmic, according to the experimental results obtained in our logarithmic model. The corresponding flow form in the w-Plane is as follows. In places far enough before the leading edges D of the cascade the flow is parallel to the real axis of the plane with a finite velocity $(c_\infty)_w = q/2\pi$, which corresponds to the radial velocity $(c_\infty)_\zeta \to 0$ for $r \to \infty$; the sink q, on the other hand, is transferred at a distance $-\infty$ behind S_0, where the flow again becomes parallel. The cascade is inclined with respect to $(c_\infty)_w$ at an angle $\pi/2 - \alpha_s$. As we know, the flow of a frictionless fluid through the cascade, most closely approximating to a real viscous fluid flow through it, is the one derived from the fulfilment of Kutta-Joukowski's condition on the trailing edges A; the circulation Γ generated in this manner along every cascade element is a function of the geometry of the cascade and the angle of attack $[(C_\infty)_w = 1{,}0]$. The result is a lift-force on the

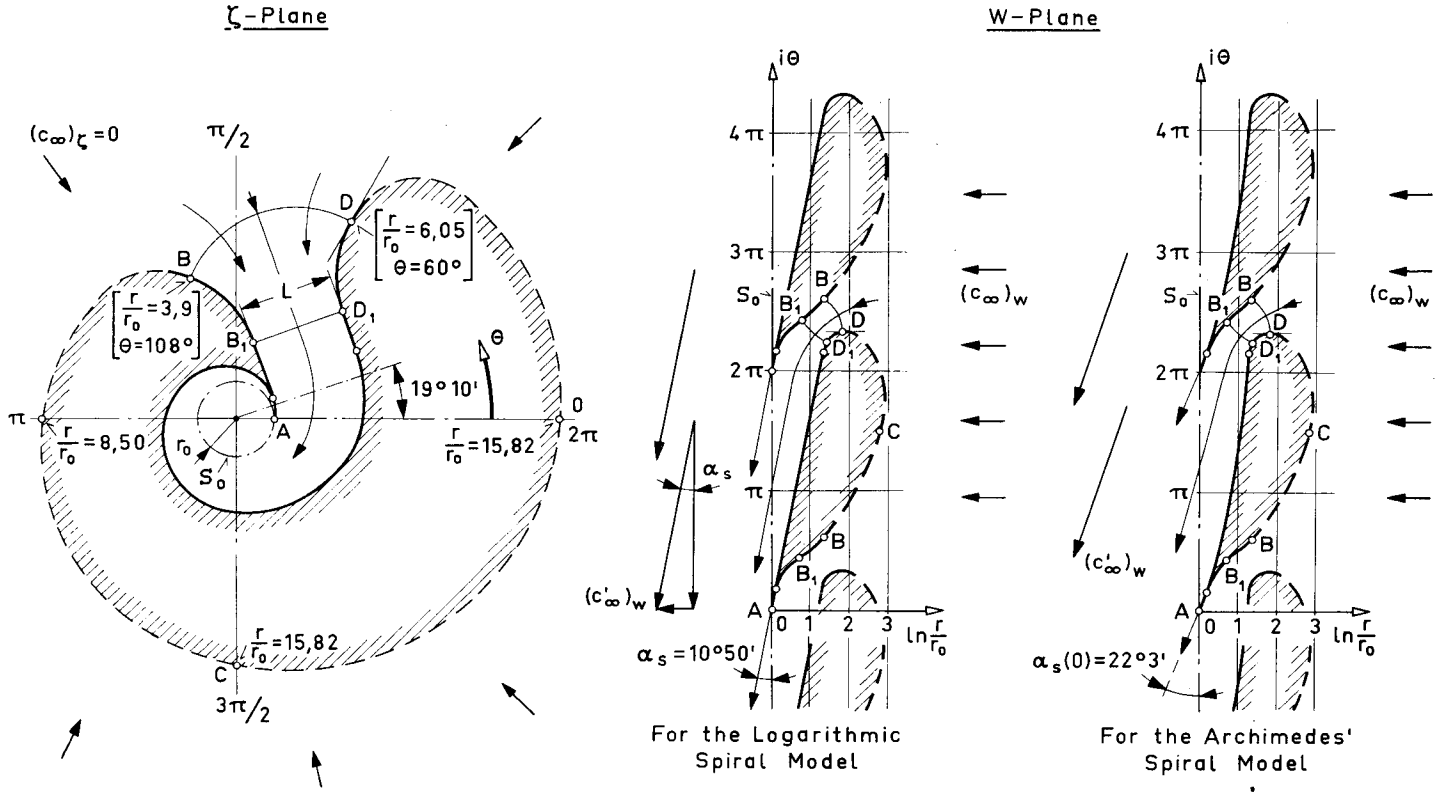

Fig. 2.42. Conformal conjunction between spiral casings and cascades by means of the transformation $w = \ln \zeta$.

cascade and a deviation of the flow direction far behind S_0, with respect to $(c_\infty)_w$. In the ζ-Plane, plane of the spiral, the result is no longer a lift-force but a torque.

In the particular case of a logarithmic spiral in which θ_D is large enough, e. g. greater than $\pi/4$, the flow downstream of S_0 in the w-Plane is parallel to the elements of the cascade, i. e.

$$(c'_\infty)_w = \frac{(c_\infty)_w}{\sin \alpha_s};$$

consequently, the circulation Γ per cascade element is

$$\Gamma = 2\pi \frac{(c_\infty)_w}{\operatorname{tg} \alpha_s} = 2\pi r_0 \frac{c_{r_0}}{\operatorname{tg} \alpha_s}, \quad (c_{r_0} = \text{const.}),$$

For any spiral form other than a logarithmic, the cascade elements in the w-Plane are curved lines and the values of the $(c'_\infty)_w$ inclination and the circulation Γ are generally different.

Fig. 2.42 shows the conformal transformation of the innermost part of the used two-dimensional spiral casings, e. g. our logarithmic and Archimedes' models, to cascades. Since these models have the same pipe width L we choose two points B and D at the entrance of the pipe to be common for both, and we enclose the spirals in an arbitrary curved wall BCD so as to obtain some convenient convex form in the w-Plane. If the parallel part of the walls of the inlet pipe between the points B, D and the entrance section at $\theta = 379° 10'$ (or $19° 10'$) is long enough to secure a parallel flow in a part of this pipe, the flow form through the spiral is nearly independent of the shape of the wall BCD. Consequently, the flow form in our region of interest, i. e. from the equipotential line $B_1 D_1$ (straight line normal to the pipe walls in the ζ-Plane) and downstream, in the w-Plane, is also nearly independent of the form BCD of the cascade elements. The important part of the cascade element is the part BAD only. We see again that for the fulfilment of Kutta-Joukowski's condition on A a circulation around every element of the cascade should take place. There are several methods proposed to solve the cascade problem when the form of its elements and the approach velocity are given.

However, our case is much more complicated since the boundary surface of a spiral casing is the S_0, whereas these methods could be applicable, by means of the transformation $w = \ln \zeta$, *only* if a sink and a vortex exist on the center of the spiral. The two cases are equivalent, as we found in our experimental investigation, only for a logarithmic spiral casing and if $C_{r_0} = \text{const.}$ along S_0. We nevertheless mentioned the above conformal relationship between casings and cascades to show the common origin of the circulation in both examples, and not to give a theoretical solution to the problem.

2.3. Measurements on the Three-Dimensional Model

2.3.1. Form of the Collector Used

The model used is shown in Fig. 2.04. As mentioned in § 2.1.2, the casing represented by this model is symmetrical to a plane perpendicular to the z-axis and is bounded by the cylindrical surface S_0 between two planes parallel

to the plane of symmetry (see also § 1.2.3). The potential flow, or the electric field, passing through S_0, is therefore, two-dimensional (c_{r_0} and c_{t_0} are independent of z, and $c_z = 0$). The design of the collector *(Collector IV)*, used in this model was thus based on experience acquired from the design of collector III (see § 2.2.1) with the difference that IV has forty equally-spaced electrodes instead of thirty-six as in III. Fig. 2.43 shows the form and the constructional details of collector IV. Fig. 2.44a shows a photograph of this collector; the same figure at (b) shows the collector assembled in the three-dimensional model. The electrodes of collector IV, as with III, are of porous graphite; likewise, the insulating material is of "Epoxide Resin". The angle $\alpha_s(0)$ of the tongue of the casing is 45°. The insulating plates are of a thickness of 5 mm and are extended to the surface S_0' ($r_0 = 118{,}5$ mm), making an angle of 35° with the respective radius. Further, by suitable plane-undercuts the side surfaces of every insulating plate are inclined to the radius at angles: $35° - 10° = 25°$ and $35° + 10° = 45°$; their front width on S_0 is 1,5 mm. This formation was used in an attempt to avoid both secondary ohmic currents and large deformations of the current lines around S_0', since we have no prior knowledge of the inclinations α_0, of these lines to S_0.

For the measurements we followed the procedure mentioned in § 2.1.5; here, it was of fundamental importance to keep the level of the water exactly at the plane of symmetry (see § 2.1.2 c)). The first step of the measurements was to adjust a constant current distribution along S_0' ($J_K = \text{const.}$;

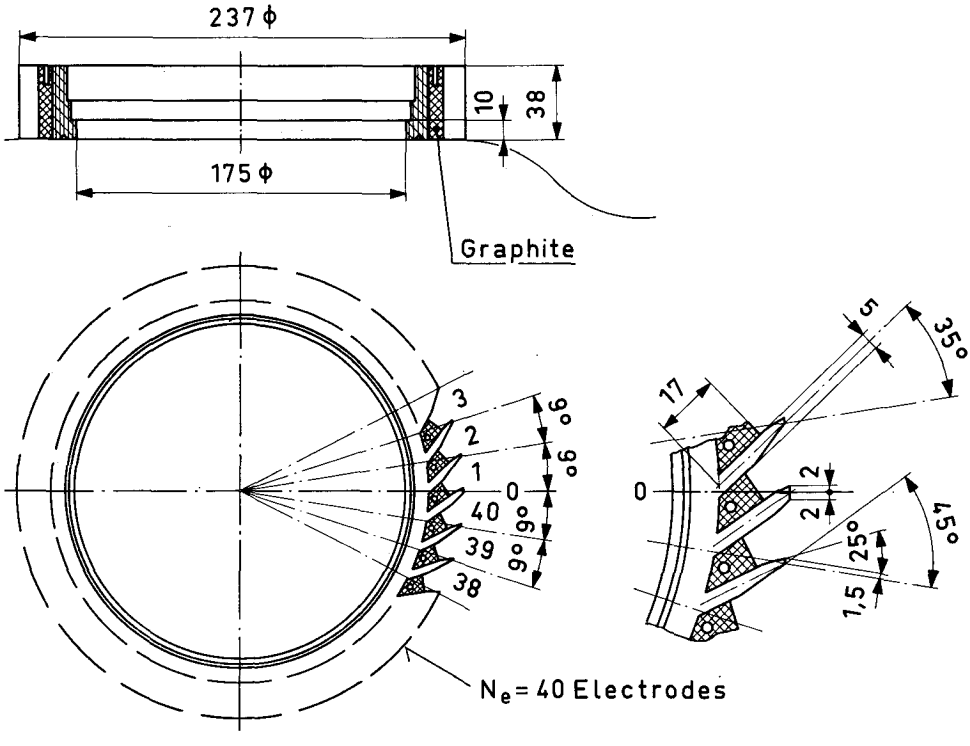

Fig. 2.43. Collector IV.

$K = 1, 2, \ldots, 40$) and to check whether secondary ohmic or capacitive currents occur. Fig. 2.45 shows, in unrolled form, the intersections between the equipotential surfaces and the plane at depth $z = 10$ mm from the level of the water ($z = 0{,}433\, h_0/2$) in the most sensitive region, in the neighbourhood of (1)- and (2)-electrodes (the z coordinate is assumed to be measured from the plane of symmetry, where $z = 0$). By applying the method mentioned in § 2.2.1 to this diagram, we found that neither secondary ohmic- nor secondary capacitive-currents occur in this model. A possible explanation is that the angle $\alpha_s(0) = 45^\circ$ is large enough, and the 3 mm diaphragm of the tongue becomes increasingly thicker with the depth. Further, the disturbance of the

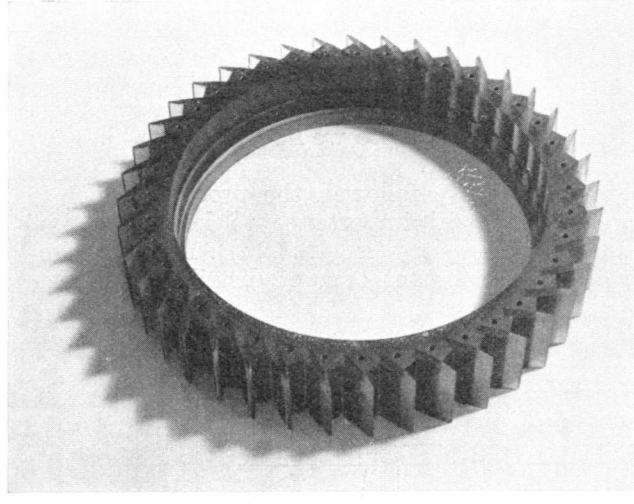

a)

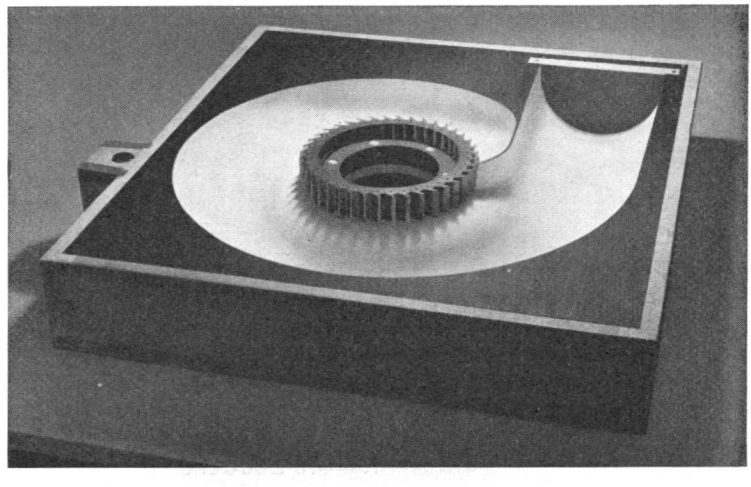

b)

Fig. 2.44. At a), a view of the Collector IV; at b) Collector IV assembled on the three-dimensional model.

electric field obtained is confined to within circles of about 2 mm radius having as center the edge of each insulating plate. Since the field is approximately two-dimensional in the region very near the surface S_0', it is plain that the picture of the field shown in Fig. 2.45 remains the same along z.

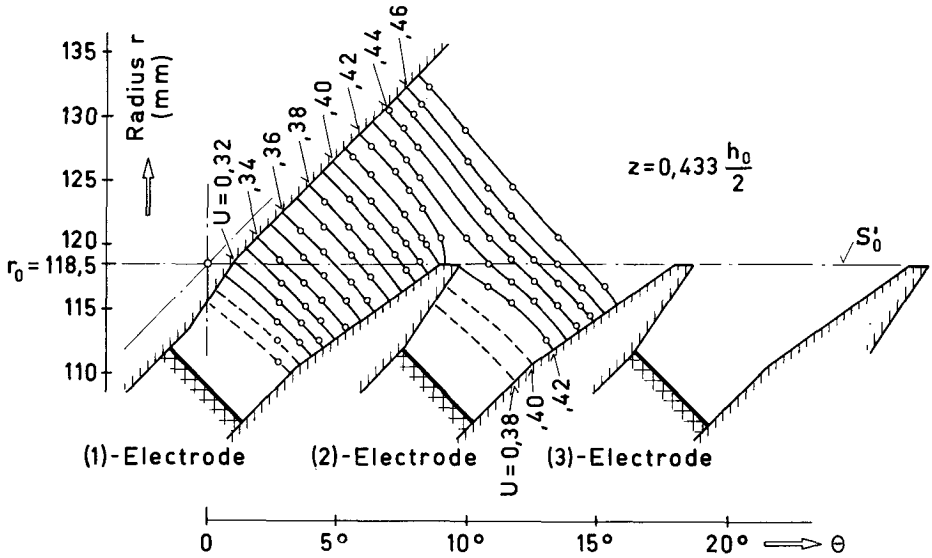

Fig. 2.45. Form of the V-field passing through S_0 in the region of the two first electrodes of Collector IV, for $C_{r_0} = \text{const.}$

2.3.2. Measurements for C_{r_0} Constant. Results

The form of the potential flow through the casing when $c_{r_0} = \text{const.}$ along S_0 is shown in Figs. 2.46, 2.47, and 2.48. The values of the velocity potential are, as in the case of the two-dimensional models,

$$\phi \rightarrow -U V_0 + \text{const.}$$

Fig. 2.46 shows the equipotential intersections on the plane $z = 0{,}433\, h_0/2$ ($z = 10$ mm); Figs. 2.47 and 2.48 show, respectively, the intersections of the equipotentials on the cylindrical surface at $r = 1{,}435\, r_0$ ($r = 170$ mm) and on three characteristic meridian-planes of the model.

The first qualitative observation from the above figures is that the equipotential surfaces seem to be of a rather small curvature; moreover, the figures suggest that from about $\phi = 4{,}5$ and upwards an equipotential surface could be approximately generated from the preceding surface by a small turm about the z-axis of the model. To study the flow more closely, therefore, we followed the same method as in the two-dimensional casings. We plotted the angle differences $\delta\phi$ obtained between successive equipotential intersections ϕ_{n+1} and ϕ_n, as shown in Fig. 2.46 (where $\phi_{n+1} - \phi_n = \delta\phi = 0{,}5$), at various radii r against the angle θ of the *meau point* of every interval. These results, given for the plane at $z = 0{,}433\, h_0/2$ are shown in Fig. 2.49 a. We see immediately from the plotted points that through the region $0 \leqq \theta \leqq 315°$ the angle difference $\delta\theta$ is a function of the angle θ *only*; as in the case of the two-dimensional

Archimedes' model, it is namely, *independent* of the radius r. Combining this knowledge with the form of the equipotential intersections shown in Fig. 2.47 and also in Fig. 2.48 we are led to suspect that the above result could be valid throughout the entire three-dimensional region $0 \leqq \theta \leqq 315°$ of the model. Hence, following the same line of thought as in the preceding Archimedes' casing (see § 2.2.2 b)) we infer that for $c_{r_0} = \text{const.}$ the relationship (2.27),

$$c_t r = \frac{\partial \phi}{\partial \theta} = \lambda f(\theta), \tag{2.27}$$

could be valid also in our three-dimensional casing for $\theta \leqq 315°$. (Of course, the constant λ and the function $f(\theta)$ *do not have* the same value in both casings.) Consequently, on a meridian section of the model Eq. (2.28),

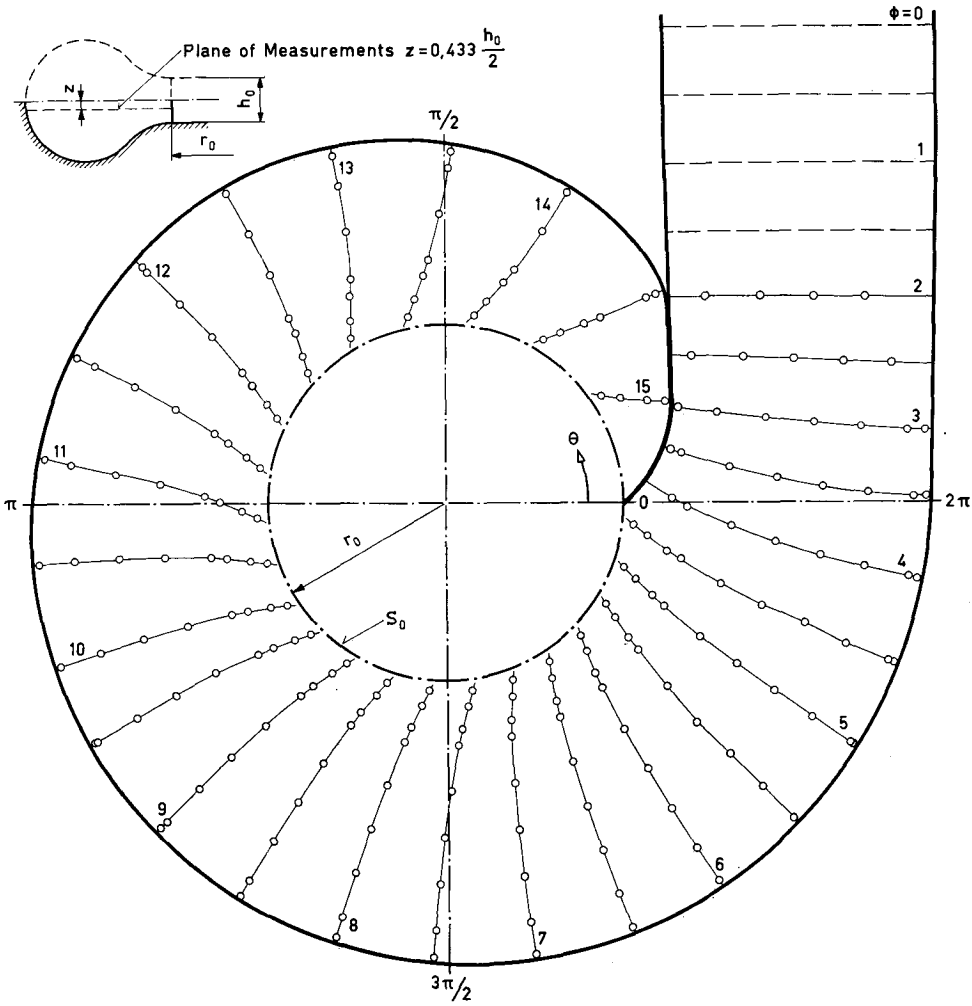

Fig. 2.46. Potential flow through the three-dimensional model (see Fig. 2.04) for boundary condition $C_{r_0} = 0{,}74$ (= const.) (see also Figs. 2.47 and 2.48).

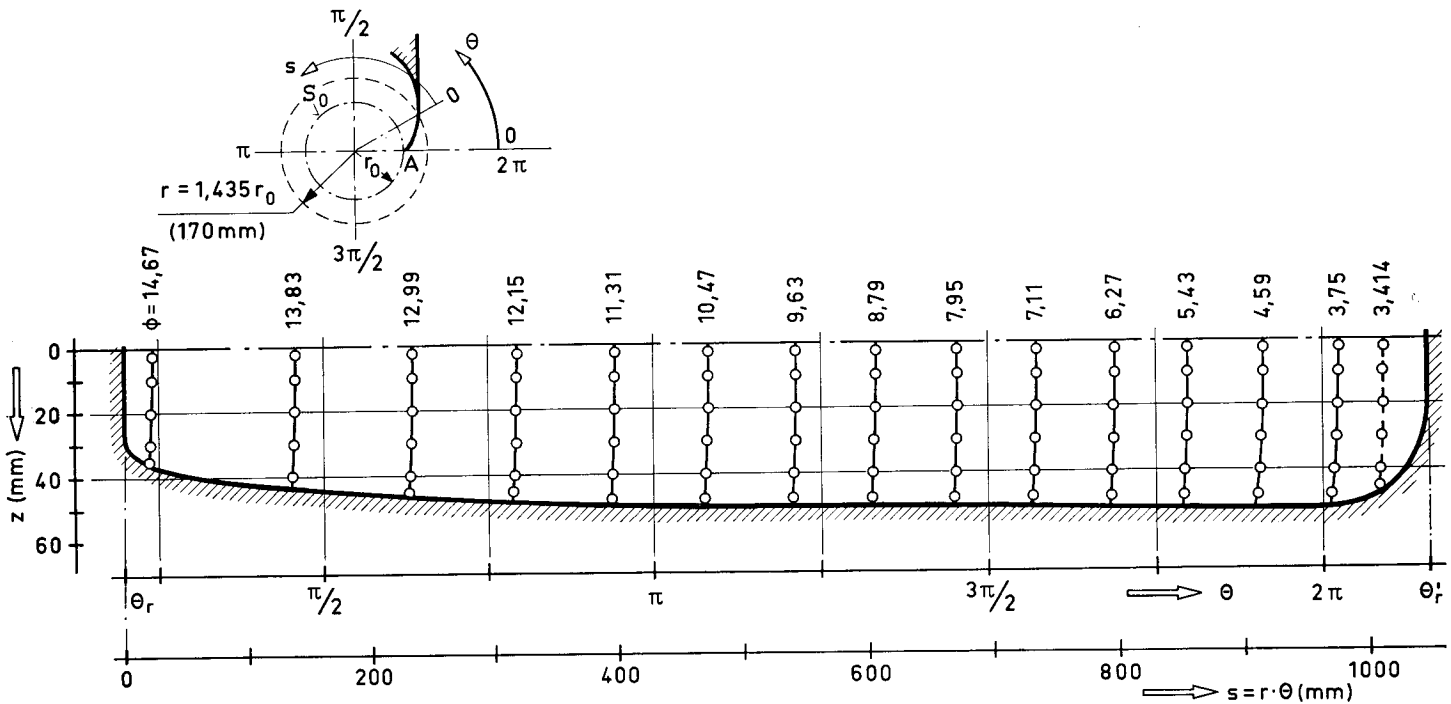

Fig. 2.47. Potential flow through the three-dimensional model (see also Figs. 2.46 and 2.48). Measurements along the cylindrical surface at radius $r = 1{,}435\, r_0$, for boundary condition $C_{r_0} = 0{,}74$.

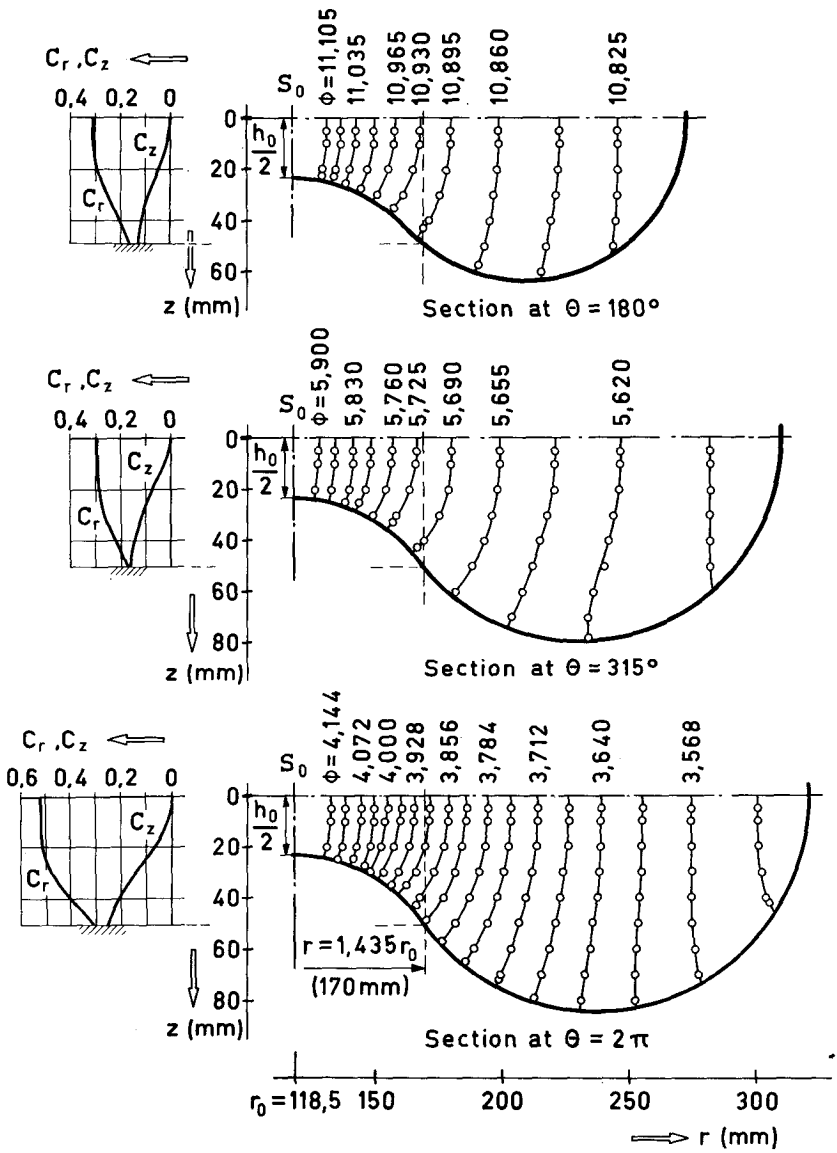

Fig. 2.48. Potential flow through the three-dimensional model (see also Figs. 2.46 and 2.47). Measurements along the meridian sections at $\theta = 180°$, 315° and 2π, for boundary condition $C_{r_0} = 0{,}74$.

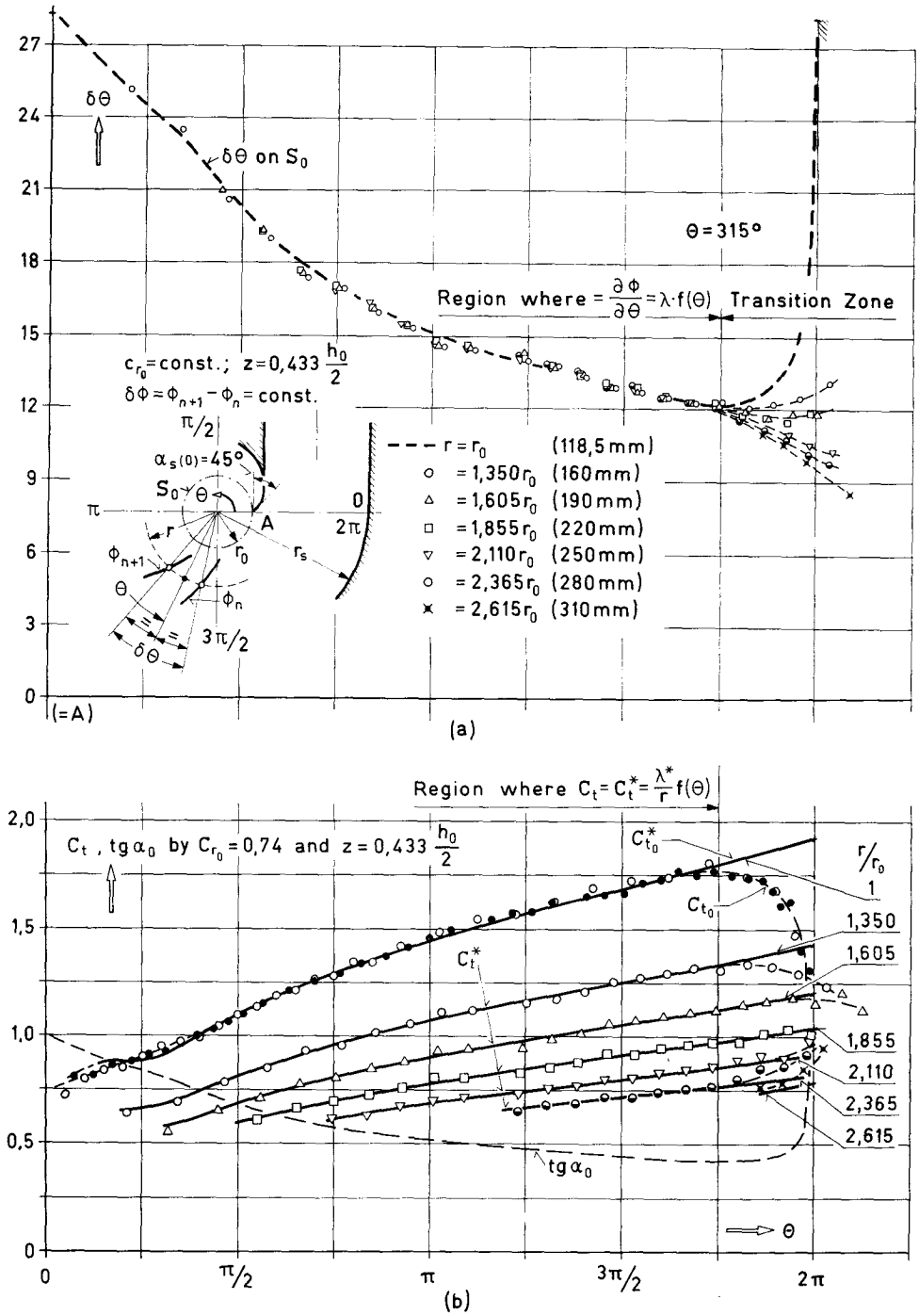

Fig. 2.49. Three-dimensional model; C_t-distribution for $C_{r_0} = \text{const.}$

$$c_t r = c_{t_0} r_0 = \lambda f(\theta), \tag{2.28}$$

could similarly be valid in $0 \leqq \theta \leqq 315°$. From $\theta = 315°$ and upwards to the entrance section at $\theta = 2\pi$ Eq. (2.27) deviates gradually from the experimental points; excluding the region $r < 1{,}35\, r_0$ near the surface S_0, however, we observe that it gives a roughly tolerable approximation for $r > 1{,}35\, r_0$, since the band-spread of the measuring-points on various radii does not exceed ± 15 per cent about a mean value corresponding to the point ($r \approx 2 r_0, \theta = 2\pi$). In the region $r < 1{,}35\, r_0$ the values of $\delta\theta$ increase rapidly with θ. Thus the $\delta\theta$-curve on S_0 (radius r_0) shows an extremely steep ascent in the region of $\theta = 2\pi$. At the tongue of the model ($\theta = 0$ and $\theta = 2\pi$),

$$(\delta\theta)_0 = (\delta\theta)_{2\pi},$$

since by $c_{r_0} = \text{const.}$ along S_0 the velocity $\vec{c}_0$ on both sides of A is the same. Thus

$$\left(\frac{c_{r_0}}{c_{t_0}}\right)_0 = \left(\frac{c_{r_0}}{c_{t_0}}\right)_{2\pi} = \operatorname{tg} \alpha_s(0) = 1{,}0; \quad (\alpha_s(0) = 45°).$$

a) The Quasi-Logarithmic Law for C_{r_0} Constant

In order to utilize the experimental fact expressed by Eq. (2.27) in this three-dimensional casing, we apply the method of the preceding section. Thus the fluid volume Q_θ passing per unit time through the segment $(0, \theta)$ of the surface S_0, $0 \leqq \theta \leqq 2\pi$ (see Fig. 2.50), is

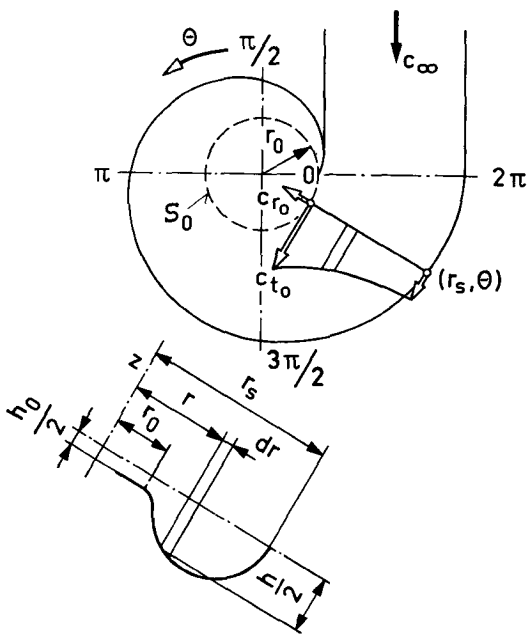

Fig. 2.50.

$$Q_\theta = \int_0^\theta d\,Q = \int_0^\theta c_{r_0} r_0 h_0 \, d\,\theta = \int_{r_0}^{r_s} c_t h \, d\,r, \tag{2.65}$$

or, using the dimensionless representation given by Eqs. (2.10),

$$\int_0^\theta C_{r_0} r_0 h_0 \, d\,\theta = \int_{r_0}^{r_s} C_t h \, d\,r.$$

Hence, since C_{r_0} is constant, we obtain

$$C_{r_0} r_0 h_0 \theta = \int_{r_0}^{r_s} C_t h \, d\,r. \tag{2.66}$$

Furthermore, introducing also here the superscript * to C_t, C_{t_0}, etc., to distinguish the values obtained by Eq. (2.28) from those derived from the measuring-points we write

$$C_t^* = \frac{r_0}{r} C_{t_0}^* = \frac{\lambda}{c_\infty r} f(\theta) = \frac{\lambda^*}{r} f(\theta),$$

where

$$\lambda^* = \frac{\lambda}{c_\infty}; \qquad C_{t_0}^* r_0 = \lambda^* f(\theta).$$

Inserting now C_t^* into Eq. (2.66) we get

$$C_{r_0} r_0 h_0 \theta = C_{t_0}^* r_0 \int_{r_0}^{r_s} \frac{h}{r} d\,r.$$

The integral on the right is a function of the spiral casing form only; thus, putting

$$H_s(\theta) \equiv \int_{r_0}^{r_s} \frac{h\,(r, \theta)}{r} d\,r \quad (\text{at } \theta) \tag{2.67}$$

we obtain

$$C_{t_0}^*(\theta) = \frac{h_0}{H_s} C_{r_0} \theta. \tag{2.68}$$

Consequently

$$\operatorname{tg} \alpha_0^*(\theta) = \frac{C_{r_0}}{C_{t_0}^*} = \frac{H_s}{h_0} \frac{1}{\theta}; \tag{2.69}$$

also

$$\lambda^* f(\theta) = \frac{h_0}{H_s} C_{r_0} r_0 \theta,$$

and

$$C_t^*(r, \theta) = \frac{h_0}{H_s} \frac{r_0}{r} C_{r_0} \theta. \tag{2.70}$$

For the casing under consideration a plot of H_s/h_0 vs. θ is given in Fig. 1.10a.

In order to show more clearly the validity of the experimentally-found Eqs. (2.68) and (2.70) in the region $\theta \leqq 315°$ and their deviations from the measured values of the C_t in the *transition zone* $\theta > 315°$, we plotted the C_t^*-curves (solid lines) and the C_t-curves (dotted lines) against θ, as shown in Fig. 2.49b. In this diagram the dimensionless value of C_{r_0} is, according to Eq. (2.14.1), 0,74 along S_0. Since the inclination α_s, of the casing wall with

respect to S_0 at the casing-tongue is 45°, the value of C_{t_0} there is:

$$C_{t_0}(0) = C_{t_0}(2\pi) = \frac{C_{r_0}}{\operatorname{tg} \alpha_s(0)} = 0{,}74.$$

The points shown in Fig. 2.49b are derived from the direct experimental values plotted in the same figure at (a), except for the points of the C_{t_0}-distribution, which are obtained from a somewhat more detailed series of measurements very near the surface S_0. These points are derived from measurements of the angle differences $\delta\theta$ for $\delta\phi = \text{const.}$, and also from measurements of the potential differences $\delta\phi$ for $\delta\theta = 9°$, which is the angular interval between successive insulating plates of the collector.

In Fig. 2.49b the region of validity of Eqs. (2.27) and (2.28), consequently of Eq. (2.70), is easily determined, as well as the magnitude of the deviation of C_t^* from C_t at various radii in the transition zone $\theta > 315°$. Eq. (2.70) appears to be exact in the region ($1{,}6\,r_0 < r < 1{,}9\,r_0$, $315° < \theta \leqq 2\pi$) while in the region ($r > 1{,}9\,r_0$, $315° < \theta < 2\pi$) it becomes less exact since C_t^* decreases gradually up to $\theta = 2\pi$; thus, at the point ($r = 2{,}615\,r_0$, $\theta = 2\pi$) the deviation of C_t^* is about -17 per cent from C_t. In the region ($r < 1{,}6\,r_0$, $\theta > 315°$) we observe that C_t^* increases from C_t; the deviation remains tolerably small up to and including the line ($r = 1{,}35\,r_0$, $\theta = 2\pi$), where it does not exceed $+13$ per cent. In the region ($r < 1{,}35\,r_0$, $\theta > 330°$), however, C_t decreases sharply, since at the point $A\,(r_0, 2\pi)$ the component $C_{t_0}(2\pi)$ must attain the value 0,74.

We see from all the above that Eq. (2.70) is valid in a considerably large part of the casing. Multiplying both members of this equation by r/r_0 we obtain

$$C_t \frac{r}{r_0} = \frac{h_0}{H_s} C_{r_0} \theta. \tag{2.71}$$

Eq. (2.71) is no other than the expression of the *quasi-logarithmic law* in a three-dimensional spiral casing. As in the two-dimensional casings, here, too, the moment of momentum per unit mass of the fluid remains constant along a meridian section; in a given spiral form and for $C_{r_0} = \text{const.}$, the value of $C_t r/r_0$ is a function of the azimuth θ of the section. Hence, Eq. (2.71) seems to express a general property of the potential flow through spiral casings of usual form. The well-known law $C_t r/r_0 = \text{const.}$ we have already shown to be valid for casings derived from an axially-symmetric flow (see § 1.1.2 and the respective Eq. (1.12)) and the law (2.40) we found for two-dimensional casings are, in fact, particular cases of the law (2.71). Thus in the first case we found $H_R/h_0 = \theta \operatorname{tg} \alpha_0$ (see Eq. (1.14)) where $\operatorname{tg} \alpha_0 = \text{const.}$; therefore Eq. (2.68) gives

$$C_t \frac{r}{r_0} = \frac{C_{r_0}}{\operatorname{tg} \alpha_0} = \text{const.}, \qquad (C_{r_0} = \text{const.}),$$

i. e. the relationship (1.12).

In the two-dimensional casings, on the other hand, we have,

$$H_s = h_0 \ln \frac{r_s}{r_0},$$

(see Eq. (2.67)).

Hence, Eq. (2.68) gives

$$C_t \frac{r}{r_0} = \frac{C_{r_0}}{\ln \frac{r_s}{r_0}} \theta,$$

i.e. the law (2.40).

b) Mean Radial-Component of the Velocity

In order to give an idea of the distributions of the other two components C_r and C_z of the velocity we plotted the C_r- and C_z-curves along the lines parallel to the z-axis ($r = 170$ mm; $\theta = 180°$, $315°$, 2π) as shown in Fig. 2.48, where the casing wall has an inclination of about $45°$ with respect to the z-axis. We see that both these components remain small in comparison with the C_t at the same radius; we see, also, that in the z direction and for $\theta \leqq 315°$, C_r does not change very much in this type of casing. It is of practical importance, therefore, to try to express the distribution of the *mean radial* component $\bar{C}_r^*$ of the velocity, as well as that of the *mean angle* $\bar{\alpha}^*$, ($\operatorname{tg} \bar{\alpha}^* = \bar{C}_r^*/\bar{C}_t^*$) on a cylindrical surface of radius r, in the region $\theta \leqq 2\pi$, following the same method as in the preceding two-dimensional casings. Thus, as shown in Fig. 2.32, the fluid volume element dQ_ν which passes per unit time through a cylindrical surface of radius r_ν at a point (r_ν, θ), is now

$$dQ_\nu = \bar{c}_{r_\nu} r_\nu h_{r_\nu} d\theta = \frac{d}{d\theta} \left(\int_{r_\nu}^{r_s} c_t h \, dr \right) d\theta.$$

Introducing in this relationship the dimensionless values $\bar{C}_r^*, C_t^*$ we obtain

$$\bar{C}_{r_\nu}^* r_\nu h_{r_\nu} = \frac{d}{d\theta} \left(C_{t_0}^* r_0 \int_{r_\nu}^{r_s} \frac{h}{r} dr \right),$$

or,

$$\bar{C}_{r_\nu}^* r_\nu h_{r_\nu} = r_0 h_0 \frac{d}{d\theta} \left(C_{r_0} \frac{\theta}{H_s} \int_{r_\nu}^{r_s} \frac{h}{r} dr \right).$$

Since r_ν is an arbitrary radius, we can write

$$\bar{C}_r^* r h_r = r_0 h_0 \frac{d}{d\theta} \left(C_{r_0} \frac{\theta}{H_s} \int_{r}^{r_s} \frac{h}{r} dr \right).$$

Putting

$$H_{rs}(r, \theta) \equiv \int_r^{r_s} \frac{h}{r} dr \tag{2.72}$$

and

$$T_3(r, \theta) \equiv \frac{H_{rs}}{H_s} C_{r_0} \theta, \quad (C_{r_0} = \text{const.}), \tag{2.73}$$

we obtain

$$\bar{C}_r^*(r, \theta) = \frac{r_0}{r} \frac{h_0}{h_r} \frac{dT_3}{d\theta}. \tag{2.74}$$

Consequently,

$$\operatorname{tg} \bar{\alpha}^*(r, \theta) = \frac{\bar{C}_r^*}{C_t^*} = \frac{H_s}{h_r} \frac{1}{C_{r_0} \theta} \frac{dT_3}{d\theta}. \tag{2.75}$$

The volume Q_r of the fluid passing per unit time through the region (θ_r, θ) of the cylindrical surface of radius r, is

$$Q_r^*(r,\theta) = c_\infty \int_{\theta_r}^{\theta} \bar{C}_r^* h_r \, d\theta = c_\infty \int_{r}^{r_s} C_l^* h \, dr, \qquad (2.76)$$

$$(\theta_r \leqq \theta \leqq 2\pi) \qquad (\text{at } \theta)$$

where θ_r is the angular coordinate of the extreme point of the intersection between this surface and the casing (see also Fig. 2.32). Dividing by $Q_0 = c_\infty S_p$, where S_p is the cross-section of the inlet pipe, we obtain from Eq. (2.76) the dimensionless expression

$$K_r^*(r,\theta) \equiv \frac{Q_r^*}{Q_0} = \frac{r_0 h_0}{S_p} \; T_3 = \frac{1}{2\pi} \frac{H_{rs}}{H_s} \theta \quad (\theta_r \leqq \theta \leqq 2\pi). \qquad (2.77)$$

All the above relations concerning the values of $\bar{C}_r^*$, C_l^*, etc., are in exact agreement with the experimental results up to $\theta = 315°$. In the remaining region $315° < \theta < 2\pi$, they are valid approximately; in the casing-form examined we can say that, excepting the region ($r < 1{,}3 r_0$, $\theta > 330°$), the approximation is tolerable for practical purposes up to $\theta = 2\pi$.

c) Moment of Momentum and Dynamical Reaction of the Fluid

To find the dynamical reaction of the fluid on the walls of the spiral we also use here the fundamental Eq. (2.44),

$$-b_\infty + b_0 - \mu_\infty + \mu_s = 0 \qquad (2.44)$$

(see § 2.2.2 at d)). Since the casing is three-dimensional, the expressions of b_∞, b_0, μ_∞, μ_s are now as follows.

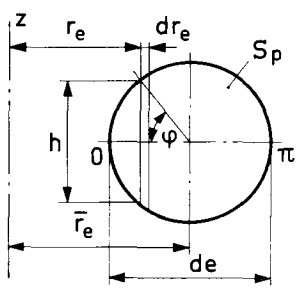

Fig. 2.51.

For b_∞, $b_\infty = \iint_{S_p} \rho c_\infty^2 r_e \, dS = \int_{\min r_e}^{\max r_e} \rho c_\infty^2 h r_e \, dr_e$.

According to Fig. 2.51, in which the inlet pipe cross-section is shown, we have

$$h = d_e \sin\varphi; \qquad r_e = \bar{r}_e - \frac{d_e}{2}\cos\varphi;$$

$$dr_e = \frac{d_e}{2}\sin\varphi \, d\varphi;$$

therefore $b_\infty = \rho c_\infty^2 \bar{r}_e S_p = 2 q_e \bar{r}_e S_p$, $\left(S_p = \frac{\pi}{4} d_e^2\right)$.

For b_0, $$b_0 = \rho h_0 \left(\frac{r_0}{c_\infty}\right)^2 \int_0^{2\pi} C_{r_0} C_{t_0} \, d\theta,$$

since the flow on S_0 is two-dimensional.

For μ_∞, $$\mu_\infty = \iint_{S_p} p_\infty r_e \, dS = p_\infty \bar{r}_e S_p.$$

For μ_s, $$\mu_s = \iint_{S_s} p_s r_s \cos(\vec{n}_t, \vec{n}) \, dS,$$

where n_l is the unit vector parallel to $\vec{c}_l$ with positive direction in the direction of increasing θ. The dimensionless expression of the above quantities with respect to b_∞ (see also Eqs. (2.45)) is

$$B_\infty = \frac{1}{2\pi}\frac{S_0}{S_p}\frac{r_0}{\bar{r}_e}\int_{min\, r_e}^{max\, r_e}\frac{h}{h_0}\frac{r_e}{r_0}d\left(\frac{r}{r_0}\right) = \frac{2}{\pi}\int_0^{\pi}\sin^2\varphi\, d\varphi = 1{,}0,$$

(see Fig. 2.51)

$$B_0 = \frac{b_0}{b_\infty} = \frac{1}{2\pi}\frac{S_0}{S_p}\frac{r_0}{\bar{r}_e}\int_0^{2\pi} C_{r_0} C_{t_0}\, d\theta \tag{2.78}$$

$$M_s = \frac{\mu_s}{b_\infty}$$

$$M_\infty = \frac{\mu_\infty}{b_\infty}.$$

Consequently

$$\delta M_s = M_s - M_\infty = 1 - B_0; \tag{2.47}$$

this is the relationship (2.47), which we first introduce in § 2.2.2 at d), but the M_s, M_∞, B_0 are now according to Eqs. (2.78). The expressions of B_θ and $(B_0)_\theta$ of the moment of momentum of the fluid passing through a meridian section at θ and through the part of S_0 between $\theta = 0$ and θ respectively, are

$$B_\theta = \frac{1}{2\pi}\frac{S_0}{S_p}\frac{r_0}{\bar{r}_e}\int_{r_i/r_0}^{r_s/r_0} C_l^2\frac{r}{r_0}\frac{h}{h_0}d\left(\frac{r}{r_0}\right), \tag{2.79}$$

(in the region $\theta \leqq 2\pi$, $r_i = r_0$)

and

$$(B_0)_\theta = \frac{1}{2\pi}\frac{S_0}{S_p}\frac{r_0}{\bar{r}_e}\int_0^{\theta} C_{r_0} C_{t_0}\, d\theta. \tag{2.80}$$

Also, according to Eq. (2.48),

$$\delta M_\theta = (M_s)_\theta - M_\theta = B_\theta - (B_0)_\theta. \tag{2.48}$$

Considering the regions $\theta \leqq 315°$ where the law (2.71) is valid and $315° < \theta \leqq 2\pi$ where this law is approximately valid, we obtain

$$B_\theta^* = \frac{1}{2\pi}\frac{r_0}{\bar{r}_e}\frac{h_0}{H_s} C_{r_0}\theta^2 \tag{2.81}$$

and

$$(B_0)_\theta^* = \frac{1}{2\pi}\frac{r_0}{\bar{r}_e} C_{r_0}\int_0^{\theta}\frac{h_0}{H_s}\theta\, d\theta, \tag{2.82}$$

since $S_0/S_p = 1/C_{r_0}$,

and

$$\delta M_\theta^* = \frac{1}{2\pi}\frac{r_0}{\bar{r}_e} C_{r_0}\left(\frac{h_0}{H_s}\theta^2 - \int_0^{\theta}\frac{h_0}{H_s}\theta\, d\theta\right). \tag{2.83}$$

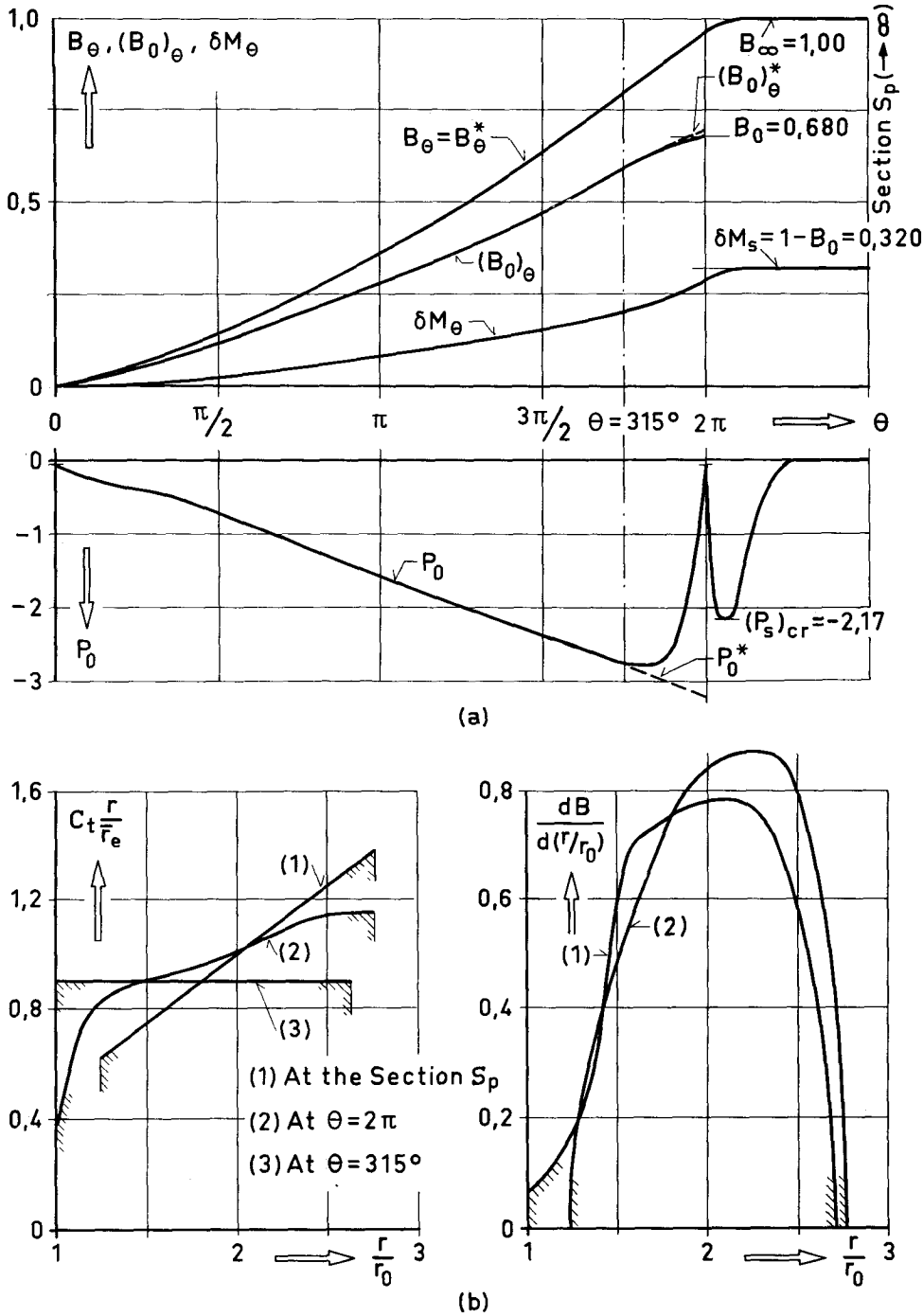

Fig. 2.52. Flow formation through the three-dimensional model for $C_{r_0} = \text{const.}$; a) distributions of P_0 and B_0 along S_0 and distributions of B_θ, δM_θ vs. θ; b) distributions of the velocity-moment $(C_t r)$ and the B of the fluid passing the transition zone of the spiral.

Fig. 2.52a shows the distribution of the additional torque δM_θ along the spiral, and also the moment of momentum $(B_0)_\theta$ and the static pressure P_0 along S_0. Fig. 2.52b shows the distribution of the moment of momentum per unit mass of the fluid, and of B_θ (B_∞ for the section S_p), along the meridian sections at $\theta = 315°$ and 2π, and along S_p. We immediately see in these diagrams that, as with the Archimedes' spiral, similarly the examined three-dimensional casing forms a *spiroid diffuser* in the case of turbines; also, that the main part of the flow transformation from parallel to spiral occurs before the section at $\theta = 2\pi$, whereas the moment of momentum remains, up to this section, practically unchangeable ($B_{2\pi} = 0{,}967$, therefore $B_\infty - B_{2\pi} = 0{,}033$).

2.3.3. Measurements for C_{r_0} Variable along S_0. The Quasi-Logarithmic Law (General Expression)

In order to complete our investigation we made some measurements for C_{r_0} variable along S_0 with the three-dimensional model. For this purpose we followed the procedure already stated in § 2.2.3. Fig. 2.53 shows the experimental C_{t_0}-distribution (points with dotted line through them), when the boundary condition on S_0 was adjusted to be

$$C_{r_0} = \bar{C}_{r_0}(1 + 0{,}25 \sin\theta)$$

(in this model $\bar{C}_{r_0} = S_p/S_0 = 0{,}74$; see Eq. (2.14.1)).

Assuming that the quasi-logarithmic law (2.27),

$$c_t r = \frac{\partial \phi}{\partial \theta} = \lambda f(\theta), \tag{2.27}$$

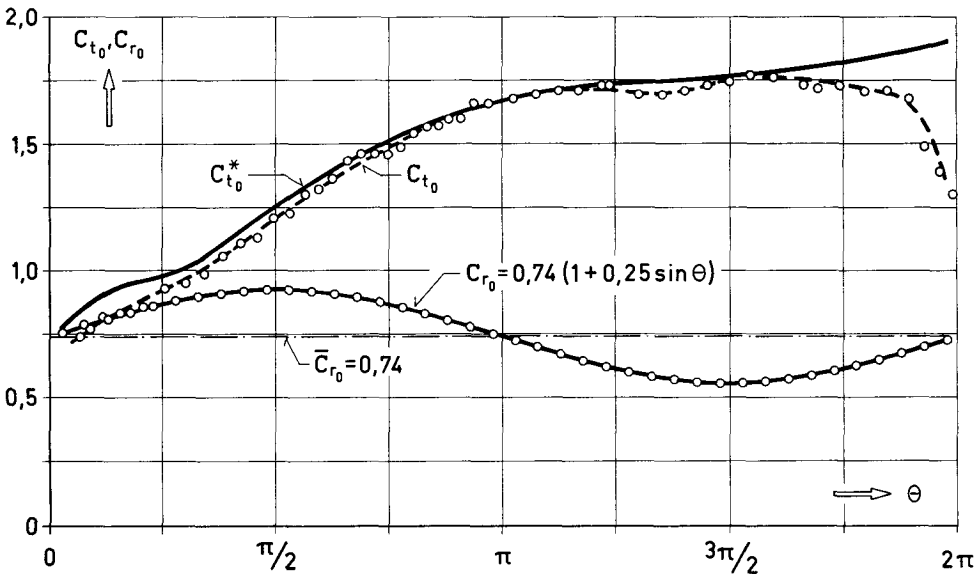

Fig. 2.53. Three-dimensional model: C_{t_0}-distribution for boundary condition $C_{r_0} = 0{,}74\,(1 + 0{,}25 \sin\theta)$.

could be valid in some region of the examined spiral, and introducing again the index * over C_t etc., we may write

$$C_t^* r = C_{t_0}^* r_0 = \lambda^* f(\theta). \tag{2.84}$$

Consequently, the fluid volume Q_θ^* passing per unit time through a segment of the surface S_0 between 0 and $\theta \leqq 2\pi$ (see Fig. 2.50) is

$$Q_\theta^* = \int_{r_0}^{r_s} c_t^* h \, d r = \int_0^\theta c_{r_0} h_0 r_0 \, d\theta.$$

Hence, using Eqs. (2.84) we obtain

$$C_{t_0}^*(\theta) = \frac{h}{H_s} \int_0^\theta C_{r_0} d\theta. \tag{2.85}$$

Accordingly

$$\operatorname{tg} \alpha_0^*(\theta) = \frac{C_{r_0}}{C_{t_0}^*} = \frac{H_s}{h_0} \frac{C_{r_0}}{\int_0^\theta C_{r_0} d\theta} \tag{2.86}$$

and

$$C_t^*(r, \theta) = \frac{r_0}{r} \frac{h_0}{H_s} \int_0^\theta C_{r_0} d\theta. \tag{2.87}$$

The solid line in Fig. 2.53 shows the C_t^*-distribution obtained by means of Eq. (2.85). We immediately see that this relationship also applies here for $\theta \leqq 315°$. For $\theta > 315°$ the C_{t_0} decreases first gradually and then rapidly until it obtains the value 0,74 at $\theta = 2\pi$. Hence the *quasi-logarithmic law* is exact in the region $\theta \leqq 315°$; in the region $315° < \theta < 2\pi$ it may be assumed to be tolerably exact, with the exception of points near S_0. The *general expression* of this law according to Eqs. (2.85) and (2.87), is

$$C_t \frac{r}{r_0} = \frac{h_0}{H_s} \int_0^\theta C_{r_0} d\theta. \tag{2.88}$$

We can easily show that the previously found laws (2.71) and (2.57) are particular cases of the law (2.88).

Hence the moment of momentum per unit mass of the fluid in a two-dimensional or a three-dimensional spiral casing of usual form remains constant along a meridian section if the relative variation of C_{r_0} along S_0 does not exceed a value, e. g. ± 25 per cent of $\bar{C}_{r_0}$. In a given spiral form the value of $C_t r / r_0$ is a function of the azimuth θ of the section and of the C_{r_0}-distribution.

Following the same method mentioned in the preceding section to determine the $\bar{C}_r^*(r, \theta)$, $\operatorname{tg} \bar{\alpha}^*$, etc., we obtain

$$\bar{C}_r^*(r, \theta) = \frac{r_0}{r} \frac{h_0}{h_r} \frac{d T}{d \theta}, \tag{2.89}$$

(see also Eq. (2.74)),

$$\operatorname{tg}\bar{\alpha}^*(r,\theta) = \frac{C_r^*}{C_t^*} = \frac{H_s}{h_r}\frac{1}{\int_0^\theta C_{r_0}\,d\theta}\frac{dT}{d\theta}, \tag{2.90}$$

(see also Eq. (2.75)),

$$K_r^*(r,\theta) \equiv \frac{Q_r^*}{Q_0} = \frac{r_0 h_0}{S_p} T(r,\theta), \tag{2.91}$$

where

$$T(r,\theta) = \frac{H_{rs}}{H_s}\int_0^\theta C_{r_0}\,d\theta. \tag{2.92}$$

It is obvious that the functions $T_1(r,\theta)$, $T_2(r,\theta)$ and $T_3(r,\theta)$, introduced in the preceding sections (see Eqs. (2.37), (2.61) and (2.73)) are particular cases of the general relationship (2.92).

PART III

Evaluation of the Experimental Results

The experimental investigation with spiral models mentioned in the preceding Part II, led us to formulate the quasi-logarithmic law (2.88). In this Part we use this general law in order to give some suggestions for the design of spiral casings and fixed blades for turbines and pumps. The problem is examined from the point of view of potential flow and, especially, for normal running conditions. However we thought it advisable to make a brief examination of some flow peculiarities occuring when turbines or pumps operate under conditions other than normal, and of some additional flow peculiarities, such as the generation of vorticity, occuring in pumps and blowers. Where it appears useful we also attempt comparisons between potential flow and viscous flow.

In engineering design, possible reductions in the dimensions of a spiral casing, particularly those involving smaller space of installation needed and smaller cost, are of greatest interest. For this purpose, the possibility of such reductions and their limits, as well as the design of fixed blades, are examined.

3.1. Comparison between the Potential Flow and the Real Viscous Flow Described in § 1.1.3

As already stated, the three-dimensional electric analogy model which we used was geometrically similar to that described in § 1.1.3, with which some experiments, which are useful for our investigation, were carried out. The results of those experiments discussed in § 1.1.4, led us to conclude that the most important boundary condition along S_0 is $C_{r_0} = \text{const.}$ (see § 1.3.2) and that the irregularity of the energy losses inside the guide-vanes should be directly related to an irregular distribution of a circulation generated along the fixed blades. The latter conclusion, however, was not based on really conclusive experimental evidence, but mainly on the particular form which the velocity distribution showed. The results of our investigation of the potential flow through the model considered, for the case of $C_{r_0} = \text{const.}$, put us in a better position to discuss the complete flow phenomena. We have plotted the C_{t_0}- and C_{t_v}-distributions against θ, as shown in Fig. 3.01 a where C_{t_v} is the (dimensionless) tangential component of the velocity along S_0, if both the guide vanes and fixed blades are present, and the fluid is again

assumed to be frictionless; the numbers (1), (2), ..., (11), shown in the figure represent the fixed blades (see also Fig. 1.09). Since the vanes and the blades are equally spaced and, according to Eq. (1.18), $(c_{r_0})_n^{n+1} = \text{const.}$, it is obvious that C_{t_v} is also constant, showing perhaps only small periodic variations between successive blades. We can immediately see in this diagram that by $C_{r_0} = \text{const.}$ the spiral casing alone, i.e. without vanes, imposes upon S_0 a circulation measured on the area between the C_{t_0} and the θ-axis, and that the form of C_{t_0} gives the distribution of this circulation along S_0 (see § 2.2.3 b)). On the other hand, the presence of the fixed blades and guide vanes results in reducing the above circulation and in giving a uniform distribution of it along S_0, as shown by the velocity C_{t_v}. The difference between these circulations is measured

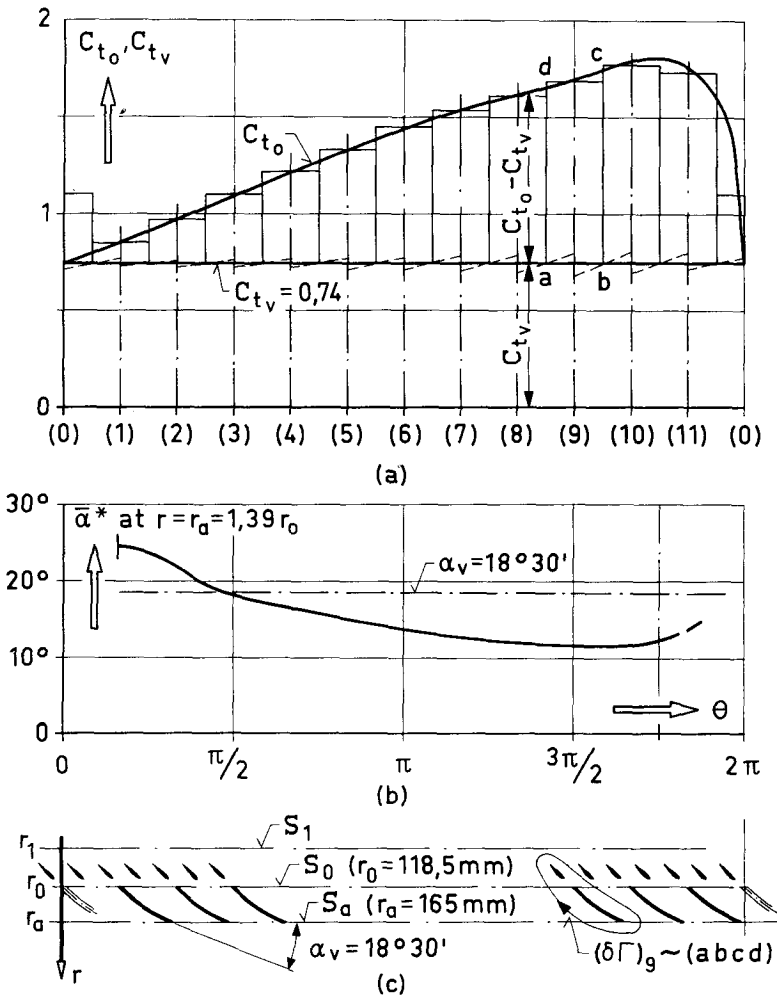

Fig. 3.01. Potential flow through the spiral casing shown in Fig. 1.09; a) distribution of the part of the circulation along S_0 which must be substructed from the fluid by means of the fixed blades in order to obtain $C_{t_0} = C_{tv} = C_{r_0}$ (guide vanes inclination $\alpha = 45°$); b) distribution of the mean angle $\bar{\alpha}$ along S_a when the fixed-blades are remouved.

over the area included between C_{t_0} and C_{t_v}. Obviously this circulation-difference is generated and distributed along the fixed blades and the guide vanes; the rectangle ($a\,b\,c\,d$), for example, represents the part of the circulation generated on the (9)-fixed blade. (Because of this, the velocity C_{t_v} should, in fact, have a periodic form from blade to blade, as shown by the dotted lines.) As we see, the intensity of the circulation generated on the fixed blades changes from blade to blade. Fig. 3.01 b shows the distribution of the angle $\bar{\alpha}^*$ along the surface S_a ($r_a = 165$ mm) when the fixed blades are removed; $\bar{\alpha}^*$ is calculated according to Eq. (2.75); $\alpha_v = 18^\circ 30'$ is the inclination of the fixed blades leading edge at S_a. Even if the angle difference $\alpha_v - \bar{\alpha}^*$ does not constitute the angle of attack of the blades, it nevertheless gives an idea of the flow irregularity imposed by the fixed blades along the spiral. Further, the unrolled picture of the blade region, shown in Fig. 3.01 c, convays a good idea of the generation of the circulation along the blades. (From one point-of-view, this picture is similar to the conformal representation of the two-dimensional casings.) Comparing the above distribution of the circulation along the fixed blades with the distribution of the maxima of the energy losses of the air shown in Fig. 1.12, we can immediately observe that both show the same form; the more intensive the circulation, the bigger the energy loss. Hence the hypothesis mentioned in § 1.1.4 should be true; the irregularity of the energy losses of a real fluid (air) observed along S_0 and the excessively high values of these losses in some places, are mainly due to a turbulence within the fixed-blade region because of different angles of attack encountered by the various fixed blades. This angle is a function of fixed-blade and guide-vane geometry and of the value of the circulation generated along each blade as shown in Fig. 3.01 a.

Returning to our frictionless fluid, we can calculate its dynamical reaction on the spiral and the fixed blades as an assembly, by the relationship

$$(\delta M_v)_s = 1 - B_v, \tag{2.93}$$

where

$$B_v = \frac{1}{2\pi} \frac{S_0}{S_p} \frac{r_0}{\bar{r}_e} \int_0^{2\pi} C_{r_0} C_{t_v} d\theta = \frac{r_0}{\bar{r}_e} C_{t_v}$$

is the moment of momentum of the fluid passing per unit time through S_0 when the blades are present. Since $r_0/\bar{r}_e = 0{,}5$ and $C_{t_v} = 0{,}74$, we obtain

$$B_v = 0{,}370$$

and

$$(\delta M_v)_s = 0{,}630,$$

whereas when the fixed blades are removed, $\delta M_s = 0{,}320$ (see Fig. 2.52 a). By reducing the original circulation of the fluid along S_0 the fixed-blade assembly acts as a strong *spiroid diffuser*.

3.2. General Considerations on Spiral-Casing Design

3.2.1. Boundary Conditions along S_0 and Spiral Form

The experimental investigation described and discussed in the sections 2.2 and 2.3 led us to conclude that the potential flow through spiral casings follows the generalized law (2.88), particular cases of which are the laws (2.40) and

(2.71) concerning the condition $c_{r_0} = \text{const.}$ in two-dimensional and three-dimensional casings respectively. On the other hand, it has been already mentioned in § 1.1.2 and § 1.1.3 that the *runner* of a turbine, or even the guide-vane assembly alone, as well as the *impeller* of a pump or blower, constitutes a rectifier of the flow passing through. Further, because of the uniformity of the vanes of the wheel (runner or impeller) and of the stability of its rotational movement, the wheel tends also to keep the tangential component c_{t_w} of the velocity constant along S_0 [1]). Hence, the wheel tends to impose upon S_0 the conditions

$$c_{r_0} = \text{const.}$$
$$c_{t_w} = \text{const.},$$

where

$$\frac{c_{r_0}}{c_{t_w}} = \operatorname{tg} \alpha_w = \text{const.} \quad (\alpha_w = \text{const.});$$

the angle α_w [2]) refers to the normal running conditions of the wheel. In the case of an actual viscous fluid, c_{r_0}, c_{t_w} and consequently α_w represent mean values in the z-direction; that is, on the generatrices of S_0. Returning now to our frictionless fluid, let us use the dimensionless expressions C_{r_0}, C_{t_w} of c_{r_0}, c_{t_w}. To obtain a perfect co-ordination between the wheel, which imposes the condition $(C_{r_0}, C_{t_w}, \alpha_w)$ from the inside on S_0, and the spiral casing, which imposes the condition $(C_{r_0}, C_{t_0}, \alpha_0)$ from the outside on S_0 we must design the latter in such a way as to get

$$C_{t_0} \equiv C_{t_w} \ (= \text{const.})$$
$$\alpha_0 \equiv \alpha_w \ (= \text{const.})$$

along S_0. The particular expressions (2.40) and (2.71) of the general law (2.88) make it possible to attain the above identities, because they connect the boundary condition C_{r_0}, along S_0, with the distribution of C_t by means of the geometrical form of the spiral; viz. it is possible to design convenient casing forms and fixed-blade shapes.

It is obvious that, in the case of the actual viscous fluid (turbines, pumps) in which the laws (2.40) and (2.71) are first approximations, a spiral so-designed can secure only an approximate identification between C_{t_0} and C_{t_w}. The same is true in the case of blowers, in which the fluid is, additionally, compressible. Nevertheless, the experimental results described in § 1.1.3 and discussed in § 3.1 led us to conclude that the main cause governing the motion of a fluid through a spiral casing should be the potential one, at least for fluids of low viscosity. Therefore, the design of a spiral according to potential flow, i.e. according to Eqs. (2.40) or (2.71), can be used as a *fundamental* design, to which further minor corrections may be made, having regard to friction and compressibility.

Let us now examine the two-dimensional and three-dimensional casings separately.

---

[1]) We shall see later that this is not absolutely true for pumps or blowers, especially when the number of impeller vanes is small.

[2]) In the literature on pumps and blowers, α_w is the angle between the absolute velocity c_0 and the surface S_0, where $\vec{c}_0 = \vec{u} + \vec{w}_0$; $\vec{u}$ is the velocity of the vane trailing-edge and $\vec{w}_0$ the mean relative velocity of the fluid passing through S_0, tangential to the vane surface at its trailing edge.

Two-dimensional spiral casings: By means of Eq. (2.40),

$$C_t \frac{r}{r_0} = \frac{C_{r_0}}{\ln \frac{r_s}{r_0}} \theta, \tag{2.40}$$

we obtain

$$C_{t_0} = \frac{C_{r_0}}{\ln \frac{r_s}{r_0}} \theta = C_{t_w} = \frac{C_{r_0}}{\operatorname{tg} \alpha_w}.$$

Therefore

$$\ln \frac{r_s}{r_0} = \theta \operatorname{tg} \alpha_w,$$

and

$$\frac{r}{r_0} = e^{\theta \operatorname{tg} \alpha_w}; \tag{3.01}$$

accordingly, the shape of the casing must be a *logarithmic spiral.* In the experimental investigation mentioned in § 2.2.2a), we found that, if the logarithmic form is extended a little further than 2π, e.g. up to $\theta \approx 390°$, the potential flow in the region $\theta \leqq 2\pi$ is purely logarithmic, with the exception of a small region ($r > 2r_0, 300 < \theta < 2\pi$), where a deviation begins; this deviation, however, is negligible, since its maximum, occuring at ($r_s, 2\pi$) is only $-9{,}5$ per cent. A picture of the flow-formation is given in Figs. 2.30 and 2.31b. The moment of momentum and the dynamical reaction of the fluid through a logarithmic casing formed in this manner are discussed in § 2.2.2 at d).

Three-dimensional spiral casings: In a symmetrical casing, by using Eq. (2.71),

$$C_t \frac{r}{r_0} = \frac{h_0}{H_s} C_{r_0} \theta, \tag{2.71}$$

we obtain

$$C_{t_0} = \frac{h_0}{H_s} C_{r_0} \theta = C_{t_w} = \frac{C_{r_0}}{\operatorname{tg} \alpha_w}.$$

Hence

$$\frac{H_s}{h_0} = \theta \operatorname{tg} \alpha_w \tag{3.02}$$

where

$$H_s = \int_{r_0}^{r_s} \frac{h}{r} dr, \quad (\text{at } \theta),$$

(see Eq. (2.67) and Fig. 2.50). The graph of H_s/h_0 vs. θ is a straight line at an angle α_w with respect to the θ-axis. At $\theta = 0$, $H_s(0) = 0$; at $\theta = 2\pi$,

$$H_s(2\pi) = 2\pi h_0 \operatorname{tg} \alpha_w.$$

Eq. (3.01) is a particular case of Eq. (3.02), where $h = h_0$. Therefore, for α_w given, Eq. (3.01) forms a single-valued function of r_s with respect to θ, whereas Eq. (3.02) is more complicated.

3.2.2. Significance of Eq. (3.02) in Spiral Casing Design

The identity $C_{t_0} \equiv C_{t_w}$, which is the desired condition along S_0, and the experimentally found law (2.71), led us to express the geometrical relationship (3.02),

$$\frac{H_s}{h_0} = \theta \operatorname{tg} \alpha_w, \tag{3.02}$$

concerning the spiral casing form. Therefore Eq. (3.02) is a *necessary* condition. To establish the validity of the law (2.71) and consequently, of the identily $C_{t_0} \equiv C_{t_w}$ when Eq. (3.02) is satisfied, we must show under what geometrical conditions Eq. (3.02) also represents a *sufficient* condition. As we see immediately, for θ constant Eq. (3.02) can be satisfied by an infinity of meridian section forms; viz. Eq. (3.02) does not constitute a single-valued function of the meridian section form as is the case of Eq. (3.01). For this purpose it is preferable to keep the form of the meridian sections similar as θ increases, or more generally, to avoid sudden local changes in the curvature of the casing walls as much as possible. For example, the three-dimensional casing we examined shows a sudden change of wall curvature in the region $30° < \theta < 60°$ (see Fig. 2.04); we accordingly observe in Fig. 2.49 b that in the same region a deviation occurs between the experimentally obtained values C_{t_0} and the values $C_{t_0}^*$ which are calculated by means of the law (2.71).

From the experimental results mentioned and discussed in § 2.2.2 b) and § 2.3.2 we concluded that, in a spiral other than one satisfying Eq. (3.02) the laws (2.40) and (2.71) cannot be valid in the entire region $0 \leqq \theta \leqq 2\pi$. However, it may apply in a large part of this region; e.g., in the above-mentioned models, the validity of the laws (2.40) and (2.71) ranges from $\theta = 0$ to $\theta \approx 315°$. In the remaining small region near $\theta = 2\pi$, the laws are approximately valid. It is however logical to say that, as long as the spiral form tends to satisfy Eq. (3.02), the region of the validity of the laws (2.40) and (2.71) (consequently the desired condition $C_{t_0} = \text{const.}$) tends to be extended up to $\theta = 2\pi$. We found this to be true for a logarithmic spiral (two-dimensional) as shown in Fig. 2.31 b; we shall prove later in this section that it is also true for three-dimensional casings. In order to keep the flow transition zone out of the region $0 \leqq \theta \leqq 2\pi$ (see Figs. 2.31, 2.34 and 2.49) it is useful to extend the spiral form given by Eq. (3.02) slightly past $\theta = 2\pi$, e.g., up to $\theta = 370°$—$390°$; also to incline the inlet (or discharge) pipe at an angle $100°$—$120°$ with respect to the $\theta = 0$ axis. The region of validity of the quasi-logarithmic law, and consequently of Eq. (3.02), is limited at $\theta = 2\pi$. We may, however, attain the above extension beyond 2π by keeping the same lower limit of the integral (3.02), i.e. the r_0, and the geometric similarity of the meridian section forms; in the actual drawing of the casing a suitable curvature of the wall must be provided to close the spiral in the outside part of the tongue diaphragm.

a) Experimental Verification: Potential Flow through a Three-Dimensional Archimedes' Model

To show experimentally the validity of the law (2.71) in the entire region $0 \leqq \theta \leqq 2\pi$ when Eq. (3.02) is extended to $2\pi^+$ and the above-stated geometrical conditions are fulfilled, we used the Archimedes' model shown in Fig. 2.02 after transforming it to three-dimensional. This transformation is handled as follows:

Consider a three-dimensional spiral casing, symmetrical to a plane perpendicular to the z-axis, included between two co-axial cones, the surface S_0, and a cylindrical surface S_s whose generatrix is parallel to the z-axis (see

Fig. 3.02). Thus, in any meridian section at azimuth θ of this casing we have

$$\frac{h}{h_0} = \frac{r}{r_0}.$$

Hence, according to the definition of H_s (see Eq. (2.67)),

$$\frac{H_s}{h_0} = \int_{r_0}^{r_s} \frac{r}{r_0} \frac{dr}{r} = \frac{r_s}{r_0} - 1.$$

To satisfy Eq. (3.02), therefore, we must have,

$$\frac{H_s}{h_0} = \frac{r_s}{r_0} - 1 = \theta \operatorname{tg} \alpha_w;$$

thus,

$$r_s = r_0 + r_0 \theta \operatorname{tg} \alpha_w, \quad (\alpha_w = \text{const.}).$$

This means, the intersection of S_s and a plane normal to the z-axis is an *Archimedes' spiral*, the *constant* τ of which is

$$\tau = r_0 \operatorname{tg} \alpha_w.$$

According to the law (2.71), where $C_{r_0} = \text{const.}$, we obtain along S_0[3]),

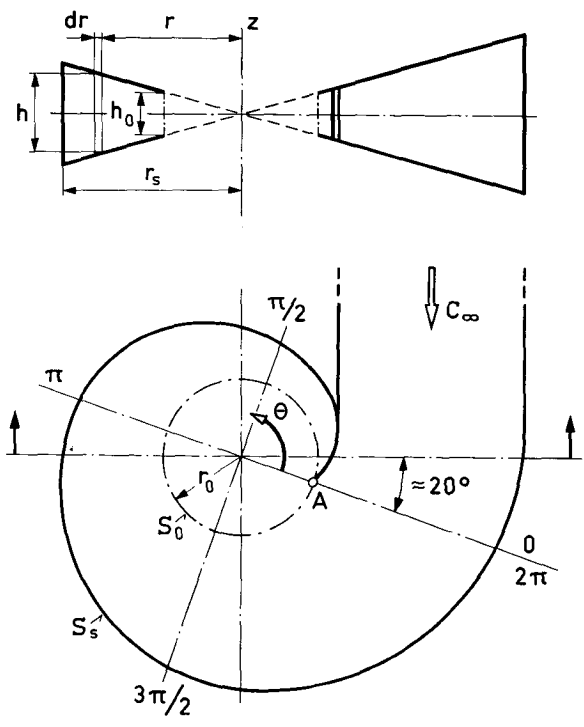

Fig. 3.02.

[3]) We should note here that the flow on S_0 is no longer two-dimensional; for C_{r_0}, we therefore use the mean value on the z-direction.

$$C_{t_0} = \frac{\theta C_{r_0}}{\theta \operatorname{tg} \alpha_w} = \frac{C_{r_0}}{\operatorname{tg} \alpha_w} = \text{const.}$$

For the three-dimensional experiments, we installed, on the Archimedes' model shown in Fig. 2.02, a conical bottom with an inclination

$$\frac{h_0/2}{r_0} = \frac{17{,}5 \text{ mm}}{75{,}0 \text{ mm}} = 0{,}233.$$

This bottom extended from $\theta = 0$ to $\theta = 379^\circ 10'$ and from there up to the P-electrode as a plane with the same inclination. So, the ratio of the surfaces $S_0 = 2\pi r_0 h_0$ and S_p (surface of the P-electrode) was

$$\frac{S_0}{S_p} = \frac{163 \text{ cm}^2}{160{,}4 \text{ cm}^2} = \frac{1}{0{,}973}.$$

Thus,

$$C_{r_0} = \frac{c_{r_0}}{c_\infty} = \frac{S_p}{S_0} = 0{,}973.$$

According to Eq. (2.02.1), on the other hand, we put

$$\operatorname{tg} \alpha_w = \frac{\tau}{r_0} = \operatorname{tg} \alpha_s(0) = 0{,}4053.$$

Hence, the value of C_{t_0} must be

$$C_{t_0} = \frac{C_{r_0}}{\operatorname{tg} \alpha_w} = \frac{0{,}973}{0{,}4052} = 2{,}400;$$

and

$$C_t = 2{,}40 \frac{r_0}{r}.$$

Fig. 3.03 shows the results obtained (experimental points) using the electric analogy method and the same procedure as in the preceding experiments. We can immediately see that the validity of the law (2.71) (solid straight lines) is extended here not only to $\theta = 2\pi$ but further up to the entrance section at $\theta = 379^\circ 10'$; the *transition zone* is out of the region $0 \leqq \theta \leqq 2\pi$. This experiment verifies the above-mentioned hypothesis, according to which, if in a three-dimensional spiral casing Eq. (3.02) is satisfied in the region from $\theta = 0$ to θ somewhat greater than 2π, the law

$$C_t \frac{r}{r_0} = \text{const.}, \quad r_0 \leqq r \leqq r_s,$$

is valid at least up to $\theta = 2\pi$.

Comparison between Eqs. (1.14) and (3.02): By means of the above experiment we proved that the fulfilment of Eq. (3.02) from $\theta = 0$ to $\theta = 2\pi^+$ will supply the desired condition $C_{t_0} = \text{const.}$ along S_0 with suitable consideration given to the geometrical form as already mentioned in this section. Hence, Eq. (3.02) constitutes an experimentally-found geometrical relationship, which is *necessary* and *sufficient* to obtain

$$C_{t_0} \equiv C_{t_w}$$

along S_0. Comparing Eq. (3.02) with Eq. (1.14) which we theoretically found in § 1.1.2, we see that both express one and the same geometrical condition. The origin of Eq. (3.02), nevertheless, is much *more general* than that of Eq. (1.14), for Eq. (3.02) is derived from the general experimental law (2.88) and is *necessary* and *sufficient* to identify C_{t_0} with C_{t_w}, whereas Eq. (1.14) was found to be only a *necessary* condition derived from an axially symmetric flow. By means of the law (2.88), we found that, to secure $C_{t_0} \equiv C_{t_w}$ along S_0 when $C_{r_0} = \text{const.}$, it is not necessary to pre-determine an axially symmetric flow, to choose one particular stream surface as a boundary, and to extend this surface to *infinity* in the θ direction, which, furthermore, cannot be put into practice. It suffices to satisfy Eq. (3.02) in the region $0 \leqq \theta \leqq 2\pi^+$ taking into account the geometrical conditions prohibiting sudden local changes of the wall curvature; from now on, we shall express all these conditions simply by saying, the casing is designed *according* to Eq. (3.02).

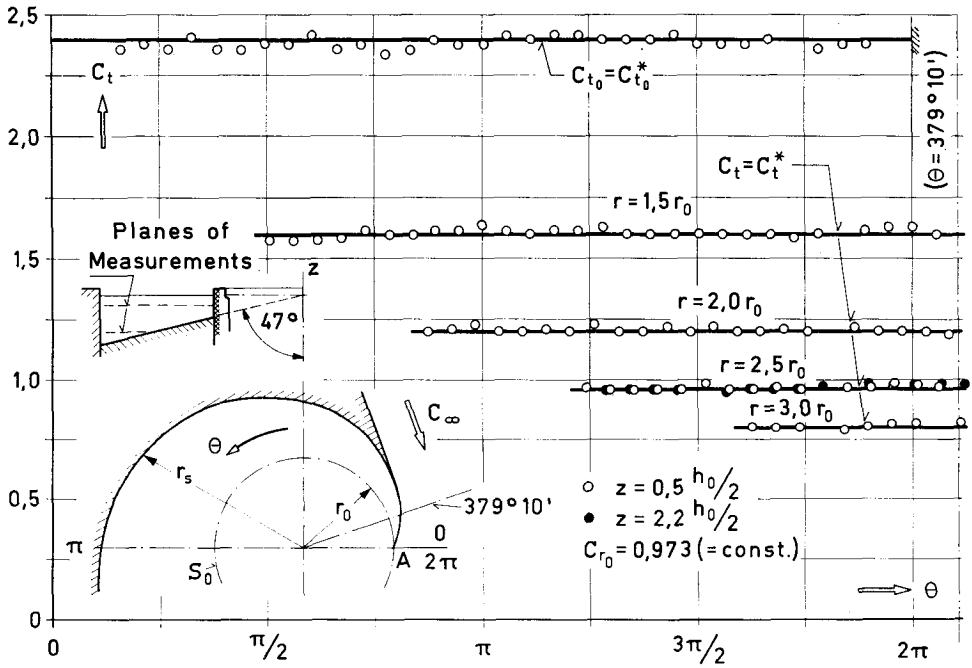

Fig. 3.03. Three-dimensional Archimedes' model; C_t-distribution for $C_{r_0} = \text{const}$. In the region $\theta = 0$ to 379° 10′ the model is according to the relations $h/h_0 = r/r_0$ and $r_s = r_0 + \tau\theta$, where $\tau = \text{const}$.

b) Moment of Momentum and Dynamical Reaction of the Fluid

The moments of momentum $(B_0)_\theta$, B_0 and B_θ of the fluid passing through a casing designed according to Eq. (3.02) are

$$(B_0)_\theta = B_\theta = \frac{1}{2\pi}\frac{r_0}{r_e}\frac{C_{r_0}}{\operatorname{tg}\alpha_w}\theta, \quad (0 \leqq \theta \leqq 2\pi), \tag{3.03}$$

(see Eqs. (2.81) and (2.82)),

and $$B_0 = \frac{r_0}{\bar{r}_e} \frac{C_{r_0}}{\operatorname{tg} \alpha_w}, \quad (\theta = 2\pi), \tag{3.03.1}$$

(see Eqs. (2.78)),

where $$\bar{r}_e = \frac{1}{S_p} \int_{min\, r_e}^{max\, r_e} h\, r_e\, d\, r,$$

The dynamical reaction δM_θ of the fluid at θ is

$$\delta M_\theta = B_\theta - (B_0)_\theta = 0, \quad (0 \leqq \theta \leqq 2\pi), \tag{3.04}$$

and the *total*, δM_s, is

$$\delta M_s = 1 - B_0 = 1 - \frac{r_0}{\bar{r}_e} \frac{C_{r_0}}{\operatorname{tg} \alpha_w}. \tag{3.04.1}$$

Hence the dynamical reaction δM_s is distributed in the transition zone only. In the region $\theta \leqq 2\pi$ the fluid has no additional reaction. The flow of a frictionless fluid through a spiral casing designed according to Eq. (3.02) is a *natural spiral flow;* such a spiral is a *natural spiral* (see § 2.2.2 at d)).

c) Meridian-Section Forms

Let us write Eq. (3.02) in a more convenient dimensionless form as follows

$$\frac{H_s}{h_0} = \frac{r_0}{h_0} \int_1^{r_s/r_0} \frac{h}{r} d\left(\frac{r}{r_0}\right) = \theta \operatorname{tg} \alpha_w. \tag{3.02.1}$$

We see from this expression that, if the ratio r_0/h_0 is given, then, as the angle α_w increases, either or both of the rations h/r, r_s/r_0 must also increase. Hence by keeping the geometrical similarity of the meridian section form vs. θ, we obtain an increase of r_s/r_0, for the same θ, as α_w increases. As an example, let us consider our three-dimensional casing, shown in Fig. 2.04 and the related Table I, whose H_s/h_0-curve vs. θ is not at all according to Eq. (3.02), as shown in Fig. 1.10a. If we try to modify this casing so as to satisfy Eq. (3.02) by keeping its circular meridian section form, and r'_s, d'_0 constant, we obtain a considerable increase in the diameter d_s and the radius r_s; thus, according to Eq. (3.02) we obtain $d_s = 329{,}5$ mm and $r_s = 494$ mm at $\theta = 2\pi$, whereas the original values are at the same angle 168 mm and 320,8 mm respectively (see Table I).

In order to reduce the ratio r_s/r_0 vs. θ, and thus save space and material (the latter is a compromise regarding strength-of-material considerations, manufacturing facilities, etc.), we may increase h. This increase is particularly favourable in the region near S_0, where r is relatively small, and can be obtained by reducing the ratio r'_s/r_0. We should note, however, that, even though this suggestion can be applied to the turbine spirals with almost no difficulty because of the acceleration of the fluid, we must be very careful with the spirals of pumps or blowers, since, in such a case, a sudden divergence of the walls outside S_0 could introduce an abnormal increase of the

boundary-layer thickness, and, accordingly, high energy losses in the case of a real viscous fluid.

Some meridian-section forms calculated according to Eq. (3.02.1) for $h_0/r_0 = 0{,}195$ and $\alpha_w = 45°$, which are the boundary characteristics of the model shown in Fig. 2.04, are given for comparison in *Table VI*. We observe that, among the four types of meridian forms given, the spiral with elliptic section needs the smallest space for its installation and, most probably, the smallest amount of material. We notice, nevertheless, that even this type of section

Table VI. Meridian Section Forms according to Eq. (3.02.1) for $h_0/r_0 = 0{,}195$ and $\alpha_w = 45°$

Section Form [4]	$\frac{r'_s}{r_0}$	$\frac{S_p}{S_0}$ [5]	θ	$\frac{H_s}{h_0}$	$\frac{d_s}{r_0}$	$\frac{r_r}{r_0}$
1. Circular	0,53	2,72	π	π	1,72	3,04
			2π	2π	2,78	4,17
2. Circular	0,10	2,37	π	π	1,63	2,68
			2π	2π	2,60	3,67
3. Half-circular	0,10	2,37	π	π	1,70	2,47
			2π	2π	2,60	3,32
4. Elliptic	0,10	2,08	π	π	1,91 (1,28)	2,35
			2π	2π	2,98 (1,99)	3,07

[4]) The drawings of the four sections shown in this table are to the same scale and give an idea of their relative form at $\theta = 2\pi$.

[5]) $S_0 = 2\pi r_0 h_0$; the pipe cross-section S_p is assumed to be equal to $\pi/4\, d_s^2$ at $\theta = 2\pi$ (for the elliptic section the area corresponds to the area of the ellipse at $\theta = 2\pi$). Thus $C_{r_0} = S_p/S_0$.

has a rather high value of the ratio S_p/S_0. Some additional recommendations, important for the design of spiral casings, are given in § 3.2.4.

d) Some Notes on the Boundary Conditions along S_0. Operating Conditions other than Normal

The spiral-casing design according to Eq. (3.02) is based on the assumption that C_{r_0} is constant along S_0. However, this assumption is not absolutely true, even if the fluid is frictionless and the turbine, pump or blower, operates under normal conditions.

Let us first examine the case of turbines, where fixed blades do not exist. Here, when the turbine operates under normal conditions and the guide-vane *camber lines* are arcs of logarithmic spirals with angle α_w a small periodic change of C_{r_0} along S_0 occurs, because of the thickness of the vanes. This irregularity is observable in the leading edge region of every blade. Since the C_{r_0}-distribution is the boundary condition of the potential flow through the casing, a periodic change also appears in the C_t-distribution; obviously the changes of C_{r_0}, due to this cause, are rather small. To obtain an idea of the influence of the thickness of the vanes on the C_t-distribution, we can apply the law (2.88),

$$C_t \frac{r}{r_0} = \frac{h_0}{H_s} \int_0^{\theta} C_{r_0} \, d\theta , \tag{2.88}$$

by putting

$$H_s = h_0 \theta \operatorname{tg} \alpha_w$$

and

$$C_{r_0} = \bar{C}_{r_0} (1 - \beta \cos (N_v \theta)) , \tag{3.05}$$

where N_v is the number of guide vanes, and β a constant. In general $0 < \beta \ll 1$ e.g., $\beta \approx 0{,}1$ (the vanes do not touch S_0). As the vanes become thicker, β increases; for vanes with zero thickness $\beta = 0$.

Suppose that the turbine does not operate under normal conditions. The guide vanes now have another inclination α'_w with respect to S_0 ($\alpha'_w \neq \alpha_w$), and therefore impose upon S_0 a tangential component C'_{t_w} of the velocity different from the C_{t_w}, since by definition $\bar{C}_{r_0}$ remains invariant; viz.,

$$C'_{t_w} = \frac{\bar{C}_{r_0}}{\operatorname{tg} \alpha'_w} \neq C_{t_w} .$$

On the other hand, the spiral casing tends to keep the value C_{t_w} invariant along S_0. The result is the generation of a circulation around every vane, which can be measured by the expression

$$(C'_{t_w} - C_{tw}) \frac{2 \pi r_0}{N_v} ,$$

where $C_{t_0} \equiv C_{t_w} = \bar{C}_{r_0} / \operatorname{tg} \alpha_w$ (see section 3.1 and the related Fig. 3.01; in this figure C_{t_v} is the same as C_{t_w}). Now the velocity C_{r_0} shows larger periodic changes; the same is also true for C'_{t_w} according to the law (2.88). The boundary condition along S_0 could again be represented by means of Eq. (3.05), with a possible phase difference because of the displacement of the vane fronts. In this case, the value of β must be larger. As the angle difference $|\alpha'_w - \alpha_w|$

increases, β also increases, approaching or even exceeding one. As already mentioned in § 1.1.4 and in section 3.1, when $|\alpha'_w - \alpha_w|$ exceeds a specified limit a turbulance can occur in the region of the guide vanes in the case of an actual viscous fluid; the result, then, is an additional increase of energy losses and possibly hydraulic shoch on the vanes of the runner.

Let us now consider the case of pumps and blowers in which the problem appears to be more complicated. In usual types there are neither guide vanes nor fixed blades provided; we choose, therefore, the surface S_0 to surround the impeller. Here, because of the limited number of impeller vanes, the flow passing through S_0 is no longer stationary even if the casing is designed according to Eq. (3.02) and the impeller runs under normal conditions. The rotating impeller imposes a *centrifugal spiral motion* to the fluid as its main motion and, in addition, a secondary *circulatory motion* within the vane passages in a direction opposite to that of the impeller rotation (we always speak about frictionless fluids; see also refs. [9], [16] and [21]). It is obvious that C_{r_0} and C_{t_w} are not constant in the interval of a vane passage, and since the impeller rotates, the boundary condition along S_0 is *not* stationary. The fluid, on the other hand, *tends* to satisfy *Kutta-Joukowski*'s condition on the trailing edges of the vanes with respect to a system fixed with the impeller (relative motion of the fluid). Hence, every vane edge is a source of continuous generation of *vortices*, which escape into the spiral casing and are washed into the discharge pipe with the fluid; consequently, there is no potential flow through a pump casing or blower casing, except in the ideal case in which the impeller has an infinite number of equally spaced vanes. It is, however, true that, when the number of the impeller vanes is not extremely low, the above vorticity is rather small and the flow can be assumed *quasi-potential.*

If we examine the circulatory motion of the fluid within a vane passage, we see that its effect is always to increase the angle α_w since the mean value $\bar{C}_{r_0}$ remains invariant. The mean periodic value $\bar{\alpha}_w$ on S_0 caused by the impeller can be expressed as

$$\bar{\alpha}_w = \alpha_w + \delta\alpha_w,$$

where $\delta\alpha_w > 0$ and, in general, $\delta\alpha_w \ll \alpha_w$. It therefore seems, that if we were to insert the angle $\bar{\alpha}_w$ instead of α_w into Eq. (3.02), the vorticity which escapes into the casing could be reduced. The determination of the angle $\delta\alpha_w$, principally dependent on the impeller design, is outside the scope of the present investigation.

Suppose now that the pump or blower does not operate under its normal conditions. The fluid tends to impose upon S_0 another mean periodic angle $\bar{\alpha}'_w$. As the angular difference $|\bar{\alpha}'_w - \bar{\alpha}_w|$ increases, so does the vorticity escaping through the casing; the flow can no longer be characterized as potential. The result, in the case of an actual viscous fluid, is an increase of the additional energy losses (see also § 3.2.3 at b)).

3.2.3. Spiral Casing Design Deviating from Eq. (3.02)

As we observe in Table VI (see § 3.2.2 at c)) even with the elliptic type of meridian section which is advantageous with respect to the space needed for the spiral, the total radial width, say in the direction of the $\theta = 0$ axis, is very

large; thus, in this type of section we obtain

$$\frac{r_s(\pi)}{r_0} + \frac{r_s(2\pi)}{r_0} = 2{,}35 + 3{,}07 = 5{,}42,$$

or, $$\text{Total Radial Width} = 5{,}42\, r_0.$$

If a further reduction of the total radial width is desired, for example when the space available for the installation of the turbine is limited, for ease of manufacturing, or for a reduction of over-all cost etc., there are two possibilities. The first, concerning a decrease of r_0 and α_w while h_0 remains constant (or another combination), which according to Eq. (3.02) could reduce r_s, is outside our scope, since it is related to the design of the runner, guide-case, etc. The second possibility, which we shall discuss, is to design the spiral-casing with $H_s(\theta)$ smaller than given by Eq. (3.02); namely

$$\frac{H_s}{h_0} < \theta \operatorname{tg} \alpha_w, \qquad (0 < \theta \leqq 2\pi^+).$$

Now, according to Eq. (2.68) (see also § 2.3.2),

$$C_{t_0}^* = \frac{h_0}{H_s} C_{r_0} \theta, \tag{2.68}$$

we obtain $$C_{t_0}^* > C_{t_w}.$$

Further, since the validity of Eq. (2.68), (i.e. $C_{t_0} = C_{t_0}^*$), does not in general extend completely to $\theta = 2\pi$, then, in the local region around $\theta = 2\pi$, $C_{t_0} < C_{t_0}^*$. The result is a change in the total value and distribution of circulation along S_0. If the wheel continues to be rectifier of the flow passing through, the difference

$$C_{t_0} - C_{t_w}$$

measures the change of the distribution of the circulation along S_0 when the spiral deviates from Eq. (3.02). From the experiments mentioned in § 1.1.3 and discussed in section 3.1., we concluded that this is true in the case of turbines; we shall discuss later how the problem appears in the case of pumps and blowers.

In order to obtain a convenient casing, which, in addition, must deviate from Eq. (3.02), it is recommended to form a smooth H_s/h_0-curve vs. θ, having at $\theta = 0$ the inclination $\operatorname{tg} \alpha_w$; i.e. the inclination given by Eq. (3.02). In this manner the value of C_{t_0} at $\theta = 0$ and $\theta = 2\pi$ is

$$C_{t_0}(0) = C_{t_w};$$

the distribution of C_{t_0} along S_0 up to about 2π can be obtained from Eq. (2.68).

The particular case $H_s \sim \theta$: Among the H_s/h_0-curves which have a predetermined value $H_s(2\pi)/h_0$ at $\theta = 2\pi$, $(H_s(2\pi) < 2\pi h_0 \operatorname{tg} \alpha_w)$, the design of the casing according to the relationship

$$\frac{H_s}{h_0} = \theta \operatorname{tg} \alpha_c, \qquad 0 < \theta_c \leqq \theta \leqq 2\pi^+, \tag{3.06}$$

where $$\operatorname{tg} \alpha_c = \frac{1}{2\pi} \frac{H_s(2\pi)}{h_0} < \operatorname{tg} \alpha_w, \qquad (\alpha_c = \text{const.} < \alpha_w),$$

seems to be *particularly* important, for, in the region between θ_c and 2π it gives a constant distribution of the velocity C_{t_0}. Thus, inserting Eq. (3.06) into Eq. (2.68) we obtain

$$C_{t_0} = C_{tc} = \frac{C_{r_0}}{\operatorname{tg} \alpha_c} = \text{const.}, \quad (C_{tc} > C_{tw}),$$

for $\theta_c \leqq \theta < 2\pi$. In the remaining region from θ_c to 0 we must deviate from Eq. (3.06) and trace a suitable curve which at $\theta = 0$ must have the inclination α_w. In general we can choose

$$\theta_c \approx 30° - 45°.$$

Between θ_c and zero, C_{t_e} begins to decrease until it obtains the value C_{t_w} at $\theta = 0$. The velocity distribution is similar on the other side of the tongue in the vicinity of the point $(r_0, 2\pi)$, where C_{t_e} decreases rapidly from $\theta < 2\pi$ and from $\theta > 2\pi$, until it becomes C_{t_w} at $(r_0, 2\pi)$. It is obvious that, in casings designed according to Eq. (3.06), the validity of the law (2.71) is extended to the meridian section at $\theta = 2\pi$ or even further, except in the vicinity of the point $(r_0, 2\pi)$. It is also evident that the flow has the same characteristics (boundary conditions, circulation, vorticity etc.) as if the casing were designed according to Eq. (3.02) but as if the wheel were running overloaded (see § 3.2.2 at d)); thus, the condition $\alpha_w > \alpha'_w$ in that case, is equivalent to the condition $\alpha_w > \alpha_c$ which we have in the present case.

Bellow we will discuss some particular problems arising in the case of turbines and pumps or blowers, in which the spiral design deviates from Eq. (3.02).

a) Turbine Spiral Casings Deviating from Eq. (3.02)

As already mentioned, the difference $(C_{t_0} - C_{t_w})$ gives the distribution of the circulation along S_0 which must be generated on the guide vanes. If the casing is designed according to Eq. (3.06), this distribution is uniform from θ_c to about 2π. In the general case in which H_s/h_0 is a smooth curve vs. θ, as for instance, the three-dimensional model we examined, Fig. 3.01 gives an idea of the circulation distribution. Thus, as θ increases, the difference $C_{t_0} - C_{t_w}$ also increases[6]); consequently, since we assume that fixed blades do not exist, a circulation of gradually increasing intensity takes place from vane to vane. In the case of an actual viscous fluid, in places where there is an intensive circulation a turbulence may appear; the result would be additional energy losses and possibly hydraulic shock on the vanes of the runner.

The particular case of low-pressure turbines: If H_s/h_0 is much smaller than $\theta \operatorname{tg} \alpha_w$, further irregularities can arise in these turbines because of the high

---

[6]) We can obtain a more detailed picture of the C_{t_0} distribution along S_0 by using the general Eq. (2.88) and by putting, for example

$$C_{r_0} = \bar{C}_{r_0}(1 - \beta \cos(N_v \theta)), \tag{3.05.1}$$

(see Eq. (3.05)), where now the coefficient β is a function of θ; in general,

$$\beta \sim (C_{t_0} - C_{t\infty}), \quad \max|\beta| < 1.$$

The value of C_{t_0} is obtained by means of Eq. (2.71) for $C_{r_0} = \bar{C}_{r_0}$. We see that, wherever the difference $(C_{t_0} - C_{tw})$ increases the amplitude of the periodic variations of C_{t_0} obtained by Eqs. (2.88) and (3.05) also increases.

values of the velocity C_0 and correspondingly low values of the static pressure P_0. Thus, as we observe in Fig. 2.37 (Archimedes' casing) and in Fig. 2.52 (three-dimensional casing) the minimum values of P_0 are $-2{,}95$ and $-3{,}23$ respectively, whereas the pressure $P_w, (P_w = 1 - C_{r_0}^2 - C_{l_w}^2)$, imposed by the runner and the guide vanes on S_0 is $-0{,}130$ and $-0{,}095$, respectively. Therefore, if the pressure p_∞ is not sufficiently above atmospheric, the possibility arises for the minimum static pressure p_0 to become *smaller* than the *vapor pressure* of the water, whereas the pressure p_w may be sufficiently above this point. The result may be cavitation effects on the guide vanes or even on the vanes of the runner; additional hydraulic shock may also occur.

To reduce the above irregularities, it is *necessary* to add suitably designed *fixed blades* outside S_0; a method for this design is described in the next section at b). Nevertheless, the problem of a considerable lowering of the static pressure on the wall of the spiral tongue (that is a little before the point A) remains, since the influence of the flow modification caused by the fixed blades, appears to be imperceptible in this particular region (see Fig. 3.05). This is due to the fact that, in the transition zone, the flow tends to obtain the form given by the law (2.71), as mentioned in § 2.2.2 d) and § 2.3.2. Observing, for example, the $(P_s)_{II}$-distributions in Figs. 2.37 and 2.52, we can see that, in both the Archimedes' casing and the three-dimensional casing examined, the minimum values $(P_s)_{cr}$ of these distributions are $-2{,}30$ and $-2{,}21$ respectively; i.e. much smaller than the corresponding values of P_w. Comparing $(P_s)_{cr}$ with $P_0^*(2\pi)$ we obtain

for the Archimedes' spiral: $$(P_s) = \frac{-2{,}30}{-2{,}95} P_0^*(2\pi) = 0{,}78\, P_0^*(2\pi)$$

for the three-dimensional spiral: $$(P_s) = \frac{-2{,}21}{-3{,}23} P_0^*(2\pi) = 0{,}68\, P_0^*(2\pi);$$

hence, if $(p_s)_{cr}$ is below the vapor pressure of the water cavitation effects and hydraulic shock may appear, even if fixed blades are present.

b) Centrifugal Pump and Blower Spirals Deviating from Eq. (3.02)

If the casing is designed according to Eq. (3.06), the flow has the same form as the one mentioned in the preceding section § 3.2.2 at d) with respect to the velocity distribution, the vorticity, etc. The case $\bar{\alpha}_w' > \bar{\alpha}_w$ there, corresponds to the case $\alpha_c < \bar{\alpha}_w$ here. Thus, for $\alpha_c < \alpha_w$, we have an increase of C_0 (decrease of $\bar{\alpha}_0$) and a decrease of P_0. These conditions cause, in turn, a significant increase in the vorticity, and tend to increase the value of C_{r_0} as θ increases; e.g., to obtain the form

$$C_{r_0} = \bar{C}_{r_0}\left(1 - \beta \cos\frac{\theta}{2}\right),$$

where $0 < \beta < 1$. In general, as the number of the vanes of the impeller increases, β becomes smaller. The irregularity of the distribution of C_{r_0} could cause hydraulic shock within the vane passages, especially when the vanes pass the spiral tongue; the increase of the vorticity, on the other hand, introduces additional losses in the case of an actual viscous fluid.

We can reduce the above irregularities, at least when a pump or blower runs under normal conditions, by using suitably-designed fixed blades (see following section).

c) Comparison between Eq. (1,17) and Eqs. (3.02) and (3.06)

We have seen in § 1.1.2 that a common method of engineering design of turbine spirals, is by making use of Eq. (1.17),

$$\frac{S_\theta}{S_{2\pi}} = \frac{\theta}{2\pi}\frac{1}{\bar{c}_t/c_T}, \tag{1.17}$$

where the original value of $\bar{c}_t/c_T$ was 1 (one); namely the mean tangential component $\bar{c}_t$ of the velocity along a meridian section at azimuth θ remains constant in the entire region $0 \leqq \theta \leqq 2\pi\,(c_T \equiv \bar{c}_t(2\pi)$, see Eq. (1.16)). As also mentioned, according to the construction and the turbine characteristics, the velocity c_T is limited to a few meters/sec. More specifically, the ratio between the radial component c_{r_0} of the velocity along $S_0\,(c_{r_0} = \text{const.})$ and the velocity c_e on the entrance cross-section S_e of the spiral (see Figs. 1.02 and 1.05) are, for engineering design, related to the specific speed n_s of the turbine. In general,

$$\frac{c_{r_0}}{c_e} \approx 0{,}5 - 0{,}9\,;$$

the smaller value corresponds to low n_s, $n_s \approx 50$, the greater value to higher n_s, $n_s \approx 400$. Since we can put $c_e \equiv c_\infty$ we see that for engineering design,

$$\frac{c_{r_0}}{c_\infty} = C_{r_0} = \frac{S_p}{S_0} \approx 0{,}5 - 0{,}9\,.$$

The velocity c_T generally assumed to exceed by about 5 per cent the value of c_e and, in general, the angle α_w in the case of turbines lies approximately between 20° and 45°; larger angles correspond to higher n_s. Comparing these empirical values with the values of S_p/S_0, given e.g. in *Table VI* (see § 3.2.2 at c)), we may say that, by means of this method of design, the meridian cross-sections S_θ obtained are smaller than those obtained by means of Eq. (3.02). To get a better picture, let us write Eq. (1.17) as follows

$$\frac{S_\theta}{r_0} = \int_{r_0}^{r_s} \frac{h}{r_0}\,dr = h_0\frac{S_{2\pi}}{S_0}\theta, \tag{3–1.17}$$

where $\bar{c}_t = c_T$ is assumed. H_s, on the other hand, is

$$H_s = \int_{r_0}^{r_s} \frac{h}{r}\,dr$$

($H_s = h_0\,\theta\,\mathrm{tg}\,\alpha_w$ only if Eq. (3.02) is valid).

We see from Eq. (3–1.17) that S_θ is proportional to θ, whereas the corresponding H_s cannot be also similarly proportional since $r_0 < r$. With exception of the origin $\theta = 0$, where both S_θ/r_0 and H_s are zero, H_s always remains smaller than S_θ/r_0; its plot vs. θ is a curve of decreasing incline whose deviation from

the line S_θ/r_0 increases as θ increases. Taking into consideration the values of S_p/S_0, c_T and α_w, as given above, we see that the ratio $S_0 \operatorname{tg} \alpha_w/S_{2\pi}$ remains bigger than 0,7 and approaches 1 (one) or even more, as n_s increases. Hence the values of H_s which correspond to meridian sections obtained by means of Eq. (3–1.17) must be found smaller than those values of H_s which are according to Eq. (3.02), either from the origin of the spiral or from an intermediate section up to 2π. The result, according to the law (2.71), will be a *non-uniform* distribution of C_{t_0} along S_0; as θ increases C_{t_0} becomes increasingly larger than the desired $C_{t_w} = C_{r_0}/\operatorname{tg} \alpha_w$ whereas, at small angles θ near the origin of the spiral both C_{t_w} and C_{t_0} are of the same order. Accordingly, as already mentioned, high and unevenly distributed energy losses and other irregularities (for the viscous fluid) could appear, if special precautions are not taken in the design of the fixed blades (see following section). We have seen in § 1.1.2 that, because of these irregularities, the manufacturers were led by experience to deviate from the law $\bar{c}_t = c_T$ and to follow families of $\bar{c}_t/c_T$-curves like those shown in Fig. 1.08, in which $\bar{c}_t$ increases with decreasing θ.

We are now in a position to explain the form of these curves by means of the law (2.71) and the related Eqs. (3.02) and (3.06); for, in designing the spiral, to accept gradually increased values of $\bar{c}_t$ form $\theta = 2\pi$ to $\theta = 0$ is, in fact, nothing other than a tendency to approach Eq. (3.02) or Eq. (3.06) and so to obtain a uniform distribution of C_{t_0} along S_0. We shall see, in the next section, that, when the spiral casing is according to Eq. (3.02) or to Eq. (3.06) it is possible to design equally-spaced fixed blades which impose upon S_0 the desired velocity C_{tw} without generation of turbulence etc.

The manufacturers following purely experimental methods which do not differentiate between potential and friction effects were led to approximately the same spiral configurations and fixed blade configurations in order to minimize energy losses and hydraulic shock. We can say, therefore, that the form of the empirical curves shown in Fig. 1.08 is an indirect verification of the law (2.71) on which Eqs. (3.02) and (3.06) are based.

3.2.4. Fixed Blade Design

It is beyond our scope to discuss the necessity of the fixed blades in spiral casings if the casings are designed according to Eq. (3.02), since this is a problem of viscous-fluid flow and of strength of material rather than a problem of potential flow where, obviously, fixed blades are not needed.

a) Fixed-Blade Design in Casings which are According to Eq. (3.02)

If fixed blades are necessary, the better solution, from the point-of-view of fluid mechanics, is to give them the form of the potential flow stream-surfaces. These surfaces can be determined by means of an electric analogy model of the spiral by putting the electrical equivalent of $C_{r_0} = \text{const.}$ along S_0. For constructional and manufacturing purposes, however, the fixed blades are, preferably, formed as surfaces of two-dimensional curvature (cylindrical surfaces parallel to the z-axis). Thus, we can avoid the above experimental investigation by designing the blades according to Eqs. (2.75) and (2.77),

$$\operatorname{tg}\bar{\alpha}^* = \frac{H_s}{h_r}\frac{1}{C_{r_0}\theta}\frac{dT_3}{d\theta} \tag{2.75}$$

$$K_r^* \equiv \frac{Q_r^*}{Q_0} = \frac{1}{2\pi}\frac{H_{rs}}{H_s}\theta, \tag{2.77}$$

(see § 2.3.2 b)). Since the casing shape satisfies Eq. (3.02), the validity of the above relationships is extended at least up to $\theta = 2\pi$ viz. for $\theta \leqq 2\pi$, $\bar{\alpha} = \bar{\alpha}^*$ and $K_r = K_r^*$. Using therefore Eq. (3.02) we obtain

$$\operatorname{tg}\bar{\alpha} = \frac{1}{h_r}\frac{d}{d\theta}(H_{rs}), \tag{3.07}$$

(see also Eq. (2.73)),

and

$$K_r = \frac{1}{2\pi}\frac{H_{rs}}{h_0}\frac{1}{\operatorname{tg}\alpha_w}. \tag{3.08}$$

If r_a is the desired outside radius of the fixed blades, the plot of K_r vs. θ gives the distribution of the volume rate of flow passing through the cylindrical surface S_a at the radius r_a. We can thus determine the position of the leading edge of every fixed blade, the trailing edges of which are equally spaced along S_0, by dividing the K_r-curve in N equal parts δK_r (see Fig. 3.04); N is the number of the openings between successive fixed blades. Consequently,

$$N\,\delta K_r = \int_{\theta_r}^{\theta_r'} K_r\, d\theta = \frac{Q_0}{Q_0} = 1{,}0,$$

where θ_r, θ_r' are the two ends of the surface S_a (see also Fig. 2.32). Hence,

$$\delta K_r = \frac{1}{N}. \tag{3.09}$$

The angle $\bar{\alpha}(r_a, \theta)$ at the leading edge of every blade can be determined by means of the $\bar{\alpha}(r_a, \theta)$-distribution vs. θ, given by Eq. (3.07). It can be seen from Eqs. (3.08) and (3.07) that, in general, the fixed blades so obtained will be neither identical nor equally-spaced along S_a. However, by means of particular precautions taken during the designing of the meridian section forms of the casing, we may reduce the above irregularities to a minimum. Thus, if in the region $(r_a \leqq r \leqq r_s, \theta_r < \theta < \theta_r')$ the casing walls are designed in a manner giving

$$K_r(r_a, \theta) = \frac{\theta - \theta_r}{\theta_r' - \theta_r} \tag{3.10}$$

namely if K_r is a straight line vs. θ, the fixed blades can be equally-spaced along S_a. It is obvious that possible irregularities of K_r in the neighbouring end-regions by θ_r and θ_r' have no influence.

Inserting Eq. (3.10) into Eq. (3.08) we obtain the geometrical condition.

$$\frac{H_{rs}(r_a, \theta)}{h_0} = \frac{2\pi}{\theta_r' - \theta_r}(\theta - \theta_r)\operatorname{tg}\alpha_w \quad (\theta_r < \theta < \theta_r'); \tag{3.11}$$

further, by using Eq. (3.11), we obtain from (3.07)

$$\operatorname{tg} \bar{\alpha}(r_a, \theta) = \frac{2\pi}{\theta_r' - \theta_r} \frac{h_0}{h_r} \operatorname{tg} \alpha_w, \tag{3.12}$$

since $d(\theta - \theta_r) = d\theta$.

If the meridian sections are designed according to Eq. (3.11), a uniform distribution of the fixed blades along S_a can be obtained; on the other hand, the condition $\bar{\alpha}(r_a, \theta) = \text{const.}$ along S_a can be obtained by using Eq. (3.12) when h_r is constant. To secure a correct fixed-blade shape, it is also recommended that Eqs. (3.11) and (3.12) be satisfied, at least at an intermediate radius between r_a and r_0 for example, at the radius

$$r = r_0 + \frac{r_a - r_0}{2}.$$

In all the above calculations, the leading edge of every fixed blade is assumed to be a straight line parallel to the z-axis, and the divergence angle between the spiral walls, along which S_a is limited, is assumed to be not very large; i. e. if it does not exceed 100° (see § 2.3.2 b)). For greater wall divergence, an additional experimental investigation of the angle $\alpha(r, \theta, z)$ in the region around r_a is required by means of the electric analogy method. In this manner, a suitable curvature of the fixed-blade leading edges, projected on a meridian section, may be determined in order to avoid angles of attack which could appear if only the mean angle value $\bar{\alpha}(r_a, \theta)$, and consequently a straight leading edge, is considered.

The particular case $\theta_r' - \theta_r \approx 2\pi, (r_0 \leqq r \leqq r_a)$: In this case, Eq. (3.11) practically becomes

$$\frac{H_{rs}}{h_0} = (\theta - \theta_r) \operatorname{tg} \alpha_w.$$

Thus, by writing

$$H_{0r} = \int_{r_0}^{r} \frac{h}{r} dr = H_s - H_{rs}, \tag{3.13}$$

we obtain from the preceding equation

$$\frac{H_{0r}}{h_0} = \theta_r \operatorname{tg} \alpha_w (= \text{const.}) \tag{3.14}$$

since, according to Eq. (3.02), $H_s = h_0 \theta \operatorname{tg} \alpha_w$. Eq. (3.12), on the other hand, becomes

$$\operatorname{tg} \bar{\alpha} = \frac{h_0}{h_r} \operatorname{tg} \alpha_w, \tag{3.15}$$

Hence, when $\theta_r' - \theta_r \approx 2\pi$ and the casing is according to Eq. (3.02), the fixed blades can be shaped *identically* if, in addition, the spiral is axially symmetric in the region $(r_0 \leqq r \leqq r_a, \theta_r < \theta < \theta_r')$ and fulfills Eq. (3.14). The inclination of the blades can be determined by Eq. (3.15), where for $r = \text{const.}$, also $h_r = \text{const.}$ Their position can be determined by the relationship

$$\theta_n = \frac{2\pi n}{N} + \theta_r \text{ rad.},$$

or,
$$\theta_n^0 = \frac{360\, n}{N} + \theta_r^0 \text{ degrees}, \tag{3.16}$$

which derives from Eqs. (3.09) and (3.10); $n = 1, 2, 3, \ldots, (N-1)$ is the number of the respective fixed blades.

b) Fixed-Blade Design in Casings Deviating from Eq. (3.02)

In casings of this type, the addition of fixed blades seems to be necessary since, if they are present, flow irregularities along S_0 (hydraulic shock or intensive vorticity in pumps and blowers) may be reduced.

As already mentioned, the deviations from Eq. (3.02) of practical interest are of the form

$$H_s < h_0\, \theta \operatorname{tg} \alpha_w;$$

viz. casings which impose increasing values of C_{t_0} as θ increases, whereas the wheel, or guide vanes, impose along S_0 a constant tangential velocity

$$C_{t_w} = \frac{C_{r_0}}{\operatorname{tg} \alpha_w};$$

C_{t_0} is always bigger than C_{t_w}, except at the points $\theta = 0$ and $\theta = 2\pi$, where they are equal. The purpose of the fixed blades in such casings is to modify the flow outside S_0 as much as possible so as to obtain the desired distributions $C_{t_w} = \text{const.}$ and $\alpha_w = \text{const.}$ along S_0. The fixed blades, in other words, must *reduce* the total circulation of the fluid passing through S_0 in the case of turbines, or *increase* it in the case of pumps or blowers. The part of the circulation which must be generated around each individual blade can be expressed as

$$(\delta \Gamma)_n = -\frac{2\pi r_0}{N} (C_{t_0} - C_{tw})\, c_\infty$$

$$(n = 1, 2, 3, \ldots (N_v - 1));$$

the blades are assumed to be equally spaced along S_0; n is the number of the respective blade (see also section 3.1 and Fig. 3.01). The distribution of $(\delta \Gamma)_n$ along the (n)-blade is

$$\gamma_n = \frac{d}{d\, s} (\delta \Gamma)_n,$$

where s represents the arc length on the blade. Let r_a be the outside radius of the fixed blades and r' an intermediate radius between r_a and r_0; let us say, $r' \approx r_a - {}^1/_8 (r_a - r_0)$. The fixed blade shape for which γ_n vanishes in the region $r_a \geqq r \geqq r'$, and for which the inclination on S_0 is α_w, seems to be the most convenient. The first condition can be approximated by designing the fixed blade form between r_a and r' so that it follows the mean angle $\bar{\alpha}(r, \theta)$. From r' to r_0 the blade can be suitably shaped to obtain the inclination α_w on S_0. In this manner angles of attack can be reduced to a minimum in the case of turbines. In the case of pumps or blowers the fluid leaving the surface S_a has

already obtained the flow conditions which the casing imposes on S_a. The design of the fixed blades according to the above recommendations can be made by using Eqs. (2.75) and (2.77), for $r=r_a$ and $r=r'$, and by following the method described above. Generally speaking, the fixed blades will not be equally spaced along S_a and the distribution of $\bar{\alpha}^*(r_a,\theta)$ will not be uniform. We could, however, obtain a uniform distribution of the fixed blades by the following method: First Eq. (3.10) must be satisfied; then according to Eqs. (2.77), (3.10) and (3.13) we get

$$K_r^* = \frac{\theta-\theta_r}{\theta_r'-\theta_r} = \frac{\theta}{2\pi}\left(1-\frac{H_{0r}}{H_s}\right).$$

Let us consider the usual case $\theta_r'-\theta_r \approx 2\pi$. Here the above relationship takes the form

$$\frac{H_{0r}}{H_s} = \frac{\theta_r}{\theta}, \quad (\theta_r < \theta < \theta_r'). \tag{3.17}$$

Introducing this expression into Eq. (2.75) and taking into account Eq. (2.73), we obtain

$$\operatorname{tg}\bar{\alpha}^* = \frac{H_s}{h_r}\frac{1}{\theta} = \frac{H_{0r}}{h_r}\frac{1}{\theta_r}. \tag{3.18}$$

Hence, in order to get uniformly-distributed fixed blades in the region between r_a and r', when $\theta_r'-\theta_r \approx 2\pi$, Eq. (3.17) must be satisfied, and the relation between H_{0r} and h_r must be chosen so that Eq. (3.18) gives $\bar{\alpha}^*$ constant in $\theta_r < \theta < \theta_r'$; namely, we must have

$$\frac{H_{0r}}{h_r} = \text{const.}, \tag{3.18.1}$$

or, the same

$$h_r \sim \frac{H_s}{\theta}.$$

The position of the blades along S_a and S_r' can be determined by Eq. (3.16),

$$\theta_n = \frac{2\pi n}{N} + \theta_r \quad (n = 1, 2, \ldots, (N-1);\ r = r_a, r').$$

In all the above relations concerning K_r and $\bar{\alpha}$, we kept the index * since the law (2.71) from which Eqs. (2.75) and (2.77) are derived is approximately valid in the region near $\theta = 2\pi$.

The particular case $\theta_r'-\theta_r \approx 2\pi$ *and* $H_s \sim \theta$: Let us examine the fixed blade design in a spiral which is according to Eq. (3.06),

$$\frac{H_s}{h_0} = \theta \operatorname{tg}\alpha_c, \quad (\alpha_c = \text{const.} < \alpha_w), \tag{3.06}$$

where $\theta_c \leqq \theta_r$; then, as mentioned in § 3.2.3, in the region $\theta_r < \theta < 2\pi^+$

$$C_{t_c} = C_t\frac{r}{r_0} = \frac{C_{r_0}}{\operatorname{tg}\alpha_c} = \text{const.} > C_{t_w},$$

except in the vicinity of the point $(r_0, 2\pi)$. Inserting Eq. (3.06) into Eqs. (3.17) and (3.18) we obtain

$$\frac{H_{0r}}{h_0} = \theta_r \operatorname{tg}\alpha_c (= \text{const.}), \tag{3.19}$$

and $$\operatorname{tg}\bar{\alpha} = \frac{h_0}{h_r}\operatorname{tg}\alpha_c. \tag{3.20}$$

The validity of Eqs. (3.19) and (3.20) is extended up to $2\pi^+$ except in the vicinity of the point $(r_0, 2\pi)$.

Hence, the fixed blades may be *identically* shaped if the spiral is axially symmetric in the region $(r_0 \leqq r \leqq r_a, \theta_r < \theta < \theta'_r)$, and if it satisfies Eq. (3.19) in this region. The blade inclination in the zone $r_a \geqq r \geqq r'$ can be determined by means of Eq. (3.20) where, for r constant, h_r is also constant; their position on S_a may be determined by means of Eq. (3.16). In the zone $r' \geqq r \geqq r_0$ the blades can be suitably curved to obtain the inclination α_w on S_0. In this manner, and since the guide vanes are inside the fixed blades, a constant *mean tangential* velocity along the openings between successive fixed blades can be obtained (normal running conditions);

$$(C_{t_0})_n^{n+1} = C_{t_w}, \quad (n = 0, 1, 2, \ldots, (N-1)).$$

The variations of C_{t_0} within every opening depend on the difference $C_{t_e} - C_{t_w}$, the number N of the fixed blades and the ratio r_a/r_0. These variations increase as $C_{t_e} - C_{t_w}$ increases and decrease as N and r_a/r_0 increase. Hence, in the case of the actual viscous fluid, additional turbulence, consequently additional energy losses within the region of the fixed blades, could appear; the determination of the ratios H_{0r}/h_r, r_a/r_0, $r_a - r'/r_a - r_0$ vs. α_w with α_c, N and the Reynold's number as parameters to obtain optimum results is a matter of experiments.

An important factor affecting the minimum permissible value of α_c, especially in the *low pressure* turbines, is the value of the static pressure p_a along S_a. Its dimensionless expression (see Eq. (2.13.1)) is

$$P_a = 1 - C_a^2 = 1 - (C_{r_a}^2 + C_{t_a}^2 + C_{z_a}^2),$$

where the components C_{r_a} and C_{z_a} are functions of r_a and z, and $C_{t_a} = C_{t_e} r_0/r_a$. In general, C_{r_a} and C_{z_a} are small in comparison with C_{t_a}. Further, if the divergence angle of the walls bounding the surface S_a does not exceed 100°, $\max C_{r_a}$ does not greatly exceed the mean value $\bar{C}_{r_a}$, while in the plane of symmetry $(z = 0)$, $C_z = 0$; therefore, we can write as a first approximation

$$\bar{P}_a \approx 1 - \bar{C}_a^2 \approx 1 - (\bar{C}_{r_a}^2 + C_{t_a}^2).$$

The mean value of the static pressure P_w along S_0 can be written, on the other hand,

$$\bar{P}_w \approx 1 - \bar{C}_w^2 = 1 - (\bar{C}_{r_0}^2 + \bar{C}_{t_0}^2),$$

$(\bar{C}_{r_0} = S_p/S_0)$. It is desirable to have

$$\bar{P}_a \geqq \bar{P}_w. \tag{3.21}$$

or, the same $$\bar{C}_a \approx \frac{C_{t_a}}{\cos\bar{\alpha}} \leqq \bar{C}_w = \frac{\bar{C}_{r_0}}{\sin\alpha_w}.$$

Since $$C_{t_a} = C_{t_e}\frac{r_0}{r_a} = \frac{\bar{C}_{r_0}}{\operatorname{tg}\alpha_c}\frac{r_0}{r_a}$$

and $$\cos\bar{\alpha} = \frac{1}{\sqrt{1+\mathrm{tg}^2\,\bar{\alpha}}} = \frac{1}{\sqrt{1+\left(\frac{h_0}{h_r}\right)^2 \mathrm{tg}^2\,\alpha_c}},$$

(see Eq. (3.20)), we obtain from the above condition (3.21)

$$0 < \frac{r_0}{r_a}\,\frac{\sin\alpha_w}{\mathrm{tg}\,\alpha_c}\sqrt{1+\left(\frac{h_0}{h_{r_a}}\right)^2 \mathrm{tg}^2\,\alpha_c} \leqq 1\,;$$

hence $$\mathrm{tg}\,\alpha_c \geqq \frac{1}{\sqrt{\left(\frac{r_a}{r_0}\right)^2 \frac{1}{\sin^2\alpha_w} - \left(\frac{h_0}{h_{r_a}}\right)^2}}. \tag{3.22}$$

In designing a spiral casing according to Eq. (3.06) it is recommended that the condition (3.22) be satisfied. (For the critical pressure $(P_s)_{cr}$ etc. see § 3.2.3 a)).

Example: Modification of the Spiral Form Shown in Fig. 2.04 by Using Eq. (3.06)

We shall attempt this modification by making the fewest possible changes to the dimensions of the original casing (see Table I in § 2.1.2, and Fig. 1.09 for the fixed blade shape). For this purpose we assume that:

a) The radius r_a of the fixed blade leading edge surface S_a will become 160 mm (the original was $0{,}6 \cdot 545/2 = 165$ mm); thus, $r_a/r_0 = 1{,}35$ ($r_0 = 118{,}5$ mm).
b) The spiral form in the region between S_a and S_0 will become axially symmetric, having $h_{r_a} = 80$ mm; thus $h_{r_a}/h_0 = 1{,}73$, ($h_0 = 46{,}2$ mm), $r_r' = 54{,}5$ mm and $d_0' = 240$ mm (see Table I). Further, according to Eq. (3.13), $H_{0r}/h_0 = 0{,}363$.
c) The radius r_s at $\theta = 2\pi$ will not exceed the original value 320,8 mm by more than 8 per cent.
d) The original value 45° for α_w (normal running conditions of the turbine) and the number $N = 12$ of the openings between fixed blades are unchanged.

Thus according to Eq. (3.22), we obtain

$$\mathrm{tg}\,\alpha_c \geqq \frac{1}{\sqrt{\left(\frac{1{,}35}{0{,}707}\right)^2 - \frac{1}{1{,}73^2}}} = 0{,}539.$$

We accept the minimum recommended value 0,539 for $\mathrm{tg}\,\alpha_c$; thus

$$\alpha_c = 28^\circ 20'.$$

Hence, according to Eq. (3.19),

$$\theta_r = \frac{1}{0{,}539} \cdot 0{,}363 = 0{,}673 \text{ rad},$$

or

$$\theta_r = 38^\circ 30',$$
$$\theta_r' = 398^\circ 30'$$

(the wall thickness is eliminated in this calculation) and, according to Eq. (3.06)

$$\frac{H_s}{h_0} = \theta\,\mathrm{tg}\,\alpha_c, \quad (\theta_r \leqq \theta \leqq \theta_r').$$

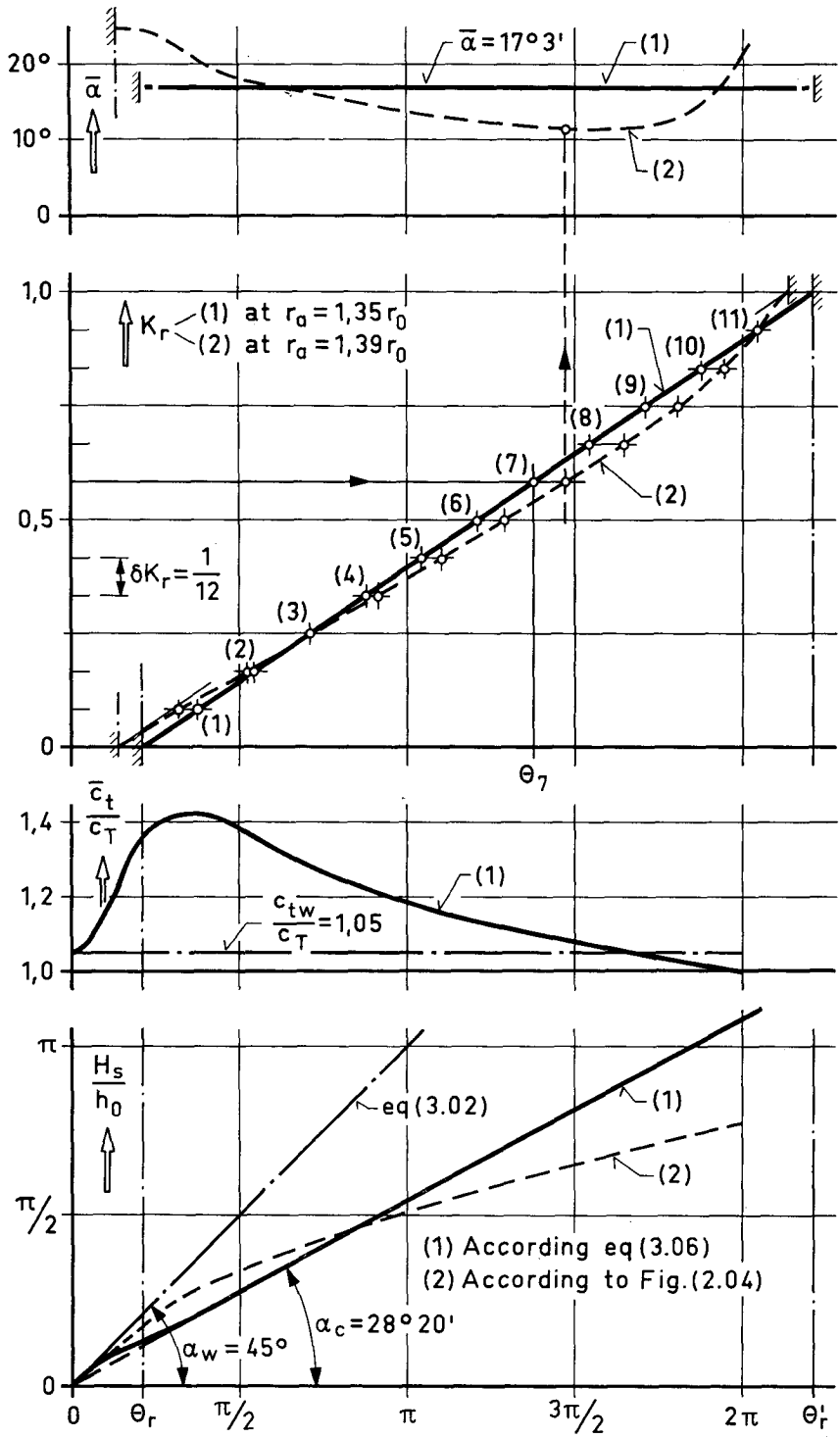

Fig. 3.04. Modification of the spiral form shown in Fig. 2.04. (1) Modified H_s/h_0-distribution and the related K_r (strength line) and $\bar{\alpha}$ (= const) at the entrance of the fixed blades; (2) The same distributions for the original spiral (Fig. 1.09).

We give below in *Table VII* the values of H_s/h_0 and the respective shapes of some characteristic meridian sections, where r_k is the radius of the center-line of the section and d_s its diameter (see also Table I). The validity of Eq. (3.06)

Table VII. Characteristics of the Spiral Casing Shown in Fig. 3.05 (Spiral Form (1))

Characteristics	Azimuth θ					
	0	$\pi/2$	π	$3\pi/2$	2π	
H_s/h_0	0	0,845	1,690	2,535	3,380	
r_s (mm)	118,5	220	282,5	315	346	
r_k (mm)	118,5	178	215	235	252,5	
d_s (mm)	0	88	135	160 180	187 230	$\perp$ z-axis $\parallel$ z-axis
S_θ (cm²)	0	65	158	249	361,5	

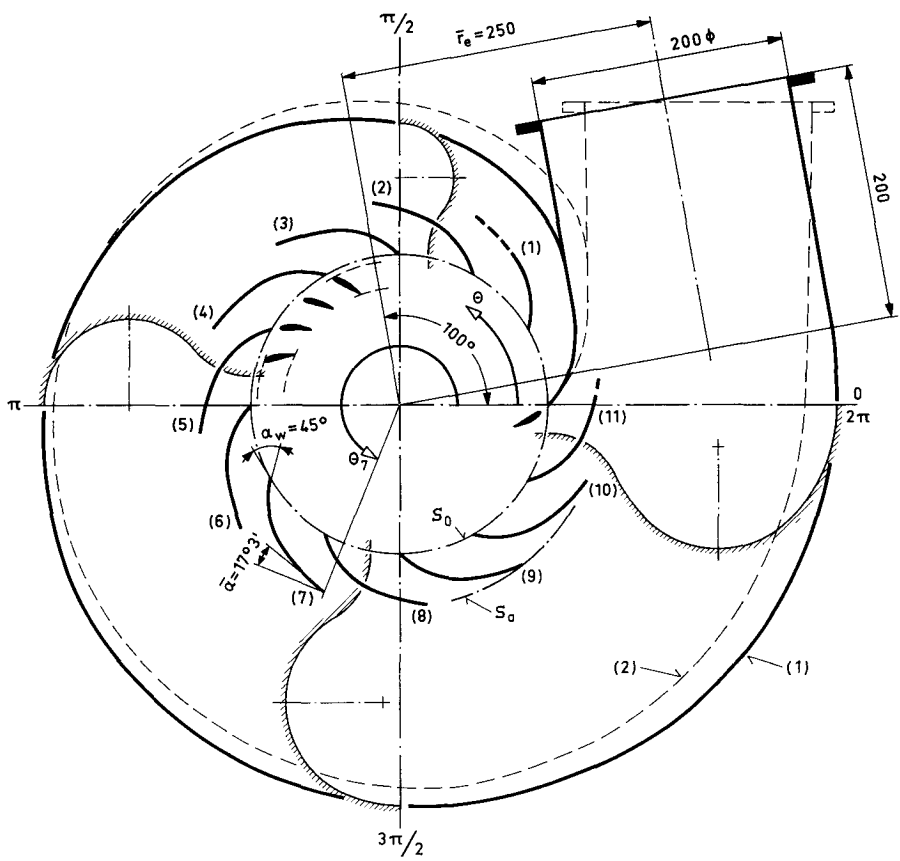

Fig. 3.05. Modification of the spiral form shown in Fig. 2.04. (1) Modified form; (2) Original form.

is extended from about 60° to 370° as shown in Fig. 3.05. In the region from 60° to 0° we assume a small deviation from the H_s/h_0 vs. θ straight-line in order to obtain an inclination of 45° at $\theta = 0°$. As we shall see below, the leading edge of the (1)-fixed blade on S_a is at $\theta = 68° 30'$; therefore, even if the value of θ_r is 38° 30', we formed the casing at $r_a = 160$ mm to pass through the point $\theta = 32°$ instead of $\theta = 38° 30'$. This small deviation has, in fact, no influence on the formation of the flow. In the region $60° < \theta < 200°$ the meridian sections are of a circular form, while from 200° they begin gradually to be quasi-elliptic up to 370°. From this point onwards, the center-line of the sections continues as straight line at an angle of 110° with respect to the $\theta = 0$ axis; the section shape is, on the other hand, gradually transformed until it becomes circular at the entrance section. The entrance cross-section S_p has a diameter of 200 mm ($S_p = 314$ cm²). Fig. 3.05 shows the general arrangement of the modified casing, spiral (1); the original casing is shown by the dotted spiral (2).

To show the similarity of the empirial curves $\bar{c}_t/c_T$ given in Fig. 1.08 (see also § 3.4.3c) with the curve obtained by Eq. (3.06), we plotted the respective values $\bar{c}_t/c_T$ for the modified casing in question vs. θ, as shown in Fig. 3.04.

For the *fixed-blade* design we use Eqs. (3.16) and (3.20); thus on S_a we obtain

$$\theta_n = \frac{360\,n}{12} + 38° 30' = 30\,n + 38° 30', \quad (n = 1, 2, \ldots, 11)$$

and
$$\operatorname{tg} \bar{\alpha} = \frac{h_0}{h_{r_a}} \operatorname{tg} \alpha_c = \frac{1}{1{,}73} \cdot 0{,}539 = 0{,}311;$$

hence,
$$\bar{\alpha} = 17° 3'.$$

Fig. 3.05 shows the fixed-blade arrangement according to this method of design. We observe that, with respect to the angle $\bar{\alpha}$, the difference between this arrangement and the original, which at $r_a = 165$ mm has $\alpha_v = 18° 30'$, is small (see Figs. 1.09 and 3.01); the main difference is in the angle θ_n of the blade leading-edges along S_a, and in the formation of the spiral shape.

As already mentioned, by using Eqs. (2.75) and (2.77), we could design the fixed blades in the original casing to reduce the angles of attack, too. But, since the plot of H_s/h_0 vs. θ of the original casing is not a straight line (see Fig. 1.10a and 3.04), the blades on S_a cannot, in general, be equally spaced and they cannot have the same inclination $\bar{\alpha}$. The dotted curves of $\bar{\alpha}$ and K_r vs. θ, curves (2) shown in Fig. 3.04, refer to the original casing and give us an idea of the irregular shape and position that the fixed blades should obtain in order to reduce the angle of attack.

Summary

An investigation has been made of the potential flow through two-dimensional and three-dimensional spiral casings. Since a purely mathematical treatment of this problem encounters nearly insurmountable difficulties, the *electric analogy* method was applied.

To form a suitable electric analogy model, the surface S_0 encircling the guide-vanes of a turbine, or the impeller of a pump, was represented by an assembly of a large number of *electrodes* which were equally spaced and insulated from each other (see Fig. 1.24); as electrolyte, *tap-water* was used. Special care was taken in arranging the electrodes and the insulators in order to avoid any possible *secondary ohmic current* between electrodes. Furthermore, special care was taken in forming the electric analogy circuit in order to reduce the influence of the *secondary capacitive currents* to a minimum, during the establishment of the electric field and during the point-by-point measurements of the electric potential (to avoid the polarization of the electrodes, alternating current was used).

In order to establish the *same* boundary condition for the electric field as for the potential flow, we had to fix along S_0 a current-distribution numerically proportional to the given volume flow-rate distribution. By *iterating* the distribution of the currents through the electrodes by means of potentiometers (see Fig. 2.08), we established the desired current-distribution. From the mathematical point-of-view, this experimental process corresponds to the method of solving an *integral equation* by iterations, since an equation of this form connects the shape of the spiral casing with the current and the resistance of each potentiometer.

The experiments were made on four spiral models (two 2-dimensional and two 3-dimensional). The results can be summarized by the following law:

The velocity-moment ($c_t r$) of the fluid passing through a spiral casing remains constant along a meridian section, but may change from one meridian section to another; its value is a function of the volume flow-rate distribution along S_0, the form of the section perimeter and the azimouth of the section.

This experimental fact enables us:

I. To formulate the general expression concerning the distribution of: a) the tangential component of the velocity, b) the volume flow-rate and c) the mean radial component of the velocity along any cylindrical section of the spiral casing at a radius r from its center-axis, etc. We note that an *axially symmetric* flow outside S_0 is a particular case of the above experimental law.

II. To give some recommandations for the formation of: a) a spiral casing giving a constant distribution of the quantities specified above in I., a) and c), in a region from S_0 to a desired greater radius, when the volume flow-rate along S_0 is constant. b) the fixed-blade shapes of turbines etc.

Zusammenfassung

Es wurde eine Untersuchung über die Potentialströmung in zwei- und dreidimensionalen *Spiralgehäusen* durchgeführt. Da eine rein mathematische Behandlung des vorliegenden Problems auf außerordentliche Schwierigkeiten führt, gelangte die Methode der *elektrolytischen Analogie* zur Anwendung.

Um eine elektrisch analoge Anordnung zu erhalten, wurde die äußere Kontur S_0, die den Leitapparat einer Turbine oder eines Pumpenrades umgibt, durch eine große Anzahl gegenseitig isolierter und gleich breiter *Elektroden* dargestellt (vergleiche Fig. 1.24). Als Elektrolyt diente *Leitungswasser*. Die Vermeidung von *sekundären Ohmschen Strömen* zwischen den Elektroden erforderte spezielle Sorgfalt bei der Ausführung der Elektroden und der isolierenden Zwischenstücke. Im weiteren wurde bei der Installation der elektrischen Kreise besonders darauf geachtet, den Einfluß der *sekundären Kapazitätsströme* beim Aufbau des elektrischen Feldes und bei der punktweisen Messung des elektrischen Potentials auf ein Minimum zu reduzieren. Die Verwendung von Wechselstrom verhinderte eine Polarisation der Elektroden.

Die Forderung nach den *gleichen Grenzbedingungen* für das elektrische Feld wie auch für die Potentialströmung verlangte eine Stromverteilung längs der Fläche S_0, die der gegebenen Durchflußmengenverteilung numerisch proportional war. Mit Hilfe von Potentiometern (Fig. 2.08) wurde durch schrittweise Änderung der Stromstärken zu den einzelnen Elektroden schließlich die gewünschte Stromverteilung erreicht. Vom mathematischen Standpunkt aus entspricht dieses experimentelle Vorgehen der Lösung einer *Integralgleichung* durch *Iteration*, denn eine solche Gleichung verknüpft die Form des Spiralgehäuses mit dem Strom und dem Widerstand jedes Potentiometers.

Die Experimente wurden an 2 zweidimensionalen und 2 dreidimensionalen Modellen durchgeführt. Die erhaltenen Resultate können durch das folgende Gesetz zusammengefaßt werden:

Das Geschwindigkeitsmoment ($C_t r$) der Strömung durch ein Spiralgehäuse bleibt längs eines Meridianschnittes konstant; hingegen kann es von Schnitt zu Schnitt ändern. Seine Größe ist eine Funktion der Durchflußmengenverteilung längs S_0, der Form des Querschnittes und des Azimutes des Schnittes.

Diese durch Experimente gefundene Tatsache erlaubt uns:

A. allgemein gültige Ausdrücke zu formulieren für die Verteilung
   a) der Tangentialkomponente der Geschwindigkeit,
   b) der Durchflußmenge,
   c) der mittleren Radialkomponente der Geschwindigkeit längs eines beliebigen zylindrischen Schnittes durch das Spiralgehäuse im Radius r von der Achse. Eine *axialsymmetrische* Strömung außerhalb der Fläche S_0 stellt einen Spezialfall dieses experimentell gefundenen Gesetzes dar.

B. Richtlinien aufzustellen für die Formgebung von:
   a) Spiralgehäusen, die eine konstante Verteilung der unter A. a) und A. c) genannten Größen liefern in einem Gebiet von S_0 bis zu einem gewünschten größeren Radius, vorausgesetzt daß die Durchflußmenge längs S_0 konstant ist,
   b) Turbinenstützschaufeln usw.

List of References

1. *Abraham M.:* The Classical Theory of Electricity and Magnetism. London 1942.
2. *Ackeret J.* und *Gerber H.:* Experimentelle Methoden zur Ermittlung von Potentialströmungsbildern; Escher-Wyss Mitt. Nr. 6, 1928, S. 171—176.
3. *Bazjanac D.:* Untersuchungen mit Hilfe der elektrolytischen Analogie über den Einfluß der Luftstrahlbegrenzung in Windkanälen auf Tragflügelmessungen; Diss. ETH 1943.
4. *Betz A.:* Konforme Abbildung; Springer 1948.
5. *Bromn W. B.* and *Bradshaw G. R.:* Design and Performance of a Family of Diffusing Scrolls with Mixed-Flow Impeller and Vanelles Diffuser. NACA Rep. 936, 1949.
6. *Detra R.:* The Secondary Flow in curved Pipes. Mitt. Inst. Aerod. ETH. Nr. 20, Zürich 1953.
7. *Eck B.:* Strömungslehre; Springer 1954.
8. *Eck B.:* Theorie und Konstruktion von Spiral-Gehäusen; Werft, Reederei, Hafen, Heft 14, 1930.
9. *Eck B.:* Ventilatoren; Springer 1952.
10. *Eckert B.:* Axialkompressoren und Radialkompressoren; Springer 1953.
11. *Ginsburg T.:* Untersuchungen über die dreidimensionale Potentialströmung durch axiale Schaufelgitter; Mitt. Inst. Aerod. ETH Nr. 22, Zürich 1956.
12. *de Haller P.:* Application de l'analogie électrique à l'étude des grilles d'aubes. Revue Technique "Sulzer" 1947, N° 3/4 p. 11—17.
13. *Hepp G.:* Aufnahme von Potentialfeldern mit dem Elektrolyttrog; Philips Techn. Nachrichten 1939, S. 235—242.
14. *Kellogg O.:* Foundations of Potential Theory. Berlin 1929.
15. *Kranz H.:* Strömung durch Spiralgehäuse von Wasserturbinen und Kreiselpumpen; Diss. Techn. Hochschule Hannover 1934.
16. *Kucharski W.:* Strömungen einer reibungsfreien Flüssigkeit bei Rotation fester Körpe; München-Berlin 1918.
17. *Lamb H.:* Hydrodynamics. Cambridge University Press, sixth Edition, 1959.
18. *Malavard L.:* Application des analogies électriques à la solution de quelques problèmes de l'hydrodynamique. Publications scientifiques et techniques du Ministère de l'air N° 57, Paris 1934.
19. *Malavard L.:* La technique des analogies électriques; CNRS, Techniques Générales du Laboratoire de Physique, Vol. II, 1950.
20. *Meyer L.:* Singularitätentheorie der Flügelgitter; Mitt. Inst. Aerod. ETH. Nr. 26, Zürich 1959.
21. *Pfleiderer C.:* Die Kreiselpumpen für Flüssigkeiten und Gase; Springer 1955.
22. *Prandtl L.* and *Tietjens O.:* Fundamentals of Hydro- and Aeromechanics. Dover Publ., New York 1934.
23. *Prandtl L.* and *Tietjens O.:* Appied Hydro- and Aeromechanics. Dover Publ., New York 1934.
24. *Prášil F.:* Über Flüssigkeitswege in Rotationshohlräumen; Schweizer Bauzeit. 41.
25. *Renard G.:* Représentation directe par analogie rhéoélectrique des gradients de fonctions harmoniques en domaine plan limité ou illimité. Publications scientifiques et techniques du Ministère de l'air, N° N.T. 78. Paris 1958.
26. *Sovoka W.:* Analog Methods in Computations and Simulation. McGraw-Hill 1954.
27. *Taylor* and *Sharman:* A mechanical Method for solving Problems of Flow in Compressible Fluids. 1928 Proc. Roy. Soc. London A 121, p. 194—217.
28. *Tenot A.:* Turbines hydrauliques et regulateurs automatiques de vitesse. Livre I, 1930.
29. *Thomann R.:* Die Wasserturbinen und Turbinenpumpen; Band II, 1931.
30. *Webster A.:* Partial Differential Equations of Mathematical Physics. Dover Publ., New York 1955.
31. *Wislicenus G.:* Fluid Mechanics of Turbomachinery. McGraw-Hill 1947.

Curriculum Vitae

I was born in Athens — Greece — on September 25th 1920. I first attended the Greek Elementary School (six years) and then the Greek Gymnasium — Grammar School — (six years), leaving in 1939. In the years 1940 to 1946 I studied at the School of Mechanical and Electrical Engineers of the National Technical University of Athens, from which I graduated.

In the years from February 1st 1948 to June 30th 1955 I was employed as an engineer in the factory of the "Technica S. Malcotsis" Co. (for general machinery and diesel-engine manufacturing).

In the years from July 1st 1955 to September 30th 1957 I was employed as an engineer in the Athens Offices of "Amman and Whitney, Consulting Engineers" Co., New York.

From 1949 to 1957 I was also engaged as Assistant in the Chair of "Heat Engines" (Internal Combustion Engines) in the National Technical University of Athens.

On October 1957 the National Technical University of Athens granted me a scholarship for post-graduate work at the Swiss Federal Institute of Technology in Zurich. After passing the "Examination of admission for a Doctoral Dissertation" in October 1958 I began the present thesis under the direction of Prof. Dr. J. Ackeret of the S. F. I. T. Institute of Aerodynamics in December 1958.

Zurich, August 1960.